Interplay of quantum Hall edge states in graphene with the tip-induced quantum dot and graphene sample fabrication techniques for advanced scanning tunneling microscopy

Von der Fakultät für Mathematik, Informatik und Naturwissenschaften der RWTH Aachen University zur Erlangung des akademischen Grades eines Doktors der Naturwissenschaften genehmigte Dissertation

vorgelegt von

Tjorven Johnsen, Master of Science

aus

Rendsburg

Berichter: Univ.-Prof. Dr. rer. nat. Markus Morgenstern
Assoc. Prof. Dr. Florian Libisch

Tag der mündlichen Prüfung: 20.12.2022

Diese Dissertation ist auf den Internetseiten der Universitätsbibliothek online verfügbar.

Eidesstattliche Erklärung

Tjorven Johnsen
erklärt hiermit, dass diese Dissertation und die darin dargelegten Inhalte die eigenen sind und selbstständig, als Ergebnis der eigenen originären Forschung, generiert wurden.

Hiermit erkläre ich an Eides statt

1. Diese Arbeit wurde vollständig oder größtenteils in der Phase als Doktorand dieser Fakultät und Universität angefertigt;

2. Sofern irgendein Bestandteil dieser Dissertation zuvor für einen akademischen Abschluss oder eine andere Qualifikation an dieser oder einer anderen Institution verwendet wurde, wurde dies klar angezeigt;

3. Wenn immer andere eigene- oder Veröffentlichungen Dritter herangezogen wurden, wurden diese klar benannt;

4. Wenn aus anderen eigenen- oder Veröffentlichungen Dritter zitiert wurde, wurde stets die Quelle hierfür angegeben. Diese Dissertation ist vollständig meine eigene Arbeit, mit der Ausnahme solcher Zitate;

5. Alle wesentlichen Quellen von Unterstützung wurden benannt;

6. Wenn immer ein Teil dieser Dissertation auf der Zusammenarbeit mit anderen basiert, wurde von mir klar gekennzeichnet, was von anderen und was von mir selbst erarbeitet wurde;

7. Teile dieser Arbeit wurden zuvor veröffentlicht und zwar in:

- **Mapping quantum Hall edge states in graphene by scanning tunneling microscopy**
  T. Johnsen, C. Schattauer, S. Samaddar, A. Weston, M. Hamer, K.Watanabe, T. Taniguchi, R. Gorbachev, F. Libisch und M. Morgenstern
  arXiv:2210.01831 [cond-mat.mes-hall] (2022)

- **An ultrahigh-vacuum cryostat for simultaneous scanning tunneling microscopy and magneto-transport measurements down to 400 mK**
  M. Liebmann, J. R. Bindel, M. Pezzotta, S. Becker, F. Muckel, T. Johnsen, C. Saunus, C. R. Ast und M. Morgenstern
  Rev. Sci. Instrum. **88**, 123707 (2017)

Abstract

The quantum Hall effect (QHE) is in large portion rationalized by the edge channel (EC) picture in which the charge transport takes place in stripe like channels along the edge of the sample. For the adequate parameters, ECs can run along a pn interface instead of the physical edge of the sample. Using such a gate-defined pn interface in graphene, compressible stripes that combined wtih incompressible stripes constitute the ECs are studied within this thesis by scanning tunneling microscopy (STM) and spectroscopy (STS). To this end, the Landau level (LL) features are investigated at an interface of different filling factors for varying gate voltages. Charging lines (CLs) emerging in the measurements reveal that a tip-induced quantum dot (QD) develops below the STM tip. Poisson simulations of the experimental setting involving the tip, the graphene layer, and the electrostatic interface are conducted with the purpose to disentangle the contributions of tip and interface on the ECs. Together with tight-binding (TB) calculations on the basis of the Poisson simulations, all experimental features are well understood establishing a useful method for the investigation of ECs. Flat plateaus of constant LL energy and about 40 nm width close to the pn interface indicate electrostatic reconstruction of the ECs into compressible and incompressible stripes due to screening. Besides branches of LL features evolve at the pn interface interconnecting neighbouring LLs. Their explanation depends on the choice of sample and back gate voltage. If a QD is below the tip, its position with respect to the tip gets shifted at the pn interface whereby states at a different position within the QD are probed by the tip. These states are at different orbital energies within the QD. Their successive measurement leads to the observed LL branches. If in contrast no QD exits below the tip, the wave function of the compressible stripe is directly probed. Its position and width are influenced by the tip but without altering the structure of the wave function significantly. This enables to map the wave function of compressible stripes of several LLs for a specific choice of parameters. Likely, the structure of the compressible stripe wave function also reflects a lateral shift of the two sublattice components at the interface.
Furthermore, various processes to fabricate graphene samples for combined electrical transport and STM investigations are described. Two of them are novelly conceived and integrate a graphite back gate into the sample structure. A third process employs a standard dry stacking technique followed by evaporating contacts through a shadow mask. A sample prepared by this method is characterized both by STM and transport measurements displaying interaction induced symmetry breaking of the LLs and the fractional 1/3 quantum Hall state yet only in transport. A different sample prepared by one of the novel methods has little improved quality and a similar outcome of symmetry broken states in transport measurements.
Linking the STM experiments and sample fabrication processes, two procedures to locate a STM tip on a micron-sized graphene sample are presented and both successfully carried out. The first one relies on the optical alignment of tip and sample by means of a long distance microscope. In the second procedure the spatially varying and externally tunable electrostatic force between tip and sample measured by a tuning fork sensor guides the tip to the sample.

Zusammenfassung

Der Quanten-Hall-Effekt (QHE) wird zum Großteil durch das Randkanal-(RK)-Bild erklärt, in dem der Ladungstransport in streifenartigen Kanälen am Probenrand entlang stattfindet. Für passende Parameter können RK auch an einem pn-Übergang anstelle des Probenrands entlang fließen. Ein derartiger pn-Übergang, der durch ein Gate erzeugt wird, wird in Graphen verwendet, um in dieser Arbeit kompressible Streifen, die zusammen mit inkompressiblen Streifen die RK bilden, mittels Rastertunnelmikroskopie (RTM) und -spektroskopie zu erforschen. Dazu werden die Landau-Niveau (LN) Zustände am Übergang zwischen unterschiedlichen Füllfaktoren für verschiedene Gate-Spannungen untersucht. Ladungs-linien (LL), die in den Messungen auftreten, lassen erkennen, dass sich ein Spitzen-verursachter Quantenpunkt (QP) unterhalb der Spitze bildet. Poisson-Simulationen der experimentellen Umgebung mit Berücksichtigung der Spitze, des Graphens und des elektrostatischen Übergangs werden mit dem Ziel durchgeführt, die Einflüsse von Spitze und Übergang auf die RK voneinander zu trennen. In Kombination mit tight-binding (TB)-Rechnungen, die auf den Poisson-Simulationen beruhen, werden alle experimentellen Kennzeichen erklärt, wodurch eine nützliche Methode zur Erforschung von RK geschaffen wird. Flache Plateaus mit konstanter LN-Energie über eine Länge von etwa 40 nm in der Nähe des pn-Übergangs sind Anzeichen elektrostatischer Rekonstruktion der RK in kompressible und inkompressible Striefen durch Abschirmung. Des Weiteren entwickeln sich am pn-Übergang Verzweigungen zwischen benachbarten LN-Zuständen, deren Erklärung von den gewählten Proben- und Gate-Spannungen abhängt. Falls sich ein QP unterhalb der Spitze befindet, verschiebt sich seine Position gegenüber der Spitze am pn-Übergang, wodurch Zustände an einer anderen Stelle innerhalb des QPs von der Spitze gemessen werden. Diese Zustände haben verschiedene orbitale Energien im QP, sodass ihre aufeinander folgende Messung zur beobachteten Verzweigung der LNs führt. Falls sich im Gegenteil kein QP unterhalb der Spitze befindet, wird direkt die Wellenfunktion des kompressiblen Streifen gemessen. Seine Breite und Position sind durch die Spitze beeinflusst, jedoch ohne die Struktur der Wellenfunktion signifikant zu verändern. Dadurch ist es möglich die Wellenfunktion der kompressiblen Streifen von mehreren LNs für speziell ausgewählte Parameter abzubilden. Wahrscheinlich spiegelt die Struktur der Wellenfunktion des kompressiblen Streifens eine räumliche Verschiebung der beiden Untergitterkomponenten am Übergang wider.
Darüber hinaus werden unterschiedlicher Verfahren zur Herstellung von Graphenproben für kombinierte elektrische Transport- und RTM-Untersuchungen beschrieben, wovon zwei neu entworfen sind und ein Gate aus Graphit in die Probenstruktur einbinden. Ein dritter Prozess verwendet eine übliche, trockene Stempelmethode gefolgt von Aufdampfen der Kontakte mittels Schattenmaske. Eine nach diesem Verfahren hergestellte Probe wird sowohl durch RTM- als auch Transportmessungen charakterisiert und weist dabei Wechselwirkungs-verursachte Symmetrieaufhebung der LNs und den fraktionalen 1/3 Quanten-Hall-Zustand auf, letzteren jedoch nur im Transport. Eine weitere, nach einem der neuen Verfahren hergestellte Probe zeigt in Transportmessungen eine geringfügig verbesserte Qualität und ebenfalls Symmetrieaufhebung der LNs.

Als Veknüpfung zwischen RTM-Experimenten und Probenfabrikation werden zwei Vorgehensweisen zur Positionierung einer RTM-Spitze auf einer Mikrometer großen Graphenprobe vorgestellt und beide erfolgreich angewendet. Die erste beruht auf optischer Ausrichtung von Spitze und Probe mithilfe eines Langdistanzmikroskops. Im zweiten Verfahren führt die örtliche veränderliche und von außerhalb einstellbare elektrostatische Kraft zwischen Spitze und Probe, die mittels tuning fork-Sensor gemessen wird, die Spitze zur Probe.

Contents

List of symbols

$\vec{a}_1, \vec{a}_2$	Graphene lattice vectors
a_i	Width of incompressible stripe
α_j	Lever arm of gate j
B	Magnetic field
$\vec{b}_1, \vec{b}_2$	Graphene reciprocal lattice vectors
b_i	Distance between incompressible stripes
$C, C_{\text{tip}}, C_{\text{bg}}$	Capacitance (between graphene and tip or back gate)
d	Distance (normal to the graphene plane)
ΔE	Energy resolution
Δf	Frequency shift (of resonance frequency)
$\Delta\mu_{\text{c,QD}}$	QD depth
$\Delta\Phi = \Phi_{\text{sample}} - \Phi_{\text{tip}}$	Work function mismatch between tip and sample
Δ_{wfm}	Electrostatic potential difference due to work function mismatch
$\mathcal{E}$	Electric field
E	Energy
$e = \lvert e \rvert$	Elementary charge
E_{C}	Charging energy
E_{F}	Fermi energy
E_N	Landau level energy
ϵ	Dielectric constant
ϵ_0	Vacuum permittivity
F, F_{ts}	Force (between tip and sample)
f, f_0	(Resonance) frequency
γ	Normalized frequency shift
$\hbar = \frac{h}{2\pi}$, h	Planck constant
I	Tunneling current
I_{sd}	Source-drain current
k	Spring constant
k_{B}	Boltzmann constant
k_K	Momentum with respect to the K, K' points
K_{v}	Valley index
k_x, k_y	Coordinates in k space
L	Length of the sample
l_B	Magnetic length
Λ	Quality factor
λ	Moiré lattice constant

m	Angular momentum quantum number
$m_\alpha = \Delta V_{\mathrm{bias}}/\Delta V_{\mathrm{pg}}$	Slope of a line in the Coulomb diamond
m_e	Electron mass
μ	Charge carrier mobility
μ_{c}	Chemical potential
N	Landau level index
$\lvert N\rangle$	Eigenfunctions of the quantum mechanical harmonic oscillator
n_{LL}	Landau level orbital degeneracy
n_r	Radial quantum number
n_{s}	Charge carrier density (negative for electrons, positive for holes)
ν	Filling factor (of Landau levels)
P	Power
Φ	Work function
ϕ	Electrostatic potential
φ	Phase
Ψ_{gr}	Graphene wave function
Ψ_{QD}	Wave function of a QD state
$\lvert\Psi_{\mathrm{QD}}\rvert^2$	Probability amplitude of a QD state
$\psi_{\mathrm{A,B}}$	Sublattice component of Ψ_{gr}
Q, q	Charge
$r = \sqrt{x^2 + y^2}$	Radial coordinate
r_{tip}	Tip radius
R	Resistance
R_{xx}	Longitudinal resistance
R_{xy}	Transversal Hall resistance
ρ	Charge density
$\varrho_{\mathrm{tip}}, \varrho_{\mathrm{sample}}$	Tip and sample density of states
S_{v}	Sensitivity of a tuning fork
$\sigma_0 = \frac{e^2}{h}$	Conductance quantum
σ_{s}	Conductivity
T	Temperature
t	Hopping parameter for TB calculation
τ_{tunnel}	Tunneling transmission probability
V, V_{bg}	(Back gate) voltage
V_{sd}	Source-drain voltage
$V_{\mathrm{tip}} = -V_{\mathrm{sample}}$	Tip or sample voltage
V_0	Tunneling barrier height
v_{F}	Fermi velocity
W	Width of the sample
x	Spatial coordinate (in the graphene plane, across pn interface)
$x_{\mathrm{tip}}, y_{\mathrm{tip}}$	Tip position (along x or y axis)
y	Spatial coordinate (in the graphene plane, along pn interface)
z	Spatial coordinate (normal to the graphene plane)

List of abbreviations

2D	Two-dimensional
2DES	Two-dimensional electron system
3D	Three-dimensional
AC	Alternating current
AFM	Atomic force microscopy
CD	Coulomb diamond
CL	Charging line
CVD	Chemical vapor deposition
DC	Direct current
(L)DOS	(Local) Density of states
EC	Edge channel
EFM	Electrostatic force microscopy
FM	Frequency modulation
FQHE	Fractional quantum Hall effect
hBN	Hexagonal boron nitride
KPFM	Kelvin probe force microscopy
LL	Landau level
LN2	Liquid nitrogen
MATBG	Magic angle twisted bilayer graphene
MIM	Microwave impedance microscopy
PDMS	Polydimethylsiloxane
PLL	Phase-locked loop
PMMA	Polymethyl methacrylate
pn	Interface between two different charge carrier concentrations
PPC	Polypropylene carbonate
PVA	Ppolyvinyl alcohol
QD	Quantum dot
QHE	Quantum Hall effect
SGM	Scanning gate microscopy
SL	Spectroscopy line
SPM	Scanning probe microscopy
STM	Scanning tunneling microscopy
STS	Scanning tunneling spectroscopy
TB	Tight-binding
TEM	Transmission electron microscopy
UHV	Ultra high vacuum
VCO	Voltage-controlled oscillator
vdW	van-der-Waals

1 Introduction

The quantum Hall effect (QHE), discovered in 1985, is an experiment with results originating from quantum mechanics. The transversal conductance as a macroscopic sample property is quantized in multiples of e^2/h and is directly related to the quantum mechanical state of the electron system in contrast tol other states with quantum mechanical origin like superconductivity or ferromagnetism. The fascinating outcome of the QHE is that the conductance can be tuned to be identical for all two-dimensional electron systems independent of sample size, geometry, and the material of the sample [1]. The relation between quantum mechanics ruling in the nano world and the macroscopic conductance of a sample is not evident at first glance. It seems to contradict the quantum mechanical correspondence principle implying that for large systems a classical outcome is expected. The introduction of edge channels (ECs) rationalizes the experimental observation [2, 3]: The macroscopic conductance is carried by a quantized number of one-dimensional back-scatter free channels each with a fixed conductance e^2/h. This straightaway builds the bridge into the quantum world. The entire charge (and heat) transport in the QHE is compressed into stripes of only few 10 nm width. Consequently the investigation of edge channels in the QHE at the nanometer scale is relevant.

Several different scanning probe methods have been used to image edge channels [4–8] confirming their existence in the QHE. However the EC picture is not complete. Experiments revealed that the edge of the sample can exhibit EC transport, when it is not expected from the bulk density of states [9]. Moreover the ECs can be accompanied by additional counter flowing currents [10, 11] or neutral modes [12]. Whereas some of these observations are rationalized by electrostatic effects [13], in particular, the influence of interactions between charge carriers on the ECs is an open question.

All spatially resolved measurements of ECs up to now have a resolution larger than the magnetic length as the relevant length scale. Here a second important milestone for the development of experimental quantum mechanics in the 1980s comes into play: The invention of the scanning tunneling microscope [14]. By imaging individual atoms of a sample surface it made the quantization of matter into atoms directly visible. The scanning tunneling microscope with its high lateral resolution is a well suited tool to explore the edge channels in the QHE. Owing to required technical developments and incompatible sample systems, the combination of QHE and scanning tunneling microscopy (STM) has however lasted until 1997 [15, 16], when the Landau quantization of electrons causing the QHE was measured employing scanning tunneling spectroscopy (STS) for the first time. ECs however remain unexplored at the nanometer scale by STM/STS up to date resulting from unsuitable samples despite attempts are reported [17, 18].

The isolation of a single two-dimensional layer of graphite called graphene has opened the new field of two-dimensional (2D) materials not only for many applications in electronics but also in (fundamental) research [19, 20]. 2D materials and graphene in particular feature many exceptional properties like mechanical strength, chemical robustness, high charge carrier mobility, cleavability and external tunability. Some of these properties enable the QHE that is frequently observed in graphene even up to room temperature [21] and reveals many interaction induced exotic phases [22–28]. This puts graphene in the first place to perform spatially resolved experiments exploring ECs at the quantum scale. Accordingly, several studies have been carried out to this end [9–11, 29] utilizing diverse scanning probe microscopy (SPM) techniques except STM. An investigation with high spatial resolution below the magnetic length as offered by STM is still missing. This calls out to be changed and is the aim of this work. Like in some of the before mentioned experiments this study is not performed at the physical edge of a graphene sample but rather at a gate tunable pn interface [30–32]. Here the edge potential is adjustable and the biggest obstacle is circumvented that prevented STM studies of ECs up to now, namely localizing the STM tip close to the physical sample edge.

As the main result, the structure of the wave function of compressible stripes that make up the EC together with incompressible stripes has been mapped with STM/STS for several Landau levels (LLs). Supported by Poisson simulations of the experimental setup and tight-binding calculations based on these, the experimental results are well understood providing a powerful tool to study the nano world of ECs. At the same time the limitations of this method are discussed caused by the perturbations of the STM tip. Extra profit is given by two novel fabrication methods for a graphene sample applicable for STM as well as electrical transport experiments one of which succeeded in the fabrication of several complete devices displaying high quality in the QHE. A similar graphene sample prepared using more conventional techniques is characterized both by STM/STS and transport experiments exhibiting high quality as is evident from the observation of interaction related symmetry broken state in the QHE. Both STM experiments share the common technical issue of aligning the STM tip to the graphene flake of few $10\,\mu$m size inside the STM setup. To this end, two different strategies are reported that rely on either optical or electric force microscopy both of which have been successfully applied.

This thesis is structured in the following way: The required theory is presented in chapter 2. Some topics like the work function mismatch between graphene and STM tip or the capacitance model of quantum dots are elaborated more extensively to avoid confusion and misunderstanding and to provide a discourse of potential handiness for future reference. The instrumental techniques to perform the experiments and the corresponding setups as well as their operation are described in chapter 3. As a link between instrumentation and experiment, the tip approach is addressed narratively in chapter 4. The key experiment of the ECs and the related analysis is covered in chapter 5. Various fabrication methods described in the literature are reviewed in chapter 6 before my own fabrication and the characterization results of a graphene sample are presented in chapter 7. The thesis is concluded with novel fabrication methods in chapter 8. After giving a summary and an outlook in chapter 9 the acknowledgements in chapter 10 complete this thesis.

2 Background

2.1 Graphene

Graphene is a two-dimensional material that consists of few layers of a graphite crystal down to the monolayer (in the following graphene refers to monolayer graphene). Monolayer graphene has a hexagonal lattice with two carbon atoms in each unit cell that is shown in the left part of figure 2.1 [33]. Two so-called A- und B-sublattices can be identified which each are composed of one atom in the unit cell shown in blue and yellow in figure 2.1, respectively. The wave function Ψ_{gr} is expressed as a spinor with one component $\psi_{\mathrm{A,B}}$ for each sublattice [34]:

$$\Psi_{\mathrm{gr}} = \begin{pmatrix} \psi_{\mathrm{A}} \\ \psi_{\mathrm{B}} \end{pmatrix}. \tag{2.1}$$

The pseudospin assigned to the charge carriers describes the relative occupation of the sublattices that is $\Psi_{\mathrm{gr}} = \uparrow$ if only sublattice A is occupied and $\Psi_{\mathrm{gr}} = \downarrow$ for sublattice B [34]. The band structure of graphene is shown in figure 2.2: At the K, K' points of the Brillouin zone (see right part of figure 2.1) the band structure is described by Dirac cones where the valence and conduction band are connected [34]:

$$E_k = \pm \hbar v_{\mathrm{F}} |k_K|, \tag{2.2}$$

where k_K is the momentum with respect to the K, K' point, $\hbar = \frac{h}{2\pi}$, h is the Planck constant, and $v_{\mathrm{F}} \approx 10^6\,\mathrm{m/s}$ is the Fermi velocity of the charge carriers in graphene.

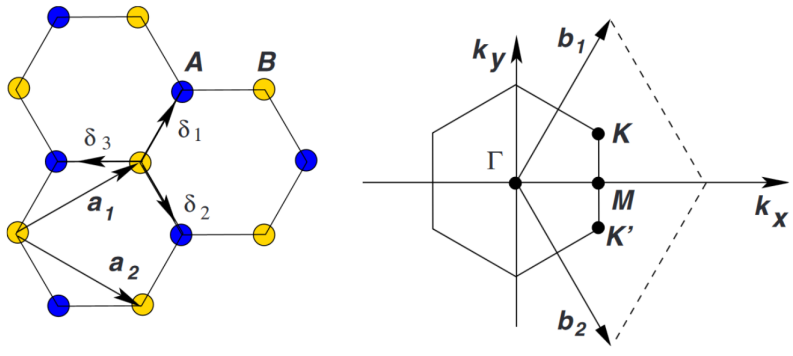

Figure 2.1: Left: Graphene lattice with the lattice vectors $\vec{a}_1, \vec{a}_2$ and the vectors $\vec{\delta}_1, \vec{\delta}_2, \vec{\delta}_3$ connecting one atom to its next neighbors. Right: Brilloiun zone of graphene with the reciprocal lattice vectors $\vec{b}_1, \vec{b}_2$. Reprinted with permission from A. H. Castro Neto, F. Guinea, N. M. R. Peres, K. S. Novoselov, and A. K. Geim, Rev. Mod. Phys. **81**, 109-162 (2009) [33]. Copyright 2009 by the American Physical Society.

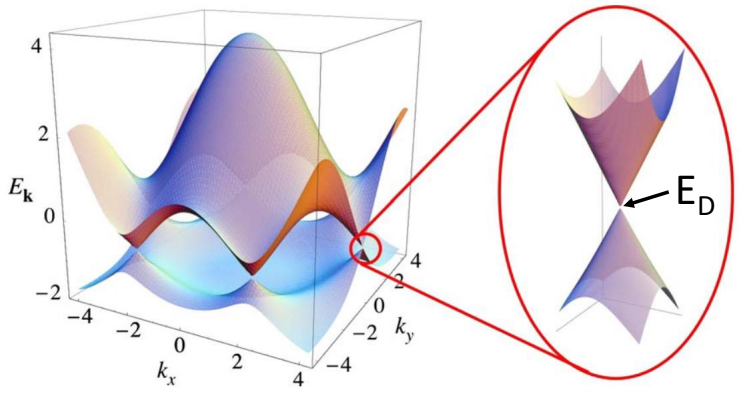

Figure 2.2: Graphene band structure in the Brillouin zone. The close-up on the right shows the Dirac cone in the vicinity of the K, K' points. Reprinted with permission from A. H. Castro Neto, F. Guinea, N. M. R. Peres, K. S. Novoselov, and A. K. Geim, Rev. Mod. Phys. **81**, 109-162 (2009) [33]. Copyright 2009 by the American Physical Society.

The Dirac cones of the K, K' points are degenerate and are distinguished by the valley index $K_\mathrm{v} = \pm 1$. In charge neutral graphene the Fermi energy E_F is at the center between the two Dirac cones called Dirac point E_D making graphene a semimetal without band gap [33]. The behavior of the charge carriers equals that of massless, relativistic fermions leading to many surprising effects like Klein tunneling that is experimentally observable in graphene [35].

2.2 Field effect

For charge neutral graphene, E_F is at the Dirac point E_D and the density of states (DOS) at E_F is minimal while the electrical resistivity reaches its maximum. The occupation of the Dirac cone can be tuned either by chemically doping or by applying a voltage V_bg between a graphene sheet and a back gate located parallel to the graphene plane forming a plate capacitor [19]. The induced charge carrier density n_s is calculated in first order by [19]:

$$n_\mathrm{s} = -\frac{\epsilon\epsilon_0 V_\mathrm{bg}}{e d_\mathrm{C}} \tag{2.3}$$

with $e = |e|$ the elementary charge, d_C is the distance between the back gate and the graphene layer, ϵ_0 is the vacuum permittivity, and ϵ is the dielectric constant of the material between back gate and graphene layer. Due to the electron-hole-symmetry of the Dirac cones for small energy E_k, the change in charge carrier density can be described as addition of either electrons or holes into the system with the same properties for both but inverse symmetries like charge or pseudospin [34]. With increased

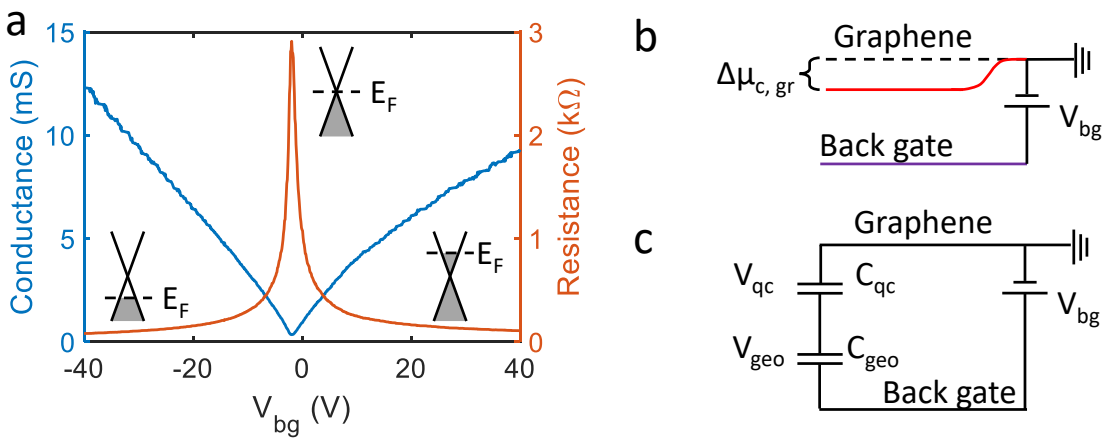

Figure 2.3: a: Resistance and conductivity over V_{bg} of graphene sample GR33BN58 measured at $T = 0.3\,K$ in four point configuration. The Dirac cones show the position of E_{F} for different ranges of V_{bg} where grey areas represent occupied states. b: Schematic of the plate capacitance between graphene layer and back gate. The change of $\mu_{\mathrm{c,gr}}$ is shown in red. c: Circuit diagram of the graphene back gate capacitance with the geometrical capacitance and the quantum capacitance.

occupation of electrons or holes the conductivity σ_{s} is increasing according to [19]:

$$\sigma_{\mathrm{s}} = |n_{\mathrm{s}}|e\mu \tag{2.4}$$

where μ is the charge carrier mobility. The resistance and the conductance of a graphene sample as a function of the applied V_{bg} is shown in figure 2.3a where additionally the position of E_{F} with respect to the Dirac point for the different transport regimes is indicated. The conductance shows an almost linear behavior as expected from the combination of equations 2.4 and 2.3. Because of the low DOS close to the Dirac point a change of the graphene occupation is related to a strong shift of E_{F} or else the chemical potential $\mu_{\mathrm{c,gr}}$ and work function Φ_{gr} that can reach few 100 meV in experiments [36] and is depicted in figure 2.3a schematically. The chemical potential is $\mu_{\mathrm{c,gr}} = 0\,\mathrm{V}$ for charge neutral graphene with E_{F} at the Dirac point and $\mu_{\mathrm{c,gr}} > 0\,\mathrm{V}$ for electron doped graphene or $\mu_{\mathrm{c,gr}} < 0\,\mathrm{V}$ for hole doped graphene. The work function Φ_{gr} and the chemical potential $\mu_{\mathrm{c,gr}}$ are related by

$$\Phi_{\mathrm{gr}} = \Phi^0_{\mathrm{gr}} - e\mu_{\mathrm{c,gr}} \tag{2.5}$$

where Φ^0_{gr} is the work function of charge neutral graphene. The applied V_{bg} drops in two different regions: firstly between the back gate and E_{F} of the graphene layer and secondly within the graphene layer as a shift of the chemical potential $\Delta\mu_{\mathrm{c,gr}}$ indicated by a red line in figure 2.3b [37, 38]. The potential difference between graphene and back gate is smaller than the applied V_{bg} and less charge carriers than expected based on the geometrical capacitance according to equation 2.3 are induced. The effect is called quantum capacitance and can be described as an additional capacitance in series to the geometrical capacitance between graphene and back gate in a circuit diagram (see figure 2.3c). The part V_{geo} of V_{bg} dropping between the back gate electrode and graphene layer is related to the geometrical capacitance C_{geo} and the voltage drop

$V_{\mathrm{qc}} = \Delta\mu_{\mathrm{c,gr}}$ inside the graphene layer, due to the quantum capacitance C_{qc}. The latter describes the energy necessary to occupy the additional charge carriers at elevated energy levels in the graphene layer (see also section 2.9 for the capacitance model describing the same effect in quantum dots). For metals, the DOS at E_{F} is large such that $\mu_{\mathrm{c}} \approx 0$ if charge carriers are added. This results in $C_{\mathrm{qc}} \to \infty$ such that the quantum capacitance is negligible.

2.3 Quantum Hall effect (QHE)

In a strong perpendicular magnetic field B the charge carriers in a two-dimensional material perform cyclotron orbits which energy is quantized [39]. In the DOS the discrete energy levels of different cyclotron orbits form narrow bands due to disorder induced potential fluctuations in the sample (see figure 2.4). These bands are called Landau levels (LLs) and their energies E_N for graphene are set by the applied perpendicular magnet field B [34, 40]:

$$E_N = \mathrm{sgn}(N)\, v_{\mathrm{F}} \sqrt{2e\hbar|N|B} \tag{2.6}$$

where N is the Landau level index with $N = -\infty, \ldots, -2, -1, 0, 1, 2, \ldots, \infty$. Positive N describe electron filled LLs and negative N hole LLs with positive and negative energies, respectively. LL0 is at energy $E_0 = 0\,\mathrm{eV}$ directly at the Dirac point due to the chiral relativistic dispersion of graphene. It is half occupied by electrons and holes. Also The LLs in graphene are not equidistantly spaced in energy as for conventional two-dimensional systems. The sublattice components $\psi_{\mathrm{A,B}}$ of the wave function Ψ_{gr} are the eigenfunctions $|N\rangle$ of the quantum mechanical harmonic oscillator such that $\Psi_{\mathrm{gr}}^{\mathrm{LL}N}$ for LLN reads [34]:

$$\Psi_{\mathrm{gr}}^{\mathrm{LL}N} = \frac{1}{\sqrt{2}} \begin{pmatrix} |N-1\rangle \\ \mathrm{sgn}(N)\, K_{\mathrm{v}}\, |N\rangle \end{pmatrix} \tag{2.7}$$

with $K_{\mathrm{v}} = \pm 1$ being the valley index.

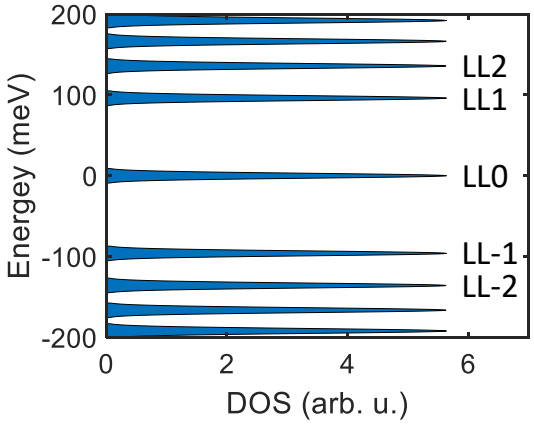

Figure 2.4: Graphene DOS consisting of LLs for $B = 7\,\mathrm{T}$.

In particular for $N = 0$ $\Psi_{\mathrm{gr}}^{\mathrm{LL0}}$ is given by [34]:

$$\Psi_{\mathrm{gr}}^{\mathrm{LL0}} = \begin{pmatrix} 0 \\ |N = 0\rangle \end{pmatrix}. \tag{2.8}$$

Both equations 2.7 and 2.8 are valid only for one K point and the sublattice components are exchanged at the K' point [34].
Due to the redistribution of the continuous DOS into LLs, these have a high (formally infinite) orbital degeneracy and in addition a four-fold degeneracy due to spin and valley degree of freedom of the charge carriers in graphene. The charge carrier density per LL n_{LL} without spin and valley degeneracy is given by [34]:

$$n_{\mathrm{LL}} = \frac{1}{2\pi l_B^2} = \frac{eB}{h} \tag{2.9}$$

$$l_B = \sqrt{\frac{\hbar}{eB}} \tag{2.10}$$

with the magnetic length l_B. By tuning the charge carrier density n_{s} or the magnetic field B the number of occupied LLs can be changed as described by the Landau level filling factor ν [34]:

$$\nu = \frac{n_{\mathrm{s}}}{n_{\mathrm{LL}}} = \frac{h n_{\mathrm{s}}}{eB} \tag{2.11}$$

which integer part gives the number of completely filled LLs.
The transport properties of the sample strongly depend on the non-integer part of ν and change periodically with ν what is called Quantum Hall effect (QHE) [1]: If the non-integer part is close to 0.5 then E_{F} is at the center of a LL and the sample conductivity is governed by an extended state. The cyclotron orbits overlap forming a percolating network of conductive channels at E_{F} and both longitudinal resistance R_{xx} and transversal Hall resistance R_{xy} show finite not quantized values. For ν close to an integer E_{F} is in between two LLs resulting in localized states at E_{F} forming around charge inhomogeneities like dopants in the sample (green areas in figure 2.5b). The interior of the sample (bulk) becomes insulating whereas the LLs bend at the edge of the sample and cross E_{F} forming one dimensional chiral edge channels (ECs) which conductance is quantized [2, 3] with the conductance quantum σ_0:

$$\sigma_0 = \frac{e^2}{h} \tag{2.12}$$

The LLs bending at the edge of the sample resulting in ECs at E_{F} are shown schematically in figure 2.5a. The chirality of the EC originates from the cyclotron orbits of the charge carriers that can be scattered at the edge of the sample (skipping orbit as in figure 2.5b). The chirality prohibits back scattering within each EC and consequently each EC can only transport charge carriers in one direction at one edge (see figure 2.5b). The EC at the opposite edge belonging to the same LL has the opposite transport direction. The number of EC formed at the edge of the sample equals the number of more than half occupied LLs in the bulk. This number also sets the two-point conductance of the sample $\sigma_{2\mathrm{p}}$ as a parallel circuit of individual ECs if contact

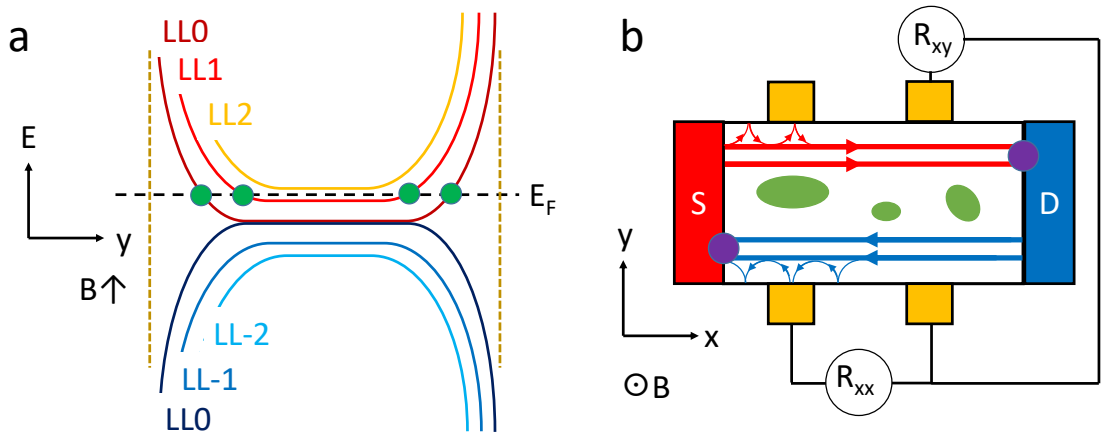

Figure 2.5: a: Cross section of the sample in the energy-y-direction plane. Graphene LLs (dark red to orange: electron LLs, dark blue to light blue: hole LLs) bend at the edge of the sample (brown). For clarity only few LLs are depicted. EC (green) form where E_F (dashed black line) crosses the LLs. b: Top view on a sample with two ECs in the QHE with negative charge carriers. Depending on the applied V_sd the charge carriers move from S to D in the upper red ECs or from D to S in the lower blue ECs. Skipping orbits represent the chirality of the ECs and the dissipation points are shown in violet. Localized states (green) are present in the bulk of the sample. Additional contacts (yellow) allow to measure R_{xx} and R_{xy}.

resistances are ignored :

$$\sigma_{2\mathrm{p}} = |[\nu]|\frac{e^2}{h} \tag{2.13}$$

where $[\nu]$ is the integer part of ν. The potential of an applied source-drain-voltage V_sd drops at the end of a EC at the contact and is constant along the EC due to the lack of back scattering [41]. This leads to a dissipation less transport of the source-drain current I_sd along the ECs with vanishing resistance $R_{xx} = 0\,\Omega$ what is depicted in figure 2.5b with red or blue color for the source or drain contact and the corresponding ECs and with violet points indicating the dissipation at the end of an EC. Because of the opposite directions in which the charge carriers move in the EC at both edges of the sample due to the chirality a voltage between opposite edge channels results. The quantized Hall resistance R_{xy} equals $\frac{1}{\sigma_{2\mathrm{p}}}$:

$$R_{xy} = \frac{h}{[\nu]e^2} \tag{2.14}$$

For graphene the conductance including spin and valley degeneracy is given by [34]:

$$\sigma_{xy} = 4(N + \frac{1}{2})\frac{e^2}{h} \tag{2.15}$$

The ECs and related measurements are described in more detail in sections 2.11, 2.12, and 2.13. Instructive lecture notes on the QHE are for example found in [42].

Besides the physical understanding of the QHE in terms of LLs and their ECs, it can also be understood by topological arguments that eventually explain the robustness of the QHE [43, 44]. In topology, certain areas get numbers called Chern numbers. At the intersection of areas with different Chern numbers, a quantized Hall conductance appears. Topology also explains straightforwardly the existence of ECs at a pn interface in the QHE: If the areas on both sides of the pn interface have different Chern number (different LL occupation), and are both insulating, the quantized Hall conductance is carried by ECs at the interface.

2.4 Symmetry breaking in QHE and relation to sample quality

The fourfold degeneracy of LLs in graphene due to spin and valley quantum numbers can be lifted both by external effects and interactions between the charge carriers [45]. External effects are the Zeeman effect lifting the spin degeneracy or a substrate induced lifting of the sublattice degeneracy in the LL0 [46, 47]. Exchange interaction between charge carriers induces Stoner ferromagnetism that is promoted by the almost identical energy of all charge carriers within a LL lifting both spin and valley degeneracies [24]. The magnitude of the exchange interaction can be estimated by two charge carriers in the distance of the magnetic length l_B [45] and is consequently tunable by the applied magnetic field making the QHE a suitable testbed for interactions. Compared to the energetic distance between LLs, the interaction energy is small and proves challenging to observe experimentally. In the QHE a lifted degeneracy of a LL can be observed in a measurement as an additional step in R_{xy} and a simultaneous minimum in R_{xx} appearing with increasing B (see figure 2.6). σ_{xy} shows values of multiple e^2/h and in particular for graphene at $\nu = 0$ the sample becomes insulating $R_{xy} \to \infty$. Additional conductance plateaus require additional localization-delocalization-transitions meaning that the percolating network of conducting channels of the delocalized state

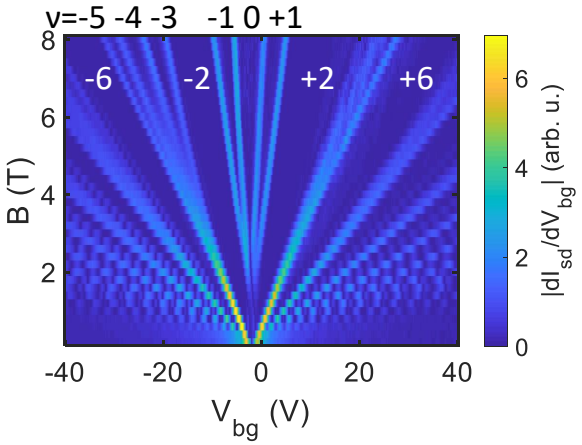

Figure 2.6: Measurement of $|dI_{\mathrm{sd}}/dV_{\mathrm{bg}}|$ of graphene sample GR33BN58 at $T = 0.3\,\mathrm{K}$. The derivative is performed numerically and the data is smoothed. The filling factors are written on the corresponding plateaus. $V_{\mathrm{sd}} = 100\,\mu\mathrm{V}$.

has to be interrupted by localized states in the disorder potential of charge inhomogeneities. This occurs if percolating states of the different symmetries are sufficiently offset in energy. To make that happen, the exchange gap must be significantly larger than $k_\mathrm{B}T$ and the exchange energy must be strong enough to overcome the disorder potential. The disorder potential prefers to have states of all four symmetries in the lowest potential areas filled with electrons counteracting the symmetry breaking that is favoured by the exchange. If localized states appear in between the percolating states of different symmetry, the ECs on both sides of the sample are no longer connected and the quantized Hall conductance sets in. However, the ECs do not necessarily follow the physical edge as the presence of larger disorder is not excluded as long as it is not connecting the ECs of both sides of the sample. At the same time, the experimentally measured energy gaps yield information about the sample quality by comparing with theoretical predictions. The energy gaps that are determined experimentally in the QHE via temperature dependent activation gap measurements are reduced by the disorder potential. In contrast a local probe can reveal degeneracy lifting related energy gaps locally and is therefor less limited by disorder putting forward STS to locally probe interactions in the QHE.

2.5 Work function mismatch and band bending

The STM tip and graphene in general have different work functions Φ_tip and Φ_gr, respectively. Whereas Φ_tip is constant Φ_gr changes according to equation 2.5 as $\Phi_\mathrm{gr} = \Phi^0_\mathrm{gr} - e\mu_\mathrm{c,gr}$ if a voltage is applied to an electrode like tip or back gate close to the graphene. The work function mismatch between tip and graphene is given by [48–50]

$$\Delta\Phi = \Phi_\mathrm{gr} - \Phi_\mathrm{tip}. \tag{2.16}$$

At large distance the vacuum energies of tip and graphene are aligned as shown in figure 2.7a for a negative $\Delta\Phi$ [51]. Once the tip is approached to the graphene enabling tunneling contact, charge transfer between tip and graphene sets in to align their Fermi energies (see figure 2.7b): The electrons move to the material with higher Φ, in the case of figure 2.7 to the tip [51]. Resulting from the removed electrons, holes appear in the graphene that build an image charge in the graphene layer below the tip screening the electric field of the tip. To compensate for the charge transfer between tip and graphene, a voltage V_tip can be applied to the tip [49, 51]. In the example of figure 2.7c, V_tip is positive such that electrons are removed from the tip and transferred to the graphene. If $V_\mathrm{tip} = -\Delta\Phi/e > 0\,\mathrm{V}$ both tip and graphene are neutral again and their vacuum levels are identical as in figure 2.7a. Equation 2.16 must be rewritten more general in terms of the electrostatic potential difference between tip and sample $\Delta\phi$ including V_tip:

$$\Delta\phi = \Delta\Phi/e + V_\mathrm{tip} \tag{2.17}$$

The condition for no charge transfer between tip and graphene is given by

$$\Delta\phi = 0. \tag{2.18}$$

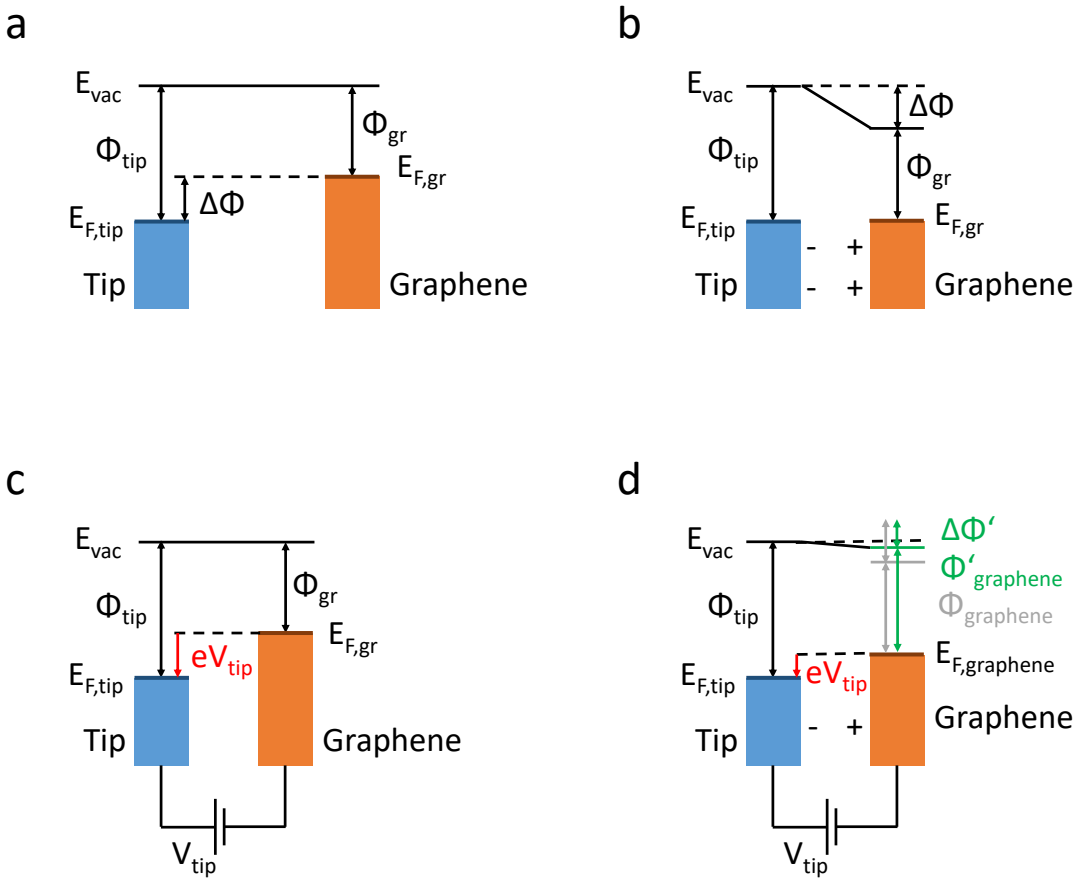

Figure 2.7: a: Tip and sample are separated with their vacuum energies aligned. $\Delta\Phi = \Phi_{\mathrm{gr}} - \Phi_{\mathrm{tip}} < 0\,\mathrm{V}$ b: Tip and sample are in electrical contact with aligned Fermi energies due to electron transfer from graphene to tip. c: A positive $V_{\mathrm{tip}} = -\Delta\Phi/e$ is applied to the tip compensates for the electron transfer. d: $V_{\mathrm{tip}} > 0\,\mathrm{V}$ applied to the tip compensating partly for the charge transfer between tip and graphene. The graphene work function Φ'_{gr} (green) is increased due to the induced holes such that $\Delta\Phi'$ (green) is reduced.

This is fulfilled if

$$\Delta\phi = 0 \iff \Delta\Phi = -eV_{\mathrm{tip}} \tag{2.19}$$
$$\iff \Phi_{\mathrm{gr}} - \Phi_{\mathrm{tip}} = -eV_{\mathrm{tip}}. \tag{2.20}$$

Replacing Φ_{gr} by $\Phi^0_{\mathrm{gr}} - e\mu_{\mathrm{c,gr}}$ (see equation 2.5) in the above equation results in

$$\Phi^0_{\mathrm{gr}} - e\mu_{\mathrm{c,gr}} - \Phi_{\mathrm{tip}} = -eV_{\mathrm{tip}} \tag{2.21}$$
$$\mu_{\mathrm{c,gr}} = \underbrace{\frac{\Phi^0_{\mathrm{gr}} - \Phi_{\mathrm{tip}}}{e}}_{=\phi_{\mathrm{tip}}} + V_{\mathrm{tip}} \tag{2.22}$$
$$\mu_{\mathrm{c,gr}} = \phi_{\mathrm{tip}}. \tag{2.23}$$

If tip and graphene potentials are identical no charge transfer takes place. The tip electrostatic potential ϕ_{tip} is given by the applied V_{tip} with an offset due to the differing work functions of tip and charge neutral graphene. If $\mu_{\mathrm{c,gr}} \neq \phi_{\mathrm{tip}}$ the tip acts as a local top gate inducing charge carriers in the graphene layer below the tip that screen the potential difference: For $\phi_{\mathrm{tip}} > \mu_{\mathrm{c,gr}}$ there are more electrons per area below the tip than in the bulk of the graphene sample and vice versa for $\phi_{\mathrm{tip}} < \mu_{\mathrm{c,gr}}$ there are more holes. In graphene, a change in charge carrier concentration is accompanied by a change in the chemical potential $\mu_{\mathrm{c,gr}}$ due to the low DOS around the Dirac point of band structure (quantum capacitance, see section 2.2). The graphene below the tip being differently doped than the remaining (bulk) sample resulting in a position dependent $\mu_{\mathrm{c,gr}}(x, y)$ is described as (tip-induced) band bending and is shown in figure 2.8a in a cross section. As a consequence of the position dependent $\mu_{\mathrm{c,gr}}(x, y)$ the graphene work function $\Delta\Phi_{gr}$ and resulting $\Delta\Phi$ are changed below the tip as well as depicted in figure 2.7d. The magnitude of the band banding scales in a simple model linearly with ϕ_{tip} via the capacitive coupling of the tip to the graphene sample. The spatial band bending depends on the tip geometry and is as well as the exact magnitude described by a solution of the Poisson equation (see sections 2.14 and 5.3).

2.6 STM measurements on graphene

The graphene chemical potential $\mu_{\mathrm{c,gr}}$ below the tip differing from the bulk value and depending on the applied V_{tip} has in particular to be considered for tunneling spectroscopy where V_{tip} is swept during the measurement (see section 3.1) resulting in three effects: Firstly the V_{tip} distance and with that the energy difference between two features in the LDOS appears larger due to the band bending depending on V_{tip} [52]. This is exemplary shown in figure 2.8b where an unoccupied LDOS feature (light blue) is shifted in energy (green) by the tip-induced band bending. In a replacement circuit diagram this effect is described by the quantum capacitance C_{qc} (see section 2.2 and figure 2.3): The band bending equals V_{qc} dropping across C_{qc} and $|V_{\mathrm{geo}}|$ across C_{geo} probing the LDOS feature is smaller than the applied $|V_{\mathrm{tip}}|$. Consequently a larger $|V_{\mathrm{tip}}|$ has to be applied to measure a LDOS feature with the energy eV_{geo}. By rescaling the V_{tip} axis this problem can be overcome if the capacitances between graphene and tip C_{tip} as well as graphene and back gate C_{bg} are known assuming a linear relation

between band bending and applied V_{tip} (see figure 2.11) [52]. The second effect describes that a feature in the LDOS is probed twice at different V_{tip}: Once the features energy is aligned with $E_{\mathrm{F,tip}}$ and the feature is probed by STS conventionally (but at shifted energy with respect to its unperturbed position) as sketched in figure 2.8b. For a different V_{tip}, the LDOS feature is pushed to the graphene Fermi energy $E_{\mathrm{F,graphene}}$. This shows up in the STS as well because of the serial circuit of the resistances between tip and sample and the LDOS feature is probed by $E_{\mathrm{F,graphene}}$ instead of $E_{\mathrm{F,tip}}$. The third effect is that the LDOS below the tip might change due to the band bending leading to confinement of charge carriers and consequently the LDOS can reflect different properties than the bulk LDOS. In an experiment resonant quasi-bound states emerge in the band bending below the tip for an appropriate set of V_{tip} and V_{bg} [53]. These so-called whispering gallery modes form due to suppression of Klein tunneling at oblique inpinging angle onto a pn interface that appears between the graphene below the tip and the remaining bulk graphene. They have a specific energy E_{WGM} that is measured as increased intensity in STS at two different biases: Once $E_{\mathrm{F,tip}}$ is aligned with E_{WGM} ("normal STS") where E_{WGM} changes with V_{tip} due to the band bending. The second signal in STS appears if E_{WGM} is aligned with $E_{\mathrm{F,graphene}}$ where $|eV_{\mathrm{tip}}| \gg |E_{\mathrm{WGM}}|$.
The back gate voltage V_{bg} changes the occupation of states in the bulk graphene as well as below the tip and LDOS features appear at different V_{tip} dependent on the applied V_{bg}. If the feature is aligned with $E_{\mathrm{F,tip}}$ in STS, its energy decreases with increasing occupation by V_{bg} and V_{tip} has to be adjusted accordingly. This can be traced in a $dI/dV_{\mathrm{tip}}(V_{\mathrm{bg}}, V_{\mathrm{tip}})$ measurement as a line called spectroscopy line (SL). If the feature is aligned to $E_{\mathrm{F,graphene}}$, V_{tip} can act as a gate to compensate a changing V_{bg} in order to keep the occupation in the graphene below the tip constant. The resulting line in the $dI/dV_{\mathrm{tip}}(V_{\mathrm{bg}}, V_{\mathrm{tip}})$ measurement is called charging line (CL) as often used in the context of transport measurements of QDs. SL and CL have slopes with opposite signs and cross at $E_{\mathrm{F,graphene}}$ that is $V_{\mathrm{tip}} = 0\,\mathrm{V}$ in the $dI/dV_{\mathrm{tip}}(V_{\mathrm{bg}}, V_{\mathrm{tip}})$ map. Because V_{bg} and V_{tip} compensate along the CL its slope equals the ratio of their capacitances $C_{\mathrm{bg}}/C_{\mathrm{tip}}$ (see section 2.9 for derivation).
A perpendicular magnetic field B applied to the graphene sample results in Landau quantization of the charge carriers (see section 2.3). Below the tip, states can localize if the magnitude of the band bending is sufficient creating a quantum dot (QD) which states are decoupled from the bulk states [54–56]. In a simplified picture, charge carriers are localized if they are surrounded by a band gap at $E_{\mathrm{F,graphene}}$ that arises between adjacent LLs (see figure 2.9a). Since E_{F} typically is located within a LL, the charging of the QD requires that the band bending is, at least, as large as the energy difference between adjacent LLs. Alternatively, E_{F} can be located within the localized states of the same LL providing an insulating area around the QD. For example, if E_{F} is at the high energy side of a LL and $V_{\mathrm{tip}} < 0\,\mathrm{V}$, hole levels can be successively moved across E_{F}, while the surrounding is insulating.
The QD has a strong impact on the STS measurements: The states that are probed are not the bulk states belonging to the LLs, but states of the QD below the tip that can display different or additional properties [55–57]. This is sketched in figure 2.9a by states with different wave functions resulting in energetic separation of the states [57, 58]. Apart from that, a change of the occupation of the localized QD states is accompanied by charging events since the additional charge leads to an altered band

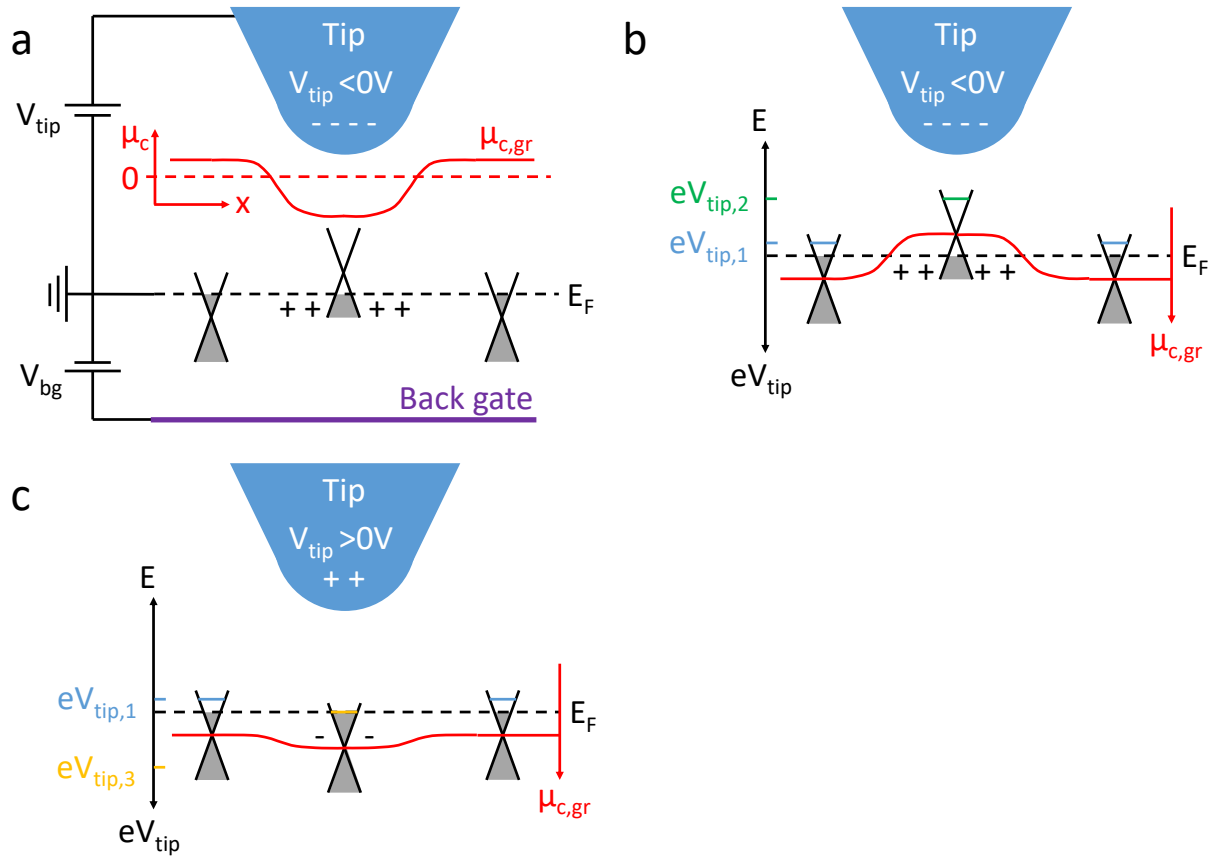

Figure 2.8: a: The graphene chemical potential $\mu_{c,gr}$ (shown in red) is changed both by $V_{bg} > 0\,V$ applied to the back gate electrode and $V_{tip} < 0\,V$ applied to the tip (indicated by - - - - , for $\Phi^0_{gr} - \Phi_{tip} = 0\,eV$ such that $V_{tip} = \phi_{tip}$). Due to its geometry the tip only influences $\mu_{c,gr}$ locally resulting in different occupation of graphene below the tip (with holes indicated by + + + +) and in the bulk as sketched by Dirac cones. b: Same situation as in subfigure a using electron energy as scale instead of $\mu_{c,gr}$ with changing sign. The energy of a LDOS feature with respect to E_D (light blue) is measured by STS at $V_{tip,2}$ (green) instead of $V_{tip,1}$ (light blue) due to $\mu_{c,gr}$ changed below the tip by $V_{tip} < 0\,V$. Unoccupied states are probed as $V_{tip} < 0\,V$. Note that the chemical potential difference are smaller than the applied voltages due to a lever arm. c: $V_{tip} > 0\,V$ (indicated by + +) inverts the direction of the band bending $\mu_{c,gr}$ (indicated by - -) and the LDOS feature (yellow) gets aligned with E_F below the tip at $V_{tip,3}$ (yellow).

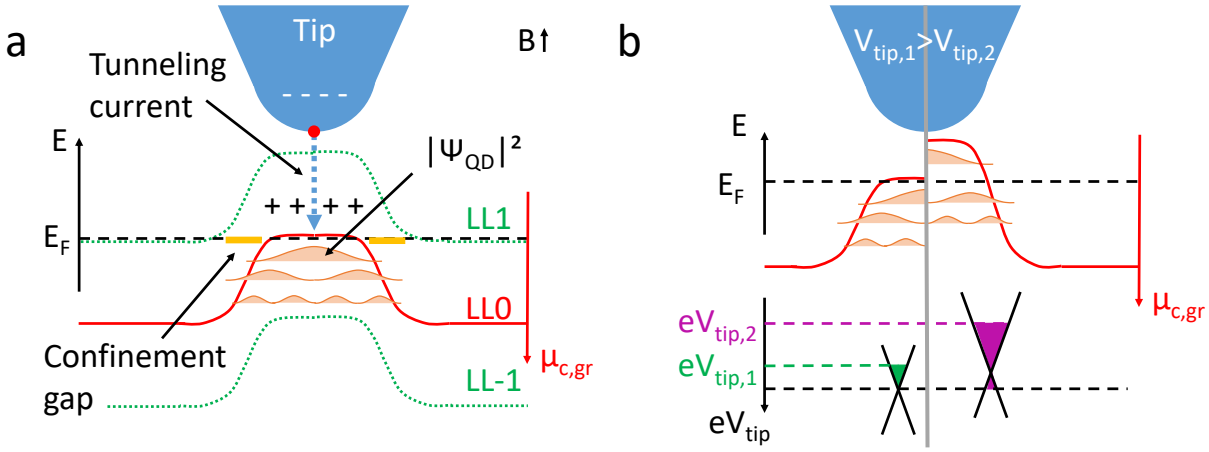

Figure 2.9: a: Confinement of a QD by band bending. A negatively charged tip (- - - -) induces positive charges (+ + + +) in graphene such that LL1 states (green dashed) are unoccupied below the tip and LL0 states (red) are occupied resulting in a gap (yellow) at $E_{\mathrm{F,graphene}}$. QD states with different orbital wave functions Ψ_{QD} (light orange) have different energies within the QD. b: The left side shows the same situation as in subfigure a. By decreasing $V_{\mathrm{tip},2} < V_{\mathrm{tip},1}$ as shown on the right side the band bending increases and the highest QD state is unoccupied. The number of states in the bias window (lower part) is increasing.

bending due to Coulomb repulsion between the additional charge carriers in the QD and the other electrons of the sample [54–56, 59] (see section 2.9 for derivation of the charging energy). For larger QDs, the addition energy spectrum of the QD is dominated by the charging energy E_{C} while the orbital energy plays only a minor role [55, 56, 59]. The charging of the QD occurs, if an energy level of the QD is aligned with $E_{\mathrm{F,graphene}}$ either via V_{tip} or V_{bg} and shows up as a peak in the measured STS signal that is caused by two effects: At first the tunneling current I is increased due to the additional current path via the state that is charged at $E_{\mathrm{F,graphene}}$. In addition, the change of the local charge due to the additional (un-)occupied state changes the number of states in the bias window of the STS as shown in figure 2.9b. The required energy to add an electron from the tip is abruptly reduced by the apparent hole below the tip, effectively shifting the Dirac cone (see figure 2.9b bottom). The resulting larger number of states in the bias window results in an increased tunneling current I and in a peak in dI/dV_{sample} [59]. That the number of states is increasing in the bias window such that a peak in the STS appears is a consequence of the graphene DOS which is changing with energy away from the Dirac point. The effect can not be observed with a constant DOS(E), since $E_{\mathrm{F,tip}} - E_{\mathrm{F,graphene}}$ is not changed by the charging event. The probed LDOS at eV_{tip} would be the same before and after the charging. As the charge in the QD is quantized each charge entering or leaving the QD leads to a single peak in the STS. The charging occurs along charging lines (CLs) in the $dI/dV_{\mathrm{tip}}(V_{\mathrm{bg}}, V_{\mathrm{tip}}$ maps as described above. These CLs prove the existence of a QD below the tip directly. Along a CL typically the same QD state is kept at $E_{\mathrm{F,graphene}}$ in the QD (the charge in the QD remains constant). At the crossing of a CL with $E_{\mathrm{F,graphene}}$ they intersect the spectroscopy line (SL) of the same QD state resulting in the observation of so-called Coulomb diamonds (CDs) that are explained in detail in sections 2.8 and 2.9.

2.7 Graphene quantum dot (QD) states

The states of a graphene QD in a perpendicular magnetic field B below the tip are characterized by three non distinct quantum numbers: N is the Landau level index as in the bulk, n_r is the radial quantum number describing the number of radial nodes of the wave function (except at the QD center) and the angular momentum quantum number m correlates with the spatial extent of the state or the azimuthal nodes real and imaginary parts of the wave function. For adequate boundary conditions, they are related by [60, 61]:

$$N = n_r + \frac{1}{2}(|m| + m) \tag{2.24}$$

where $0 \leq n_r \leq |N|$ and $m \leq |N_{LL}|$. Possible solutions are given in table 2.1. Whereas in the bulk the energy of a state is given only by N (see equation 2.6) the orbital degeneracy of the bulk LL is lifted in the QD due to the confinement potential and states with same the N but different n_r and m are separated in energy as shown in figure 2.10b [57, 58]. Additionally, each state is four-fold degenerate due to the spin and valley degeneracy in graphene. In a STS measurement only the states with high probability amplitude $|\Psi_{\mathrm{QD}}|^2$ below the tunneling center of the tip are probed. These states typically have $m = 0$ [62], that is they have an antinode in the center of the QD. In figure 2.9a the tunneling center of the tip is indicated by a red dot and the tunneling current a a blue dashed vertical arrow that ends at the antinode of $|\Psi_{\mathrm{QD}}|^2$ and in figure 2.10 the position of the tunneling center is at $r = 0\,l_B$. The radial distribution of $|\Psi_{\mathrm{QD}}|^2$ shown in figure 2.10a is nonzero at $r = 0\,l_B$ only for one of the states with the same N. The other states with $m \neq 0$ are probed indirectly by STS once they are (un-)occupied by their charging peak but barely contribute to the STS signal at $E_{\mathrm{F,tip}}$ [62]. The measured LDOS of the QD exhibits peaks corresponding to the energies of the $m = 0$ states. This energy sequence equals the bulk values for the LL energies E_N while the offset due to band bending of the QD remains undiscovered. Consequently the LL quantization of charge carriers in the QD shows the expected $\sqrt{B}$ and $\sqrt{N}$ dependencies of their energies (see equation 2.6 and figure 2.11a) as for the bulk LLs as reported in [52]. In this measurement CLs are present indicating the QD below the tip (see figure 2.11b). While the QD occupation is changed via V_{bg} the LL pin the $E_{\mathrm{F,graphene}}$ ($V_{\mathrm{sample}} = 0\,\mathrm{V}$) for a certain range of V_{bg} until the next LL jumps

Table 2.1: Possible combinations of the quantum numbers N, n_r, m for $|N| \leq 2$ according to equation 2.24 in a graphene QD. The corresponding wave functions, theirs energies for $B = 10\,\mathrm{T}$ and the LDOS of a graphene QD are shown in figure 2.10.

$\lvert N\rvert$	n_r	m
0	0	0, -1, -2, ...
1	0	1
1	1	0, -1, -2, ...
2	0	2
2	1	1
2	2	0, -1, -2, ...

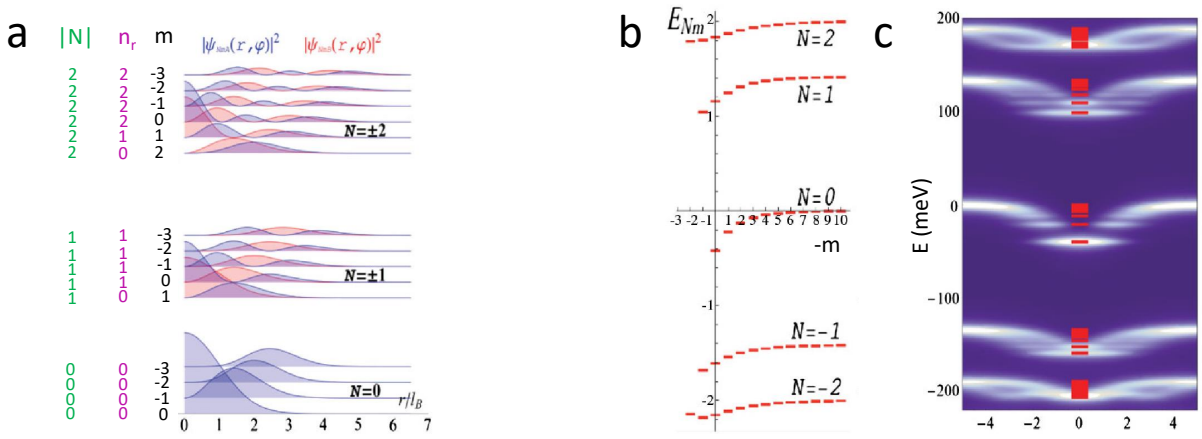

Figure 2.10: a: Wave functions of the states in agraphene QD with quantum numbers N, n_r, m. The wave functions are shown in blue and red for the different sublattices (see eqautions 2.7 and 2.8). b: Corresponding energies to the wave functions plotted in subfigure a. c: Resulting LDOS of a graphene QD at $B = 10\,\mathrm{T}$. Red lines in the center are the energies shown in subfigure b. Reprinted with permission from A. Luican-Mayer, M. Kharitonov, G. Li, C.-P. Lu, I. Skachko, A.-M. B. Gonçalves, K. Watanabe, T. Taniguchi, and E. Y. Andrei, Phys. Rev. Lett. **112**, 036804 (2014) [57]. Copyright 2014 by the American Physical Society.

to $E_{\mathrm{F,graphene}}$ in a step. The resulting staircase pattern of the LL features is evident in figure 2.11b. The pinning is caused by the bulk LLs huge orbital degeneracy that pins the LLs to the Fermi energy in the bulk graphene outside the QD [52, 63, 64]. As soon as the next LL is filled it jumps to the Fermi energy and this step like behaviour of the graphene chemical potential $\mu_{\mathrm{c,gr}}$ with changing LL occupation transfers to the states in the QD. Consequently it is also observed in STS [52]. In parallel to the changing LL features at $E_{\mathrm{F,graphene}}$ in the QD, CLs and CDs appear for small V_{tip}, since a state crosses $E_{\mathrm{F,graphene}}$ in the QD and the number of charge carriers in the QD changes [54]. For constant $\mu_{\mathrm{c,gr}}$ (within a LL), typically no CLs are observed.
Measurements similar to [52] have been performed at $B \leq 14\,\mathrm{T}$ [65] and on graphene samples with a graphite back gate [66]. In both cases, symmetry breaking of the LL features (see section 2.4) appears and the resulting sublattice dependent LDOS pattern of LL0 is imaged [67–72]. Many CLs and clear CDs are observed throughout LL0 in the $dI/dV_{\mathrm{tip}}(V_{\mathrm{bg}}, V_{\mathrm{tip}})$-map in [65]. In [66] skyrmions around localized charges are imaged using STM/STS [73]. Here, the influence of V_{tip} on $\mu_{\mathrm{c,gr}}$ below the tip resulting in the band binding is overcome by a purposely narrow shaped tip. The idea is that the resulting band bending only occurs on length scales that are smaller than the wave functions in the graphene $\propto l_B$ such that the charge carriers do not follow the potential variation. As a consequence no QD is formed below the tip as is evident by the absence of CLs.
States can not only be localized in the band bending below the tip, but at a local dip or peak of $\mu_{\mathrm{c,gr}}$ of the sample as well. Instead of the applied V_{tip}, in addition to $\Delta\Phi/e$, localized charges in the graphene layer or in the underlying substrate originating for example from defects or dopant result in confinement potentials. In particular for

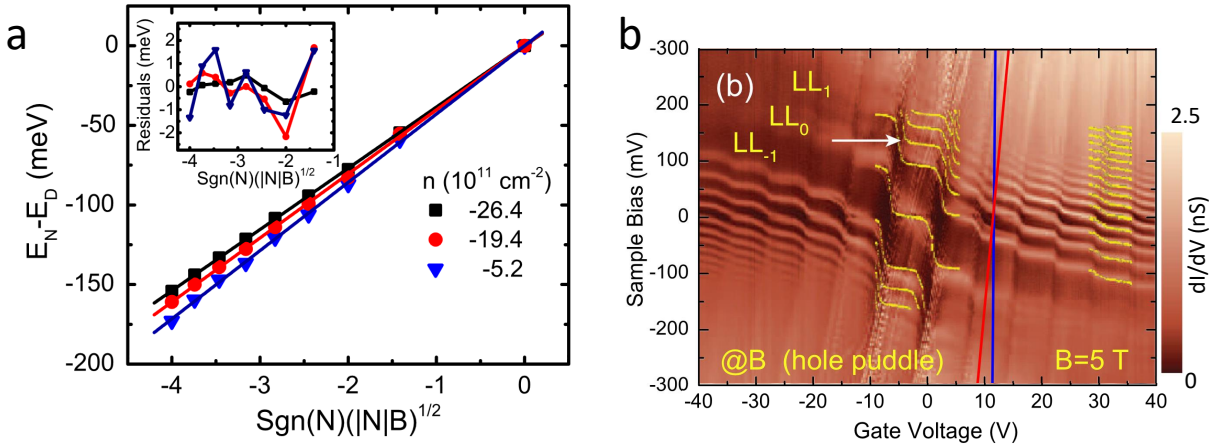

Figure 2.11: a: LL energies E_N plotted against $\mathrm{sgn(N)}\sqrt{|\mathrm{N}|\mathrm{B}}$ (see equation 2.6) for three different charge carriers concentrations n_s extracted from STS measurements. The Dirac point energy E_D due to initial doping is subtracted. b: STS measurement of graphene at $B = 5\,\mathrm{T}$ in dependence of V_bg. The blue vertical line shows constant V_bg whereas the red inclined line indicates constant n_s below the tip. Yellow lines show the positions of LLs based on a simulation. Reprinted with permission from J. Chae, S. Jung, A. F. Young, C. R. Dean, L. Wang, Y. G. K. Watanabe, T. Taniguchi, J. Hone, K. L. Shepard, P. Kim, N. B. Zhitenev, and J. A. Stroscio, Phys. Rev. Lett. **109**, 116802 (2012) [52]. Copyright 2012 by the American Physical Society.

disordered samples with a SiO_2 substrate, this is often observed [54, 74, 75]. The localization mechanism via the band gap between LLs is the same as for the QD below the tip and CLs as well as CDs are observed [54]. Depending on the sign of the local $\mu_\mathrm{c,gr}$ variation in the sample, both electron- or hole-like QDs are detected by STS [54]. They differ by the onset of the CLs with the step region of the SL appearing during the change of LL occupation.

If a LL state is almost completely filled with electrons in a hole-like QD, the same LL in the bulk must be fully occupied such that the bulk is insulating and CLs appear in the measurement [54]. This situation is sketched in figure 2.12a. In the $dI/dV_\mathrm{tip}(V_\mathrm{bg}, V_\mathrm{tip})$-map the CLs show up on the right of the corresponding LL plateau at E_F. For an electron-like QD the situation is inverted (see figure 2.12b) and CLs appear for an nearly empty LL state in the QD since the same LL in the bulk is completely empty and the bulk is insulating [54]. Accordingly the CLs are the left end of a LL plateau in the $dI/dV_\mathrm{tip}(V_\mathrm{bg}, V_\mathrm{tip})$-map.

QDs that exist in a local potential of the sample offer the advantage that their states can be mapped spatially by STS, whereas this is not possible for a tip-induced QD that moves with the tip such that it is always probed at the same position r with respect to the tip. Local potentials can be deterministically created in the hBN substrate underneath the graphene via voltage pulses applied to the tip. This way the QD states are mapped by STS in [76–78].

In order to (de-)populate the next state in the QD, the band bending magnitude has to be (de-)increased either by V_tip or V_bg to overcome the addition energy. The distance between CLs in the $dI/dV_\mathrm{tip}(V_\mathrm{bg}, V_\mathrm{tip})$ map is given by the capacitance of either QD

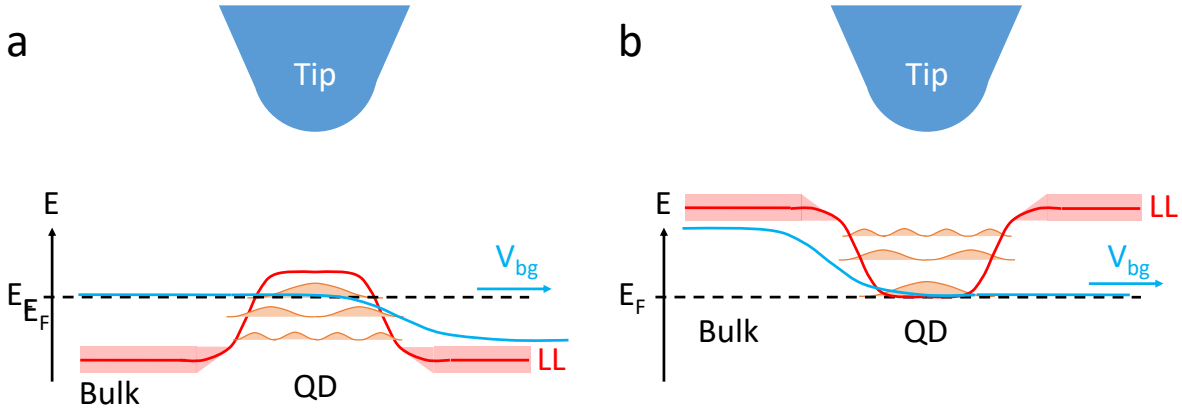

Figure 2.12: Position of charging lines in a $dI/dV_{\mathrm{tip}}(V_{\mathrm{bg}}, V_{\mathrm{tip}})$-map depending on the QD type. a: A LL state in a hole-like QD is occupied with the last electron if the same bulk LL is completely filled. With increasing V_{bg} (light blue) the LL state moves below E_{F} (right end of plateau). b: A LL state in a electron-like QD is occupied with the first electron if the same bulk LL is completely empty. With increasing V_{bg} (light blue) the LL state remains at E_{F} (left end of plateau).

and back gate C_{bg} or QD and tip C_{tip} and corresponds to both the charging and orbital energies, see section 2.9 for derivation. Due to the four-fold spin and valley degeneracy of each QD state, it turns out that the CL distance between degenerate QD states is smaller than between states with different orbital quantum numbers. For these transitions, both the orbital and charging energy has to be overcome whereas for degenerate states only the charging energy has to be overcome. This leads to the arrangement of CLs in groups of four. The four-fold degeneracy of each (n_r, m)-state is lifted when charging a single electron or hole into the corresponding QD state. For perfect graphene, this symmetry breaking is spontaneous and no spin or valley is favored. In [56] it is shown that the underlying hBN substrate favours a different valley degree of freedom depending on the QD position in the Moiré unit cell that forms in the graphene sheet placed on a hBN substrate.
Further experiments involving graphene QDs probed by STS are presented in a review article [79].

2.8 Coulomb diamonds in transport and scanning tunneling spectroscopy

Quantum dots and its states can be characterized in transport measurements where the conductance of a QD is measured depending on source-drain voltage V_{bias} and local gate voltage V_{pg}. The QD is contacted by the source and drain electrodes via tunnel barriers with capacitances C_{S} and C_{D}, respectively and the voltages V_{S} and V_{D} applied to them. $V_{\mathrm{bias}} = V_{\mathrm{S}} - V_{\mathrm{D}}$ is the difference between source and drain voltages that is used to drive a current through the QD. The plunger gate is insulated from the QD and used to change the occupation of the QD by applying V_{pg} similar to the

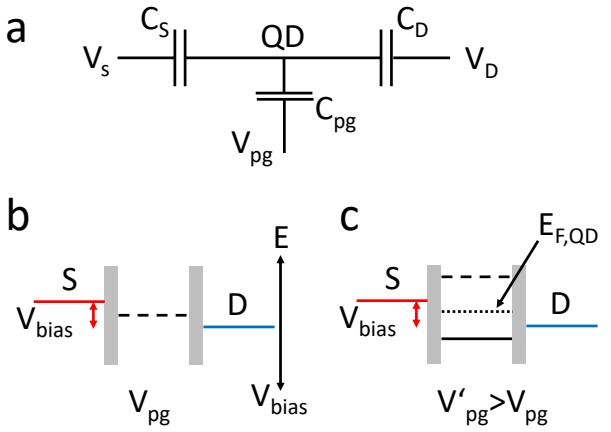

Figure 2.13: Transport measurement of a QD. a: Source and drain contacts are connected to the QD via tunneling barriers with capacitances C_S and C_D, respectively and voltages V_S and V_D. The plunger gate has the capacitance C_pg to the QD and V_pg applied. b: The tunneling barriers of source (S) and drain (D) are shown in gray. A QD state enabling transport (dashed line) is in the bias window and transport is possible. c: By increasing V_pg, no QD states are in the bias window any more and the lower state is occupied (solid line).

back gate in graphene samples (see section 2.2). The schematic arrangement of the electrodes is shown in figure 2.13a. If the QD chemical potential enables both N and N+1 states on the QD within the bias window, current is flowing from source to drain as depicted in figure 2.13b. The energetic position of a corresponding QD state in the bias window is tuned by V_pg. A charge state can be realized once its energy is lower than the electrostatic potential of one of the contacts by an electron tunneling from the contacts into the QD occupying this state. If no state is in the bias window, no transport is possible as can be seen figure 2.13c. If the bias window is larger than the energy spacing of adjacent QD states, transport is always possible where the current is increasing with the number of states in the bias window. For smaller bias windows, the conductance follows an oscillatory function depending on V_pg resulting in Coulomb Diamonds (CD) that describe the transport behaviour of a QD in the V_pg-V_bias-map shown in figure 2.14 [80].
Inside the CD, the bias window is too small to allow for transport through the QD rendering it insulating. At both corners of the CD for $V_\mathrm{bias} = 0\,\mathrm{V}$, a state is at E_F source and drain contacts and transport is possible. With increasing V_pg the state is moved from E_F to lower energies. At the left red rising solid line in figure 2.14, a QD state (solid black line) is aligned with the electrostatic potential of the source contact (red) and the line marks the transition of this state into the bias window. Here, V_bias is assumed to be applied symmetrically across the QD such that $V_\mathrm{S} = +1/2\,V_\mathrm{bias}$ and $V_\mathrm{D} = -1/2\,V_\mathrm{bias}$. This way the electrostatic potential $V_\mathrm{S} = +1/2\,V_\mathrm{bias}$ can be aligned to the QD state. For reversed V_bias, the drain contact is aligned with this QD state (blue falling solid line). Further increasing $|V_\mathrm{bias}|$ leads to the next QD state (dotted black line) entering the bias window. These points define the top and bottom corners of the CD where the electrostatic potentials of both source and drain contact are each

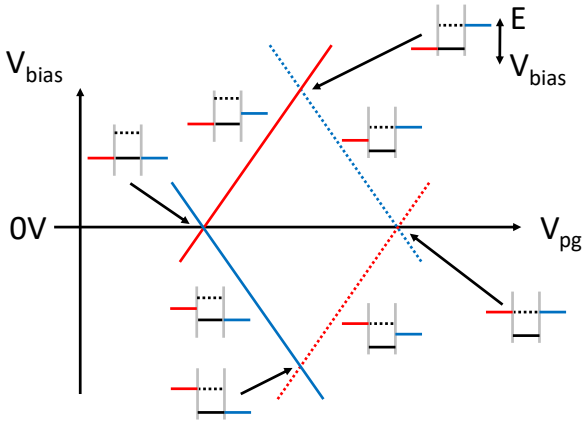

Figure 2.14: Coulomb diamond: Solid lines of the CD belong to the current onset via the QD state symbolized by a solid, black, horizontal line. Dotted lines of the CD belong to the next energetically higher state of the QD symbolized by a dotted, black, horizontal line. Both states are either aligned with the source (red) or the drain (blue) contact as indicated with the respective colour. Representations of the QD states, the source and drain contacts are given along the lines and for the corners of the CD.

aligned with a QD state. On the right half of the diamond, the new state (dotted black line) is closer to E_F than the old state (solid black line). Depending on the sign of V_bias the dominating state is either aligned to the source potential (red rising dotted line, $V_\mathrm{bias} < 0\,\mathrm{V}$) or to the drain potential (blue falling dotted line, $V_\mathrm{bias} > 0\,\mathrm{V}$). The next CD on the right repeats the sequence with the state represented by a dotted line and the energetically next state. The height and the width of the CD are calculated by a capacitance model in the next section 2.9.
In STS measurements of graphene in the QHE, CDs are observed in $dI/dV_\mathrm{tip}(V_\mathrm{bg}, V_\mathrm{tip})$-maps [54, 65]. The principle is the same as for transport experiments (gate induced energy shift of states probed by aligning to electrostatic potentials of different contacts) but the role of the involved contacts and gates is more complex. The bulk of the graphene around the QD below the tip acts as the drain electrode and the back gate as the plunger gate. The tip serves both as a plunger gate and source contact. V_bias is not symmetrically applied across the QD, but instead $V_\mathrm{tip} = V_\mathrm{bias}$ and the drain contact is grounded $V_\mathrm{D} = 0\,\mathrm{V}$. Anything else is similar. If E_F of the tip (red horizontal line in figure 2.14) is aligned with a QD state, a SL is observed (see section 2.6) and if E_F of the surrounding graphene is aligned with a QD state, a CL is observed (see section 2.6). The slope of the two lines have opposite sign as they have in the CD of figure 2.14. The SL separates into two states, an occupied and an unoccupied, in the QD.
Once the state is occupied for $V_\mathrm{tip} = 0\,\mathrm{V}$ the sequence is repeated and another CD is measured.
Because of the four-fold degeneracy of the QD states in graphene CDs often appear in groups of four. The detailed description of the CD shape in particular for STS experiments depends strongly on the involved capacitances C_tip and C_bg as will be clear in the following section.

2.9 Capacitance model of QDs

In this chapter a model is presented that describes slope of charging lines (CL) and spectroscopy lines (SL) which encircle the Coulomb diamond in a STM experiment (see section 2.8). To this end, the QD is initially described by a plate capacitance without any further contacts. This model is stepwise extended by additional contacts until formulas for the slope of the lines rendering the Coulomb diamond (CD) and the distance between the lines can be derived. A concise derivation of the equations can be found in section 18.2.2 of [80] and is the basis for this section. The derivation presented here follows a different route with the intention to give a more intuitive understanding. One plate of the capacitance is the plunger gate and the other the plate is the QD. The QD is accordingly represented by a classical, metallic object without charge or energy quantization. The electrostatic potential of the QD is set to $\phi_{\mathrm{QD}} = 0\,\mathrm{V}$. The voltage $V_{\mathrm{pg}} = \phi_{\mathrm{pg}} - \phi_{\mathrm{QD}}$ is the electrostatic potential difference between plunger gate and QD. Figure 2.15a shows this in a diagram. If $V_{\mathrm{pg}}^{(0)} > 0\,\mathrm{V}$ is applied to the plunger gate, a charge $Q_{\mathrm{QD}}^{(0)} = -Q^{(0)} < 0\,\mathrm{C}$ is induced in the QD:

$$-C \cdot V_{\mathrm{pg}}^{(0)} = Q_{\mathrm{QD}}^{(0)} = -Q^{(0)} \tag{2.25}$$

where C is the capacitance between plunger gate and QD. Due to conservation of charge, the plunger gate has the charge $Q_{\mathrm{pg}}^{(0)} = -Q_{\mathrm{QD}}^{(0)} = +Q^{(0)}$:

$$C \cdot V_{\mathrm{pg}}^{(0)} = Q_{\mathrm{pg}}^{(0)} = Q^{(0)}. \tag{2.26}$$

In the next step, V_{pg} is increased by ΔV_{pg} (see figure 2.15b). As a consequence, the charge on the capacitance is increased by q where

$$-C \cdot \Delta V_{\mathrm{pg}} = q_{\mathrm{QD}} = -q \tag{2.27}$$

$$\Delta V_{\mathrm{pg}} = \frac{q}{C} = V_{\mathrm{pg}} - V_{\mathrm{pg}}^{(0)} \tag{2.28}$$

with $q_{\mathrm{QD}} = -q_{\mathrm{pg}}$ is the increased charge on the QD as labeled above. The total charge of the QD is given analogous to equation 2.25 by:

$$-C(V_{\mathrm{pg}}^{(0)} + \Delta V_{\mathrm{pg}}) = -Q^{(0)} - q. \tag{2.29}$$

Now source and drain contacts are added to the model of the QD. The drain contact is assumed to be well coupled to the QD, such that its electrostatic potential $\phi_{\mathrm{D}} = \phi_{\mathrm{QD}}$. In contrast, the electrostatic potential of the source contact ϕ_{S} is assumed to have no influence on ϕ_{QD}. This situation is realized in STM measurements of graphene where the tip is the source contact and the graphene surrounding the QD below the tip is the drain contact. A source-drain voltage $V_{\mathrm{bias}} = \phi_{\mathrm{S}} - \phi_{\mathrm{D}}$ can be applied between source and drain contacts. For $V_{\mathrm{bias}} = 0\,\mathrm{V}$, the results from above are not affected. The situation changes, if $V_{\mathrm{bias}} > 0\,\mathrm{V}$ ($V_{\mathrm{bias}} < 0\,\mathrm{V}$) what corresponds to probing (un)occupied states of the QD in the same way as STS (see section 3.1). To figure out which state is probed by a specific $V_{\mathrm{bias}}^{(1)}$, the situation of equation 2.25 is considered with $V_{\mathrm{pg}}^{(0)} > 0\,\mathrm{V}$ and $Q_{\mathrm{QD}}^{(0)} = -Q^{(0)} < 0\,\mathrm{C}$. The electrostatic potential difference between the plunger gate and the state being probed at V_{bias} is (see figure 2.15c):

$$\phi_{\mathrm{pg}} - \phi_{\mathrm{S}} = V_{\mathrm{pg}}^{(0)} - V_{\mathrm{bias}}^{(1)}. \tag{2.30}$$

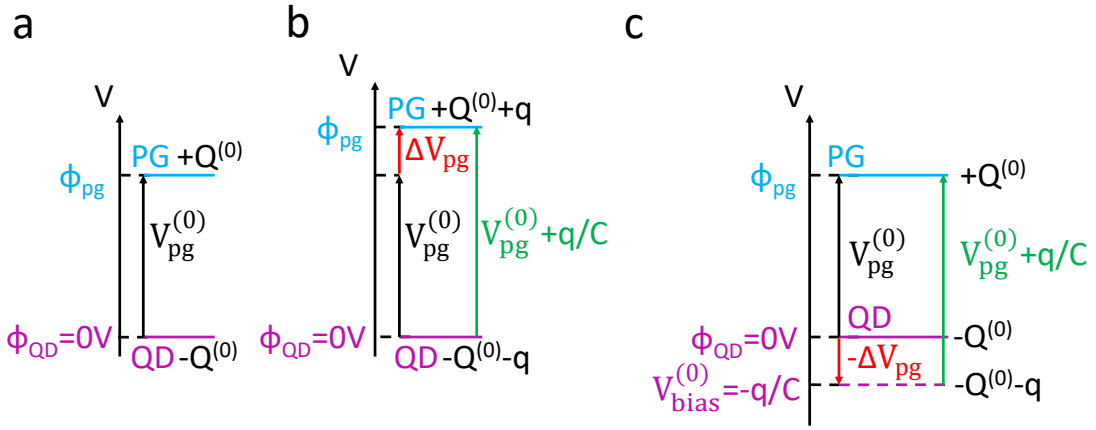

Figure 2.15: a: Potential diagram of a capacitance describing the QD (violet) and the plunger gate (light blue) with charge $\pm Q^{(0)}$ due to the potential $V_{\mathrm{pg}}^{(0)}$ between them. b: The charge is increased to $\pm(Q^{(0)}+q)$ as a result of the raised potential $V_{\mathrm{pg}}^{(0)}+q/C$. c: A negative $V_{\mathrm{bias}}^{(0)}=-q/C$ is applied to probe $-Q^{(0)}-q$ in the QD (dashed violett line).

By comparison with equation 2.29 it turns that the $Q_{\mathrm{QD}}=-Q^{(0)}-q$ state is probed, if

$$-V_{\mathrm{bias}}^{(1)}=\Delta V_{\mathrm{pg}}=\frac{q}{C}. \tag{2.31}$$

To put the above results into words, there are now two possibilities to probe the $Q_{\mathrm{QD}}=-Q^{(0)}-q$ state: For $V_{\mathrm{bias}}\approx 0\,\mathrm{V}$ the plunger gate has to be tuned to $V_{\mathrm{pg}}^{(0)}+\Delta V_{\mathrm{pg}}$ to occupy this state. In this case the state is aligned with E_{F} of both source and drain contacts resulting in a current flow (Coulomb peak). The other possibility is to set $V_{\mathrm{bias}}^{(1)}=-\frac{q}{C}$ for $V_{\mathrm{pg}}=V_{\mathrm{pg}}^{(0)}$. The $Q_{\mathrm{QD}}=-Q^{(0)}-q$ state is aligned with E_{F} of the source contact and the situation resembles a SL of the CD.
Up to now the QD itself is considered as a metal plate such that no orbital energy is required to add charges into the metal (and the chemical potential $\mu_{\mathrm{c,QD}}$ is not changed by adding charges into the metal). In reality there is however an energy Δ_q related to the addition of the charge $-q$ into the QD, in particular for semiconductors or semimetals like graphene (see section 2.2) or for small QDs due to confinement energy. It can be described by an additional capacitance in series to the geometrical capacitance which is called quantum capacitance (see figure 2.3c). The energy Δ_q is added as chemical potential difference $\Delta\mu_{\mathrm{c}}=\frac{\Delta_q}{q}$ into equation 2.28. ΔV_{pg} now contains potential contributions from both the geometrical and the quantum capacitance, that is

$$\Delta V_{\mathrm{pg}}=\frac{q}{C}+\frac{\Delta_q}{q}. \tag{2.32}$$

The same term $\frac{\Delta_q}{q}$ is added on the right side of equation 2.31 as well:

$$-V_{\mathrm{bias}}^{(1)}=\Delta V_{\mathrm{pg}}=\frac{q}{C}+\frac{\Delta_q}{q}. \tag{2.33}$$

Finally more gates i with capacitances C_i and electrostatic potentials ϕ_i are included in the model. The gates act as additional plunger gates and the plunger gate from above is one of them. Each gate has the voltage $V_i = \phi_i - \phi_{\mathrm{QD}}$ applied to it. A specific set of gate voltages $V_i^{(2)}$ leads to the charge $Q_{\mathrm{QD}}^{(2)} = -Q^{(2)}$ for $V_{\mathrm{bias}} = 0\,\mathrm{V}$ what is captured by

$$\sum_i -C_i \cdot V_i^{(2)} = Q_{\mathrm{QD}}^{(2)} = -Q^{(2)} \tag{2.34}$$

where the contribution of each gate i captured in equation 2.25 is added up for all i. Following the same concept as above, all voltages $V_i^{(2)}$ are increased by ΔV_i such that the additional charge $-q$ is induced in the QD: $Q_{\mathrm{QD}} = -Q^{(2)} - q$. Here it is important to note that not the single ΔV_{pg} leads to q, but instead each gate i contributes with its ΔV_i and C_i. Accordingly, equation 2.32 is multiplied by C_i and again added for all gates i:

$$\sum_i C_i \Delta V_i = q + \frac{\Delta_q}{q} \sum_i C_i \tag{2.35}$$

$$C_\Sigma = \sum_i C_i. \tag{2.36}$$

With the definition of C_Σ it follows:

$$\sum_i C_i \Delta V_i = q + C_\Sigma \frac{\Delta_q}{q}. \tag{2.37}$$

If $V_{\mathrm{bias}}^{(3)} \neq 0\,\mathrm{V}$ is applied to the source contact, equation 2.33 is similarly added for all gates i after multiplying with C:

$$-\sum_i C_i V_{\mathrm{bias}}^{(3)} = \sum_i C_i \Delta V_i = q + C_\Sigma \frac{\Delta_q}{q}. \tag{2.38}$$

Because $V_{\mathrm{bias}}^{(3)}$ is independent of i, equation 2.38 can be divided by C_Σ:

$$-V_{\mathrm{bias}}^{(3)} = \frac{q}{C_\Sigma} + \frac{\Delta_q}{q}. \tag{2.39}$$

Equations 2.37 and 2.39 contain all ingredients to eventually derive the formulas of the CD. The lines that define the shape of a CD can be divided according to their slope. Lines with negative slope $m_\alpha = \Delta V_{\mathrm{bias}}/\Delta V_{\mathrm{pg}}$ (solid and dotted blue lines in figure 2.14) correspond to the situation in a transport measurement, where a state of the QD is aligned to E_{F} of the drain contact and labeled charging line (CL). Because V_{pg} and V_{bias} compensate each other along the CL, the charge in the QD remains constant. Using the description of a QD with continuous charge, this situation is captured by equation 2.37.
To get the slope of the CL, two points (4,5) with voltage changes $\Delta V_i^{(4)}$, $\Delta V_i^{(5)}$ are considered that have the same $q^{(4)} = q^{(5)} = q$ as along a CL and thereby also the same Δ_q:

$$\sum_i C_i \Delta V_i^{(4)} = q + C_\Sigma \frac{\Delta_q}{q} \tag{2.40}$$

$$\sum_i C_i \Delta V_i^{(5)} = q + C_\Sigma \frac{\Delta_q}{q}. \tag{2.41}$$

The difference of these equations yields:

$$\sum_i C_i \Delta V_i^{(5)} - \sum_i C_i \Delta V_i^{(4)} = 0 \tag{2.42}$$

For all $\Delta V_i^{(4)} = \Delta V_i^{(5)} = 0\,\mathrm{V}$ except $\Delta V_{\mathrm{pg}}^{(4,5)}$ and $\Delta V_{\mathrm{bias}}^{(4,5)}$ one ends up with

$$C_{\mathrm{bias}} \Delta V_{\mathrm{bias}}^{\Delta} + C_{\mathrm{pg}} \Delta V_{\mathrm{pg}}^{\Delta} = 0 \tag{2.43}$$

$$\Delta V_{\mathrm{bias}}^{\Delta} = -\frac{C_{\mathrm{pg}}}{C_{\mathrm{bias}}} \Delta V_{\mathrm{pg}}^{\Delta} \tag{2.44}$$

where $\Delta V_{\mathrm{bias}}^{\Delta} = \Delta V_{\mathrm{bias}}^{(5)} - \Delta V_{\mathrm{bias}}^{(4)}$ and similar for $\Delta V_{\mathrm{pg}}^{\Delta}$. The slope of these CLs equals $m_{\alpha}^{\mathrm{CL}} = \frac{\Delta V_{\mathrm{bias}}^{\Delta}}{\Delta V_{\mathrm{pg}}^{\Delta}} = -\frac{C_{\mathrm{pg}}}{C_{\mathrm{bias}}}$.
For the lines with positive slope within the CD, $V_{\mathrm{bias}} \neq 0\,\mathrm{V}$ probes for varying ΔV_{pg} the state at which the QD would enable charge $-Q^{(2)} - q$ while it has $-Q^{(2)}$ for $V_{\mathrm{bias}} = 0\,\mathrm{V}$. These lines are spectroscopy lines (SL) (solid and dotted red lines in figure 2.14). For the analysis, equation 2.37) and equation 2.39) are combined reading:

$$\sum_i C_i \Delta V_i - C_{\Sigma} V_{\mathrm{bias}} = q + C_{\Sigma} \frac{\Delta_q}{q} \tag{2.45}$$

Also along the SL line q remains constant since $-Q^{(2)} - q$ always is probed at V_{bias}. Considering two points (6,7) on the line as before leads to:

$$\sum_i C_i \Delta V_i^{(6)} - C_{\Sigma} V_{\mathrm{bias}}^{(6)} = \sum_i C_i \Delta V_i^{(7)} - C_{\Sigma} V_{\mathrm{bias}}^{(7)} \tag{2.46}$$

Setting all $\Delta V_i^{(6)} = \Delta V_i^{(7)} = 0$ except $V_{\mathrm{pg}}^{(6,7)}$ and $V_{\mathrm{bias}}^{(6,7)}$ results to the following outcome:

$$C_{\mathrm{pg}} \Delta V_{\mathrm{pg}}^{\Delta} + (C_{\mathrm{bias}} - C_{\Sigma}) \Delta V_{\mathrm{bias}}^{\Delta} = 0 \tag{2.47}$$

$$\Delta V_{\mathrm{bias}}^{\Delta} = \frac{C_{\mathrm{pg}}}{C_{\Sigma} - C_{\mathrm{bias}}} \Delta V_{\mathrm{pg}}^{\Delta} \tag{2.48}$$

where $\Delta V_{\mathrm{bias}}^{\Delta} = \Delta V_{\mathrm{bias}}^{(7)} - \Delta V_{\mathrm{bias}}^{(6)}$ and similar for $\Delta V_{\mathrm{pg}}^{\Delta}$. Since C_{Σ} per definition 2.36 contains C_{bias} it always is $C_{\Sigma} \geq C_{\mathrm{bias}}$ and the slope $m_{\alpha}^{\mathrm{SL}} = \frac{\Delta V_{\mathrm{bias}}^{\Delta}}{\Delta V_{\mathrm{pg}}^{\Delta}} = \frac{C_{\mathrm{pg}}}{C_{\Sigma} - C_{\mathrm{bias}}}$ of this line is always positive.
For the case of a symmetrically applied V_{bias} as often used in quantum transport experiments, that is the source contact is at the electrostatic potential $+\frac{1}{2} V_{\mathrm{bias}}$ and the drain contact at $-\frac{1}{2} V_{\mathrm{bias}}$, the factor $\pm\frac{1}{2}$ has to be multiplied to $-C_{\Sigma} V_{\mathrm{bias}}$ in equation 2.45.
It is important to notice that V_{bias} enters equation 2.45 twice with different physical interpretation. Once via the capacitive coupling in the first term and a second time as a *probe* for the state of the QD at the corresponding energy. In STM experiments on graphene, the tip and the voltage applied to it can either have just the gating effect (charging line) or the double function of probing and gating at the same time (spectroscopy line).
Finally the lever arm is introduced that eventually relates voltages and energies in the QD. Using equation 2.37, the distance $\Delta V_j^{(8)}$ between the two points $q^{(8)} \neq 0\,\mathrm{C}$ and

$q = 0\,\mathrm{C}$ is calculated. At $q = 0\,\mathrm{C}$ the QD contains the charge $-Q^{(2)}$, such that equation 2.37 does not exhibit a divergence. Setting all $\Delta V_i^{(8)} = 0\,\mathrm{V}$ except $\Delta V_j^{(8)} \neq 0\,\mathrm{V}$, equation 2.37 for $q^{(8)}$ reads:

$$C_j \Delta V_j^{(8)} = q^{(8)} + C_\Sigma \frac{\Delta_{q^{(8)}}}{q^{(8)}}. \tag{2.49}$$

Dividing by C_Σ gives:

$$\frac{C_j}{C_\Sigma} \Delta V_j^{(8)} = \frac{q^{(8)}}{C_\Sigma} + \frac{\Delta_{q^{(8)}}}{q^{(8)}}. \tag{2.50}$$

The factor $\frac{C_j}{C_\Sigma} = \alpha_j$ is called the lever arm α_j of gate j [80]. In a CD measurement, the occupation of the QD changes by $\pm e$ going from one corner to the opposite. Equation 2.50 consequently gives the relative sizes of a CD in V_{pg} or V_{bias} direction for $|q^{(8)}| = e$ and $V_j = V_{\mathrm{pg}}$ or V_{bias}.
Multiplying equation 2.50 with $q^{(8)}$ gives the involved energies:

$$q^{(8)} \alpha_j \Delta V_j^{\Delta} = \frac{(q^{(8)})^2}{C_\Sigma} + \Delta_{q^{(8)}} \tag{2.51}$$

where the first term on the right side is called charging energy $E_{\mathrm{C}} = \frac{e^2}{C_\Sigma}$ [80] for $|q^{(8)}| = e$ and the second term is the orbital energy.

2.10 Gate defined pn interfaces

In graphene, pn interfaces are created by different charge carrier concentrations in adjacent parts of the sample controlled via the field effect of two or multiple back or top gates (see section 2.2). A common design with a top and a back gate is shown in figure 2.16a [30] and an alternative layout with two back gates in figure 2.16b [81]. Depending on the gate voltages, either both parts of the graphene sample have opposite type of charge carriers (bipolar configuration, pn or np, see figure 2.16c) or both parts have the same type of charge carriers but with different concentration (unipolar configuration, nn' or pp', see figure 2.16d). In the following, the term pn interface is used to describe a gate tunable interface between two parts of a graphene sample and is not restricted to the case with opposite type of charge carriers but includes the cases with same type of charge carriers as well.
The creation of the pn interface by the gate voltages makes pn interfaces in graphene more versatile in comparison to conventional semiconductors where pn interfaces are typically induced by dopants. On the other hand, graphene pn interfaces show no rectifying behaviour due to Klein tunneling leading to only slightly increased resistance for the pn or np configurations in comparison to the nn' or pp' configuration [30]. STM measurements of gate-defined graphene pn interfaces show that interfaces can be created by a graphite flake as back gate electrode placed partly below the hBN flake [82]. For a 10 nm thick hBN flake a pn interface width of 40 nm is achieved across which the graphene chemical potential $\mu_{c,gr}$ changes roughly linear by 200 mV. However, the tip-induced band bending is not considered in this evaluation. A hBN thickness of 23 nm results in a width of 70 nm for the same $\mu_{c,gr}$ difference between both parts of the pn

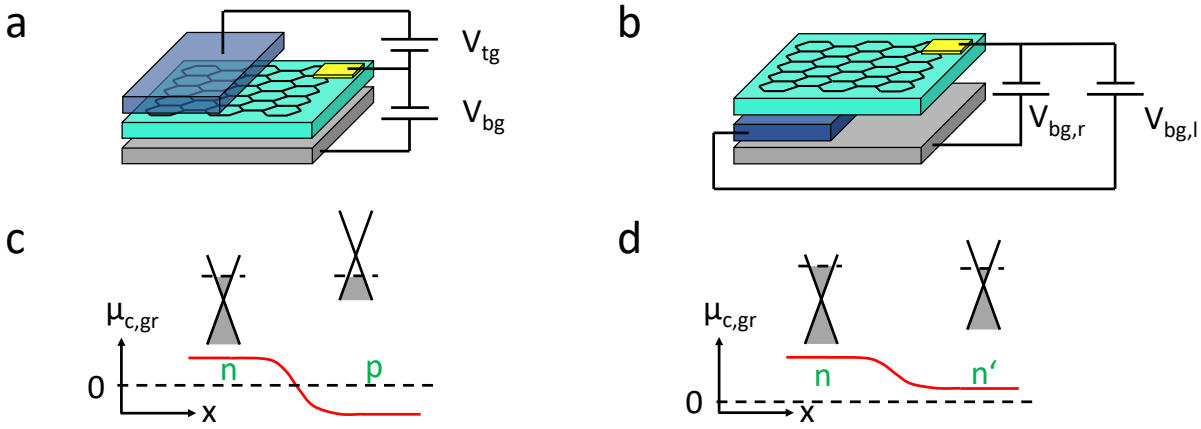

Figure 2.16: a: Pn interface defined by a top gate (transparent dark blue) for the left side and a back gate (gray) for both the left and the right side of a graphene sample. b: Pn interface defined by two back gates. The dark blue back gate is affecting the left side of the graphene sample, the gray back gate the right side. c: Graphene chemical potential $\mu_{c,gr}$ across a np interface (bipolar regime). The doping of the left (n) and right (p) side is written in green letters. Schematic representations of the Dirac point show occupied states (gray) and E_F as a dashed line. d: same as subfigure c but for a nn' interface (unipolar regime).

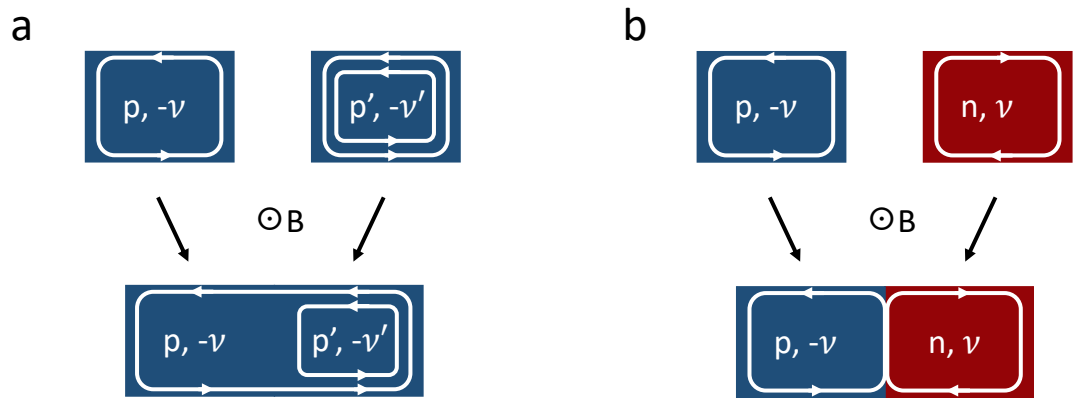

Figure 2.17: a: Upper panel: Two separated samples occupied with holes in different concentration p and p' resulting in different filling factors $-\nu$ and $-\nu'$ and ECs (white lines with arrows indicating the charge carrier movement) in the QHE. Lower panel: Both samples combined in a pp' interface (unipolar case) exhibiting one EC crossing the interface. b: Upper panel: Same as subfigure a for the bipolar case with holes (p) and electrons (n) such that the ECs have opposite direction. Lower panel: At the pn interface both ECs run in parallel and can mix.

interface as measured by Kelvin probe force microscopy (KPFM, see section 3.2) that is not causing band bending [29].
Parts of the sample having different charge carrier concentration affect the transport properties of the sample in the quantum Hall regime as well (see section 2.3). If the difference in charge carrier concentration is large enough, a different number or types of LLs is occupied in both parts of the sample and similarly a different number or types of edge channels are formed in each part of the sample. In the unipolar regime, the overall resistance of the sample is limited to the highest resistance of both parts: Only the LLs and ECs that are occupied in both parts contribute to the transport as sketched in figure 2.17a [30, 31]. Additional LLs and ECs occupied in only one part of the sample are restricted to this area. The excess ECs propagate along the interface and are consequently not bound to the physical edge of the sample (see figure 2.17a). They follow the topological edge created at the pn interface by the different Chern numbers of each part of the sample (see section 2.3). The situation is different in the bipolar case where no common LL is occupied in both parts and all ECs are restricted to either part of the sample. At the interface, the ECs of both parts meet (figure 2.17b). Due to the opposite type of charge carriers they have opposite chirality leading to parallel motion of electrons and holes along the edge, whereas the charge transport is counter flowing. Transports experiments show that the ECs mix at the pn interface and equilibrate as the resulting resistance is not infinite but given by the sum of the two-point resistances of both parts of the sample [30, 31]. Further evidence for the EC equilibration is given by shot noise measurements that show larger values in the bipolar than in the unipolar regime [83]. The transport is carried by the same backscatter free ECs throughout the sample for the unipolar case, whereas in the bipolar regime the charge is transported by different ECs in both parts generating noise at the transition between ECs at the pn

interface by probabilistic charge transfer [83]. With increasing length of the interface the noise decreases exponentially with a decay length of 15 μm [84]. For the case of symmetry broken ECs (see section 2.4), the equilibration and the resulting shot noise depends on the spin and valley index of the ECs involved [81, 85].
In small magnetic fields, the charge carriers perform large orbits that are not completed due to scattering and consequently the charge carriers are not quantized into LLs. If the charge carrier orbits are close to a pn interface the sense of rotation is changing once they move from n to p or vice versa via Klein tunneling. This way charge carriers move along the interface and are called snake states [86]. In a transport measurement, they are detected via oscillations in the longitudinal resistance depending whether the charge carriers end on the p or n part of the sample. In order to observe snake states very clean samples are required to prevent scattering of the charge carriers and allow for large enough orbits without scattering.

2.11 Edge channels

In the QHE, the measured current is carried dissipation-less by the edge channels (ECs) [2]. In a single particle picture, the LLs are expected to follow the electrostatic confinement potential of the sample edge as sketched in figure 2.18b [13]. The charge carrier density changes in a step-wise manner for each additional occupied LL (see figure 2.18c). In this case, the ECs consist of lines along the edge where the LLs intersect E_F (see figure 2.18a) and the area in between adjacent EC is incompressible. The charge carriers perform cyclotron orbits and are either backscattered at a hard edge potential (see figure 2.5b) or their orbits are asymmetric due to $\mathcal{E} \times B$ at a soft edge potential leading to drift motion along the edge, where $\mathcal{E}$ is the electric field. Both mechanisms result in a motion of the charge carriers along the edge and are the origin of the chirality in ECs. If interactions between charge carriers are included, they screen the electrostatic potential of the sample edge [13]. The screening length of the charge carriers strongly depends on whether the sample is compressible (short screening length) or incompressible (large screening length) [13]. In compressible areas the electric field is screened such as in a metal requiring a non-uniform charge carrier density according to Maxwell's 1. equation. In figure 2.18d compressible areas are shaded and in figure 2.18f, the increasing charge carrier density is visible compared to figure 2.18c with incompressible areas only exhibiting constant charge carrier density. In contrast, the incompressible areas exhibit a strong change of the electrostatic potential that is barely screened resulting from a constant charge carrier density (non-shaded areas in figure 2.18d). The width of the incompressible areas a_i (see figure 2.18f) depends on the energy difference between the LLs ΔE_N and the charge carrier density gradient dn_s/dx at the edge [13, 76]:

$$a_i = \sqrt{\frac{8\Delta E_N\, \epsilon_0(\epsilon+1)}{\pi\, e^2\, dn_\mathrm{s}/dx}}. \tag{2.52}$$

Each occupied LL leads to both a compressible and an incompressible stripe at the edge resulting in compressible stripes separated by incompressible ones along the edge as shown in figure 2.18d [13]. The distance between the incompressible stripes b_i (see

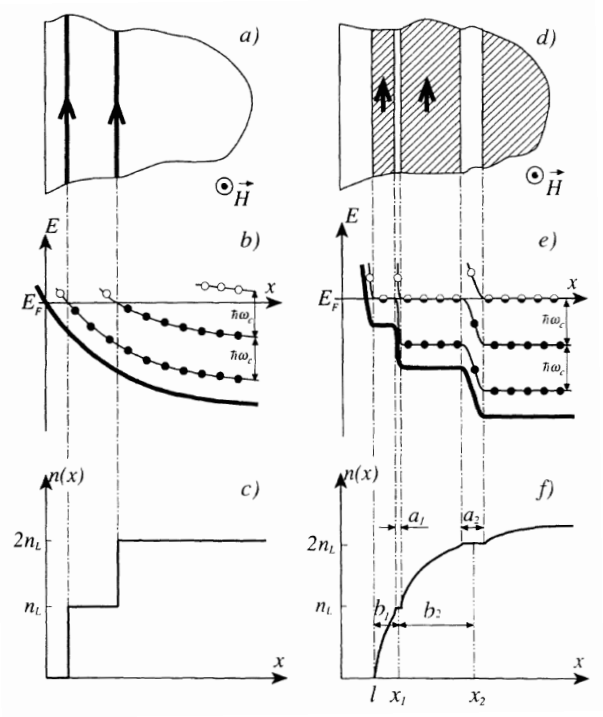

Figure 2.18: a: Edge channels (lines with arrows) along the sample edge in a single particle picture. b: LLs (thin lines with dots) that follow the electrostatic potential (bold solid line) at the edge of the sample and are filled up to E_F. (Un-)occupied states are represented by (empty) full circles, respectively. c: Charge carrier density corresponding to the LLs of subfigure b, n_LL is the LL degeneracy density. d-f: same as subfigures a-c but for interacting charge carriers. The width of the incompressible stripes is labeled a_i and the distance between incompressible stripes b_i. Reprinted with permission from D. B. Chklovskii, B. I. Shklovskii, and L. I. Glazman, Phys. Rev. B **46**, 4026 (1992) [13]. Copyright 1992 by the American Physical Society.

figure 2.18f) depends on the LL degeneracy n_LL (see equation 2.9) and the charge carrier density gradient $dn_\mathrm{s}/dx|_{x_i}$ evaluated at the position x_i of the incompressible stripe of the same LL [13]

$$b_i = \frac{n_\mathrm{LL}}{dn_\mathrm{s}/dx|_{x_i}}. \tag{2.53}$$

In another calculation, the width ratio of compressible and incompressible stripes is found to depend on the potential gradient and the interaction strength [87].

2.12 Scanning probe measurements of edge channels at a pn interface

Experimental investigations of ECs remain challenging in particular for conventional semiconductor heterostructures in which the two-dimensional electron system (2DES) is not exposed to the surface. The possibility to create tunable edge channels (ECs) in the center of a graphene pn sample (see section 2.10 and figure 2.17) has inspired many experiments. At the chemical potential step of a pn interface ECs form in a similar way as at the electrostatic potential at the edge of a sample and compressible as well as incompressible stripes develop if the interactions between charge carriers are sufficient.

A spatial mapping of the equilibrium current distribution along a bipolar graphene pn interface in the quantum Hall regime is shown in figure 2.19a. It reveals currents (label 'T' with blue arrows) in both parts of the pn interface with opposite current direction [10]. As no source-drain voltage is applied in this experiment, the currents are equilibrium currents. No net charge transfer between the channels is expected because both sides are on the same electrostatic potential. There are additional currents observed (label 'N' with red arrows in figure 2.19a) which counter flow that means two counterflow currents are located in the same part of the graphene pn interface. As expected without source-drain voltage, the net current is close to zero because the two currents almost cancel each other. The counterflow current does not contribute in transport experiments because it does not connect to the Fermi level of the electrical

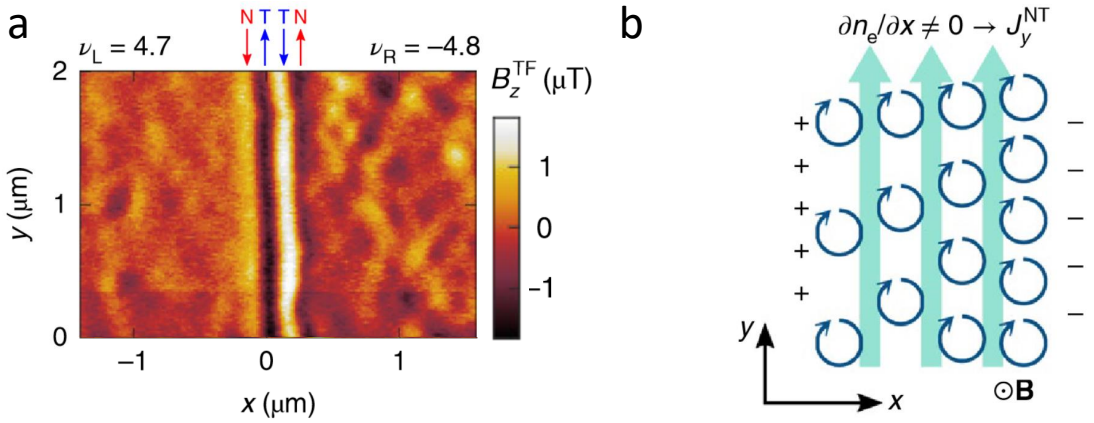

Figure 2.19: a: Local measurement of the out of plane magnetic field $B_z \propto I_{\mathrm{in-plane}}$ that is proportional to the in-plane current $I_{\mathrm{in-plane}}$. The pn interface is located at $x = 0\,\mu$m and the filling factors ν_L, nu_R describe the LL filling in both parts. ECs ('T') are indicated by blue arrows and the counter flow currents ('N') by red arrows. b: Sketch to explain current flow (turquoise arrows) due to a non-constant charge carrier density in compressible stripes. Both subfigures reprinted by permission from Springer Nature: Nature Physics **16**, 164-170, *Nanoscale imaging of equilibrium quantum Hall edge currents and of the magnetic monopole response in graphene.* A. Uri, Y. Kim, K. Bagani, C. K. Lewandowski, S. Grover, N. Auerbach, E. O. Lachman, Y. Myasoedov, T. Taniguchi, K. Watanabe, J. Smet, and E. Zeldov [10]. Copyright 2019.

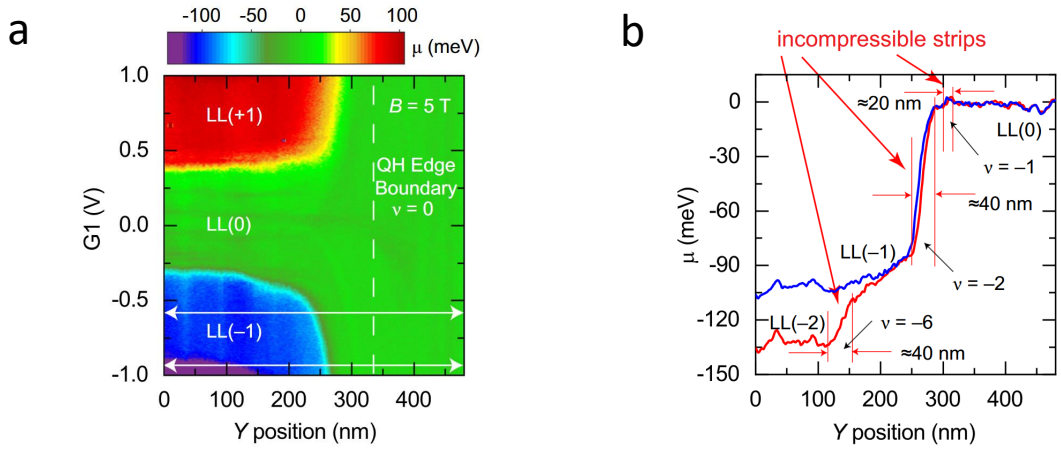

Figure 2.20: a: KPFM measurement of the chemical potential $\mu_{c,gr}$ across a pn interface for changing back gate voltage in the left part while the right part is constant. Different LLs appear in separate colours as indicated. b: Line cuts from subfigure a along the white arrows. Steps in $\mu_{c,gr}$ correspond to incompressible stripes (see figure 2.18e). Reprinted from Nature Communications **12**, 2852 (2021), *Edge channels of broken-symmetry quantum Hall states in graphene visualized by atomic force microscopy.* S. Kim, J. Schwenk, D. Walkup, Y. Zeng, F. Ghahari, S. T. Le, M. R. Slot, J. Berwanger, S. R. Blankenship, K. Watanabe, T. Taniguchi, F. J. Giessibl, N. B. Zhitenev, C. R. Dean, and J. A. Stroscio [29]. Licensed under a Creative Commons Attribution 4.0 International License https://creativecommons.org/licenses/by/4.0/.

contacts. The ECs are typically assumed to be located in the compressible stripes that form along the interface. In the incompressible stripes, the electrostatic potential perpendicular to the interface is changing even in equilibrium resulting in an in-plane electric field $\mathcal{E}_x$ that leads to an $\mathcal{E} \times B$ drift of the charge carriers along the interface leading to current flow in equilibrium. The counter flow currents reside in the compressible stripes where no in-plane electric field is present but a charge carrier density gradient that screens the edge potential (see figure 2.18e and f). No current is expected because of the missing $\mathcal{E} \times B$ drift. As the charge carrier density, however, is not spatially constant, the orbital motion of the charge carriers locally does not average out (see figure 2.19b) resulting in the counter flow currents that have opposite direction than the ECs. The width of the observed ECs is in the range of $80 - 380\,\mathrm{nm}$ depending on the chemical potential step at the interface.
In [29] ECs at a pn interface are investigated by means of KPFM (see section 3.2). The filling factor is tuned to $\nu = 0$ in one part rendering it insulating and ECs only appear on the other side of the pn interface, what equals a physical edge of a sample in the QHE. Also here, interactions lead to compressible and incompressible stripes which are identified by the accompanied chemical potential steps of incompressible stripes and the flat chemical potential of compressible stripes as can be seen in figure 2.20. The width of the incompressible stripe is about 40 nm. At higher magnetic fields even the degeneracy lifted ECs at $\nu = \pm 1$ of LL0 are visible. Measurements along the pn interface for several filling factors show the transition from extended states (into the bulk) to an EC where the width of the EC depends on the filling factor [29]. Furthermore

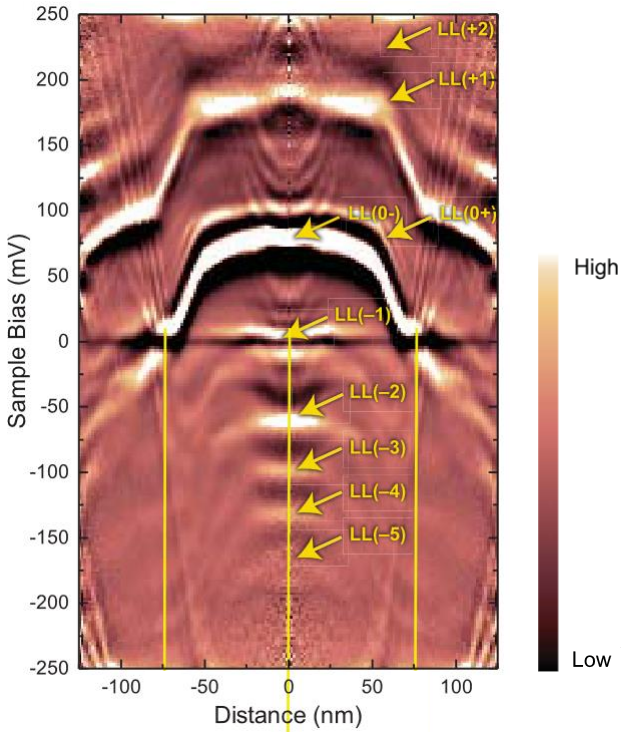

Figure 2.21: STS measurement of a graphene QD defined by a localized charge in the hBN substrate at $B = 4\,\mathrm{T}$. From Science **361**, 789-794 (2018) *Interaction-driven quantum Hall wedding cake-like structures in graphene quantum dots.* C. Gutiérrez, D. Walkup, F. Ghahari, C. Lewandowski, J. F. Rodriguez-Nieva, K. Watanabe, T. Taniguchi, L. S. Levitov, N. B. Zhitenev, and J. A. Stroscio [76]. Reprinted with permission from AAAS.

the EC does not form a straight line but is meandering along the pn interface with few 10 nm amplitude.
Incompressible stripes of similar 40 nm width are measured by STM at the edge of a QD that is created by a charge localized in the hBN substrate underneath the graphene [76]. The graphene above the charge is doped differently than the surrounding graphene and an annular pn interface appears confining charge carriers in the QD at large magnetic fields B. The initially bell-shaped electrostatic confinement potential of the QD takes a staircase shape resulting form flat compressible and steep incompressible rings (see figure 2.21). They form in the same way as at a straight pn interface. Additional effects due to the confinement of charge carriers in the QD might play a role since CLs are visible in the measurement of figure 2.21.
In a different experiment no compressible or incompressible stripes are observed in a graphene npn interface [18]. The npn interface is created by locally varying graphene substrate distances that occur due to lattice mismatch during the growth of graphene on metallic substrates like Rh in the case of [18]. The resulting npn interface is about one order of magnitude sharper than gate defined pn interfaces (see section 2.10) due to the close distance between graphene and the metallic substrate and the chemical potential $\mu_{\mathrm{c,gr}}$ changes by up to $30\,\mathrm{mV/nm}$. The LLs do not form (in-)compressible stripes in such steep potentials such that no stripes are observed similar to [17, 88].

2.13 Scanning probe measurements of other edge channels

Using STM/STS to probe ECs at the physical edge of a sample is challenging due to the vanishing tunneling current through the tip away from the conductive sample on an insulating substrate. This can be overcome by placing graphene on a conductive graphite substrate [17, 88, 89]. The conductive graphite substrate however screens the edge potential in the graphene layer such that it is atomically sharp and as a consequence compressible and incompressible stripes are not formed and no ECs are observed [17, 88] similar to the sharp npn interface [18]. For bilayer graphene however a bending of the LLs at the sample edge of about 20 meV amplitude and $2l_B$ length is reported [88].
Employing different scanning probe microscopy (SPM) methods not relying on conductive samples, ECs can be investigated at the physical edge of the sample. In [9] the local conductivity of a graphene sample is measured by microwave impedance microscopy (MIM) and compared to the global transport properties R_{xx} and σ_{xy} of the sample. On a transport plateau, where the bulk of the sample is supposed to be insulating and the current is supposed to be carried by the conductive ECs, however, a conductive bulk is measured by MIM [9]. An insulating bulk and conductive ECs are measured, in contrast, for transition between transport plateaus. These findings are tentatively explained by a different charge carrier concentration at the edge of a graphene flake placed on an insulating substrate compared to the bulk [9]. A single conductive channel of several 100 nm width is observed at the edge and individual edge channels for each LL are not resolved [9]. The differing transport and MIM results could arise from reconstruction of the ECs or even counterflowing ECs thtat are not resolved with MIM.
Via scanning gate microscopy (SGM), it is shown that the charge carrier concentration at the edge of a graphene sample is not only enhanced, but that a maximum exists close to the edge as a result of a non monotonous edge potential induced by fringe fields from the back gate [11]. The potential is increasing towards the edge and shows a maximum at few 100 nm away from the edge before it drops directly at the edge. The non monotonous edge potential results in two sets of ECs running along the edge in opposite directions that are spatially separated preventing back scattering between them. Antidots localized at defects in between these sets of ECs, however, can cause a connection between the opposite ECs, if tuned correspondingly via the SGM tip. This shows up as increased R_{xx} caused by the backscattering of charge carriers. The defects are observed at $50 - 150$ nm from the physical sample edge giving a rough estimate for the extent of the edge potential.
In conventional semiconductor heterostructures, ECs are measured by MIM [90] or scanning capacitance microscopy [7]. In both experiments, the width of the compressible stripes varies from about 100 nm to about 1 μm in dependence of the filling factor ν in good agreement with the theoretical estimates in[13]. An example of such a measurement depicting the ν dependence of the EC width is shown in figure 2.22: At (even) integer ν, the bulk is insulating and a narrow conductive stripe is located close to the physical edge of the sample. Towards half (or uneven) ν this stripe becomes wider until the complete bulk is conductive. ECs with even larger width than 1 μm are also observed by scanning single electron transistor measurements [8].

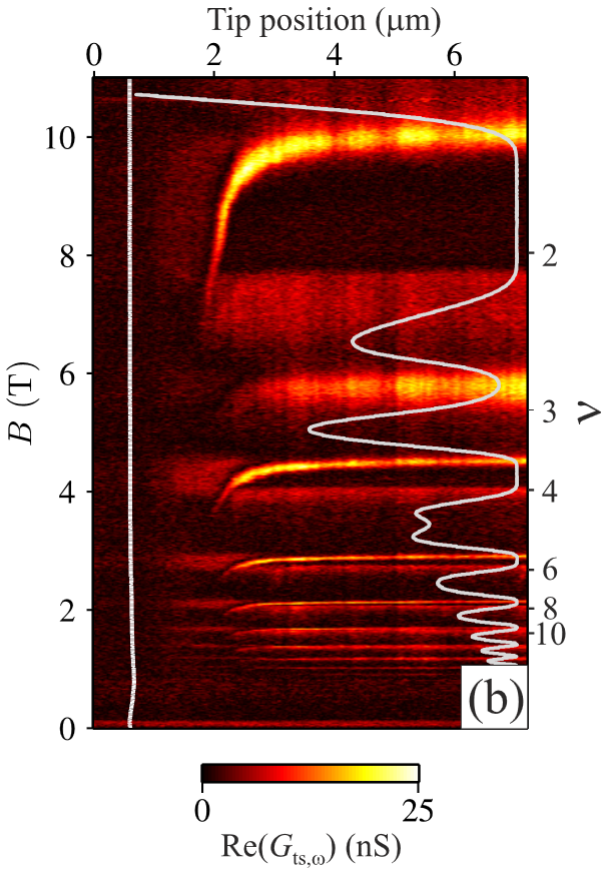

Figure 2.22: Real part of the signal of a scanning capacitance microscopy that is proportional to the local conductivity. The white vertical line on the left represents the physical edge of the sample. The white curve on the right is a measurement of the longitudinal sample resistance R_{xx}. Reprinted from New J. Phys. **14**, 083015 (2012), *Scanning capacitance imaging of compressible and incompressible quantum Hall effect edge strips.* M. E. Suddards, A. Baumgartner, M. Henini, and C. J. Mellor [7]. Licensed under a Creative Commons Attribution-NonCommercial-ShareAlike 3.0 license https://creativecommons.org/licenses/by-nc-sa/3.0/.

2.14 Poisson solver

In this thesis, a Poisson solver is used that was developed and programmed by Christian Holl for 3D semiconductors based on [91]. Afterwards the functionality was increased by Nils Freitag [59] in order to include graphene as a 2D material in the calculations. Employing the finite difference method the Poisson solver approximates a solution to the Poisson equation

$$\Delta\phi = \frac{\rho}{\epsilon\epsilon_0} \tag{2.54}$$

that relates the electrostatic potential ϕ with the charge density ρ. The solution depends on the boundary conditions that include the geometry of the problem via Dirichlet boundary conditions that fix the value of ϕ at a certain position. Additionally the dielectric constant ϵ is defined spatially as well the positions where the charge density ρ can vary. The Poisson equation is solved numerically on a grid. The Poisson solver solves the electrostatic problem of a metallic tip above an extended semiconductor or graphene surface and a metallic back gate underneath both with voltages applied. It reveals the spatial distribution of induced charge density below the tip. The problem is solved in cylindrical symmetry sketched in figure 2.23a. This renders the 3D (x, y, z) coordinates to 2D $(r = \sqrt{x^2 + y^2}, z)$ coordinates assuming identical results for all polar angles at the same radial coordinate r. Whereas this is suitable for tip-induced band bending and QDs in an extended graphene sample, it is not applicable for a linear pn interface. To this end, the geometry of the Poisson solver is changed to a 2D (x, z) Cartesian symmetry allowing the solution of electrostatic problems perpendicular to the pn interface as defined by two distinct back gates (see figure 2.23b). The possibility to extend the Poisson solver to a full 3D geometry was discarded in favour of

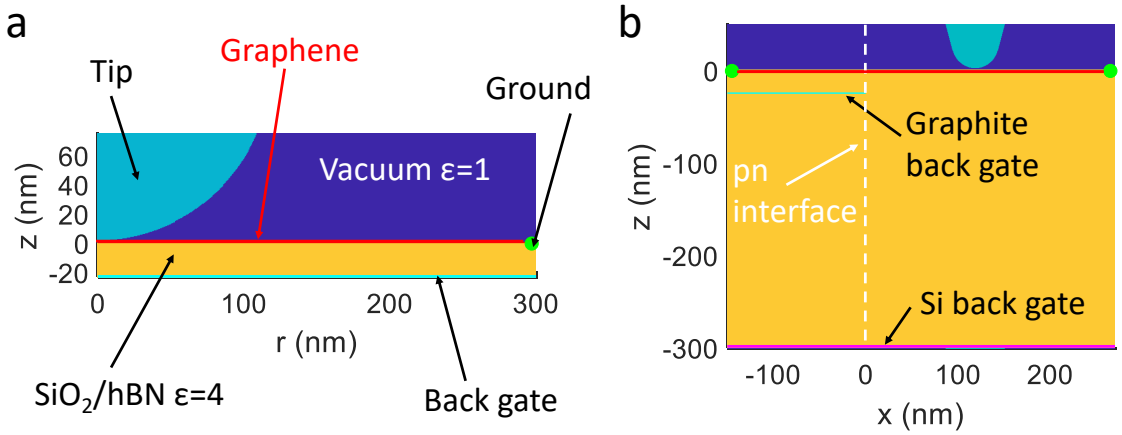

Figure 2.23: a: Geometry used for the Poisson solver that assumes cylindrical symmetry including a tip (turquoise) above a graphene layer (red) and a back gate (light blue). b: 2D Cartesian symmetry used for the Poisson solver for a tip above a graphene layer and two separate back gates (light blue and magenta) to create a pn interface indicated by the vertical white dashed line. The colours of the individual parts are the same as in subfigure a. The tip is shown for one specific position that can be changed along x.

faster simulation results due to limited computational power. Nevertheless, the 2D results approximate the solution along the cross section of the QD (x, z plane)for the used parameters if a mirror symmetry is assumed perpendicular to the pn interface ($y = -y$). The pn interface is included via additional (Dirichlet) boundary conditions at the second back gate for the solution of the Poisson equation similar as for the tip and for the first back gate electrode.
The graphene band structure as well as magnetic field induced LLs are captured via the density of states. The (local) graphene chemical potential $\mu_{\mathrm{c,gr}}$ and charge carrier density n_{s} are calculated via the Poisson equation as well as the electrostatic potential distribution in the dielectric materials (vacuum $\epsilon = 1$, hBN/SiO_2 $\epsilon = 4$). Depending on the applied potentials via the Dirichlet boundary conditions of tip and back gate, band bending occurs below the tip. The electrostatic interaction energy of the charge in the QD is contained in the Poisson equation and considered in the Poisson calculations (see section 2.9 for derivation of charging energy). As in the derivation in section 2.9, the graphene electrostatic potential is set to ground via Dirichlet boundary conditions at the edge of the graphene layer (green dot in figure 2.23). The Poisson solver considers charge continuous in energy and space. As a consequence it does not consider energy quantization within the QD. Localized states in the quantum Hall regime, that are available for screening, are not considered as well. Also more complex quantum mechanical interactions between charge carriers are not included in the model. Nevertheless, the interaction induced stripes as ECs at the pn interface and similar wedding cake like QD potential profiles are qualitatively reproduced by the Poisson solver. The mechanism is the strongly changing DOS of the LLs that leads to pinning of LLs at E_{F}. The screening length is different whether the DOS at E_{F} is large or small. On the microscopic scale of the magnetic length this mechanism is modified since the LDOS is altered by interactions.
For comparison of the solution from the Poisson calculations with the measured STS results, a code is written that plots the graphene LDOS spatially and as a function of V_{tip}. For this purpose, the LDOS below the tip is calculated for each V_{tip} and position by shifting the DOS of graphene in a magnetic field according to the calcularted $\mu_{\mathrm{c,gr}}$ directly below the tip. Subsequently, the DOS at E_{F} of the tip is plotted. The chemical potentials are interpolated between different points to increase the density of the plotted LDOS values.

3 Instrumentation

3.1 Scanning tunneling microscopy (STM)

In scanning tunneling microscopy (STM) a metalic tip is approached to a conductive surface to a distance d_{tunnel} below 1 nm. Electrons can tunnel from the tip to the sample and vice versa due to the quantum mechanical tunneling effect. Binnig and Rohrer invented the STM which images the topography of a sample by scanning the tip over its surface [14]. The transmission probability τ_{tunnel} for a single electron with charge $-e$ and mass m_e depends exponentially on the distance d_{tunnel} between tip and sample. For a rectangular tunneling barrier [51]:

$$\tau_{\text{tunnel}} = \frac{16E_{\text{electron}}(V_0 - E_{\text{electron}})}{V_0^2} \exp\left[-2d_{\text{tunnel}} \sqrt{\frac{2m_{\text{e}}}{\hbar^2}(V_0 - E_{\text{electron}})}\right] \tag{3.1}$$

where E_{electron} is the energy of the electron, V_0 the barrier height and $\hbar = \frac{h}{2\pi}$ the Planck constant. If a voltage V_{tip} between tip and sample is applied a tunneling current I sets in as shown in figure 3.1. Considering the density of states (DOS) of tip ϱ_{tip} and sample ϱ_{sample} the tunneling current I is described by the one-dimensional Bardeen model [51, 92]:

$$I = \frac{4\pi e}{\hbar} \int_0^{-eV_{\text{tip}}} \varrho_{\text{tip}}(E + eV_{\text{tip}})\ \varrho_{\text{sample}}(E)\ \tau_{\text{tunnel}}(\epsilon, V_{\text{tip}}, d_{\text{tunnel}})\ dE. \tag{3.2}$$

Here $\tau_{\text{tunnel}}(E, V_{\text{tip}}, d_{\text{tunnel}})$ takes into account the tunneling barrier with trapezoidal shape resulting from tip and sample work functions Φ_{tip} and Φ_{sample} as depicted in figure 3.1. In the Tersoff-Hamann-model the tip wave function is assumed to be s-like and the tunneling current depends on density of states of the sample measured at the position of the tip [93, 94]. The derivative of the tunneling current with respect to the applied tip voltage dI/dV_{tip} is then proportional to the density of states of the sample ϱ_{sample} assuming an voltage-independent transmission probability τ_{tunnel} and an energy independent ρ_{tip}:

$$dI/dV_{\text{tip}} \sim \varrho_{\text{sample}}(-eV_{\text{tip}}). \tag{3.3}$$

This quantity is measured in practice by modulating V_{tip} with a small alternating current (AC) voltage $V_{\text{tip}}^{\text{mod}}$ with frequency f^{mod} and detecting the resulting AC component of the tunneling current with a lock-in amplifier what is called scanning tunneling spectroscopy (STS) [51]. For positive (negative) V_{tip} (un-)occupied states of the sample are probed, respectively. By recording dI/dV_{tip} while varying V_{tip}, the sample LDOS(E) is obtained in first order (see figure 3.1). For these measurements, the tip is stabilized at $V_{\text{tip}}^{\text{stab}}$ and I^{stab} and the feedback loop of the STM is opened. The energy resolution ΔE

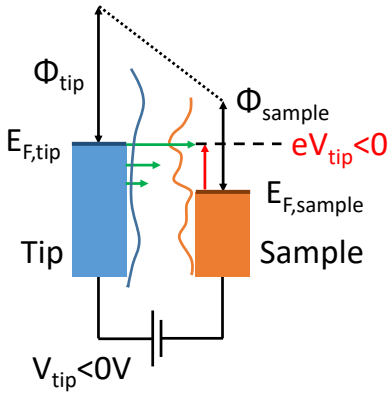

Figure 3.1: Tip and sample in tunneling contact with applied negative V_{tip} and resulting tunneling current I (green arrows). Tip and sample DOS are represented by curved, vertical lines and the trapezoidal tunneling barrier by the inclined dotted black line.

of the STS is given by the the temperature dependent width of the Fermi-distribution functionand the amplitude of V_{mod} [51]:

$$\Delta E \approx \sqrt{(1.4eV_{\mathrm{mod}})^2 + (3.2k_{\mathrm{B}}T)^2} \tag{3.4}$$

with the temperature T and the Boltzmann constant k_{B}. The modulation V_{mod} must be chosen as little as possible and is limited by the setups noise level and the available measurement time. To reduce the broadening of the energy resolution it is required to perform the STS at cryogenic temperatures. The cryostats used in this thesis that are presented in sections 3.4 and 3.5.

3.2 Atomic force microscopy (AFM)

The force F_{ts} between tip and sample is measured in atomic force microscopy (AFM) and mapped over the sample surface. The force consists of electrostatic, chemical, and van-der-Waals (vdW) forces between tip and sample as well as the Pauli repulsion occurring if wave functions of occupied states of tip and sample overlap. For a large tip-sample distance d_{ts}, all forces are vanishing and with decreasing d_{ts} the force F_{ts} becomes increasingly attractive (vdW force) before it gets repulsive at very close distance (chemical, Pauli repulsion). This behaviour of F_{ts} as a function of distance is sketched in figure 3.2a. The forces acting on the tip are detected by a shift Δf of the resonance frequency f_0 of the oscillating tip that is mounted on a spring-like cantilever or a tuning fork (see figure 3.2b) [51]:

$$\Delta f = -\frac{f_0}{2k}\frac{\partial F_{\mathrm{ts}}}{\partial z}\bigg|_{z_{\mathrm{tip}}=0} \tag{3.5}$$

This description assumes that the force gradient $\frac{\partial F_{\mathrm{ts}}}{\partial z}\big|_{z_{\mathrm{tip}}=0}$ is linear over the oscillation amplitude z_{tip} of the tip resulting in a validity for small amplitudes z_{tip} [51]. Furthermore $\frac{\partial F_{\mathrm{ts}}}{\partial z}\big|_{z_{\mathrm{tip}}=0}$ has to be much smaller than the spring constant k of the cantilever or

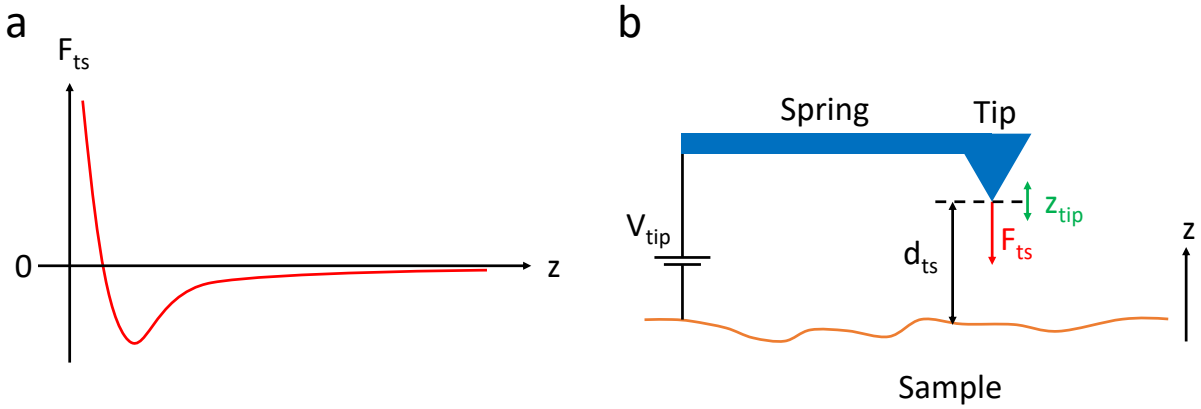

Figure 3.2: a: Qualitative dependence of F_{ts} with increasing distance. b: AFM tip mounted on a cantilever spring above the sample surface. The relevant quantities F_{ts}, d_{ts}, V_{tip}, and z_{tip} are indicated.

tuning fork [51]. For oscillation amplitudes z_{tip} much larger than the range of F_{ts} the frequency shift is described by [51]:

$$\Delta f = \frac{f_0}{\sqrt{2}\pi k z_{\mathrm{tip}}^{3/2}} \int_0^\infty \frac{F_{\mathrm{ts}}(d_{\mathrm{ts}} - z_{\mathrm{tip}} + u)}{\sqrt{u}}\, du \tag{3.6}$$

$$= \gamma \frac{f_0}{k z_{\mathrm{tip}}^{3/2}} \tag{3.7}$$

$$\gamma = \frac{1}{\sqrt{2}\pi} \int_0^\infty \frac{F_{\mathrm{ts}}(d_{\mathrm{ts}} - z_{\mathrm{tip}} + u)}{\sqrt{u}}\, du \tag{3.8}$$

where d_{ts} is the tip sample distance for zero oscillation amplitude and γ is the normalized frequency shift that is independent of the oscillation amplitude z_{tip}.
The electrostatic force F_{el} between tip and sample is tunable by applying a voltage V_{tip} between them [51]:

$$F_{\mathrm{el}} = -\frac{1}{2}\frac{\partial C_{\mathrm{tip}}}{\partial z}\left(V_{\mathrm{tip}} + \frac{\Delta\Phi}{e}\right)^2 \tag{3.9}$$

$$\Delta f \sim \left(V_{\mathrm{tip}} + \frac{\Delta\Phi}{e}\right)^2 \tag{3.10}$$

$$\Delta\Phi = \Phi_{\mathrm{sample}} - \Phi_{\mathrm{tip}} \tag{3.11}$$

where C_{tip} is the capacitance between tip and sample and $\Delta\Phi$ the work function mismatch between tip and sample as defined in equation 2.16 (see section 2.5). $F_{\mathrm{el}} = 0\,\mathrm{N}$ corresponds to the condition for no charge transfer between tip and sample and no band bending below the tip according to equations 2.19 to 2.23. As shown in equation 3.10 also the frequency shift has a parabolic dependence of the applied V_{tip}. This opens a possibility to measure $\Delta\Phi$ experimentally by determining the extremum of Δf as a function of the applied V_{tip}. If Φ_{tip} is known Φ_{sample} can be determined spatially what is called Kelvin probe force microscopy (KPFM).

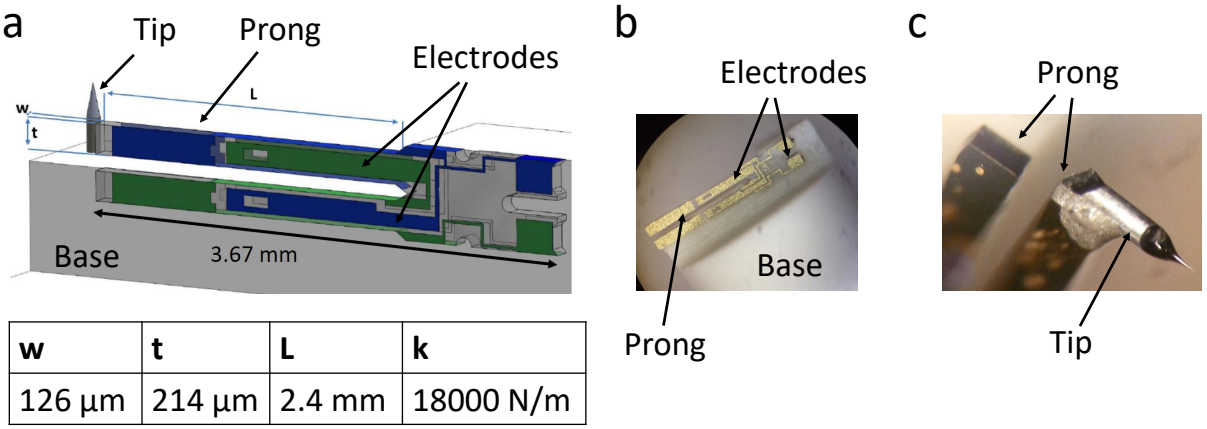

w	t	L	k
126 µm	214 µm	2.4 mm	18000 N/m

Figure 3.3: a: 3D drawing of a tuning fork sensor with tip mounted on a solid base. The dimensions indicated are given in the table in the lower part. b: Photo of a tuning fork without tip mounted on a base. c: Photo of an etched tip glued onto one prong of a tuning fork.

The implementation of an AFM requires that the tip can be mechanically excited and that the resulting oscillation z_{tip} and its frequency f can be detected. For both purposes many different arrangements are developed where in the following a tuning fork sensor is described which is also used in the 003 setup (see section 3.4). The tuning fork consists of two parallel prongs made out of quartz that are connected at the end. One of the prongs is glued to a solid base such that it can not oscillate and the other prong is used to oscillate the tip. This arrangement desribed in [95] is shown in figure 3.3. An etched metallic tip is glued to the end of the free prong and interacts with the sample surface for sufficient small distances (see figure 3.3c). If required it can be used for STM/STS as well (see section 3.1). The fabrication process in our research group is described in [96].
The tuning fork sensor is mechanically excited either by a piezoelectric actuator mounted below the base or via a longitudinal oscillation of tube piezo of the microscope. The resulting oscillation of the free prong is detected through the piezoelectric effect of the quartz, the tuning fork is made out of. To this end, two metallic electrodes (blue and green parts in figure 3.3a and golden in figure 3.3b) are located at the side of each prong [95]. The current between the electrodes generated by the piezoelectric effect is amplified by a current amplifier in close distance to the tuning fork sensor and converted into a voltage V_{tf} (see figure 3.4)[95]. This voltage is given as an input in a phase-locked loop (PLL) which consists of a phase detector, a feedback controller and a voltage-controlled oscillator (VCO) as schematically depicted in figure 3.4. The phase detector analyzes the phase difference φ_{tf} between V_{tf} and the VCO output V_{exc}. Depending on the phase difference φ_{tf} the frequency of the VCO is adjusted via the feedback controller to achieve a constant φ_{tf} between V_{tf} and V_{exc} [51]. This way of operating an AFM is called frequency modulation (FM). In the PLL tracking Mode, V_{exc} is used to excite the tuning fork sensor where an additional amplitude controller is used to keep the oscillation amplitude of the tip z_{tip} constant [51]. The tuning fork sensor is excited a its resonance frequency such that the phase difference $\varphi_{\text{tf}} = 90°$.

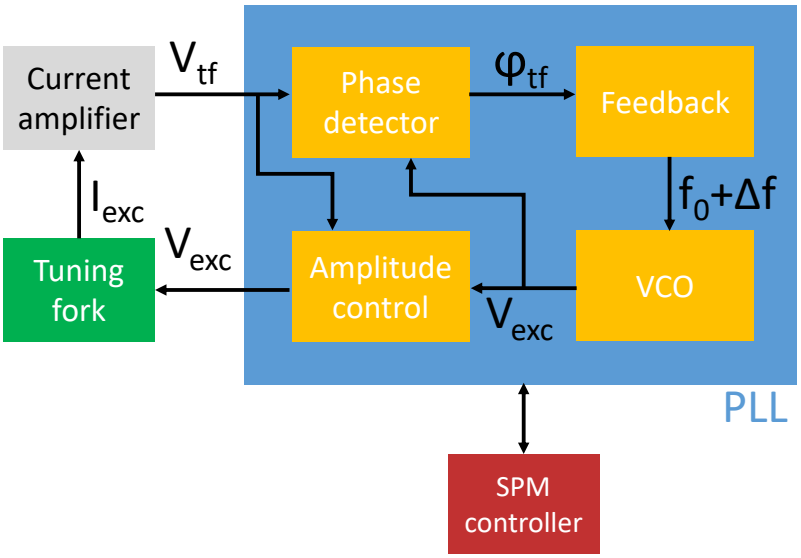

Figure 3.4: Working principle of a PLL (blue) with its constituents in yellow. The tuning fork sensor (green) as well as the current amplifier (gray) and the SPM controller (dark red) are represented by colored rectangles. The signals exchanged between the elements are shown as black arrows indicating the direction of the signal transfer.

As the resonance frequency changes with the distance dependent tip sample force F_{ts} according to equations 3.5 and 3.6, the oscillation frequency at resonance $f_0 + \Delta f$ is used as feedback signal for the height control of the tip by the SPM controller. More specific the tip sample distance is adjusted by the feedback to maintain a constant frequency shift Δf of the resonance frequency of the tuning fork sensor and thereby to keep the tip sample force gradient constant. A sensitive phase detection of φ_{tf} is crucial to keep the tuning fork sensor at resonance. This requires a narrow resonance peak in the frequency axis. This is the case, if little damping is present in the oscillator as described by the formula [51]

$$\Delta\varphi_{\mathrm{tf}} = \frac{\Lambda}{k}\frac{\partial F_{\mathrm{ts}}}{\partial z}\bigg|_{z_{\mathrm{tip}}=0} \tag{3.12}$$

where $\Delta\varphi_{\mathrm{tf}}$ is the difference from $\phi_{\mathrm{tf}} = 90°$ and Λ is the quality factor of the tuning fork sensor that is inverse proportional to the damping of the oscillation. A large $\Delta\varphi$ implying a high phase change for a small frequency change, that is high sensitivity, results from high Λ values. Atomic resolution of molecules is achieved with a tuning fork sensor at $T = 5\,\mathrm{K}$ oscillating with an amplitude of $z_{\mathrm{tip}} = 20\,\mathrm{pm}$ at a resonance frequency of 23 kHz with $\Lambda \approx 5 \cdot 10^4$ [97].

3.3 AFM electronics

The frequency modulated AFM based on the tuning fork sensor operated at cryogenic temperatures and controlled with a PLL offers many applications in addition to the STM/STS. It requires however at least three electrical lines (V_{exc}, I_{tf}, I or V_{tip}) to the tip stage of the microscope (if the tuning fork is not excited by the scanner piezo tube) and even further lines if a preamplifier is used at cryogenic temperatures as well. To implement an AFM in setups with lower number of lines an, AFM electronics has been developed at the University of Grenoble Alpes that requires only two lines at the tip stage for both AFM and STM measurement [75]. A schematic of the AFM electronics and its connection to a tuning fork sensor is shown in figure 3.5. It is used as a current amplifier as shown in figure 3.4 that connects tuning fork sensor and PLL. The two lines each connect one of the two electrodes of the tuning fork each. One electrode is grounded during AFM operation and can be used in STM operation to connect the tip as depicted in figure 3.5 by the black box connected to one contact of the tuning fork by a dotted line. In practice the tunneling current amplifier simply remains connected due to its cut off frequency of 1 kHz. To this end, the tip is electrically connected to this electrode via conductive glue that attaches the tip to the tuning fork (see figure 3.3c). The excitation signal V_{exc} is guided to the input of the AFM electronics where it is connected to the to inverting input (-) of two operational amplifiers. Following the concept of virtual ground of operational amplifiers V_{exc} is applied to the non-inverting input (+) of the operational amplifiers as well. One of the operational amplifiers non-inverting input is connected to the other electrode of the tuning fork. The tuning fork is excited by V_{exc} via the piezo electric effect of the quartz it is made of. The current flowing through the excitation line is amplified and converted into a voltage signal at the input of the AFM electronics by the operational amplifier (feedback resistances not shown in figure 3.5). It has contributions from the setups line capacitance and resistance V_{line} and a smaller contribution from the tuning fork V_{tf}. Both contributions depend on the frequency of the excitation voltage V_{exc} but with different resonance frequency and quality factor. This is used to compensate the

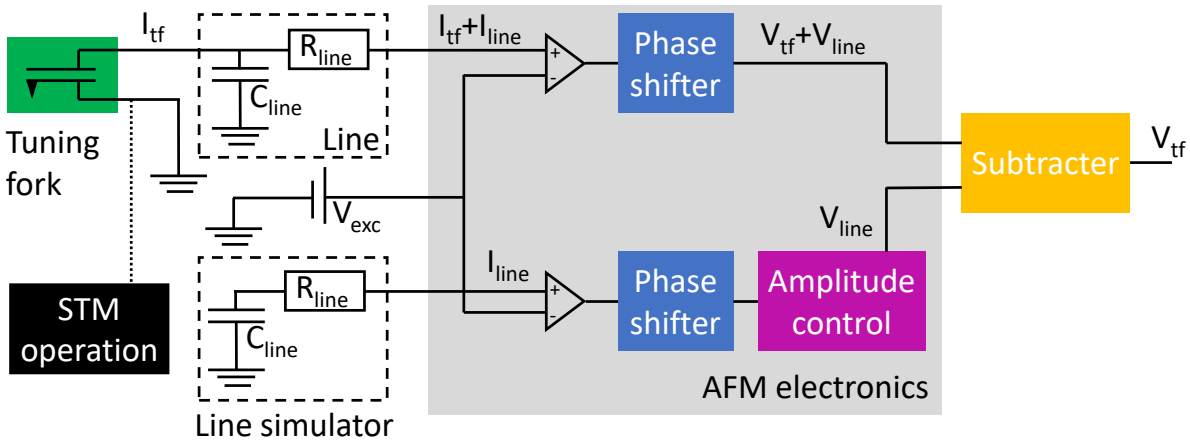

Figure 3.5: Diagram of the AFM electronics (gray box). On the left side the tuning fork (green box), the line simulator and V_{exc} are the inputs. The subtracter (yellow) is the output of the AFM electronics and given as input to the PLL.

line contribution V_{line}. An exchangeable RC element matched with the line capacitance and resistance (line simulator in figure 3.5) is connected to the non-inverting (+) input of the second operational amplifier of the AFM electronics. The line simulator is also excited by the excitation voltage V_{exc} in the same way as the tuning fork via the virtual ground principle. The signals from both input operational amplifiers pass through adjustable low pass filters with cut off frequency about 2/3 of the tuning fork resonance frequency. They are used to shift the phase such that both signals can be aligned in phase. The signal of the simulated line can additionally be amplitude corrected. The phase shifters as well as the amplitude control are adjustable by potentiometers which are accessible from the outside of the AFM electronics. Both signals, from the tuning fork and the line simulator, are given to the input of a PLL where they are subtracted from each other. One signal is given to the core and the other one to the shield of the coaxial input.
The following procedure is carried out to compensate the line contribution V_{line}: The frequency of the excitation signal V_{exc} is chosen lower than the tuning fork resonance frequency f_0 and phase as well as amplitude of the simulated line are altered in the AFM electronics until the PLL input is minimal. At this point the signals from both inputs of the AM electronics almost match each other and cancel out. The process is repeated for a frequency higher than the tuning fork resonance frequency until compensation is reached both below and above the resonance. Additionally different excitation amplitudes going from high to low can be tried. In the end, a sweep of the frequency shift should exhibit a clear resonance peak of the PLL input V_{tf}. Displaying both signals on an oscilloscope might help during the compensation process to visualize the effect of phase shift and amplitude control. To avoid a ground loop the excitation signal V_{exc} is decoupled by a transformer between PLL and AFM electronics (not shown in figure 3.5, but in figure 3.9).
After calibration, the interface between a SiO_2 surface and a gold contact is measured with a tuning fork sensor and the AFM electronics. The resulting topography is shown in figure 3.6a. The measurements are conducted at ambient conditions and room temperature with $\Delta f = 4\,\text{Hz}$, $V_{\text{exc}} = 7\,\text{mV}$ and $V_{\text{sample}} = 1.4\,\text{V}$ (for practical reasons $V_{\text{tip}} = -V_{\text{sample}}$ is connected to the sample in this experiment). The height of the gold contact is about 50 nm and the smallest imaged topographical features have a height of about $5 - 10\,\text{nm}$. The oscillation amplitude z_{tip} is calibrated in the following way: The oscillation amplitude is changed while the normalized frequency shift γ is kept constant and the resulting tip height d_{ts} with respect to the sample is measured. As γ and by this the tip sample force remains constant an increase in oscillation amplitude z_{tip} results in an increased tip height d_{ts}. It is assumed that the shortest distance between tip and sample during the tip oscillation remains constant such that a larger amplitude translates one-to-one into increased tip height. In the beginning, the tip is approached to the surface with setpoint $V_{\text{tf},1}$ and $\Delta f_1 = 0.5\,\text{Hz}$ and the height of the tip as well as V_{exc} are noted. In the next step, the V_{tf} setpoint is increased while the Δf setpoint is decreased such that the normalized frequency shift γ (see equation 3.6) remains constant where a linear relation between z_{tip} and V_{tf} is assumed:

$$\Delta f_2 = \Delta f_1 \left(\frac{z_{\text{tip},1}}{z_{\text{tip},2}} \right)^{3/2} = \Delta f_1 \left(\frac{V_{\text{tf},1}}{V_{\text{tf},2}} \right)^{3/2}. \tag{3.13}$$

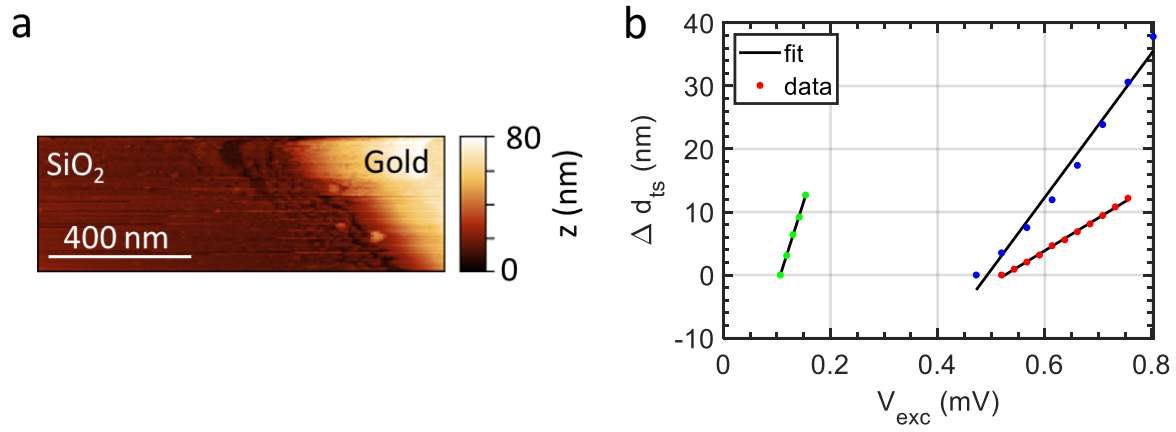

Figure 3.6: a: Topography of a gold contact and a SiO_2 surface measured with AFM at ambient conditions and room temperature. $\Delta f = 4\,\mathrm{Hz}$, $V_{\mathrm{exc}} = 7\,\mathrm{mV}$, $V_{\mathrm{sample}} = 1.4\,\mathrm{V}$. b: Calibration of the oscillation amplitude z_{tip} of the tuning fork sensor at $T = 8\,\mathrm{K}$. For $\Delta d_{\mathrm{ts}} = 0\,\mathrm{nm}$, $\Delta f = 0.5\,\mathrm{Hz}$ that is reduced according to equation 3.13 for the following points. Three series of measurements recorded with several days interval (green, blue, red) are shown and the resulting slopes are $S_{\mathrm{v}}^{\mathrm{green}} = 267\,\mathrm{nm/mV}$, $S_{\mathrm{v}}^{\mathrm{blue}} = 115\,\mathrm{nm/mV}$, and $S_{\mathrm{v}}^{\mathrm{red}} = 52\,\mathrm{nm/mV}$, respectively.

Again tip height and V_{exc} are recorded. This procedure is repeated several times and the recorded tip height Δd_{ts} subtracted by the initial value as an offset over the excitation voltage V_{exc} is shown in figure 3.6b. Linear fits to the data taken at $T = 8\,\mathrm{K}$ reveal slopes ranging from $S_{\mathrm{v}} = 50 - 270\,\mathrm{nm/mV}$. The resulting minimal oscillation amplitude is about 30 nm for each slope in figure 3.6b. The resonance frequency out of contact is $f_0 = 23.964\,\mathrm{kHz}$ and the quality factor $\Lambda \approx 70.000$ for $V_{\mathrm{exc}} = 5\,\mathrm{mV}$. Compared to [97], both resonance frequency and quality factor are similar, however the minimal oscillation amplitude is 1000 times larger our measurements. This results from the use of the AFM electronics only instead of additional amplifiers close to the tuning fork at cryogenic temperatures. The performance of the tuning fork operated with the AFM electronics is nonetheless sufficient to safely move the tip towards conductive areas on partly insulating samples either by direct imaging or via the EFM method (see section 4.4) as required for subsequent STM/STS measurements.

3.4 The 003 setup: 400 mK 14 T cryostat for STM/AFM and transport measurements

The setup consists of liquid nitrogen (LN_2) and He tanks which are surrounded by ultra high vacuum (UHV) that thermally decouples the tanks from ambient conditions as shown in figure 3.7. The central part of the setup is the insert which includes a closed ^{3}He system that cools down the bottom of the insert to $T = 0.4\,\mathrm{K}$ where the microscope body is mounted. The insert can be moved vertically and can be (de-)coupled to or from cold stages at 4 K (He main bath) or 1.5 K (1K pot) via pressurized cold switches that are necessary for the operation of the closed ^{3}He system. Tips and samples can be exchanged in situ with a wobble stick (not shown in figure 3.7) at the transfer position of the insert. Here, also optical access to the sample is possible for the alignment of tip and sample (see section 4.2) making STM measurements of flake-sized samples feasible. In measurement position, the microscope is inside the bore of a superconducting solenoid that can reach magnetic fields up to $B = 14\,\mathrm{T}$. Further UHV chambers with access to the main UHV chamber include possibilities for sample preparation such as

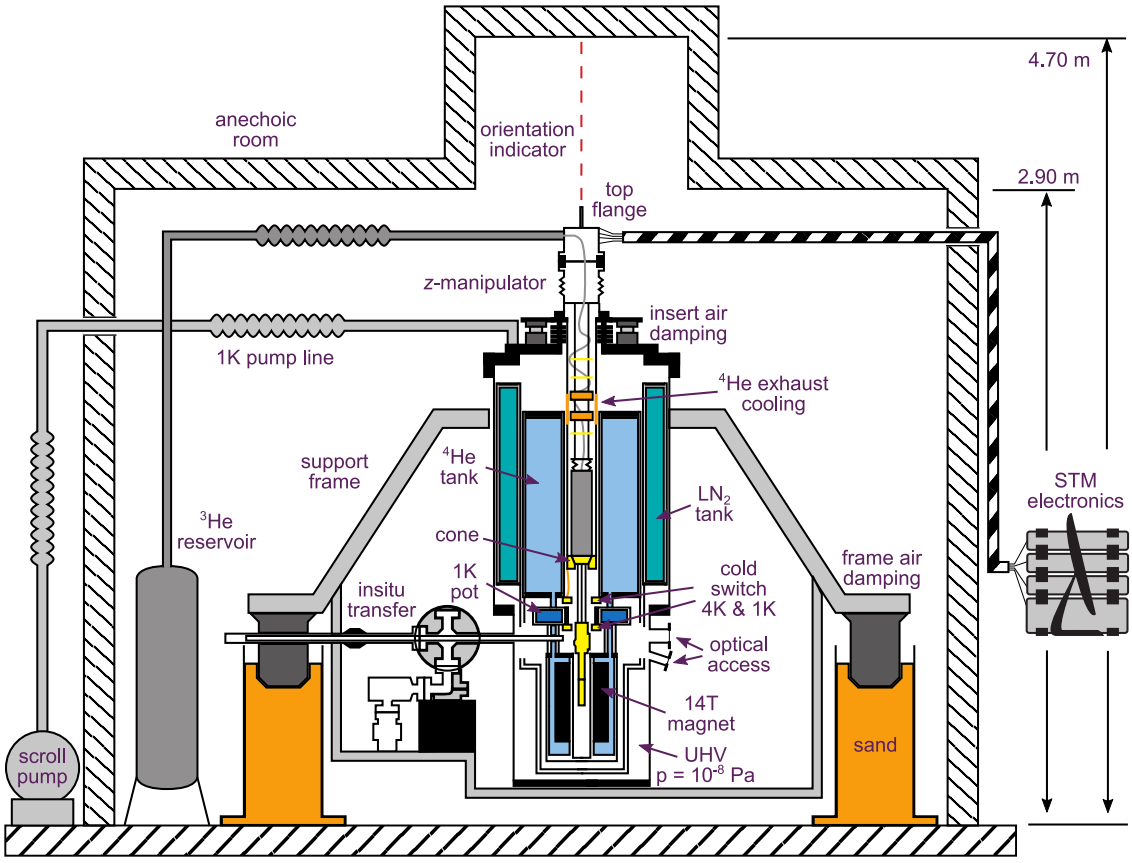

Figure 3.7: The 003 setup with He tank (light blue) and LN_2 tank (green) resting on a damped frame (gray). Reprinted by permission from AIP Publishing: Rev. Sci. Instrum. **88**, 123707, *An ultrahigh-vacuum cryostat for simultaneous scanning tunneling microscopy and magneto-transport measurements down to 400 mK.* M. Liebmann, J. R. Bindel, M. Pezzotta, S. Becker, F. Muckel, T. Johnsen, C. Saunus, C. R. Ast, and M. Morgenstern [98]. Copyright 2017.

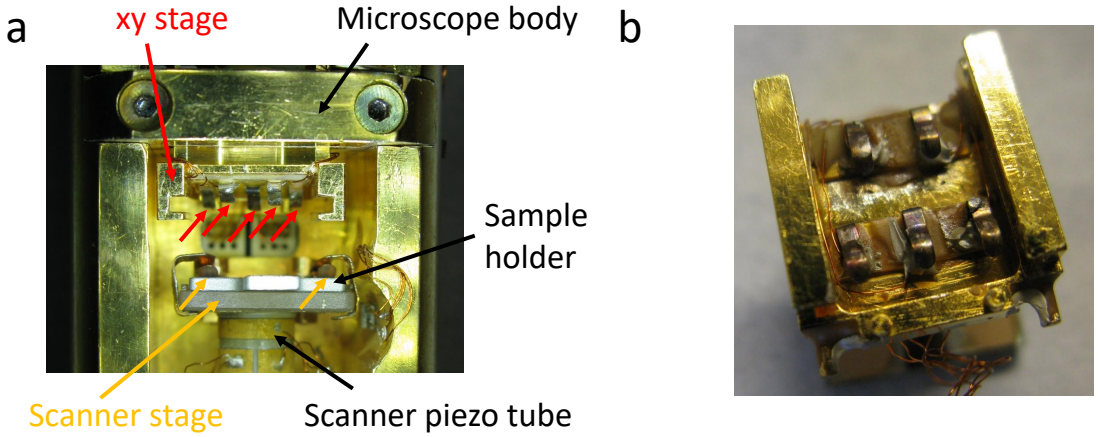

Figure 3.8: a: Scanner stage and xy stage of the microscope as mounted in the 003 setup (see figure 3.7). The springs for electrical contacts on the scanner stage (two orange arrows) and the xy stage (five red arrows) are indicated. b: Top view on the unmounted xy table with five contact springs.

sputtering, heating or evaporators as well as sample storage. A load lock allows to exchange samples and tips from UHV to ambient conditions. Detailed descriptions of the entire setup are found in [98–101].
The setup is mechanically decoupled from the ground floor via pressurized air damping legs resting on sand (orange in figure 3.7). Furthermore the insert is placed on a second damping stage also consisting of pressurized air damping legs with different resonance frequency that mechanically decouples the insert from the remainder of the setup, in particular the LN_2 and He tanks. With these arrangements, the microscope shows a noise level of about 1 pm in z direction [98]. The microscope offers multiple electrical contacts to either tip or sample stage [102]: The scanner stage has two electrical contacts marked with orange arrows in figure 3.8a and the xy stage has six electrical contacts: five contact springs marked with red arrows in figure 3.8a, and the xy stage itself. The arrangement of the contact springs is shown in figure 3.8b. Both tip and sample can either be mounted in the scanner or xy table stage depending on the number of required contacts provided the sample holder or tip holder fits with the contact springs of the respective stage. The xy stage has a clearance of $2 \times 2\,\mathrm{mm}^2$ that allows for tip positioning by relative motion of tip and sample. The electron temperature is $520 \pm 20\,\mathrm{mK}$ for the scanner stage and $440 \pm 10\,\mathrm{mK}$ for the xy stage [98]. The higher number of contacts compared to other STM setups allows for a larger variety of experiments in parallel to STM studies such as four-probe magneto transport experiments including a back gate (see section 3.6 for technical details and section 7.3 for results) or AFM (see section 3.3). The combination of transport measurements probing global sample properties and STM/STS measurements on the local scale of the same sample in one setup is rarely found in other setups [103, 104].
STM measurements on a back gated sample are carried out in this setup (see sections 7.4 and 7.5 for results). The wiring scheme for back gated AFM/STM/STS measurements developed by the in-house electronics workshop is shown in figure 3.9: The tip is grounded by the tunneling current amplifier and the bias $V_{\mathrm{sample}} = -V_{\mathrm{tip}}$

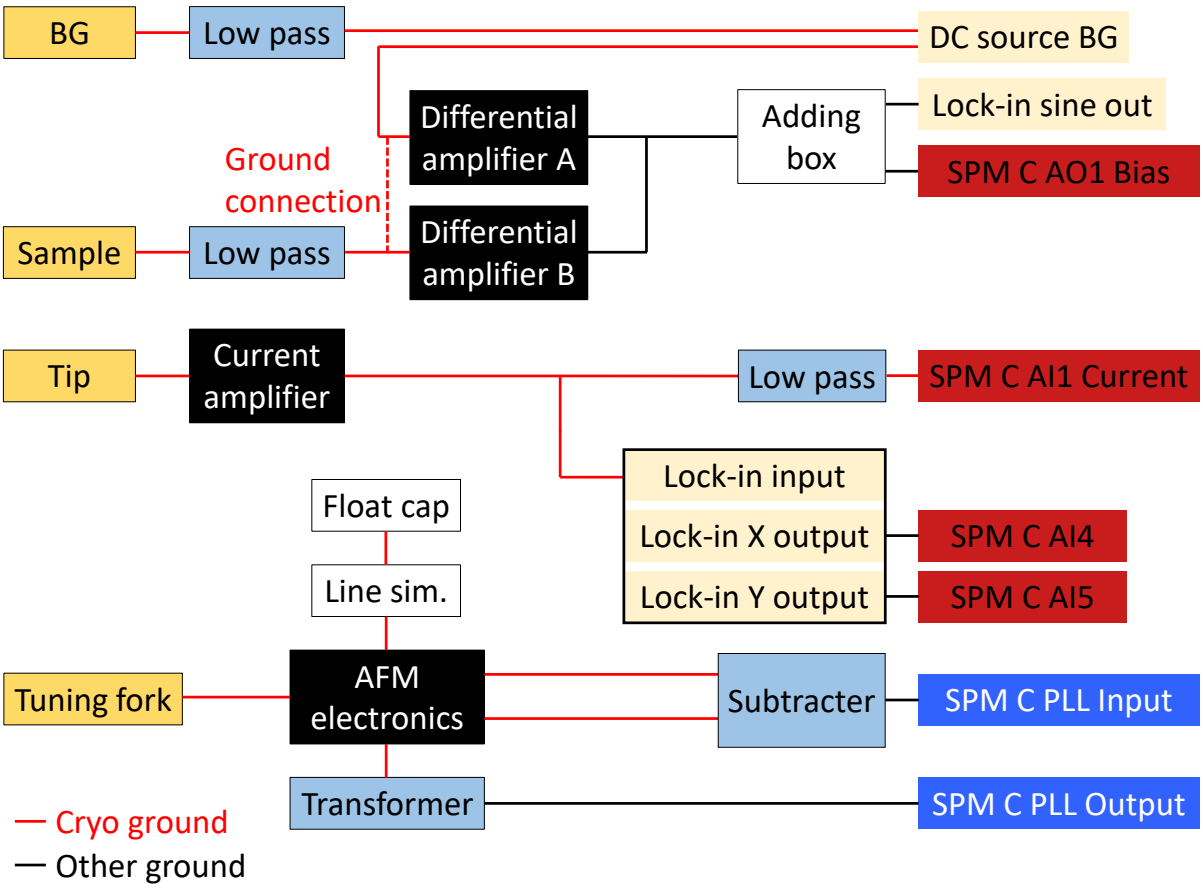

Figure 3.9: Wiring schematic for AFM/STM/STS measurements on a sample (yellow) with back gate (BG, yellow) as used in the 003 setup. Yellow boxes on the left show parts inside the cryostat (BG, sample, tip, tuning fork). Other parts in the left half are connected in close distance to the feedthroughs (low pass filters, differential amplifiers, tunneling current amplifier, AFM electronics, transformer). Boxes on the right are placed outside the acoustically insulated room: SPM controller ('SPM C', dark red) including PLL (dark blue), lock-in amplifier (beige), DC voltage source (beige), adding box (white), low pass filter (blue) and subtracter (blue). The low pass filters have a cut off frequency of about 700 Hz (23 nF, 10 kΩ) and the differential amplifiers have a cut off frequency of 1 kHz. The line simulator (white) has 310 Ω and 560 pF. Red lines are coaxial cables which shield is connected to the ground of the cryostat whereas black lines are coaxial cables which shield is connected to other ground connections. The red dashed line between the differential amplifiers is a connection of both shields that is needed to ensure the correct reference for the upper differential amplifier A.

is applied to the sample through differential amplifier B that decouples the ground between setup (cryostat) and SPM electronics to avoid ground loops. The back gate voltage V_{bg} is applied with respect to V_{sample} by a floating DC voltage source. The reference for V_{bg} is V_{sample} and taken between SPM electronics and differential amplifier B and is itself given in the second differential amplifier A before entering the reference input of the DC voltage source. Following this scheme, the ground remains decoupled between setup and SPM electronics. The output of the DC voltage source is $V_{\mathrm{bg}} + V_{\mathrm{sample}}$ with respect to (cryostat) ground and V_{bg} with respect to its reference input. The shield of the coaxial cable between the differential amplifier and the DC voltage source has to be connected to (cryostat) ground to maintain the correct reference for V_{bg}. In an alternative wiring scheme, the sample would remain grounded by the tunneling current amplifier while V_{sample} would be applied to the tip. This has the disadvantage that any change in V_{bg} results in a capacitive displacement current measured by the tunneling current amplifier. In the lower part of figure 3.9, the schematic wiring for the AFM electronics (see section 3.3) is shown including the transformer that decouples the ground between cryostat and PLL. It operates similar as the differential amplifiers for V_{sample} and V_{bg} that are mostly DC.
For convenient automated data acquisition with varying external parameters like V_{bg} or B, an existing software is used. Within the software, the DC voltage source and the magnetic power supply can be controlled as well as the STM electronics for specific tasks. Employing this software, automated STS measurements while sweeping parameters like V_{bg} or B can be performed. Examples of such measurements are found in figures 7.8b, 7.9, and 7.10.

3.5 The 004 setup: 7 K (7, 3, 0.5) T vector magnetic field cryostat for high frequency STM

A He bath cryostat is the main component of this setup. It contains a superconducting solenoid that can reach $B_z = 7\,\mathrm{T}$ perpendicular to the sample surface and $B_y = 3\,\mathrm{T}$ or $B_x = 0.5\,\mathrm{T}$ in-plane magnetic fields. A tube like UHV chamber placed in the bore of the solenoid hosts the microscope mounted on an insert. The UHV tube is thermally coupled to the He bath by a He exchange gas. Thereby the He tank is mechanically decoupled from the UHV tube. The insert with the microscope can be mechanically and thermally coupled to the UHV tube. Then the microscope reaches $T = 7\,\mathrm{K}$ in equilibrium. From this measurement position, the insert with the microscope can be raised vertically. This enables to exchange tips and samples in-situ. If the insert is raised further, one gets optical access to the sample inside the microscope for tip-sample alignment (see section 4.2). UHV chambers next to the main chamber contain sample preparation facilities like heaters, sputter guns, evaporators and garages. Extensive descriptions of the setup are given in [105, 106].
The microscope is optimized for high frequency STM measurements [107] that are however not employed within this thesis. The tip is mounted in a xy stage that can move the tip about $2 \times 2\,\mathrm{mm}^2$ with respect to the sample placed on the scanner stage. The xy stage is grounded and connects the tip to a high frequency compatible con-

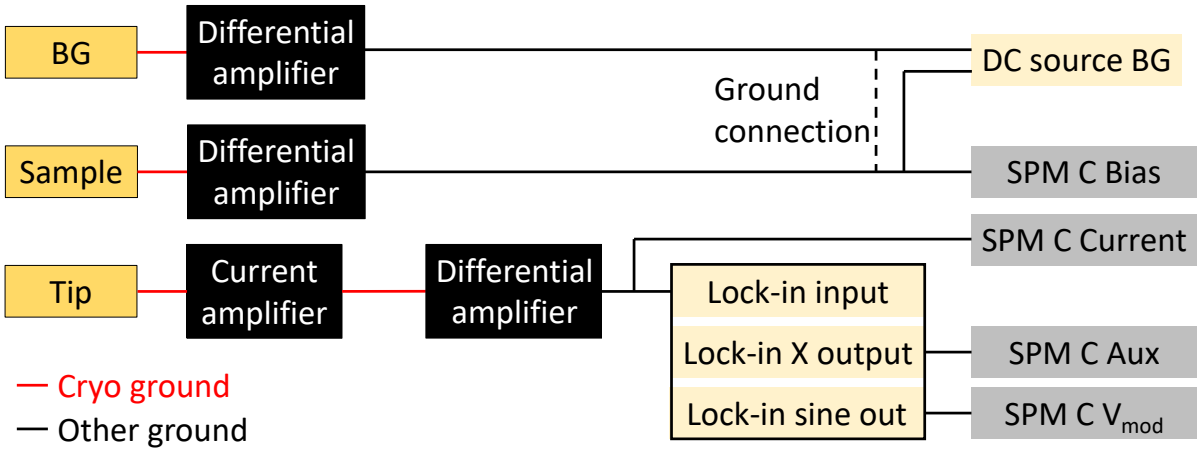

Figure 3.10: Wiring schematic for STM/STS measurements on a sample with back gate and small V_{bg} as used in the 004 setup. Tip, sample, and back gate (BG) are inside the cryostat (yellow boxes) and the corresponding amplifiers (black boxes, cut off frequency 1 kHz) are connected close to the feedthroughs. Boxes on the right are placed outside the acoustically insulated room: SPM controller ('SPM C', gray), lock-in amplifier (beige) and DC voltage source (beige). Red lines are coaxial cables which shield is connected to the ground of the cryostat whereas black lines are coaxial cables which shield is connected to other ground connections. The black dashed line between the differential amplifiers is a connection of both shields that is needed to ensure the correct reference for the upper differential amplifier.

nector. This arrangement allows for the implementation of an AFM as presented in section 3.3, if one of the two electrodes of the tuning fork is permanently on ground. The other electrode is used both for exciting the tuning fork in AFM operation and for contacting the tip for STM operation. The scanner stage has two electrical contacts such that STM/STS measurements on a back gated sample are possible. In contrast to the 003 setup (see section 3.4), no transport measurements of back gated samples can be conducted because of the lower number of electrical contacts. The back gate voltage could be applied following the scheme presented in section 3.4 and figure 3.9. For the measurements of this thesis (see section 5), an alternative scheme was used as shown in figure 3.10. The sum $|V_{\mathrm{sample}}|+|V_{\mathrm{bg}}|$ always remains smaller than the maximum output voltage of 10 V of the decoupling box. This is because $|V_{\mathrm{bg}}| \leq 3.5\,\mathrm{V}$ due to the thin hBN gate dielectric of 23.5 nm. The floating DC voltage source for V_{bg} is referenced to V_{sample} at the output of the STM electronics. The output of the DC voltage source is then passed through a differential amplifier before entering the setup. Compared to the wiring schematic in figure 3.9 the position of the differential amplifier in the back gate branch is changed from in between SPM controller and DC source to in between DC source and back gate. The tip is connected to the tunneling current amplifier and kept grounded while the sample is biased with V_{sample}.

3.6 Transport measurements

Transport measurements are carried out at low temperature either in the 003 setup (see section 3.4) or in a commercial closed system ^{3}He bath cryostat reaching $T = 0.3\,\mathrm{K}$ and $B = 10\,\mathrm{T}$ (for more details see [108]). For room temperature transport measurements, a setup designed for LN_2 is used, in which the sample can be held in vacuum during the measurements [109]. To apply a bias V_{sd} and measure the resulting current I_{sd} through the sample, an IV converter constructed by the in-house electronics workshop is used. It applies 1/10.000 of the AC input voltage $V_{\mathrm{in}}^{\mathrm{AC}}$ between source and drain contacts of the sample, where $+V_{\mathrm{sd}}/2$ is given to one contact and $-V_{\mathrm{sd}}/2$ to the other (see figure 3.11). This way, the central part of the sample is at ground potential, if contact resistances are similar for both contacts. The current I_{sd} is measured via the feedback resistances of two operational amplifiers through which $\pm V_{\mathrm{sd}}/2$ is applied. The measured current I_{sd} is converted into a voltage that is amplified by an adjustable gain and available at the output of the IV converter as $V_{\mathrm{out}}^{\mathrm{AC}} \sim I_{\mathrm{sd}}$. In practice, a lock-in amplifier is employed which reference signal is used as $V_{\mathrm{in}}^{\mathrm{AC}}$ for the IV converter such that V_{sd} has no DC component except offsets. The amplitude of V_{sd} is in the range of $100\,\mu\mathrm{V}$ with a frequency below 100 Hz. The IV converter output $V_{\mathrm{out}}^{\mathrm{AC}} \sim I_{\mathrm{sd}}$ is connected to the lock-in amplifier as input. By applying a constant amplitude of V_{sd}, the maximum of dissipated power P in the sample is limited even if the resistance R_{sd} of the sample changes according to $P = V_{\mathrm{sd}}^2/(R_{\mathrm{sd}} + R_{\mathrm{line}})$, where R_{line} is the line resistance of the setup (not shown in figure 3.11). Four-probe measurements eliminate the contributions of line and contact resistances. For them an additional lock-in amplifier is employed

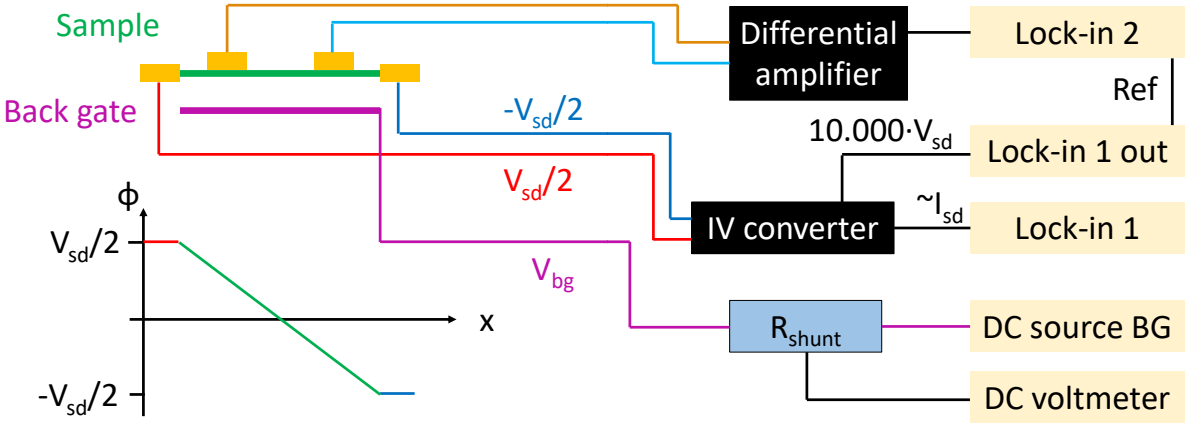

Figure 3.11: Wiring schematic for transport measurements of a sample (green) with back gate (violet). The IV converter applies $\pm V_{\mathrm{sd}}$ (red or dark blue lines) to the sample contacts (golden). Additional contacts are used in four-probe-configuration to measure the voltage drop with a differential amplifier (brown and light blue lines). Both IV converter and differential amplifier are connected to lock-in amplifiers (beige) that are using the same reference signal. V_{BG} (violet line) is applied via s shunt resistance R_{shunt} (light blue box) by a DC voltage source (beige). The voltage drop at R_{shunt} is measured with a DC voltmeter (beige). The electrostatic potential ϕ across the sample is shown in the lower left corner.

and synchronized with the first lock-in amplifier via the reference signal. The voltage drop along the sample is measured between the two additional contacts by a differential amplifier (see figure 3.11). This *van-der-Pauw* amplifier is constructed by the in-house electronics workshop as well. The output of the *van-der-Pauw* amplifier is given as input into the second lock-in amplifier. To measure both R_{xx} and R_{xy} simultaneously, at least five contacts are required. Moreover, another differential amplifier as well as a lock-in amplifier are necessary. If only four contacts are available, R_{xx} and R_{xy} are measured sequentially by switching the contact geometry. The back gate voltage V_{bg} is supplied by a DC voltage source via a large shunt resistance $R_{\mathrm{shunt}} \sim 1\,\mathrm{M\Omega}$ to the sample. The voltage drop across the resistance is measured by a DC voltmeter to detect a possible short cut of the back gate. In this case, R_{shunt} also protects the sample against destruction by large currents. The ground connection between measurement setup and lock-in amplifiers is interrupted by the IV converter and the differential amplifier. For the V_{bg} line, the DC voltage source as well as the DC voltmeter have floating connectors.

4 Approach of an STM tip to a flake-sized sample

4.1 Literature overview

The challenge is to position the tip of the STM close to or directly on the graphene flake, that typically is $10 - 20\,\mu$m in size. The tip navigation procedure reduces the number of STM topography measurements to find the graphene flake that could possibly degrade the tip. Moreover, potential tip crashes are avoided as the graphene flake is often surrounded by an insulating substrate. Different methods from the literature are described below: In [110], the use of an optical telescope is mentioned to position the tip onto a graphene flake. If STM measurements are conducted inside an UHV chamber, the working distance of the telescope has to be large (working distance $> 10\,$cm) compared to optical microscopes (working distance $< 1\,$cm). This limits the resolution to about $20\,\mu$m. Instead a scanning electron microscope inside the UHV chamber can be used [111]. This, however, implies additional instrumental effort.
The metallic leads contacting the graphene flake can be used as a guide line for the tip positioning as well. For example, the leads are patterned with alternating thickness in a fan like structure in [29]. The tip can easily be positioned on the lead fan optically compared to the graphene flake only. The lead fan is locally imaged by the tip (in the case of [29] in AFM mode) and the tip moved along the fan until it reaches the graphene flake. In a different approach, the capacitance between tip and leads is used to find out the position of the tip with respect to the leads [112]. Thereby, the tip is not in tunneling contact to the sample but moved with a defined distance larger than $1\,\mu$m across the leads [112]. During the motion different voltage signals from both the lead and the back gate electrode are capacitively induced in the tip and allow for the position estimation. The flake is found at the end of the leads and by identifying features in the lead. Instead of using the leads as a guide, also markers in the insulating substrate can serve for this purpose [75]. This method however fully relies on the use of an AFM. Once a marker is identified by its topography, the tip can be moved accordingly towards the graphene flake. A different approach to the tip positioning challenge is presented in [113], where a large part of the sample is covered with a graphene flake grown by chemical vapor deposition (CVD) that is subsequently transferred onto a Si/SiO_2 chip with exfoliated hBN flakes. The tip is approached on the large graphene flake in STM mode and then moved until a hBN flake below the graphene is identified by its topography.

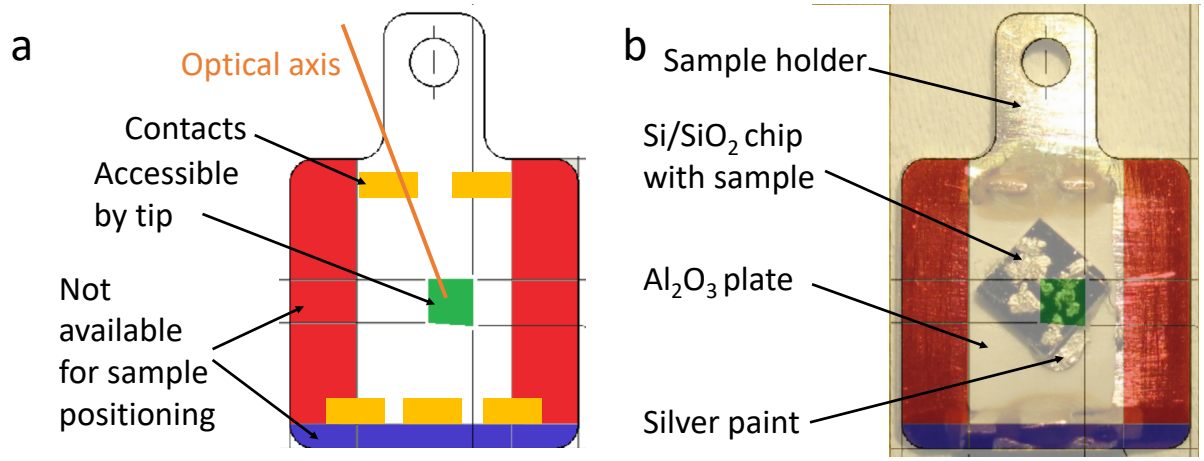

Figure 4.1: a: Drawing of a $12 \times 12\,\mathrm{mm}^2$ sample holder for the 003 setup (see section 3.4). The tip can reach the green area in the center of the sample holder. Red and blue areas are required for rails during the sample transfer and in the storage. Golden boxes show the position of the electrical contacts. The orange line is the optical axis towards the view port of the UHV chamber. b: The drawing overlaid on the sample holder with the Si/SiO_2 chip of the graphene sample GR10BN24. Silver parts are silver paint that is used to glue the sample on the sample holder and to contact the sample.

4.2 Optical approach

In order to successfully position a tip on a graphene flake several things have to be considered before the optical alignment of tip and sample in the microscope body itself starts. First the area of the sample holder has to be identified that can be reached by xy coarse movement of the tip (green area in figure 4.1). This can be done by intentionally crashing a tip into a bulk graphite sample in the extreme positions of the xy coarse movement [114]. The graphene sample should be located in the center of that area. Consequently the chip of the graphene sample has to be significantly smaller than the free area of the sample holder, where typically $4 \times 4\,\mathrm{mm}^2$ chips are used. To check the correct position of the graphene sample on the sample holder photos taken with a digital camera can be overlaid in a image manipulation software with a drawing of the sample holder (see figure 4.1b). For this purpose, a drawing of the sample holder is prepared. It includes the area that can be reached by the tip and all areas that have to be kept clear for sample transfer and storage in the UHV chamber. Moreover, the direction from where the telescope is looking at the sample is marked (see figure 4.1a). If possible, the chip on the sample holder is rotated such that the metallic leads on the sample are in line (0° or 90°) or at 45° with respect to the direction between view port of the UHV chamber and microscope body. A possible path of the tip from a contact lead to the graphene flake should be in line with one of the xy coarse movement directions. Any contact wires should not be in the optical path from the view port to the sample.
The telescope should be aligned to the graphene flake where an angle of roughly 45° between sample surface and optical axis proved suitable. For this purpose, an additional mirror has been mounted into the 003 setup. It makes the xy table optically

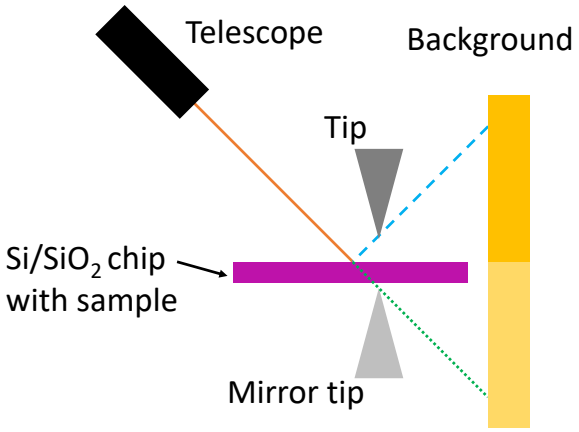

Figure 4.2: Side view of the optical path (solid orange line) from the telescope (black) to the sample (violet) acting as a mirror (not in scale, the UHV chamber including view port not shown). The mirrored optical axis is shown as a dashed light blue line that hits the tip (dark gray) and the background of the microscope (dark yellow). Both appear mirrored along the dotted green line (mirror tip in light gray and mirrored background in light yellow).

accessible under this angle compared to an angle of only 23 ° without mirror. A mirror that allows for even larger angles up to 90° can be placed on the tip holder. It is transferable from ambient into the UHV chamber. Different angles can be used without the need to vent the UHV chamber.
Compared to a table-top optical microscope with 90° angle between optical axis and sample surface, the contrast between different parts of the sample is different and more importantly the sample surface acts as a mirror as sketched in figure 4.2. This implies two outcomes: Firstly the tip appears twice as real tip (dark gray in figure 4.2) and mirror tip (light gray in figure 4.2), if it is close to the sample surface. Both tips are sharply visible at different working distances of the telescope. Secondly, the contrast of the sample (once in focus) strongly depends on what is imaged via the mirror from the background behind the sample (yellow in figure 4.2). The background consists of a part of the microscope body that is imaged out of focus (blurry). Previously, this background part of the microscope body has not been considered during its design. Recently, the contrast of the sample in the 003 setup was improved by adding non reflective, white aluminum oxide plates on the back of the microscope body [115]. In the 004 setup, the background mirror image exhibits a better contrast, if a long tip of 8.5 mm length measured from the surface of the tip holder is used. This might be further improved by adding aluminum oxide plates on the tip holder. To get a high contrast of the sample surface, the illumination is the key, for which powerful gooseneck lamps are used. In the 004 setup, the illumination from the view port below the optical microscope turned out to be practical such that the light from the lamp is reflected from the microscope body to the sample surface and further towards the telescope. In the 003 setup, parallel illumination to the telescope as well as from the other view port of the transfer plane and the lower view port is used. To find out whether a gooseneck lamp is adjusted correctly it is moved manually while looking through the telescope

until the intensity and contrast are maximized. A C-mount camera is attached to the telescope and the telescope image is recorded by a software that enables to change contrast, intensity, colors, gain and exposure time. Multiple images are taken at different tip positions and overlaid to optically approach the tip on the graphene flake with the following procedure: Firstly the tip is safely approached to a contact lead in STM (or AFM) mode using a low tunneling current and moderate bias (or small frequency shift) (auto coarse approach). Then, it is directly withdrawn ($\sim 100\,\mathrm{nm}$). In this position, the first optical image is afterwards recorded. An example is shown in figure 4.3a. Afterwards the tip is withdrawn by a fixed number of steps (50) and another image with the telescope is recorded (tip out of contact, figure 4.3b). Both images are overlaid. The edges of the gold contacts (turquoise lines) and debris on the gold contacts (violet circles) are marked in figure 4.3a and are used as reference to align figure 4.3b. Furthermore, the position where tip and mirror tip touch is estimated and marked with a red circle in figure 4.3a (and copied to figure 4.3b) as well as the outlines of the withdrawn tips are marked with red lines in figure 4.3b. In the next step, the tip is moved towards the graphene flake and a third image is captured with the telescope (tip over flake, figure 4.3c). In the example of figure 4.3c, the tip is placed at the corner of the upper left gold contact from where it will be moved in STM mode onto the near-by graphene flake. The red outlines of the tips and the red circle from figure 4.3b are overlaid and allow to estimate the position where tip and mirror tip will touch, that is where the tip approaches the sample surface. This position is compared to the position of the graphene flake and, if necessary, the tip is repositioned. To verify the position of the graphene flake, extended lines from the contact leads or other optical features on the sample might help. Additionally an optical microscope image of the sample recorded prior to the sample transfer into UHV can be overlaid with the telescope image as shown in figure 4.3d. The optical microscope image is aligned to the telescope image by the outline of the visible flakes in figure 4.3c. It turned out that contact leads can appear at shifted positions in the telescope images compared to the optical microscope image what is indicated by the light blue lines in figure 4.3d. Probably this is induced by reflections due to the $45\,^\circ$ angle of the telescope to the sample surface. It is assumed that this problem is not appearing for the much thinner flakes such that they are used for the alignment.
The overlaying process of three different telescope images is required because the contrast changes once the tip is in close distance to the sample surface and the graphene flake is hardly visible anymore. Additionally the mirror tip covers part of the sample surface. The fixed number of steps to withdraw the tip also helps in the following STM or AFM approach since the expected number of steps is known. Accordingly the approach can be stopped if too many steps have elapsed indicating an STM approach on an insulating area. This method enables to position the tip with respect to the corner of the contact with a precision of about $20\,\mu\mathrm{m}$.

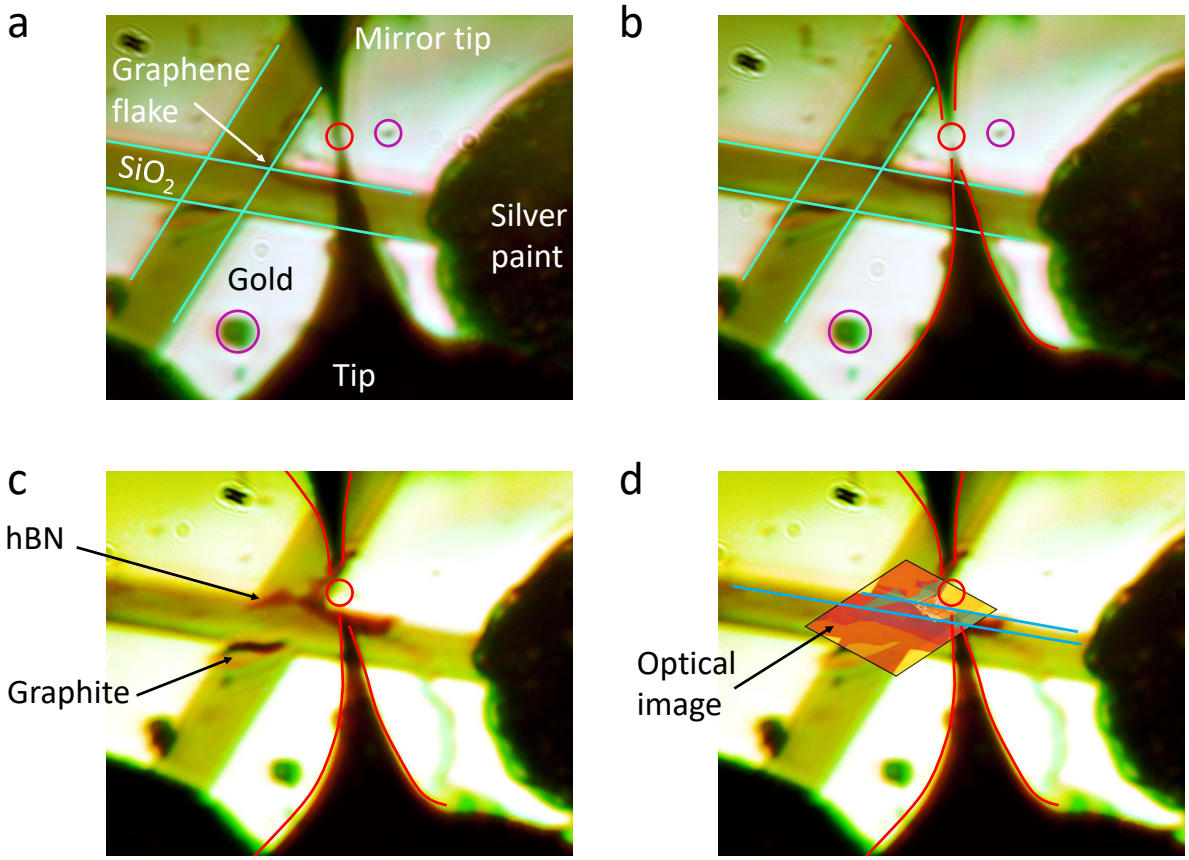

Figure 4.3: Optical approach of the tip to a graphene flake (graphene pn sample). All images are recorded with a camera through a telescope. a: The tip is about 100 nm away from the gold contact such that tip and mirror tip apparently touch each other (red circle). Turquoise lines and violet circles are used in subfigure b as markers. b: The tip is withdrawn 50 by coarse steps from the gold contact. The outlines of tip and mirror tip are highlighted in red. c: The tip is aligned to the corner of the gold contact close to the graphene flake. The red outlines and the red circle are taken from subfigure b and a, respectively, and moved to the new lateral tip position. d: Optical microscope image of the sample recorded prior to transfer into UHV overlaid with the telescope image. The blue lines show the position of the edge of the gold contact in the optical microscope image (upper line) and the telescope image (lower line).

4.3 Capacitive approach

The optical approach in the 003 setup was not precise enough to approach the tip on a graphene sample before the additional mirror was installed. Instead the capacitive approach reported in [112] has been tried out. The tip is optically approached to a contact lead and then in STM mode before it is withdrawn by a fixed number of steps. The wiring is changed to detect the capacitance following the circuit of [112]. An AC voltage is applied to the contact leads and another one with a phase difference of 180° to the back gate. The voltage source is the output of a lock-in amplifier V^{AC} that either by a transformer or by a second lock-in amplifier is split into the two phase shifted signals. The AC voltage capacitively induces an AC current in the tip which is connected to the current amplifier of the STM setup and grounded. The voltage output signal of the current amplifier is connected to the input of a lock-in amplifier and proportional to the capacitance. The amplitude of one of the two AC signals can be changed by a voltage divider and is adjusted such that the AC current signal of the tip is minimized (compensation). Now the tip is moved towards the edge of the contact lead over the back gate ('trench') and to the next contact lead by the xy coarse movement (see schematic inset in figure 4.4a) where preferably only motion in one direction is used. This motion and the data acquisition is automatized with a program and an example of a recorded current-position trace is plotted in figure 4.4a. As the tip is moved across contact lead and back gate the voltage contributions from both change at the tip resulting in a increased current signal due to missing compensation. From the recorded current-position trace the position of the tip with respect to the contact lead is estimated as shown in figure 4.4a. Recording several traces including the graphene area allows for the navigation towards the graphene flake. Unlike to the back gate trench, the signal is not increasing on the graphene flake because it has the AC voltage of the contact leads applied and screens the AC voltage applied to the back gate. In figure 4.4b a map recorded on an area with trench along x and a graphene

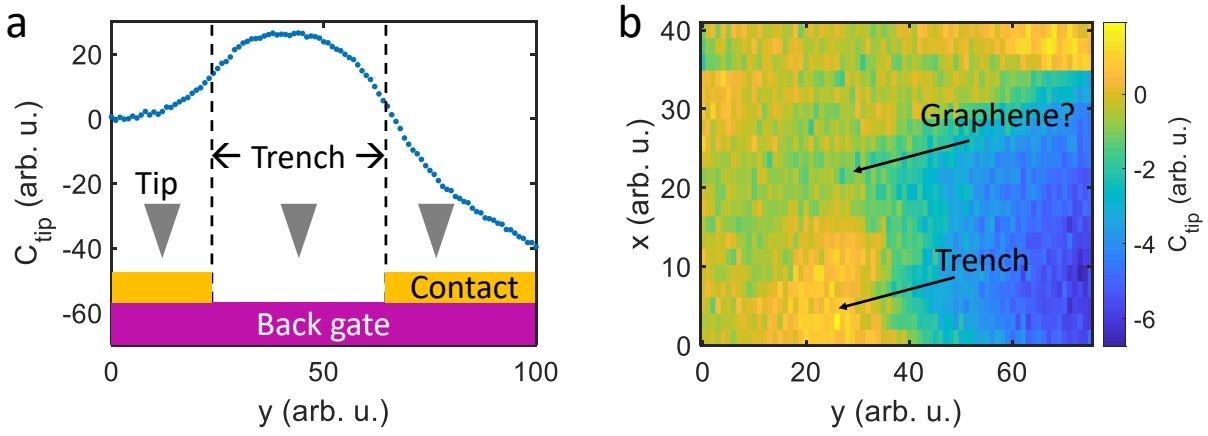

Figure 4.4: a: Capacitance trace recorded while moving the tip (grey triangle) from a contact lead (golden) on the left over the back gate (violet) to the contact lead on the right. $V^{\mathrm{AC}} = 50\,\mathrm{mV}$, $f = 5\,\mathrm{kHz}$. b: Map of the recorded capacitance over an area with the graphene flake in the center and a vertical trench. The size is about $100 \times 160\,\mu\mathrm{m}^2$ ($y \times x$). $V^{\mathrm{AC}} = 50\,\mathrm{mV}$, $f = 5\,\mathrm{kHz}$.

flake in the center is shown. At the bottom the increased signal over the trench is visible between $y = 20 - 30$ arb. u.. It gets weaker at about $x = 20$ arb. u. where the graphene flake is assumed to the located. In contrast to [112], the AC current trace is used not its derivate with respect to the movement direction because of more clear features. While moving the tip closer to the graphene flake also the adjusted minimal signal on the contact lead changes. Often, sequentially recorded current traces are not similar. Eventually, the signal-to-noise ratio is too high to identify the area of the graphene flake with the required precision of below 10 μm. The reason is not clear, but likely is related to uncontrolled stray capacitances. Additionally, the xy stage is not constructed for a precise movement, such that one can not go back to a position after completing a full xy image. Consequently, this method is not further used.

4.4 Electrostatic force microscopy approach

Electrostatic force microscopy (EFM) is employed to find out above which electrode of the sample the tip is located. The tip is optically aligned as near as possible to the graphene flake and approached in AFM mode to the sample surface. The frequency shift Δf is then recorded as a function of the voltage applied either to the sample $V_{\text{sample}} = -V_{\text{tip}}$ or to the back gate V_{bg} while the tip is grounded and lifted by 20 nm. If the tip is located on a contact lead as shown in the inset of figure 4.5a, Δf will respond to V_{sample} forming a parabola (see figure 4.5a) described by equation 3.10, but it will not respond to V_{bg} (see figure 4.5b). Vice versa Δf depends on V_{bg} for a tip located on top of the back gate independent of V_{sample} (not shown in figure 4.5). On the graphene flake Δf follows both V_{sample} and V_{BG} but each in different ways. Because V_{sample} changes the electrostatic force between tip and sample directly Δf shows a parabola-like behaviour as a function of V_{sample} (see figure 4.5e). In contrast, V_{bg} changes the work function Φ_{gr} of the graphene flake according to equation 2.5 and thereby the work function mismatch $\Delta\Phi = \Phi_{\text{gr}} - \Phi_{\text{tip}}$ between tip and sample. In most cases the change of Φ_{gr} is smaller than $\Delta\Phi$ and the resulting $\Delta f(V_{\text{bg}})$ curve is monotonic and not parabolic (see figure 4.5f). By this feature also interface areas between contact lead and back gate where Δf changes both with V_{sample} and V_{bg} can be distinguished from the graphene flake because both will result in a parabolic Δf dependence (see figure 4.5c and d).
A strategy to move the tip towards a graphene flake follows either a narrow contact lead or an exposed back gate area ('trench') up to the graphene flake. The advantage compared to the capacitance method (see section 4.3) is that the position of the tip with respect to any electrode is known on the spot and does not require to record a capacitance trace moving the tip across the electrode. By the EFM approach, the not reliably working xy coarse movement is less important. Moreover, it is very safe to approach the tip in AFM/EFM mode compared to STM, where the tip might crash on an insulating area. For the final approach on the graphene flake, only few coarse steps have to be made to approach the tip from AFM/EFM contact into STM contact. This requires an implemented AFM/STM setup. In the 003 setup (see section 3.4), several approaches using this method could be successfully completed.

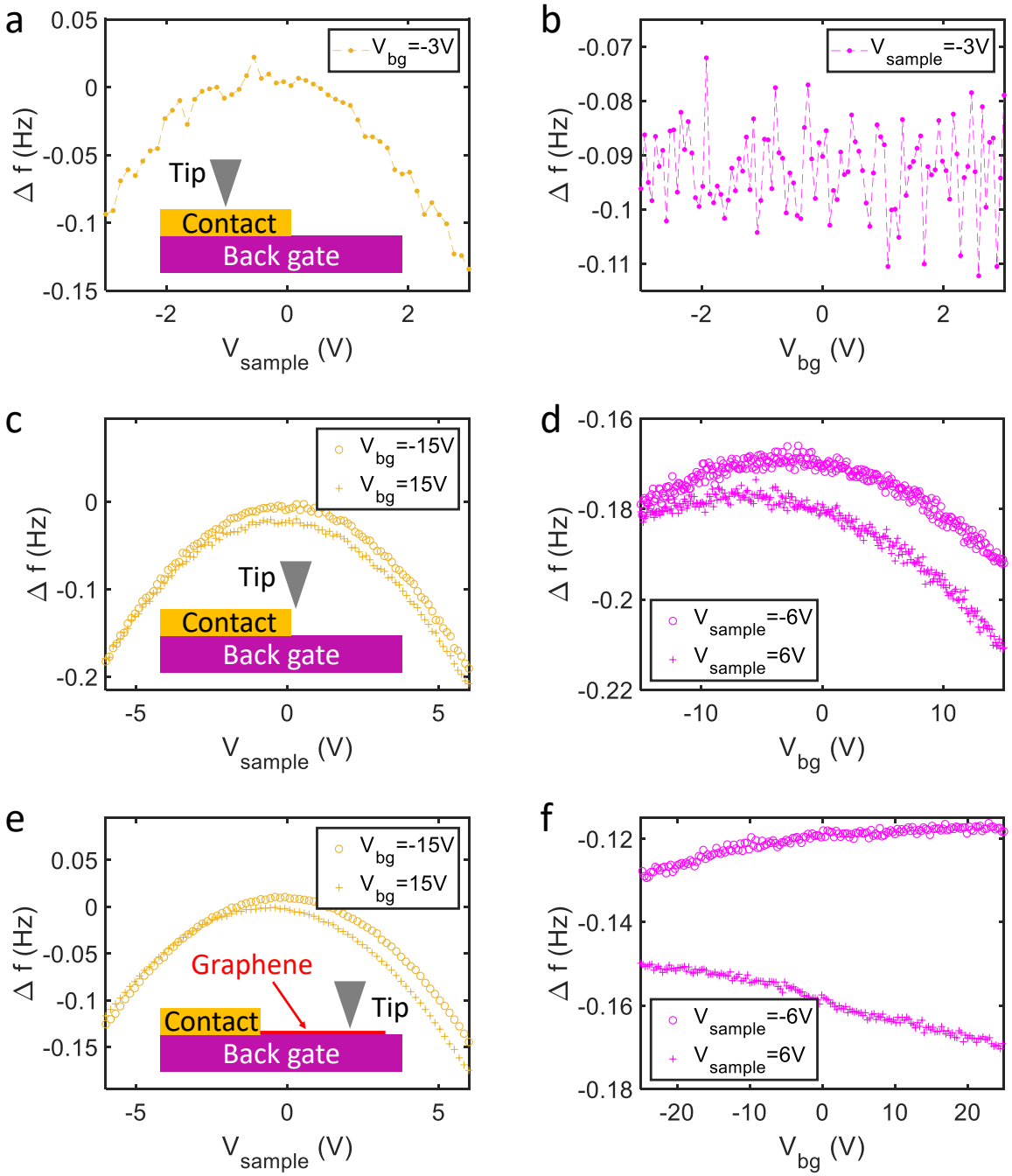

Figure 4.5: Local measurement of Δf in dependence of V_{sample} (a,c,e) or V_{bg} (b,d,e). The tip (gray) is positioned on a gold contact (a,b), at the interface of the gold contact (golden) and the back gate (violet) covered with SiO_2 (c,d), or on a graphene flake (red, e,f) as sketched in the insets. Insulators as SiO_2 or hBN are not depicted in the sketches for clarity. $T = 5\,\text{K}$ (a-d), $32\,\text{K}$ (e,f), $V_{\text{tf}}^{\text{setpoint}} = 2.5\,\text{mV}$ (a, b), $9\,\text{mV}$ (c, d), $7\,\text{mV}$ (e,f), $f_0 = 23963\,\text{kHz}$, $d_{\text{ts}} = d_{\text{ts}}^{\text{contact}} + 20\,\text{nm}$.

5 Interplay of edge channels and tip-induced quantum dot at a graphene pn interface

Parts of this chapter have been published in [116]:

Mapping quantum Hall edge states in graphene by scanning tunneling microscopy
T. Johnsen, C. Schattauer, S. Samaddar, A. Weston, M. Hamer, K.Watanabe, T. Taniguchi, R. Gorbachev, F. Libisch, and M. Morgenstern
arXiv:2210.01831 [cond-mat.mes-hall] (2022)

5.1 Sample layout and experimental details

The sample consist of a graphene flake placed on a hBN flake on a SiO_2/Si chip. In addition a graphite flake is located below the hBN and reaches partly below the graphene flake. The schematic composition of the sample is depicted in figure 5.1a and an optical image is shown in figure 5.1b. The thicknesses are $d_{\mathrm{hBN}} = 23.5\,\mathrm{nm}$ (green flake in figure 5.1b) and $d_{\mathrm{graphite}} = 3\,\mathrm{nm}$ as taken from the AFM topography of the sample (see figure 5.1c). The charge carrier concentration in graphenr is either controlled by the Si back gate or by the graphite back gate in the different areas creating a pn interface at the boundary between the areas. The graphite flake is patterned with stripes to intentionally induce several pn interfaces and to ease the positioning of the STM tip at a pn interface. Due to cracks in the graphene flake, the part above the stripes is disconnected from the remaining flakes. This made it more favourable to use the edge of the graphite flake as a pn interface instead. The sample is fabricated by Astrid Weston and Matthew Hamer in the group of Roman Gorbachev at the University of Manchester employing the PMMA transfer (see section 6.5). Afterwards, gold pads as electrical contacts are deposited at room temperature both onto the graphene and graphite flake using a shadow mask with $50\,\mu$m holes (see section 7.2).
The 004 setup (see section 3.5) used to conduct the measurements offers two electrical lines to the sample, whereas three would be required for both back gates and the graphene flake. Therefore, it was decided to connect the Si back gate to the graphene flake such that it can not be used as a gate anymore (see circuit diagram in figure 5.1a). Consequently, in the left part of the sample, the charge carrier density can be tuned via the graphite back gate while in the right part above the Si back gate the charge carrier concentration remains constant (E_{F} close to the Dirac point). The STM tip is grounded via the tunneling current amplifier and V_{sample} is applied to the graphene flake. The voltage V_{bg} at the graphite back gate is applied with respect to V_{sample}

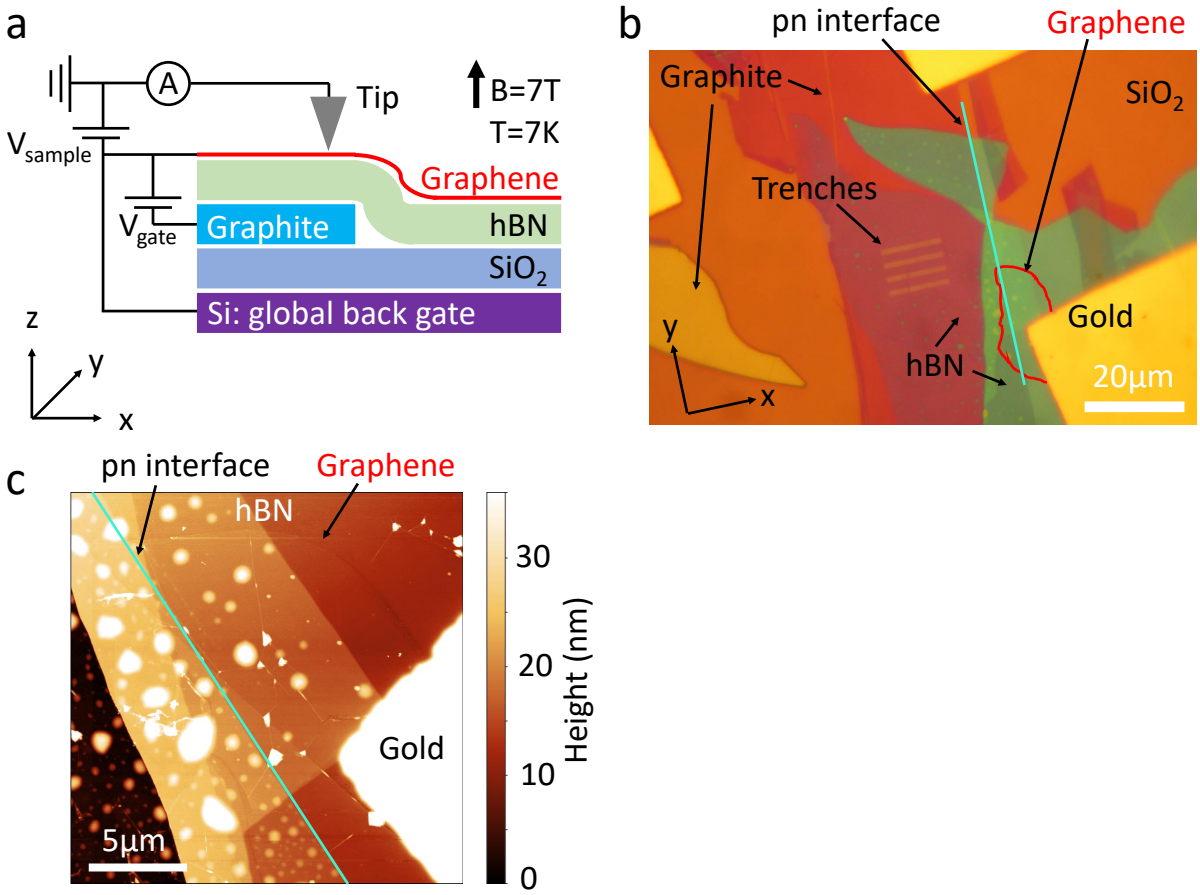

Figure 5.1: a: Schematic layout of the pn sample including the circuit diagram. b: Optical microscope image of the pn sample where the pn interface is shown by a light green line. The SiO_2 appears as orange brown background with the graphite more reddish and the hBN either purple or green depending on the thickness. The graphene flake is not visible and outlined in red based on the AFM image of subfigure c. c: AFM topography of the pn sample recorded in tapping mode at ambient conditions.

following the wiring schematic of figure 3.10.This way, V_{bg} corresponds to the typical arrangement in transport experiments where the sample is grounded (see figure 3.11). For the tip approach, the tip is first optically aligned to a gold contact a few μm away from the pn interface (see section 4.2). After approach on the gold contact the tip is moved in one direction towards the pn interface via the graphene. Graphene and the underlying hBN form a Moiré pattern with a lattice constant $\lambda = 1.28\,\mathrm{nm}$ shown in figure 5.2a. This corresponds to an angle of 11.1° between the graphene and hBN lattices [117]. The pn interface in the graphene sample is identified by the step in the topography (see figure 5.2b) resulting from the 3 nm thick graphite flake below the left part of the graphene. The dependence of STS measurements on V_{bg} in the left area and the independence of V_{bg} in the right area confirm the position of the pn interface. All measurements are carried out in the 004 setup at a magnetic field of B=7 T and at a temperature of T=7 K if not specified differently. At these conditions the graphene sample is in the quantum Hall regime (see section 2.3).

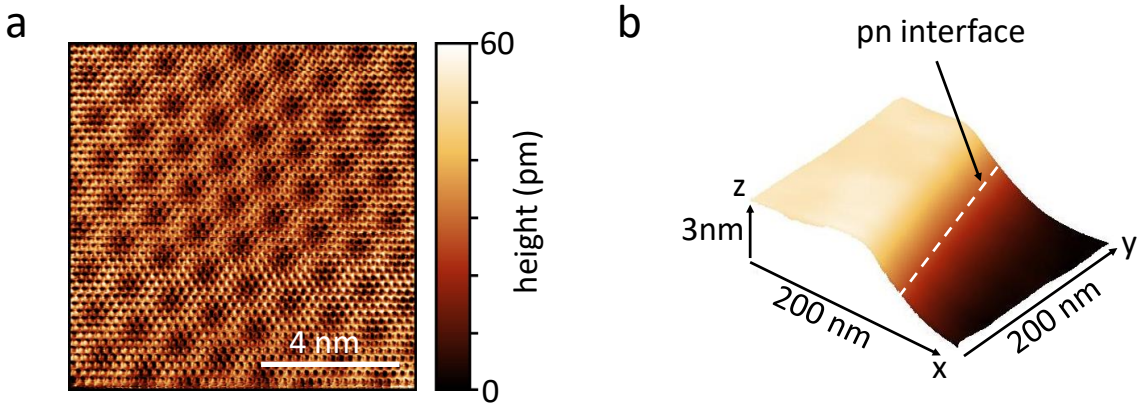

Figure 5.2: a: Atomically resolved topography of graphene on hBN. $V_{\text{sample}} = -250\,\text{mV}$, $I = 1\,\text{nA}$. b: Topography of the step edge at the pn interface indicated with a white dashed line. $V_{\text{sample}} = -500\,\text{mV}$, $I = 200\,\text{pA}$.

5.2 Characterization of QD

The tip induced band bending leads to the formation of a QD below the tip (see section 2.6). In order to characterize the QD, measurements are carried out in the left part of the graphene above the tunable graphite back gate and far away from the pn interface (see figure 5.3a). At constant V_{bg}, the $dI/dV_{\text{sample}}(V_{\text{sample}})$ shows the expected sequence of LL features (see equation 2.6 and figure 2.4). They are filled with increasing V_{bg}. Pinning of the bulk LLs at E_{F} in the surrounding sample due to their large DOS results in a downwards staircase pattern of each LL feature (spectroscopy line (SL)) with increasing V_{bg} as seen in figure 5.3a. Similar features are reported elsewhere [52, 65] and in sections 7.4 and 7.5. They are described in more detail in section 2.6 (see figure 2.11).
Charging lines (CLs) are indicated with white arrows in figure 5.3a. They occur whenever a LL feature crosses E_{F}, from where they extend to larger $|V_{\text{sample}}|$. This proves the existence of the QD below the tip. To visualize the CLs better, a numerical derivate along V_{bg} is performed and shown in figure 5.3b. The CLs show up as almost vertical blue-yellow double lines. Since for increasing V_{sample} additional CLs with lower intensity appear (for example at $V_{\text{bg}} \approx 2\,\text{V}$), the QD is hole-like where hole-like describes the shape of the QD with upwards (unoccupied) band bending (see figures 2.8 and 2.9). For $N < 0$ the LL features in the QD pin at E_{F} similar to the bulk LLs whereas for $N \geq 0$ the LL features do not pin at E_{F} but are at $V_{\text{sample}} = 30 - 100\,\text{mV}$ above E_{F}. This is in agreement with a hole-like QD which LL states are at a higher energy compared to the corresponding LL state in the bulk. On both sides of LL0 CLs with larger intensity, flatter slope and different distance in both V_{sample} and V_{bg} compared to the CLs originating from other LLs are observed (orange arrows in figure 5.3a, figures 5.3b and c). These flat CLs set in for $V_{\text{sample}} > 50\,\text{mV}$ on the right side and for $V_{\text{sample}} > 150\,\text{mV}$ on the left side of LL0 and even show negative slopes for a small V_{bg} interval as more clearly visible in figure 5.3c. These flat CL slopes are an exception dealt with in section 5.5 in more detail.

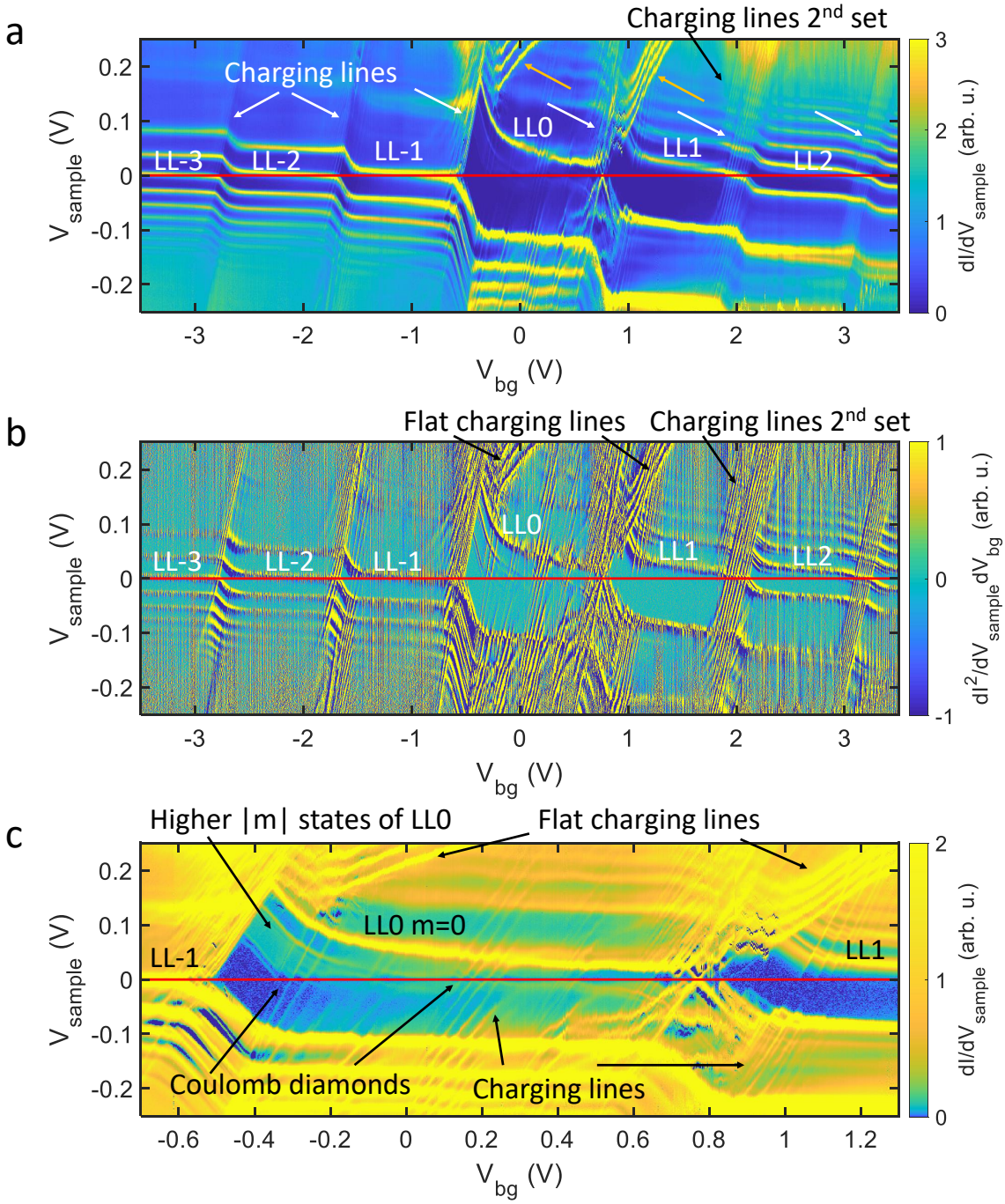

Figure 5.3: a: dI/dV_{sample} measurement of graphene on a single spot far away from the pn interface for varying V_{bg}. The LL features appearing with high intensity are labeled according to their indices. Some charging lines are marked with white arrows. A 2nd set of charging lines is marked with a black arrow whereas less steep charging lines are marked with orange arrows. E_{F} of graphene is shown as a red line. $V_{\text{sample}}^{\text{stab}} = -250\,\text{mV}$, $I^{\text{stab}} = 1\,\text{nA}$, $V_{\text{sample}}^{\text{mod}} = 1$ mV, $f^{\text{mod}} = 386.2\,\text{Hz}$. b: Numerical derivation $dI^2/dV_{\text{sample}}\,dV_{\text{bg}}$ of the measurement of subfigure a revealing enhanced contrast of the charging lines. c: Detail of the dI/dV_{sample} measurement of subfigure a with enhanced contrast.

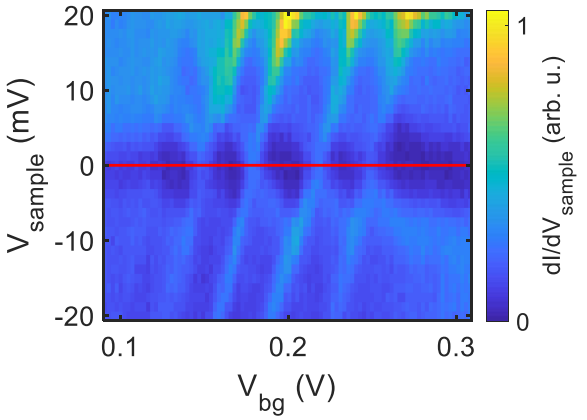

Figure 5.4: Detail of the dI/dV_{sample} measurement of figure 5.3 with enhanced contrast. Charging lines cross E_{F} (red line) resulting in Coulomb diamonds. $V_{\text{sample}}^{\text{stab}} = -250\,\text{mV}$, $I^{\text{stab}} = 1\,\text{nA}$, $V_{\text{sample}}^{\text{mod}} = 1\ \text{mV}$, $f^{\text{mod}} = 386.2\,\text{Hz}$.

In addition to the CLs around the crossing points of the sharpest LL feature and E_{F}, CLs also appear in the center of LL0 (see figures 5.3b and c). The slopes of all CL in the V_{bg}-V_{sample} plane as observed for LL0 range from 0.2 to 1.4, where most CL slopes group around either 0.3 or 1. For other LL features crossing E_{F}, the CL slopes are about 1 as well. Coulomb diamonds (see section 2.8) appear at each crossing of a CL and E_{F}, where an example is shown in figure 5.4. For $N = 0$ close to E_{F}, the LL0 features consist of several spectroscopy lines (SLs) most of them with lower intensity than the large main peak as indicated in figure 5.3c. These lower intensity peaks are QD states with $|m| > 0$. Their wave functions have less intensity in the central area of the QD due to a node at the very center [62] (see section 2.7). Therefore the main intensity corresponds to the $m = 0$ state that has its amplitude maximum in the center of the QD. From the measurement of the $|m| > 0$ states it can be concluded that these QD states have some intensity at the tunneling center of the tip. This points to the QD being slightly asymmetric with respect to the tunneling center of the tip. The subsequent charging of the $|m| > 0$ states in the QD is directly observable by the CLs that appear as the $|m| > 0$ states cross E_{F} where a series of CDs as presented in figure 5.4 appears. The fact that the $|m| > 0$ states are measured at lower energies than the $m = 0$ state, corroborates that the QD is hole-like. Then, the $m = 0$ state has the highest energy. Apart from that, the intensity of all LLs features of figure 5.3a is higher below E_{F} than above E_{F} for what no explanation is found.

5.3 Poisson calculations details

The Poisson calculations are carried out with the intention to gain inside into the chemical potential distribution $\mu_{\text{c,gr}}(x, y)$ in the graphene below the tip. This quantity is experimentally not accessible. This is the starting point to understand the measurements in detail, in particular in combination with tight-binding calculations of the graphene wave functions (see section 5.6). For comparison with the measurements far away from the pn interface (see figure 5.3a), the Poisson solver described in

section 2.14 for cylindrical symmetry (see figure 2.23a) is used. The radial chemical potential distribution $\mu_{\mathrm{c,gr}}(r)$ in the graphene for different combinations of ϕ_{tip} and ϕ_{bg} is calculated. The electrostatic potentials ϕ_{tip} and ϕ_{bg} are related to the experimentally applied voltages as follows

$$\phi_{\mathrm{tip}} = \Delta_{\mathrm{wfm}} + V_{\mathrm{tip}} = \Delta_{\mathrm{wfm}} - V_{\mathrm{sample}}, \tag{5.1}$$

$$\phi_{\mathrm{bg}} = V_{\mathrm{bg,0}} + V_{\mathrm{bg}}. \tag{5.2}$$

By comparison with equation 2.22, Δ_{wfm} is identified with

$$\Delta_{\mathrm{wfm}} = \frac{\Phi^0_{\mathrm{gr}} - \Phi_{\mathrm{tip}}}{e} \tag{5.3}$$

and the offset Δ_{wfm} between ϕ_{tip} and V_{tip} is due to the work function mismatch between tip and graphene. Similarly the offset $V_{\mathrm{bg,0}}$ is induced by the work function mismatch between graphite back gate and graphene (which probably is small) as well as initial doping of the graphene for example by dopants or impurities.
The circuit diagram in the Poisson solver differs from the experimental one depicted in figure 5.1a as the graphene flake instead of the tip is grounded (see figure 2.23a). Therefore, $V_{\mathrm{tip}} = -V_{\mathrm{sample}}$ is applied to the tip in the Poisson solver. This also makes it easier to understand the gating effect of the tip. It is similar to the back gate, if both V_{tip} and V_{bg} have the same sign with respect to the graphene flake.
A dI/dV_{sample} signal is constructed from the Poisson simulations by simply shifting the single particle DOS by $\mu_{\mathrm{c,gr}}$ below the tip and reading the DOS value corresponding to $V_{\mathrm{tip}} = -V_{\mathrm{sample}}$. This dI/dV_{sample} signal allows to compare the Poisson calculation with the measurement. The Poisson calculation depends on many parameters among which some are set by the experimental conditions (T, B, hBN thickness d_{hBN}). The LL broadening of $\Delta E_N \approx 3\,\mathrm{meV}$ is estimated from the measurements. The Fermi velocity $v_{\mathrm{F}} = 1 \cdot 10^6\,\mathrm{m/s}$ [22, 52] is taken from the literature as well as the dielectric constants $\epsilon_{\mathrm{hBN}} = \epsilon_{\mathrm{SiO_2}} = 4$ [52, 118]. The remaining geometrical parameters tip-sample distance $d_{\mathrm{ts}} = 0.6\,\mathrm{nm}$ and the opening angle of 30° of the cone extending from the spherical end of the tip are taken from [59]. The tip radius r_{tip} correlates with the size of the QD whereas ϕ_{tip} and ϕ_{bg} effect the depth of the QD.
The remaining offsets Δ_{wfm} and $V_{\mathrm{bg,0}}$ are determined as follows: The sign of Δ_{wfm} is readily found from the measurements (see section 5.2 and figure 5.3a). As marked in figure 5.3a and b for LL1, the CLs develop on a particular from the right towards the left. The first charge belonging to LL1 is introduced into the QD on the right. Decreasing V_{bg} introduces further charges into the QD. The same is true for increasing V_{sample}, that is decreasing V_{tip}. Consequently a more negative V_{tip} results in more charges in the QD rendering the charges positive, that is holes. Further evidence is given by the $|m| > 1$ states observed for LL0 features that show up at lower energy than the $m = 0$ state (see figure 5.3c). Finally the pinning of the m states of LL0 above E_{F} for $N > 0$ is consistent with a hole like QD.
A more detailed view on the CLs at negative V_{bg} reveals that CLs originating from different LLs cross each other. The CLs on the left in figure 5.5a originate from LL-2 and represent the first holes that are charged into the QD. The situation is sketched in figure 5.6a. At this point, E_{F} of the bulk surrounding the QD is in between LL-1 and LL-2 providing an insulting barrier for the confined charge carriers in the QD. The CLs

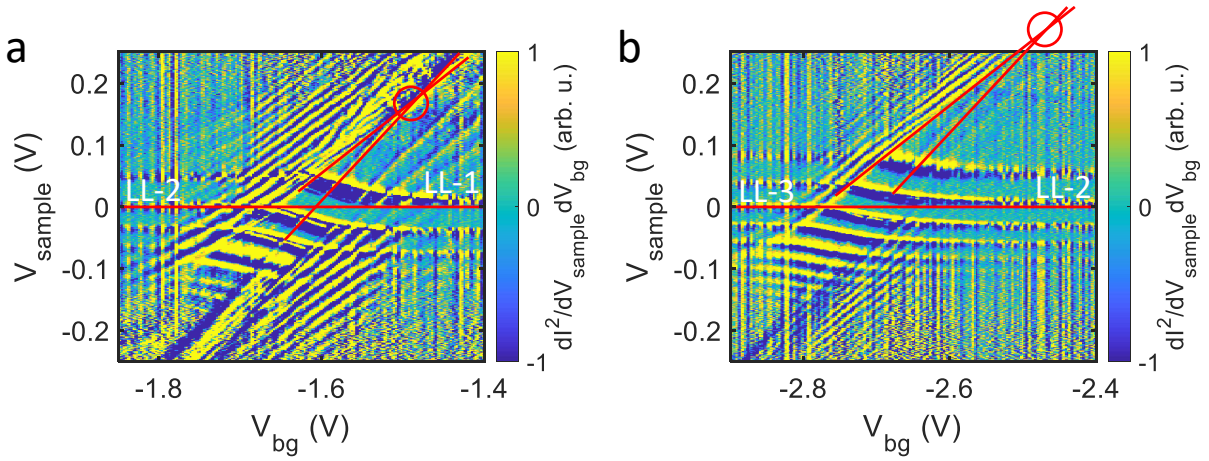

Figure 5.5: Numerical derivation $dI^2/dV_{\text{sample}}\, dV_{\text{bg}}$ of the measurement of figure 5.3a leading to enhanced contrast of the CLs. The LL features are labeled according to their indices. $V^{\text{stab}}_{\text{sample}} = -250\,\text{mV}$, $I^{\text{stab}} = 1\,\text{nA}$, $V^{\text{mod}}_{\text{sample}} = 1$ mV, $f^{\text{mod}} = 386.2\,\text{Hz}$. a: CL crossing from LL-2 and LL-3. b: CL crossing from LL-1 and LL-2.

Table 5.1: Positions of CL crossing points in the V_{bg}-V_{sample} map shown in figure 5.5 and the corresponding QD depths $\Delta\mu_{\text{c,QD}}$. The differences between the crossing points are given in the third row. The adapeted difference from the Poisson simulations given in the fourth row are limited in precision by the calculation grid.

CL crossing	V_{sample} (V)	V_{bg} (V)	$\Delta\mu_{\text{c,QD}}$ (mV)
LL-1, LL-2	170	1.5	-39.8
LL-2, LL-3	300	2.5	-30.5
Difference (experiment)	130	-1	
Difference (Poisson)	150	-1	

on the right belong to the last holes of LL-1 in the QD as depicted in figure 5.6b. For $V_{\text{sample}} = 0\,\text{V}$, E_{F} of the bulk around the QD still has to be in LL-1 because the filling factor of the bulk is higher than the filling factor of the hole like QD. Consequently it is assumed that the bulk around the QD is in a localized state (see figure 5.6b). A CL depicts a charging event at E_{F} and at the crossing point of the CLs in figure 5.5a both states from LL-1 and LL-2 have to be at E_{F} in the QD. This points to a ring like QD [77, 119] with states from both LLs in the center and an annulus of states from LL-1 only around it as sketched in figure 5.6c. E_{F} of the bulk around the QD is assumed to be in the localized states of LL-1 as well as described above for the last CL of LL-1 (see figure 5.6b). This requires a QD depth that equals the energy gap between LL-1 and LL-2 as indicated in figure 5.6c and reads -39.8 mV according to equation 2.6 neglecting the width of the LLs and minimal confinement energies. It reads $\Delta\mu_{\text{c,QD}} = -39.8\,\text{meV}$ for the situation in figure 5.6c according to equation 2.6 such that it is negative (positive) for hole (electron) type QDs. The QD depth $\Delta\mu_{\text{c,QD}}$ is defined as the difference of $\mu_{\text{c,gr}}(r)$ at the QD center and the bulk outside the QD:

$$\Delta\mu_{\text{c,QD}} = \mu^{\text{QD center}}_{\text{c,gr}} - \mu^{\text{bulk}}_{\text{c,gr}}. \tag{5.4}$$

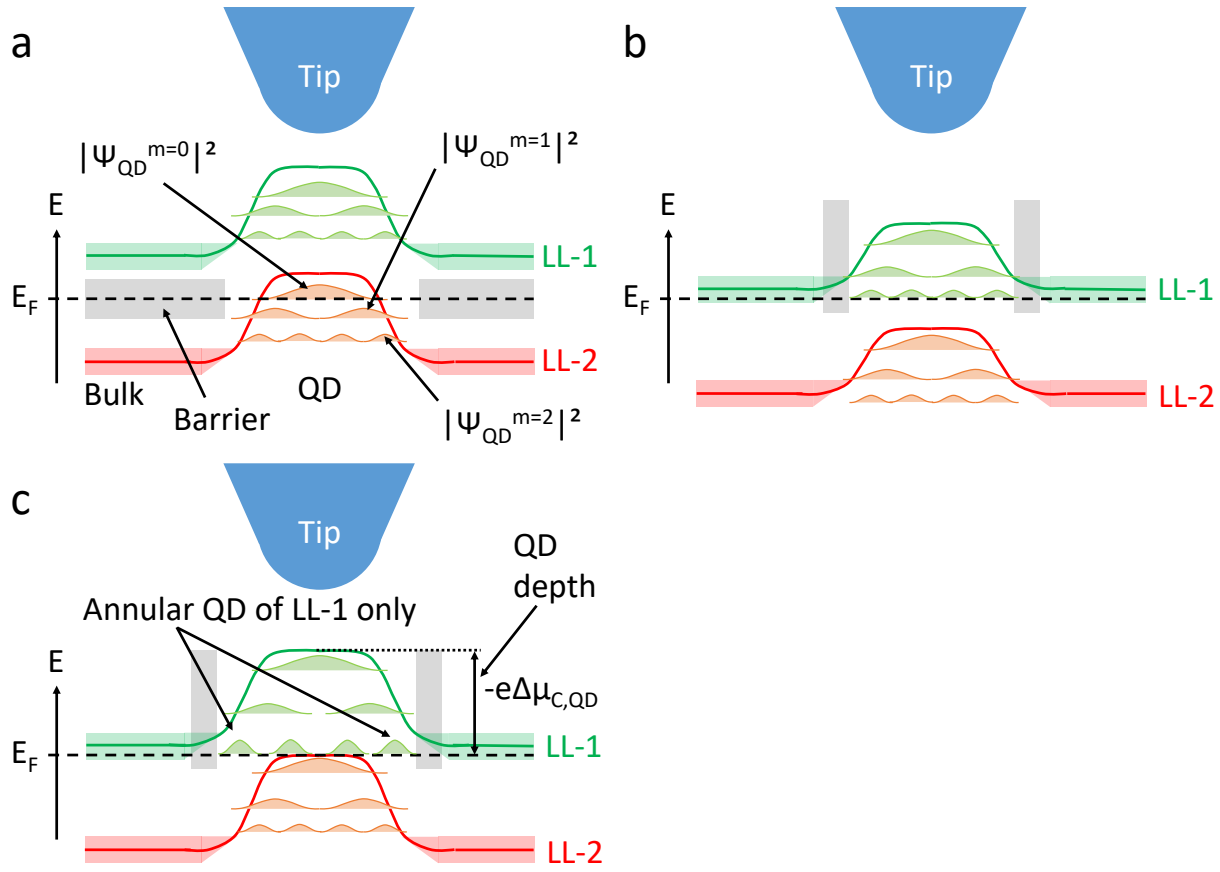

Figure 5.6: Schematic representation of the QD potentials below the tip (blue) for different CLs found in figure 5.5a. a: The highest energy state of LL-2 (red) is charged in the QD at E_F (black dashed line) while the LL-1 states (green) are unoccupied. The bulk around the QD is insulating creating the QD barrier (gray). The LL broadening in the bulk is depicted by light colors. b: The lowest energy state of LL-1 is charged in the QD. c: Both situations of subfigures a and b take place at the same time. The selected states are not the exact wave function of the QD in magnetic field (see equation 2.24).

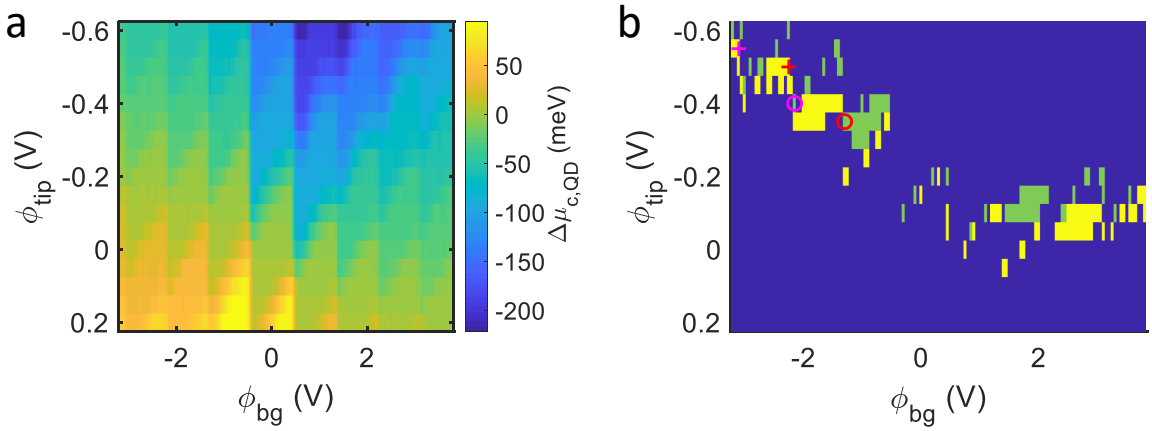

Figure 5.7: a: QD depth $\Delta\mu_{c,QD}$ from the Poisson simulation for $r_{tip} = 25\,nm$. b: Same data as in subfigure a with color code: $\Delta\mu_{c,QD} = -30.5 \pm 2.5\,mV$ in yellow, $\Delta\mu_{c,QD} = -39.8 \pm 2.5\,mV$ in green, all other $\Delta\mu_{c,QD}$ in blue. Possible crossing points with the respective $\Delta\mu_{c,QD}$ and distances as listed in table 5.1 are marked in the same color where circles label $\Delta\mu_{c,QD} = -39.8 \pm 2.5\,mV$ (green) and crosses label $\Delta\mu_{c,QD} = -30.5 \pm 2.5\,mV$ (yellow).

For the transition from LL-2 to LL-3 features, a similar crossing of CLs is expected and the estimated crossing point is marked in figure 5.5b. The positions of both crossing points in the $dI/dV_{sample}(V_{bg}, V_{sample})$ map and the corresponding $\Delta\mu_{c,QD}$ are listed in table 5.1. The known $\Delta\mu_{c,QD}$ of both crossing points and its distances in V_{bg} and V_{sample} are directly compared to the Poisson simulation. To this end, $\Delta\mu_{c,QD}$ is evaluated in the Poisson simulation for varying ϕ_{tip} and ϕ_{bg} as plotted in figure 5.7a. Possible crossing points are identified by firstly listing all positions with $\Delta\mu_{c,QD} = -39.8 \pm 2.5\,mV$ (green in figure 5.7b). Afterwards points of $\Delta\mu_{c,QD}$ with distances in V_{bg} and V_{sample} as given in table 5.1 and $\Delta\mu_{c,QD} = -30.5\,mV$ are selected. The resulting combinations are marked with crosses and circles in figure 5.7b. Since there are still two choices, the $dI/dV_{sample}(V_{sample}, V_{bg})$ map from the Poisson simulations shown in figure 5.8b and c is compared to the experiment in figure 5.8a and the best match is chosen. In the case of figure 5.7b, it is the red combination more on the left which $dI/dV_{sample}(V_{sample})$ map is depicted in figure 5.8b. Equations 5.1 and 5.2 give $\Delta_{wfm} = -180 \pm 50\,mV$ and $V_{bg,0} = 200 \pm 50\,mV$ from the red data points of figure 5.7b. The uncertainty of $\pm 50\,mV$ is due the resolution of 50 mV of the Poisson simulation. By using the distances in V_{bg} and V_{sample} for comparison with the Poisson simulations, the offsets Δ_{wfm} and $V_{bg,0}$ with respect to ϕ_{tip} and ϕ_{bg} are eliminated in the first place simplifying the comparison.
The CLs left and right of LL0 change their slopes above a certain V_{sample}. In the Poisson simulation the QD depth at these points equals the energy gap of about 100 meV between LL0 and LL1 or LL-1. This is similar to the other LL transitions where the CLs of neighbouring LLs intersect. Albeit the change of the slope is not fully understood, it gives further evidence for the assumed situation of a circularly separated filling factor of the QD and the choice of the Δ_{wfm}.
Another method to experimentally determine Δ_{wfm} and $V_{bg,0}$ is presented in [53] where whispering gallery modes in the $dI/dV_{sample}(V_{bg}, V_{sample})$ map are analyzed. These

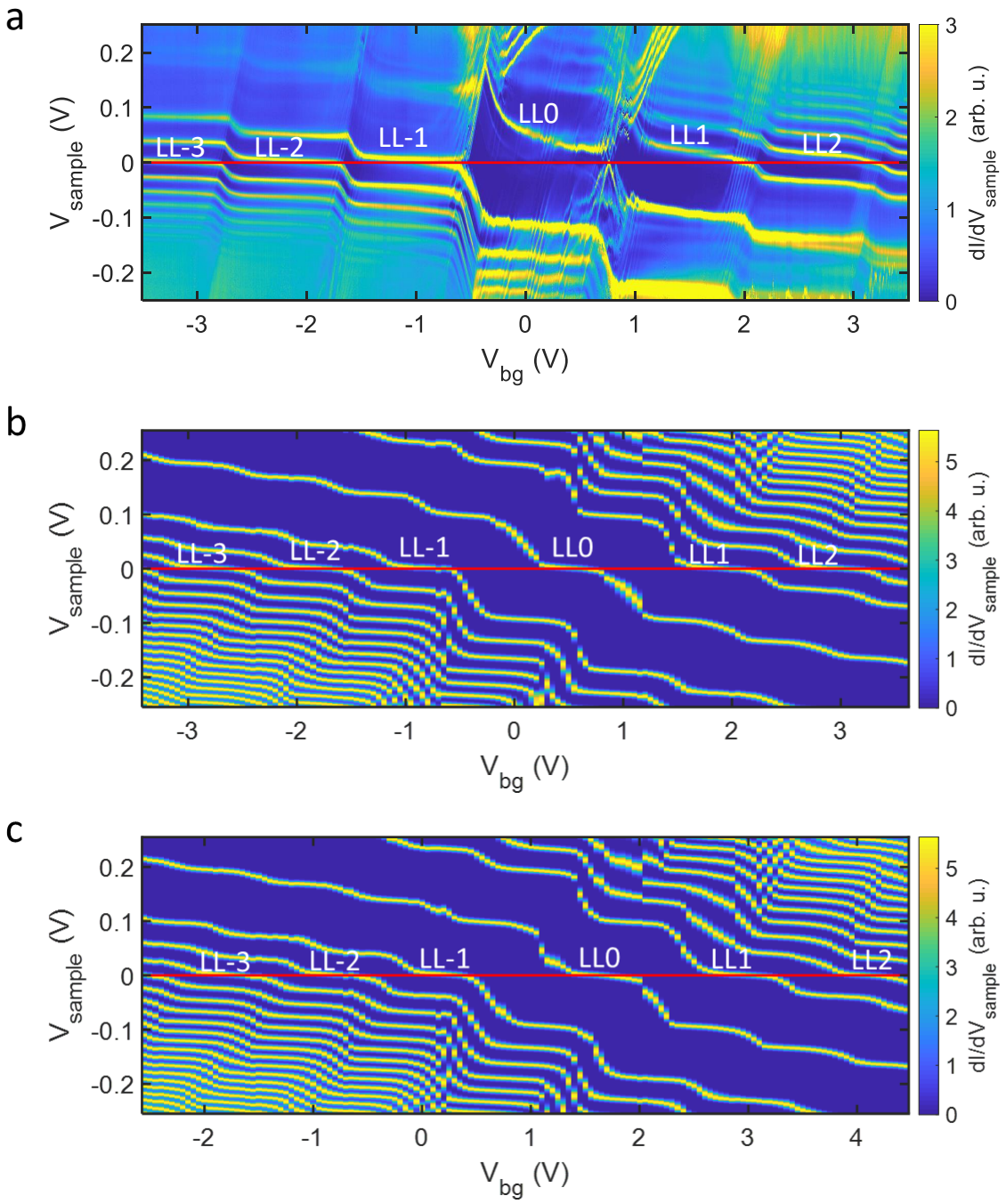

Figure 5.8: a: $dI/dV_{\mathrm{sample}}(V_{\mathrm{bg}}, V_{\mathrm{sample}})$ measurement of graphene (same as figure 5.3a). $V_{\mathrm{sample}}^{\mathrm{stab}} = -250\,\mathrm{mV}$, $I^{\mathrm{stab}} = 1\,\mathrm{nA}$, $V_{\mathrm{sample}}^{\mathrm{mod}} = 1$ mV, $f^{\mathrm{mod}} = 386.2\,\mathrm{Hz}$. b: Constructed dI/dV_{sample} for varying V_{bg} based on a Poisson simulation with $r_{\mathrm{tip}} = 25\,nm$, $\Delta_{\mathrm{wfm}} = -180\,\mathrm{mV}$ and $V_{\mathrm{bg},0} = 200\,\mathrm{mV}$. c: $\Delta_{\mathrm{wfm}} = -230\,\mathrm{mV}$ and $V_{\mathrm{bg},0} = -650\,\mathrm{mV}$. Note the shifted V_{bg} axis.

features rely on a pn interface encircling the graphene below the tip. The pn (or np) interface is created by band bending below the tip for opposite signs of ϕ_{tip} and ϕ_{bg}. Same signs of ϕ_{tip} and ϕ_{bg} result in nn' or pp' interfaces that do not exhibit whispering gallery modes. In switching from electron- to hole-like band bending or vice versa of the pn (or np) interface in the $(V_{\mathrm{bg}}, V_{\mathrm{sample}})$ map, the point of no band bending is crossed which implies $\phi_{\mathrm{tip}} = \phi_{\mathrm{bg}} = 0\,\mathrm{V}$ [53]. From this Δ_{wfm} and $V_{\mathrm{bg,0}}$ are determined with equations 5.1 and 5.2, respectively. Apart from that, KPFM (see section 3.2) could be used if an AFM is implemented. In chapter 9.5 of [51], a different method is described. A capacitive current dependent on Δ_{wfm} is measured while oscillating the tip-sample distance and nullified by adjusting V_{sample}. This method should be applicable for STM setups without AFM as well. Finally, the intrinsic doping of a graphene sample due to $V_{\mathrm{bg,0}}$ could be determined experimentally from a transport measurement (see for example figure 2.3a). For this, the particular sample lacks a second electrical contact to the graphene.
The remaining fit parameter, the tip radius r_{tip}, is determined by analyzing the CLs as well. The distance between CLs in V_{sample} and V_{bg} depends on the capacitance C_j between QD and tip or back gate, if the orbital energy contribution of graphene $\Delta\mu_{c,gr}$ is neglected ($\Delta_q = 0\,\mathrm{eV}$, see equation 2.49):

$$\Delta V_j = \frac{e}{C_j} \tag{5.5}$$

for $|q| = e$. The slope of a CL is given by the ratio of back gate and tip capacitances (see equation 2.44 with bias $\rightarrow$ tip and pg $\rightarrow$ bg):

$$m_\alpha^{\mathrm{CL}} = \frac{\Delta V_{\mathrm{tip}}}{\Delta V_{\mathrm{bg}}} = -\frac{C_{\mathrm{bg}}}{C_{\mathrm{tip}}}. \tag{5.6}$$

In the first step, the CL slopes and distances are extracted from the experimental data as shown in figure 5.3a and b. Here only CLs for $V_{\mathrm{bg}} < 0\,\mathrm{V}$ are considered since on this side the plateaus of LL features are close to E_{F} indicating a flat QD and the charging lines are relatively regular and thereby well understood. To make sure that the orbital energy of the QD states can be neglected as in equation 5.5, the distance between CLs is only determined for groups of four CL where the distances are similar assuming that these groups belong to the same orbital state. Afterwards, these values are analyzed leading to slopes $m_\alpha^{\mathrm{CL}} = 1 \pm 0.25$.
To extract m_α^{CL} from the Poisson simulations, the change of the charge in the QD is used. The charge of the QD is calculated by integrating the charge density ρ from the center of the QD up to its the edge. The edge of the QD is defined as the point where the conductive bulk begins and includes the insulating ring around the conductive inner part of the QD. Calculating the resulting change of QD charge ΔQ per applied tip or back gate potential ϕ_j reveals $C_j = \Delta Q/\Delta\phi_j$ and thereby m_α^{CL} after devision of both back gate and tip capacitances (see equation 5.6). Afterwards, all points with $m_\alpha^{\mathrm{CL}} = 1 \pm 0.25$ are selected in the ϕ_{vbg}-ϕ_{tip} map for a particular r_{tip}. For each of these points, the distances between CLs in V_{sample} and V_{bg} are calculated as changes of charge by e (see equation 5.5). The mean values for $\phi_{\mathrm{vbg}} < 0\,\mathrm{V}$ and $\phi_{\mathrm{tip}} < 0\,\mathrm{V}$ and the corresponding standard deviations are compared to the mean values and the standard deviations of the experiment in figure 5.9. The restriction for $\phi_{\mathrm{vbg}} < 0\,\mathrm{V}$ and

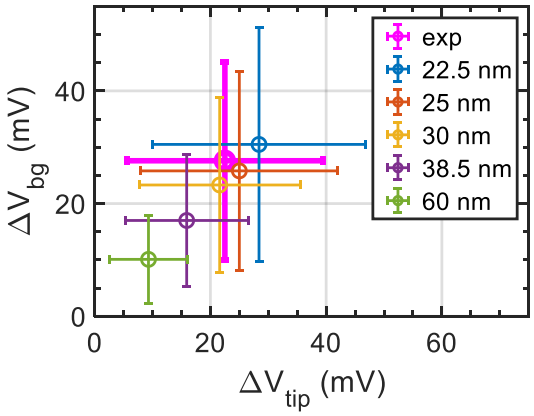

Figure 5.9: The average distances between CLs for ΔV_{tip} and ΔV_{bg} in V_{tip} and V_{bg} direction, respectively and their standard deviations are plotted for different tip radii in the Poisson simulation and compared to the experimental values. $\Delta_{\mathrm{wfm}} = -180\,\mathrm{mV}$ and $V_{\mathrm{bg},0} = 200\,\mathrm{mV}$.

$\phi_{\mathrm{tip}} < 0\,\mathrm{V}$ is based on the good agreement of the constructed dI/dV_{sample} from the Poisson simulation with the experiment in this regime as shown in figure 5.8a and b. The mean values and even their standard deviations match best for $r_{\mathrm{tip}} = 25\,\mathrm{nm}$ as can be seen in figure 5.9. Note that the capacitances calculated by this method include the graphene quantum capacitance.

5.4 Comparison of experimental dI/dV_{sample} data to Poisson calculations

The dI/dV_{sample} constructed from the potentials of a Poisson calculation with $\Delta_{\mathrm{wfm}} = -180\,\mathrm{mV}$, $V_{\mathrm{bg},0} = 200\,\mathrm{mV}$, and $r_{\mathrm{tip}} = 25\,\mathrm{nm}$ is presented in figure 5.8b. The calculated dI/dV_{sample} can directly be compared with the measurement in figure 5.8a (or figure 5.3) revealing that the SLs mostly match the experiment whereas the CLs are not captured due to the way the signal is created. Main differences occur in the pinning of the LL features. In the simulation, the LL features pin for a shorter V_{bg} interval and the LL features pinned above E_{F} for $N \geq 0$ are not reproduced. In addition, for some V_{sample}, the energy spacing of subsequent LL features is smaller for the simulation than the measurement. The reason for these discrepancies is likely the simplified pinning implemented in the Poisson solver where quantum mechanical confinement effects taking the microscopic structure of the wave function into account are neglected. Also a likely offset between QD center and tunneling center of the tip is not considered.
The flat band condition without QD below the tip can be estimated from the Poisson simulations. Therefor, the electrostatic potential difference between tip potential ϕ_{tip} and bulk graphene chemical potential $\mu_{\mathrm{c,gr}}$ (tip far away from sample) is analyzed

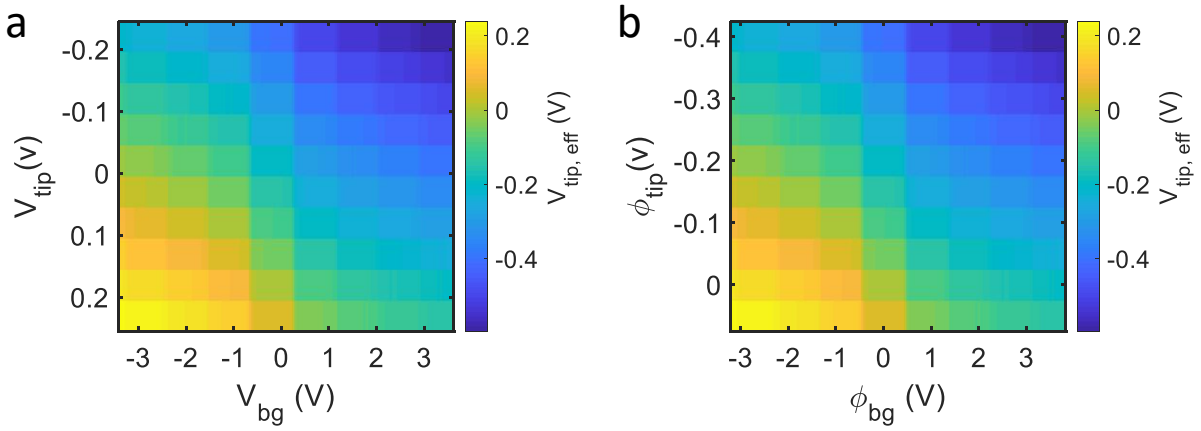

Figure 5.10: a: $V_{\mathrm{tip,eff}} = \phi_{\mathrm{tip}} - \mu_{\mathrm{c,gr}}$ evaluated from a Poisson simulation with $\Delta_{\mathrm{wfm}} = -180\,\mathrm{mV}$, $V_{\mathrm{bg,0}} = 200\,\mathrm{mV}$, and $r_{\mathrm{tip}} = 25\,\mathrm{nm}$. b: same as subfigure a but with ϕ_{bg} and ϕ_{tip} axis.

reading:

$$V_{\mathrm{tip,eff}} = \phi_{\mathrm{tip}} - \mu_{\mathrm{c,gr}} \tag{5.7}$$
$$= \Delta_{\mathrm{wfm}} + V_{\mathrm{tip}} - \mu_{\mathrm{c,gr}} \tag{5.8}$$
$$= \Delta_{\mathrm{wfm}} - V_{\mathrm{sample}} - \mu_{\mathrm{c,gr}} \tag{5.9}$$

where equation 5.1 is used. This voltage causes the band bending below the tip, that means only for $V_{\mathrm{tip,eff}} = 0\,\mathrm{V}$ there is no band bending (see sections 2.2, 2.5, and 2.6, and equation 2.23). A map of $V_{\mathrm{tip,eff}}$ calculated from the potentials of the Poisson simulation is shown in figure 5.10. The applied V_{tip} including Δ_{wfm} gives the first contribution to $V_{\mathrm{tip,eff}}$, whereas the increasing occupation with V_{bg} changes $\mu_{\mathrm{c,gr}}$ resulting in larger $|V_{\mathrm{tip,eff}}|$ for positive V_{bg} at $V_{\mathrm{tip}} = 0\,\mathrm{V}$ and vice versa. $V_{\mathrm{tip,eff}} = 0\,\mathrm{V}$ is achieved if $\phi_{\mathrm{tip}} = \mu_{\mathrm{c,gr}}$. An example is $-0.2 < \phi_{\mathrm{tip}} < -0.15\,\mathrm{V}$ at $\phi_{\mathrm{bg}} = -3\,\mathrm{V}$. This corresponds to $V_{\mathrm{tip}} \approx 0\,\mathrm{V}$ where no QD is expected. It coincides with a small intensity of the CLs in this area in figure 5.3a and b. Also the LL features pinning rather exactly at E_{F} in this regime is an indication for a vanishing QD depth resulting from small $|V_{\mathrm{tip,eff}}|$.
The QD depth $\Delta\mu_{\mathrm{c,QD}}$ shown in figure 5.7a has the same general trend as $V_{\mathrm{tip,eff}}$. It increases with ϕ_{bg} and ϕ_{tip}. However, the pinning of the LL features at E_{F} in the QD results in a repetitive staircase pattern of $\Delta\mu_{\mathrm{c,QD}}$. The LL gap around LL0 leads to a larger possible QD depth for LL0 at E_{F} in the bulk. This depth is decreasing for higher or lower LLs due to the smaller LL gap. The hole-type QD gets also deep, if the hole LL is barely filled with electrons. Because less electrons can be removed from this almost empty LL, the hole-like QD has to become deeper and wider to contain the same number of holes. Consequently, $|\Delta\mu_{\mathrm{c,QD}}|$ is continuously increasing with decreasing V_{bg} as long as the same LL is at E_{F} in the bulk.

5.5 Flat charging lines

In figure 5.11 (see figure 5.3 a to c) charging lines are visible for different V_{bg} and V_{sample}. Once the $m = 0$ state of LL0 is tuned across E_{F} in the QD at $V_{\mathrm{bg}} \approx 0.75\,\mathrm{V}$, additional CLs appear at $V_{\mathrm{sample}} > 50 - 200\,\mathrm{mV}$ with flat slope of $m_\alpha^{\mathrm{CL}} \approx 0.2$ (light blue arrow in figure 5.11) compared to $m_\alpha^{\mathrm{CL}} \approx 1$ for all other CLs (black arrows in figure 5.11). These CLs are labeled flat and dealt with in detail in this section. The flat CLs belong to LL0 states in the QD while LL1 is at E_{F} in the bulk. Similarly flat CLs are observed at $V_{\mathrm{bg}} = -0.3 - +0.2\,\mathrm{V}$ and $V_{\mathrm{sample}} > 100 - 250\,\mathrm{mV}$ (green arrow in figure 5.11). They belong to charging of LL-1 states in the QD, while LL0 is pinned to E_{F} in the bulk. Here, the CLs even change slope direction close to $V_{\mathrm{bg}} = -0.4\,\mathrm{V}$ (violet arrow in figure 5.11). Since the slope m_α^{CL} of a CL is (see equation 2.44):

$$m_\alpha^{\mathrm{CL}} = \frac{\Delta V_{\mathrm{tip}}}{\Delta V_{\mathrm{bg}}} = -\frac{C_{\mathrm{bg}}}{C_{\mathrm{tip}}} \tag{5.10}$$

a change in slope equals a relative change of the involved capacitances (see also section 2.6). The capacitance of the QD to tip or back gate could change, for example, by changing the distances between the electrodes or their geometry. A change of another capacitance, for example, to the surrounding graphene, would not affect the ratio of tip and back gate capacitances and would not result in a change of the CL slope.
In [65] CLs at the transition between LL0 and LL1 features also show a flatter slope than the other CLs without further explanation. Most measurements, like [52, 54] or the ones presented in chapter 7.5, do not exhibit an abrupt change of the CL slopes. However, some of these CLs show a continuous change of the slope. Such change can be related to a changing QD size with increasing V_{bg} and V_{sample}. Along a CL the QD charge Q remains constant and the QD size and depth change only due to the

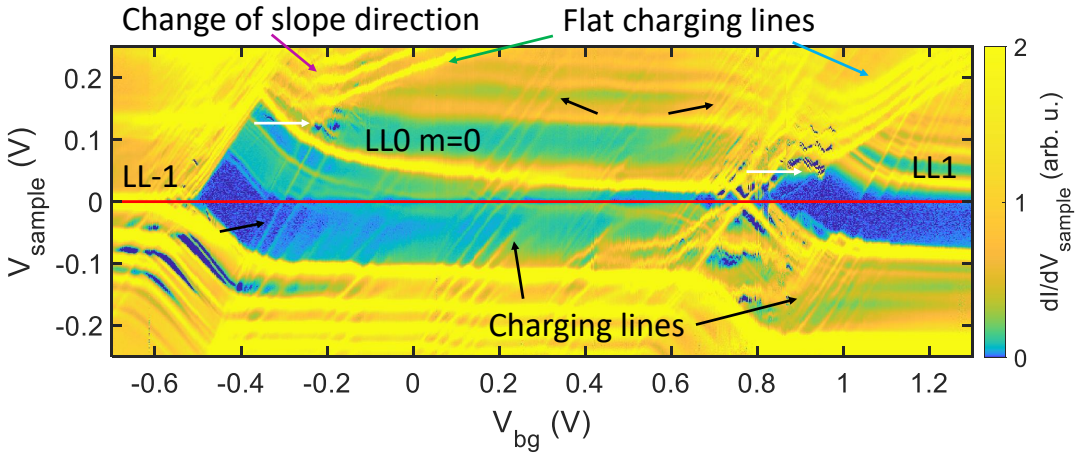

Figure 5.11: a: Detail of the dI/dV_{sample} measurement of graphene (same as figure 5.3c). The LL features are labeled according to their indices. Flat charging lines with $m_\alpha^{\mathrm{CL}} \approx 0.2$ are indicated with green and light blue arrows. Some charging lines with $m_\alpha^{\mathrm{CL}} \approx 1$ are marked with black arrows. The purple arrow shows a position where the sign of m_α^{CL} is reserved. $V_{\mathrm{sample}}^{\mathrm{stab}} = -250\,\mathrm{mV}$, $I^{\mathrm{stab}} = 1\,\mathrm{nA}$, $V_{\mathrm{sample}}^{\mathrm{mod}} = 1\ \mathrm{mV}$, $f^{\mathrm{mod}} = 386.2\,\mathrm{Hz}$.

changing screening properties of the bulk graphene. The screening properties depend on the LL filling in the bulk that changes with V_{bg} as explained in section 5.4. For a nearly full LL the depth of a hole-like QD is small and so is its radius whereas both are large for an almost empty LL (see figure 5.7a). A larger QD is less coupled to the tip, whereas the coupling to the back gate is relatively independent of the QD size. A smaller capacitance to the tip requires a larger $\Delta V_{\mathrm{sample}}$ to compensate ΔV_{bg} leading to a steeper CL. Therefor, the CL slope for an empty LL in the bulk is steeper than for a full LL. This is indeed observed for the intersecting CLs at the transitions between LLs (see figure 5.5).
The abrupt change in CL slope can however not be explained by this since the LLs fill continuously. Additionally, the flat CLs appear in the measurement only around LL0. It is not known whether they would appear for other LLs at larger V_{sample} as well. The observed change by about 100 mV in the onset V_{sample} of the flat CLs between left and right end of the LL0 plateau (see white arrows in figure 5.11) could be related to the chemical potential change during the increasing LL0 population in the bulk since the energy gap between LL0 and LL1 is almost 100 meV as well. This hints towards an electrostatic effect that might be unique to the tip used in this experiment.
Different scenarios to understand the flat CLs are considered. However, no complete explanation for the change of the CL slope is found. In the first scenario, the QD shrinks in diameter and is consequently on average closer to the spherical tip resulting in a larger capacitance and a flatter slope. A possible reason for a smaller QD is given by the large energy gap between LL0 and LL$\pm$1 of about 100 meV at $B = 7\,\mathrm{T}$ in comparison to the other LL transitions where the energy gaps are smaller than 40 meV. The reduction of the QD diameter is estimated using the results of the Poisson simulations: For the ϕ_{bg}-ϕ_{tip} map, using the parameters of figure 5.10, the points with capacitance ratios of 1 ± 0.25 and 0.25 ± 0.0625 are selected and the average QD radius is calculated. It turns out to be $15.4 \pm 4.5\,\mathrm{nm}$ to $5.1 \pm 3.3\,\mathrm{nm}$, respectively. This is in line with the expected shrinkage of the QD as soon as a flat CL slope is observed. It gives a straightforward explanation with increased C_{tip} resulting from a smaller distance between tip and QD. The distance between CLs with slope 0.25 ± 0.0625 in the Poisson simulation is about $\Delta V_{\mathrm{tip}} = 40\,\mathrm{mV}$ and $\Delta V_{\mathrm{bg}} = 160\,\mathrm{mV}$ in comparison to the experimental values of $\Delta V_{\mathrm{tip}} = 20 - 25\,\mathrm{mV}$ and $\Delta V_{\mathrm{bg}} = 50 - 120\,\mathrm{mV}$. The deviation of a factor of 2 could hint towards an improper model of the QD based on the Poisson simulation. A possible reason for this is the small QD radius of 5 nm during the flat slope of the CLs that puts the size of the QD below the magnetic length of $l_B = 9.7\,\mathrm{nm}$ at $B = 7\,\mathrm{T}$. Here, quantum mechanical effects not captured by the Poisson solver will lead to a different behaviour. A possible explanation would be an additional QD with a radius of 5 nm. A shrinking QD is described in [119], where the QD states separate in large outer and small inner states with different couplings to the electrodes. Similar observations are made in [77], where a double quantum dot of an outer ring and an inner circle is created that both have different CL slopes. On one hand, the formation of separated outer and inner states of the QD gives a good explanation for different CL slopes. Consistent with a reduced QD size is also the measurement of well separated $|m| > 0$ states of LL0 that coincides with the appearance of flat CLs (see figure 5.3c) and could indicate that these QD states are pushed into the QD center. On the other hand, the strength of CL slope change remains questionable. Whereas for other LL

transitions the CLs slopes of the crossing CL branches differ by $\Delta m_\alpha^{\mathrm{CL}} = 0.2$, for LL0 the difference is $\Delta m_\alpha^{\mathrm{CL}} = 0.8$. It is not clear, why the CL slope should be so much flatter for LL0. In both experiments from the literature, [119] and [77], simultaneous charging of both parts of the QD is observed for a wide range of gate voltages whereas here the two type of CLs appear only for a small back gate voltage window, where the LL0 feature is close to E_{F}.
Another scenario describes two QDs A and B formed next to each other below the tip at the same time where only QD B is probed by STS but both can be charged by the tip. Due to the close distance between the two QDs, the charging of QD A changes the potential of QD B so that charging events in both QDs are detected by STS. Both QDs could have different capacitances to the tip that result in different CL slopes. The presence of CLs with steep slopes throughout all LL transitions in fig 5.3b shows that QD B is probed by STS below the tip for all LL transitions. Consequently it is QD A that appears additionally only for LL0. This seems as a contradiction since it would require that QD A is much closer to the tip than the STS probed QD B in order to have flat CLs. Such a scenario seems geometrically challenging. Also the charging for LL0 close to E_{F} in the bulk remains difficult to explain as $\mu_{\mathrm{c,gr}}$ and thereby also $V_{\mathrm{tip,eff}}$ changes substantially when (de-)occupying LL0.

5.6 Tight-binding calculations

Tight-binding (TB) calculations are performed by Christoph Schattauer in the group of Florian Libisch at TU Vienna. They explain experimental features observed at the pn interface in detail by calculating the quantum mechanical wave functions of both QD and bulk graphene. The graphene chemical potential $\mu_{\mathrm{c,gr}}$ provided by the Poisson simulations is the basis for the TB calculations. These are performed on a 2D (x, y) graphene flake of $200 \times 400\,\mathrm{nm}^2$. To this end, the (x, z) potential distribution from the Poisson simulation has to be transformed into a 2D (x, y) potential. This is done by firstly approximating the Poisson potentials with analytic functions. In the next step, the analytic functions are used to generate the 2D (x, y) potential distribution for the TB calculations. Additionally, the potentials are slightly rescaled such that the LL energies E_N from the TB calculation and the Poisson potentials match. This compensates for different v_{F} in simulation and experiment (see equation 2.6). The TB calculations are carried out on a rescaled graphene lattice [120] with ten times enlarged lattice constant and ten times reduced hopping parameter t. Up to 3^{rd} nearest neighbours are included. A finite magnetic field B is captured by a Peierls phase reproducing the quantization of charge carriers into LLs with energies E_N. The resulting wave functions are plotted for the entire graphene flake and are evaluated at the position x_{tip} of the tip to construct a signal that compares directly to measured dI/dV_{sample} for varying V_{sample} and V_{bg}.

5.7 QD at pn interface

Up to now, the QD has been investigated in a static position under the influence of V_{sample} and V_{bg} (see section 5.2). Now, the STM tip and with it the QD is moved laterally across the pn interface. If the filling factor $\nu_{\text{QD,left}}$ on the left side of the interface (see figure 5.1a) is different than $\nu_{\text{QD,right}}$ on the right side, the QD occupation must change across the pn interface without changing V_{sample} or V_{bg}. The occupation change can be observed in a $dI/dV_{\text{sample}}(x_{\text{tip}}, V_{\text{sample}})$ measurement where x_{tip} is the position of the STM tip with respect to the pn interface. This measurement corresponds to a section of the $dI/dV_{\text{sample}}(V_{\text{bg}}, V_{\text{sample}})$ map shown in figure 5.3a, if V_{bg} is exchanged with x_{tip}. Due to the presence of the electrostatically defined pn interface new features appear in the measurements that will be presented in detail below.
Again, the QD influence the results. The bulk filling factors on the left and right side of the pn interface are labeled $\nu_{\text{bulk,left}}, \nu_{\text{bulk,right}}$ and the QD filling factors $\nu_{\text{QD,left}}, \nu_{\text{QD,right}}$ for $V_{\text{sample}} = 0\,\text{V}$ (see equation 2.11). Because of the different graphene chemical potential $\mu_{\text{c,gr}}$ on the left and right side of the pn interface, $V_{\text{tip,eff}}$ is changing for fixed V_{sample}. As a consequence the QD depth and with that the difference between the bulk and QD filling factors on each side is not necessarily the same. In particular, $V_{\text{tip,eff}} = 0\,\text{V}$, indicating the absence of a QD, can only be achieved simultaneously on both sides of the pn interface for one V_{bg} on the left side such that $\nu_{\text{bulk,left}} = \nu_{\text{bulk,right}}$. Note that $\nu_{\text{bulk,right}}$ is constant for all measurements due to the grounded Si back gate. Additionally, V_{sample} has to match Δ_{wfm} such that $\nu_{\text{bulk,left}} = \nu_{\text{QD,left}}$ and correspondingly on the right side. This corresponds to the positions in the V_{bg}-V_{sample} map where $V_{\text{tip,eff}} = 0\,\text{V}$. It can be concluded that the bare graphene chemical potential $\mu_{\text{c,gr}}(x)$ across the pn interface is not present during STS below the tip except for $\nu_{\text{bulk,left}} = \nu_{\text{bulk,right}}$. Nevertheless, also with a distorted $\mu_{\text{c,gr}}(x)$ important insights are gained by conducting STS measurements across the pn interface as the following sections will show.

5.8 STS across pn interface

The bending of the LL features at the pn interface is investigated by performing STS for varying tip positions x_{tip} along a line in x direction perpendicular to the pn interface. The resulting data is shown in figure 5.12. The position of the pn interface at $x_{\text{tip}} = 0\,\text{nm}$ is given by the step edge of the graphite flake below the left part of the sample. Any vertical cut along V_{sample} at fixed position x_{tip} resembles a vertical line of figure 5.3a at a certain V_{bg} (see section 5.2). Both, on the left and the right side of the interface for $|x_{\text{tip}}| \gtrsim 50\,\text{nm}$, the LL occupation is spatially constant but different. The LL features on the left side are shifted by V_{bg} evident by comparing figures 5.12a and b, while on the right side they are independent of V_{bg} and consequently the occupation of the QD is identical for all measurements presented. Due to the different occupation, the LL features at the pn interface either bend upwards or downwards from left to right depending on the sign of the applied V_{bg}. In addition, $\mu_{\text{c,gr}}(x)$ differs on the left and right side. It exhibits a step for every LL that crosses E_{F} (see section 2.11 and figure 2.18). Poisson simulations of the pn interface shown in figure 5.13 reveal that the positions of such $\mu_{\text{c,gr}}$ steps are changed by the presence of the STM tip via Δ_{wfm}

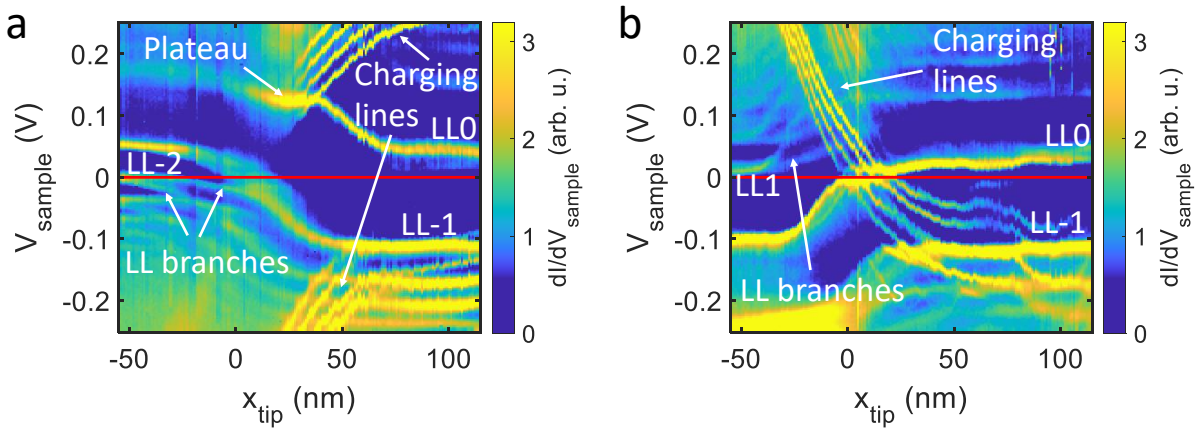

Figure 5.12: $dI/dV_{\mathrm{sample}}(V_{\mathrm{sample}})$ along a line perpendicular to the pn interface which is located at $x_{\mathrm{tip}} = 0\,\mathrm{nm}$. $I^{\mathrm{stab}} = 200\,\mathrm{pA}$, $V^{\mathrm{stab}}_{\mathrm{sample}} = -250$ mV, $V^{\mathrm{mod}}_{\mathrm{sample}} = 5$ mV, $f^{\mathrm{mod}} = 1386\,\mathrm{Hz}$. a: $V_{\mathrm{bg}} = -2\,\mathrm{V}$ in the left part. b: $V_{\mathrm{bg}} = 2\,\mathrm{V}$ in the left part.

and by the applied V_{sample}. Partly, no extremum of the band bending below the tip is observed but instead the pn interface is dragged by the tip. If ϕ_{tip} and ϕ_{bg} have the same sign, the position of the $\mu_{\mathrm{c,gr}}$ step is extended and moved to the right (see figure 5.13a). Oppositely, for different signs of ϕ_{tip} and ϕ_{bg} the position of the $\mu_{\mathrm{c,gr}}$ step is shifted to the left and the step width is decreased (see figure 5.13b). Following the energy of a single LL feature for varying x_{tip} in figure 5.12 allows to extract $\mu_{\mathrm{c,gr}}(x)$ if the changing $\Delta\mu_{\mathrm{c,gr}}$ and the broadening by the QD below the tip is ignored. Therefor, one has to choose $\Delta\mu_{\mathrm{c,gr}}$, for example from analysis of the QD on the left side (see section 5.3). The LL0 feature exhibits a plateau in figure 5.12a at $V_{\mathrm{sample}} = 120\,\mathrm{mV}$, which origin is elaborated in section 5.9.
CLs are present at the pn interface as well and indicate the QD below the tip. In figure 5.12b with $V_{\mathrm{bg}} = 2\,\mathrm{V}$, CLs appear on both sides of the pn interface and for all V_{sample} values. Here, the QD is deep resulting from nonzero $V_{\mathrm{tip,eff}}$ as on the righ side of figure 5.3a. In contrast, the CLs fade out on the left part of figure 5.12a at $x_{\mathrm{tip}} \approx 20\,\mathrm{nm}$ and $V_{\mathrm{sample}} < 150\,\mathrm{mV}$. At this position, $V_{\mathrm{tip,eff}} \approx 0\,\mathrm{V}$ for $V_{\mathrm{sample}} \approx 0\,\mathrm{V}$ as $E_{N=-2} \approx e\Delta_{\mathrm{wfm}}$ (see equations 2.6 and 5.9). This is similarly seen in figure 5.3a on the very left. For these parameters, the QD is vanishing, that means it has a small depth not sufficient to confine charge carries. The LL0 feature appears on the right side of both figure 5.12a and b at $V_{\mathrm{sample}} \approx 20\,\mathrm{mV}$ above E_{F} as expected for a hole-like QD as described in section 5.2. This is also seen in the measurements of figure 5.3a and c for LL0 close to E_{F}.
The $N < 0$ LL features split each into two branches in figure 5.12a and similarly for $N > 0$ for in figure 5.12b. These splittings occur close to the pn interface and branches of different LL features merge or intersect each other. Such LL branching does not occur in the static $dI/dV_{\mathrm{sample}}(V_{\mathrm{bg}}, V_{\mathrm{sample}})$ map of figure 5.3. The mechanism behind it is explained in section 5.10.

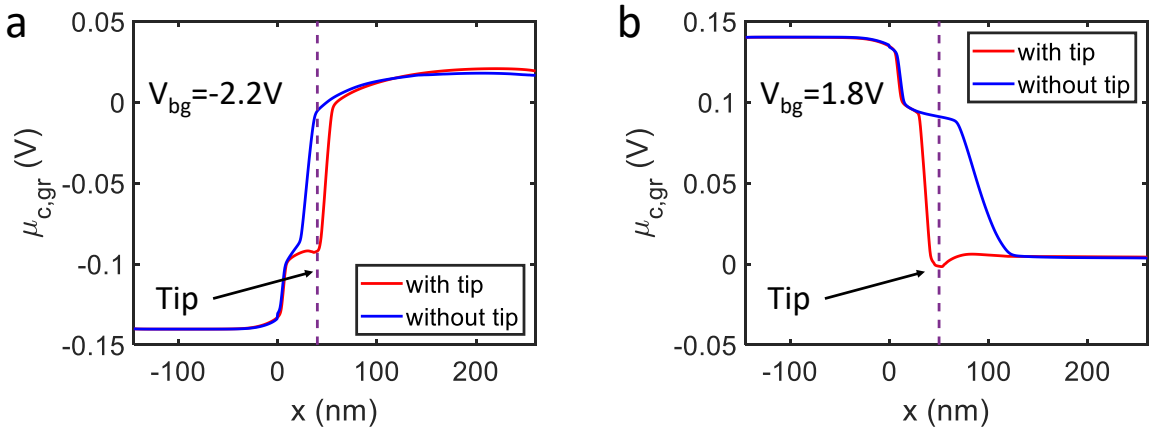

Figure 5.13: $\mu_{c,gr}$ from a Poisson simulation of the pn interface ($x = 0\,\text{nm}$) without tip (blue) and with the tip (red, $r_{tip} = 25\,\text{nm}$) for $V_{sample} = 0\,\text{V}$ and $\Delta_{wfm} = -180\,\text{mV}$. a: $V_{bg} = -2.2\,\text{V}$ in the left part, $x_{tip} = 40\,\text{nm}$. b: $V_{bg} = 1.8\,\text{V}$ in the left part, $x_{tip} = 50\,\text{nm}$.

5.9 Compressible stripe

The LL0 feature in figure 5.12a exhibits a flat plateau of about 40 nm width at $V_{sample} = 120\,\text{mV}$ and $x_{tip} = 5 - 45\,\text{nm}$. This is $10 - 20\,\text{nm}$ on the right of the position where the LL-1 feature crosses E_F. On this plateau the energy of the LL0 feature is constant despite the QD is moved across at the pn interface. Apparently $\mu_{c,gr}$ must have a plateau as well, since otherwise the LL state energy in the QD would change as happens left and right of the plateau. Flat plateaus of $\mu_{c,gr}$ are indeed expected to form due to interactions as described in section 2.11. They are called compressible stripes with LLs pinned to E_F (see figure 2.18). The $\mu_{c,gr}$ gradient is locally screened by anisotropic n_s to form a plateau of constant $\mu_{c,gr}$ [13]. In the case of figure 5.12a, LL-1 is pinned at E_F forming the plateau of constant $\mu_{c,gr}$. Consequently, the LL0 state of the QD is imaged at constant energy across the plateau. The position of the LL-1 feature measured at $V_{sample} = 0\,\text{V}$ and the LL0 feature plateau at $V_{sample} = 120\,\text{mV}$ is different because $V_{sample} = 120\,\text{mV}$ changes the QD depth and thereby the potential across the pn interface as shown in figure 5.13a. The changing n_s on the plateau manifests by CLs that appear separated by about 10 nm at $V_{sample} \gtrsim 150\,\text{mV}$. While the QD is moved across the pn interface, states from LL-1 are increasingly charged into the QD. Here, again the four-fold degeneracy of the graphene LLs results in four adjacent CLs indicating that the plateau is maintained by charging a single orbital state.
Plateaus of constant $\mu_{c,gr}$ are called compressible stripes that are separated by incompressible stripes which are characterized by a steep $\mu_{c,gr}$ gradient [13] (see figure 2.18). The width of the incompressible stripes depends on the inverse of the charge carrier density gradient dn_s/dx [13] and is shown in figure 5.14 as a function of dn_s/dx calculated by equation 2.52 for the LL-1 to LL-2 transition at E_F with $\Delta E_{N=2-1} = 39.8\,\text{meV}$. Combined with the distance between incompressible stripes given by equation 2.53 the width of the compressible stripe follows as the difference of both (see figure 5.14). The incompressible stripe is about $5 - 20\,\%$ of the stripe-stripe distance and so the com-

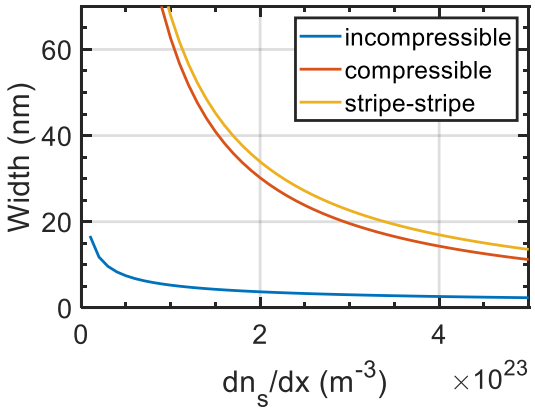

Figure 5.14: Width of the incompressible (blue) and compressible (red) stripe as well as the stripe-stripe distance (yellow) for $\Delta E_{N=2-1} = 39.8\,\mathrm{meV}$ calculated by equations 2.52 and 2.53.

pressible stripes are much wider than the incompressible stripes. In order to compare the measurement with a width of 40 nm to the calculated theoretical width, dn_s/dx of the experimental pn interface is required. As it does not come out of the measurement, it is extracted from the Poisson simulation of the pn interface. Without tip dn_s/dx is about $3 - 4 \cdot 10^{23}\,\mathrm{m}^{-3}$ resulting in a compressible stripe of $10 - 20\,\mathrm{nm}$ about quarter to half of the experimental results. If however the tip is included in the Poisson simulation, dn_s/dx is about $1.5 - 2 \cdot 10^{23}\,\mathrm{m}^{-3}$ at $V_\mathrm{sample} = 100\,\mathrm{mV}$ as the tip leads to a pn interface broadening. The resulting width of $30 - 40\,\mathrm{nm}$ is in good agreement with the measurement.
In figure 5.12b, LL0 features form a plateau when crossing E_F at $x_\mathrm{tip} = -5 - 30\,\mathrm{nm}$. However, the QD below the tip dominates resulting in four CLs and CDs at the plateau undermining conclusions about the width. An example of a LL plateau at E_F that is

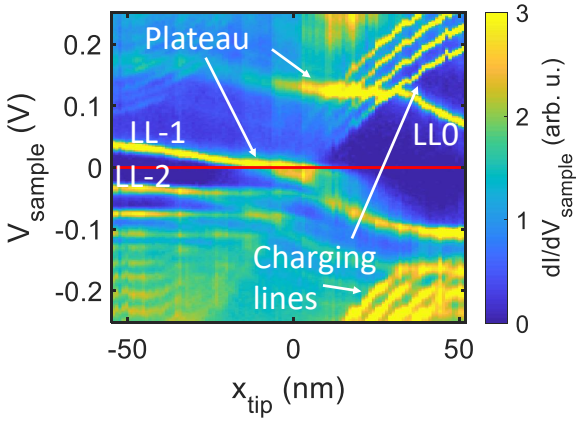

Figure 5.15: $dI/dV_\mathrm{sample}(V_\mathrm{sample})$ along a line perpendicular to the pn interface which is located at $x_\mathrm{tip} = 0\,\mathrm{nm}$. $V_\mathrm{bg} = -1.6\,\mathrm{V}$ in the left part. $I^\mathrm{stab} = 200\,\mathrm{pA}$, $V^\mathrm{stab}_\mathrm{sample} = -250$ mV, $V^\mathrm{mod}_\mathrm{sample} = 5$ mV, $f^\mathrm{mod} = 1386\,\mathrm{Hz}$.

less influenced by the QD and consequently directly probes the compressible stripe is shown in figure 5.15 for the LL-1 feature at $V_{\mathrm{bg}} = -1.6\,\mathrm{V}$. Here the plateau width is considerably smaller ($\approx 15\,\mathrm{nm}$). The LL0 feature plateau at $V_{\mathrm{sample}} = 120\,\mathrm{mV}$ appears as in figure 5.12a shifted with respect to the LL-1 feature plateau at E_{F}.

5.10 Landau level branching

The branching of LL features appears once the LL features approach the pn interface and is observed for occupied as well as unoccupied LL states where each LL feature energetically splits into branches. It is found both in $dI/dV_{\mathrm{sample}}(V_{\mathrm{sample}})$ (see section 5.8) and in $dI/dV_{\mathrm{sample}}(V_{\mathrm{bg}})$ recorded at $V_{\mathrm{sample}} = 0\,V$ (see section 5.11). Interaction induced symmetry breaking or Zeeman splitting (see section 2.4) can be excluded as well as the lifting of the sublattice degeneracy, because it should be observable in the static measurement in figure 5.3a as well. The absence of the LL branching in a static measurement leads to the conclusion that the pn interface is crucial for its observation. Indeed the in-plane electric field $\mathcal{E}_x$ resulting from the $\mu_{\mathrm{c,gr}}$ step present at the pn interface distinguishes it from the static measurement.
In [121], the effects of $\mathcal{E}_x$ on the graphene LLs are described. If $\mathcal{E}_x$ has a similar magnitude as the Lorentz force divided by e, that is $(v_{\mathrm{F}} \cdot B)$, the drift velocity is similar to the Fermi velocity v_{F}. Indeed, one finds $\mathcal{E}_x \approx 5\,\mathrm{mV/nm} = 5 \cdot 10^6\,\mathrm{V/m}$ (see figure 5.13) and $v_{\mathrm{F}} \cdot B \approx 7 \cdot 10^6\,\mathrm{V/m}$ to be similar. Due to the relativistic behaviour of the graphene charge carriers, the drift velocity can not exceed v_{F} but instead a rescaling of the energy scale sets in. As a consequence, the LL energy spectrum (see equation 2.6) is offset in energy as well as the energy gaps between LLs are reduced. The down shift in energy could explain the lower branch of the split LLs in the experiment whereas the upper branch is not accounted for. A reduction of the LL energy gaps at the pn interface is also not observed experimentally. Summarized, this effect is not sufficient to explain the LL branching.
The orbital degeneracy of the LLs in a QD is lifted because states with different wave functions are energetically separated by the confinement potential of the QD (see section 2.7). This effect is experimentally observed in [57, 58, 122] where a single LL splits into several branches in the vicinity of a localized charge. States with increasing $|m|$ quantum number have a larger radial extent and are energetically shifted from the $m = 0$ state as can be seen in the calculated LDOS of a QD in figure 5.16a [76] or figure 2.10b and c. This is observed experimentally in [76] where the states of a static QD are probed by STS (see figure 2.21).
For a circular QD the wave functions of the different m states are simplified described by rings with increasing diameter where n_r gives the number of radial nodes (see figure 2.10a). For LL0, the wave function maxima follow the confinement potential with increasing $|m|$ because these wave functions do not have radial nodes. For LL$\pm$1 and higher $|N|$, the wave functions have radial nodes which result in finite intensity of the wave function close to the QD center. In this case, wave functions of different m states of the same LL can have finite amplitude at the same radial position r but at different energy. The LL LDOS splits into separate branches with increasing r that belong to different m states. Moreover, the energetic distance between the m state probed at a particular r and the $m = 0$ state increases with r (see figure 5.16a). This effect can

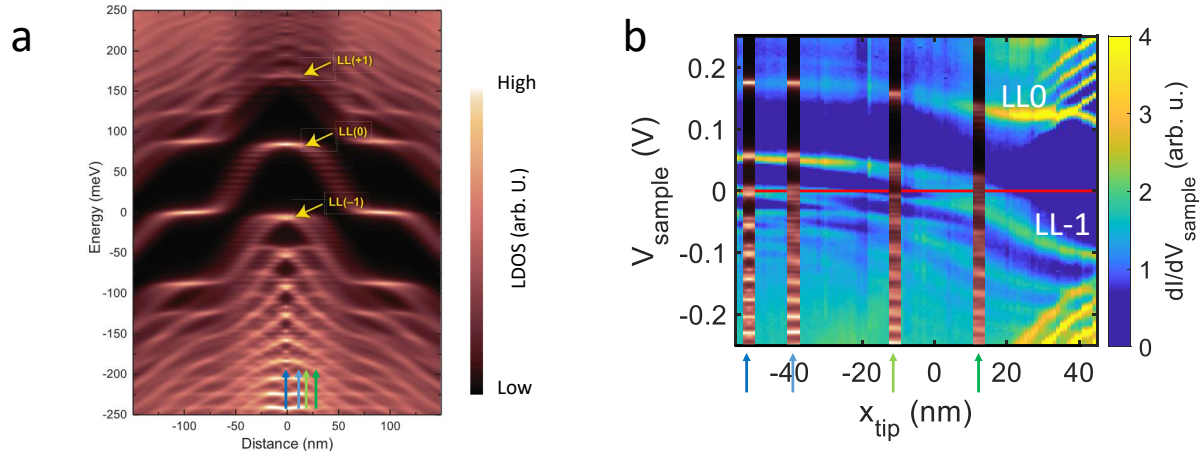

Figure 5.16: a: Simulated LDOS for a hole-like QD potential. From Science **361**, 789-794 (2018) *Interaction-driven quantum Hall wedding cake-like structures in graphene quantum dots.* C. Gutiérrez, D. Walkup, F. Ghahari, C. Lewandowski, J. F. Rodriguez-Nieva, K. Watanabe, T. Taniguchi, L. S. Levitov, N. B. Zhitenev, and J. A. Stroscio [76]. Reprinted with permission from AAAS. b: $dI/dV_{\mathrm{sample}}(V_{\mathrm{sample}})$ for $V_{\mathrm{bg}} = -2\,\mathrm{V}$ from figure 5.12a. Sections taken from subfigure a at the positions indicated by vertical arrows are overlaid. Modification with permission by J. A. Stroscio [76].

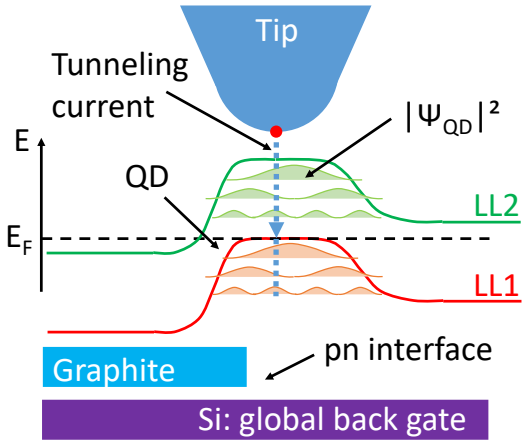

Figure 5.17: Sketch of the QD below the tip that is displaced from the tunneling center of the tip at the pn interface. As a consequence QD states with amplitude not in the QD center are probed by STS.

be related to the observation of LL branching at the pn interface. The QD below the STM tip is moved off center because of $\mathcal{E}_x$ present at the pn interface as sketched in figure 5.17. The tunneling center of the STM tip measures various $|m|$ states off-center simultaneously. These higher $|m|$ states are separated in energy because of different orbitals. The difference is, that the tip is moved with respect to the static QD in [76], in contrast to our experiment where the tip in the QD is moved by the presence of the pn interface. The similarity between both results is shown in figure 5.16b. Sections with increasing distance from the center of the simulated static QD shown in figure 5.16a are compared to the experiment at different positions across the pn interface. The observed LL branches at the pn interface are reasonably reproduced by the overlaid simulations partially including even changes in the width of a LL peak. Once the tip has passed the pn interface, the tunneling center gets aligned to the QD center again and the LL branching disappears. As an additional effect, wave function antinodes of states with lower $|N|$ but higher $|m|$ can overlap with wave function antinodes of higher $|N|$ but lower $|m|$, because they are orthogonal. Whether these wave functions overlap or are spatially separated depends on the specific confinement potential of the QD. The overlap results in the merger of different LL features and is found for example for LL1 in figure 5.12b. There branches of LL1 and LL2 intersect ($V_{\text{sample}} > 0\,\text{V}$, $x_{\text{tip}} < 0\,\text{nm}$). The overlap of wave functions of different LL features shows that the $|m| >> 0$ states can be energetically separated from the $m = 0$ state by as much as the energy gaps between the LLs.

The TB calculations based on the Poisson simulations of the experiment reproduce the displacement of the QD below the tip at the pn interface as depicted in figure 5.18a: In figure 5.18a the wave function of the QD below the tip is shown at different positions x_{tip}, while the tip is crossing the pn interface. The displacement between the wave function maximum and the tip becomes clearly visible. At the same time, the radial extent of the wave function is decreasing as explained by the shrinking QD poten-

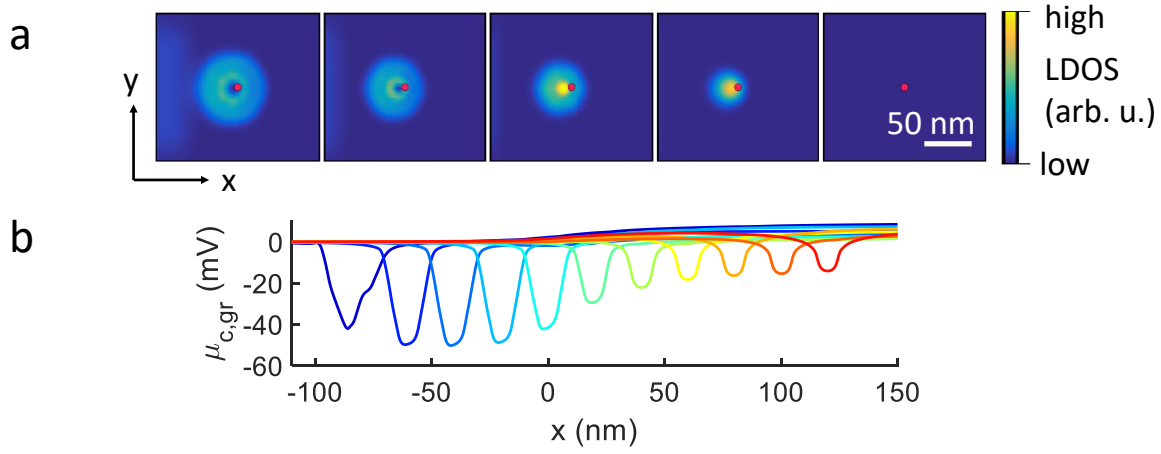

Figure 5.18: a: LDOS of the QD by TB calculations at different tip positions $x_{\text{tip}} = -64, -33, -21, -8, 27\,\text{nm}$ with respect to the pn interface. The tip center is marked by a red dot. $V_{\text{bg}} = -0.5\,\text{V}$, $V_{\text{sample}} = 0\,\text{V}$. The QD states belong to LL0. b: Corresponding QD potentials from the Poisson simulations at $x_{\text{tip}} = -80, -60, \ldots, 120\,\text{nm}$ with $V_{\text{bg}} = -0.2\,\text{V}$, $V_{\text{sample}} = 0\,\text{V}$, $\Delta_{\text{wfm}} = -180\,\text{mV}$ and $r_{\text{tip}} = 25\,\text{nm}$. The pn interface is at $x = 0\,\text{nm}$.

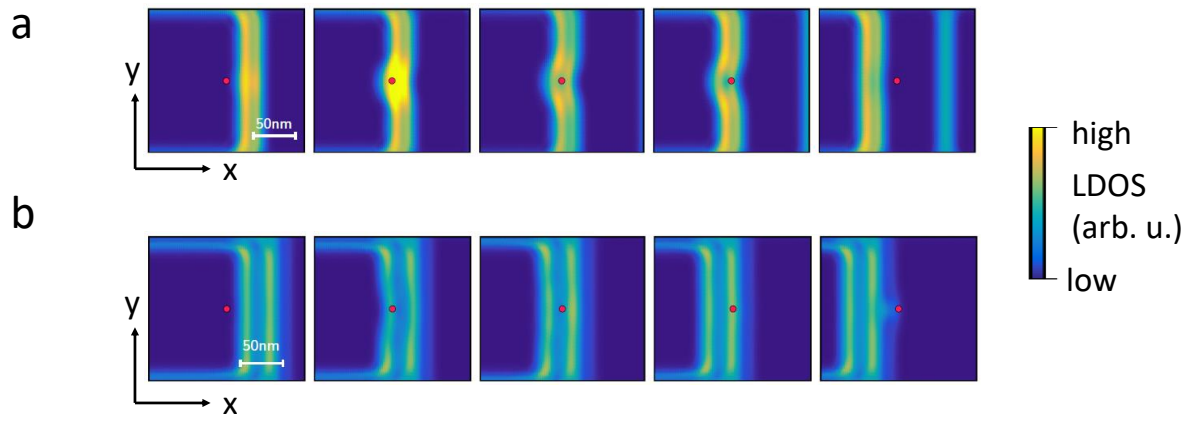

Figure 5.19: a: LDOS at the pn interface by TB calculations at different tip positions $x_{\mathrm{tip}} = -40, -21, -11, -4, 20\,\mathrm{nm}$ marked by a red dot across the pn interface at $x = 0\,\mathrm{nm}$. $V_{\mathrm{bg}} = 2.15\,\mathrm{V}$, $V_{\mathrm{sample}} = 0\,\mathrm{V}$. The compressible stripe belongs to LL1 (and LL0 in the right most figure). b: Tip positions $x_{\mathrm{tip}} = -48, -18, -6, 6, 35\,\mathrm{nm}$, $V_{\mathrm{bg}} = -2.45\,\mathrm{V}$, $V_{\mathrm{sample}} = 0\,\mathrm{V}$. The compressible stripe belongs to LL-2.

tials plotted in figure 5.18b. The depth of the QD is decreasing due to different LL occupation on the left and right part of the pn interface. The QD potentials at the pn interface exhibit an asymmetric shape explaining in the displacement of tip and QD in figure 5.18a.
If no QD is present, a LL state can get localized by a localized charge. The orbital degeneracy of the wave function is lifted by the local potential gradient similar as in a QD [122, 123]. The two components $|N\rangle, |N-1\rangle$ of the LL wave function $\Psi_{\mathrm{gr}}^{\mathrm{LL}N}$ (see equation 2.7) have different radial extent resulting in different energetic position at the potential gradient [122]. As a consequence, each LL splits into, at least, two branches (one for each component) that are however not restricted to one sublattice because of the exchanged sublattice components of $\Psi_{\mathrm{gr}}^{\mathrm{LL}N}$ at K and K'. The energetic splitting translates in a spatial separation of the two branches at the potential gradient. The lower branch of LLN with component $|N-1\rangle$ has the same radial extent as the upper branch of LL$N-1$ with component $|N-1\rangle$ [122] (for N>0, see equation 2.7). Eventually these two branches merge if the potential gradient is strong enough. This scenario requires an asymmetric potential gradient at the pn interface, that might be induced by the QD below the tip, by local charges or could result from the varying screening of the potential step leading to plateaus.
TB calculations in figure 5.19 show that the wave functions of the compressible stripe along the pn interface for different LLs indeed split into two prominent branches: The LL1 compressible stripe exhibits two maxima with different intensities while the LL-2 compressible stripe has two maxima with the same intensity that are however further apart. This results from the larger extent of the wave function with increasing $|N|$. Two explanations or a mixture of both are possible. Either, the branches are the most prominent antinodes of the two overlapping LL wave functions that are crossing E_{F} simultaneously (see equation 2.7) or an asymmetric potential gradient splits the two contributions. At branches, where the distance of the two contributions changes with energy (see figure 5.12b), the later scenario must be contributing, while for more

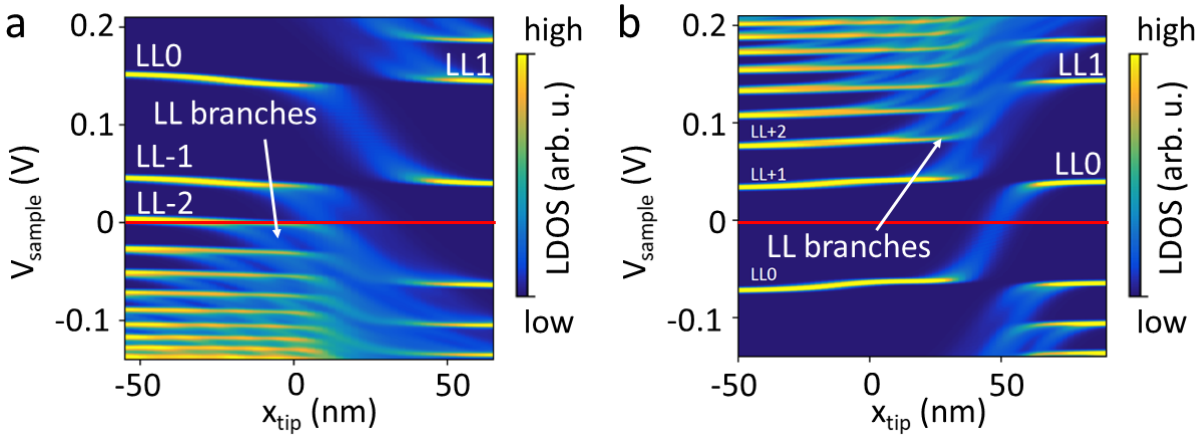

Figure 5.20: $dI/dV_{\mathrm{sample}}(x_{\mathrm{tip}}, V_{\mathrm{sample}})$ at the pn interface from TB calculations across the pn interface at $x = 0\,\mathrm{nm}$. The simulations qualitatively reproduce the LL branching observed in the measurements of figure 5.12a and b, respectively. a: $V_{\mathrm{bg}} = -1.9\,\mathrm{V}$. b: $V_{\mathrm{bg}} = 2\,\mathrm{V}$.

constant distances, the former scenario could be sufficient. A quantitative evaluation of these two scenarios has not been performed yet. Probing the split wave functions reveals the energy dependent shape of the interface potential [122, 123]. In the measurements of figure 5.12a, the energetic and spatial separation of the LL branches is clearly resolved. The branches of LL-1 and LL-2 features merge but do not cross in contrast to the branches in figure 5.12b. The absence of crossings is in line with the scenario of sublattice symmetry broken states. In contrast, the crossings observed in figure 5.12b could be explained by QD states of different LLs or by intersecting compressible stripes of different LLs at the pn interface.
The TB calculations in figure 5.19 show that the ECs get disturbed by the band bending below the tip. Their inner structure, however, remains preserved such that a local mapping of the compressible stripe is possible (see sections 5.11 and 5.12).
The accuracy of the combined Poisson and TB simulation modeling the experiment is demonstrated by the calculated $dI/dV_{\mathrm{sample}}(x_{\mathrm{tip}}, V_{\mathrm{sample}})$ shown figure 5.20. The simulations are performed with the experimental parameters of figure 5.12a and b, respectively. The LL branching sets in as soon as the tip approaches the pn interface and the lateral extent as well as the energy gaps of the branches match the experiment such that the branches connect and partially cross neighbouring LLs. Charging lines are not included in the theoretical description and consequently do not show up in figure 5.20.

5.11 Gate dependence of compressible stripes

To better understand the behaviour of LL states crossing E_F, $dI/dV_{sample}(x_{tip}, V_{bg})$ is performed across the pn interface for fixed position y along the interface at $V_{sample} = 0\,V$. On the left side of figure 5.21a, one can see the LL states passing E_F one after the other with increasing V_{bg}. This part corresponds to a cut along $V_{sample} = 0\,V$ in figure 5.3a. On the right edge, the intensity is low as no LL state is pinned at E_F since the LL0 state appears about 20 mV above E_F (see figure 5.12). The right edge of figure 5.21a (with constant Si back gate $\approx 0\,V$) is represented by a single point in figure 5.3a at $V_{bg} = -0.4 - 0.7\,V$ and $V_{sample} = 0\,V$. Moving from left to right the LL states either band upwards or downwards depending whether they are occupied on the right side (downwards bending) or not (upwards bending). For an unoccupied LL state on the right, $V_{bg} > 0\,V$ in the left part is necessary in order to occupy this LL state and make it cross E_F. With increasing V_{bg} the potential step at the interface gets larger and moves towards the right side via stray fields. This shifts the LL state crossing E_F in the same manner towards the right. The same mechanism applies for the occupied LL states in the right part which need to be depleted in the left part to cross E_F requiring $V_{bg} < 0\,V$.
All LL states form a plateau when crossing E_F as explained in sections 2.11 and 5.9 due screening of the potential step. The plateaus of LL states in the $dI/dV_{sample}(x_{tip}, V_{bg})$ map indicate such compressible stripes as observed in the measurements of section 5.8. The lateral width depends on dn_s/dx as set by the applied V_{bg} (see figure 5.14) and the QD spatial extent. In experiment, such stripes are apparent on the right side of figure 5.21a as the profile line across the LL feature along x_{tip} for constant V_{bg}. The width decreases towards the right, that is if the filling factors are strongly different between left and right and thereby the potential drop at the pn interface is high. This is in line with equation 2.53.
The LL0, LL1 and partly LL-1 states do not exhibit a single line, but instead consist of

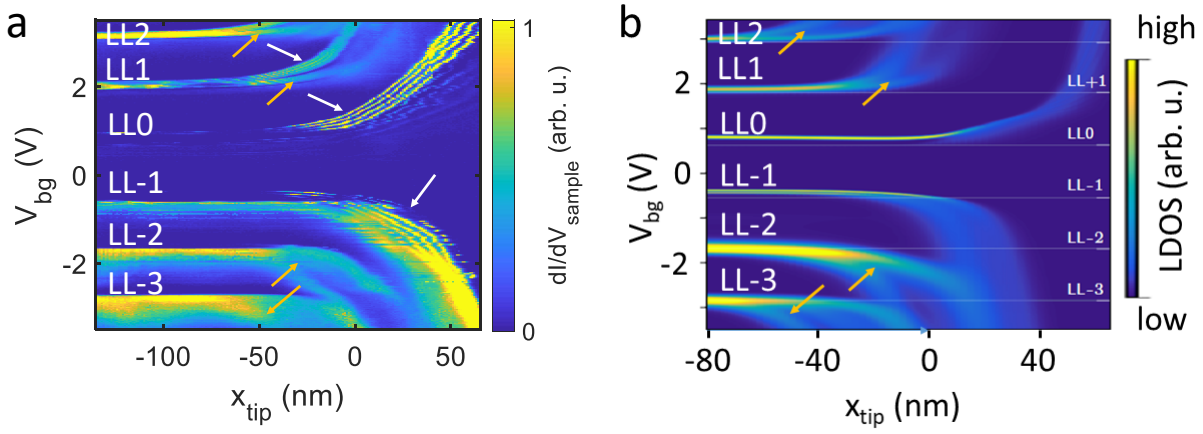

Figure 5.21: a: $dI/dV_{sample}(x_{tip}, V_{bg})$ for $V_{sample} = 0\,V$ across the pn interface at $x = 0\,nm$. $V_{sample}^{stab} = -250\,mV$, $I^{stab} = 1\,nA$, $V_{sample}^{mod} = 1$ mV, $f^{mod} = 386.2\,Hz$. Charging lines are marked with white arrows and LL branches with orange arrows, respectively. b: Corresponding simulation by TB calculation. The bulk LLs are given on the right and indicated with white horizontal lines. LL branches are marked with orange arrows.

several narrow lines on the right of figure 5.21a. These are CLs as is evident for the LL0 states by comparison with a line profile of the measurement in figure 5.12b for $V_{\text{sample}} = 0\,\text{V}$. They show that the number of confined charge carriers in the QD is changing as expected for the charge carrier density gradient in a compressible stripe [13]. For positive $V_{\text{bg}} > 0\,\text{V}$, the band bending below the tip results in confined charge carriers as the CLs of the LL0, LL1 and partly LL-1 states prove. Interestingly, for LL-1 the CLs are only observed at $V_{\text{bg}} > -2\,\text{V}$. At this point, the $V_{\text{tip,eff}}$ (see equation 5.9) between tip and graphene on the left side of the pn interface is small, such that no QD is formed. For these settings, the wave function of the compressible stripe is measured without the QD below the tip.
As in the $dI/dV_{\text{sample}}(x_{\text{tip}}, V_{\text{sample}})$ measurements, the LL features develop branches while approaching the pn interface that partly connect adjacent LLs as explained in section 5.10. The spatial distance of the branches increases with $|V_{\text{bg}}|$ as partially expected from the lower lever arm of V_{bg} for positions far apart from the pn interface position towards the right. The LL-1 feature exhibits a varying intensity along x_{tip}. The LL-2 stripe exhibits a pronounced branching in agreement with the TB calculation in figure 5.18. For LL-3 the onset of a threefold stripe is visible in the TB data for $V_{\text{bg}} < -3\,\text{V}$ (see figure 5.21b), that might be present in the experimental data as well. The TB results shown in figure 5.21b model the data of figure 5.21a rather well. The widths as well as the branches of the stripes are covered confirming the good validity of this method to account for the experiment. White horizontal lines show where a LL is at E_{F} in the bulk on the left side of the pn interface: For $N < -1$, there is no difference between this bulk and the LL feature observed, that is the $m = 0$ state of the QD. This is in agreement with $V_{\text{tip,eff}} \approx 0\,\text{V}$. The V_{bg} difference for the other LLs is small compared to the distance between LLs and nearly vanishes for $N > 0$ again. As a consequence, no charge carriers are confined below the tip in the TB simulation in this V_{bg} regime in contrast to the experiment, where CLs are observed. This is likely a result of an underestimated QD radius in the Poisson simulation that the neglects quantum mechanical confinement energy taken into account in the TB simulation. Nevertheless,

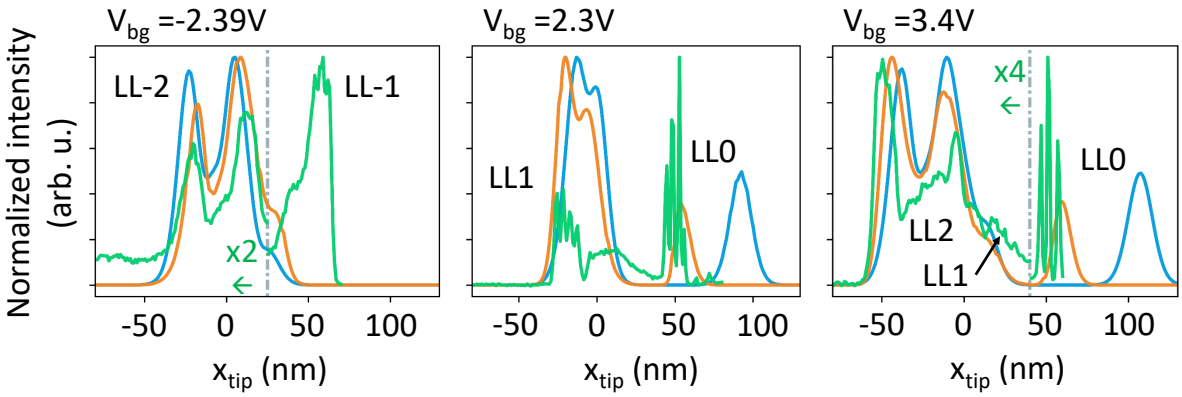

Figure 5.22: Intensity profile line of $dI/dV_{\text{sample}}(x_{\text{tip}})$ (green) for $V_{\text{sample}} = 0\,\text{V}$, corresponding TB simulation (orange) for different V_{bg} as marked deduced from figure 5.21. The blue curves are the results of a TB simulation without tip. The $dI/dV_{\text{sample}}(x_{\text{tip}})$ data are shifted by 5 nm, 20 nm and 10 nm (left to right).

the good agreement between TB simulation and experiment for $dI/dV_{\mathrm{sample}}(x_{\mathrm{tip}}, V_{\mathrm{bg}})$ remains.
In order to probe the strength of perturbation of the compressible stripe by the QD, line cuts of the TB simulation and the experiment are compared with the compressible stripe that appears in TB simulations without QD (see figure 5.22). The distance between the branches and the intensity profiles agree for LL-2 in the left subfigure and LL2 in the right subfigure, that is for minimal QD depth. In contrast the LL-1 feature in the left subfigure is not reproduced by both simulations, and the unperturbed LL0 feature in the middle and the right subfigures is shifted to the left by simulation and experiment with QD. This shift might be induced by the changed pn interface due to the presence of the QD. The good correspondence for LL-2 and LL2 indicates, that these states can indeed be mapped undisturbed by STS.

5.12 Mapping a compressible stripe along the pn interface

The plateau forming once the LL-1 feature crosses E_{F} for $V_{\mathrm{bg}} = -1.6\,\mathrm{V}$ shown in figure 5.15 is mapped spatially along the pn interface. It is selected because CLs do not perturb it. As can be seen in figure 5.23, the plateau area is not forming a straight line along the interface but meanders with an amplitude of about 10 nm. The edge of the graphite flake, that electrostatically defines the pn interface, is likely atomically sharp based on mechanical exfoliation resulting in edges preferably along crystallographic directions. Consequently it can not explain the meandering. Possibly, localized charges alter the position of the plateau with respect to the edge of the graphite flake. They could exist in defects of the hBN flake [124] or in the SiO_2 substrate as depicted in figure 5.24a. Another source of localized charges could be residues trapped in the van-der-Waals stacked sample. They can accumulate in bubbles in between different layers (see figure 5.24b), but also along the graphite flake edge between the SiO_2 substrate

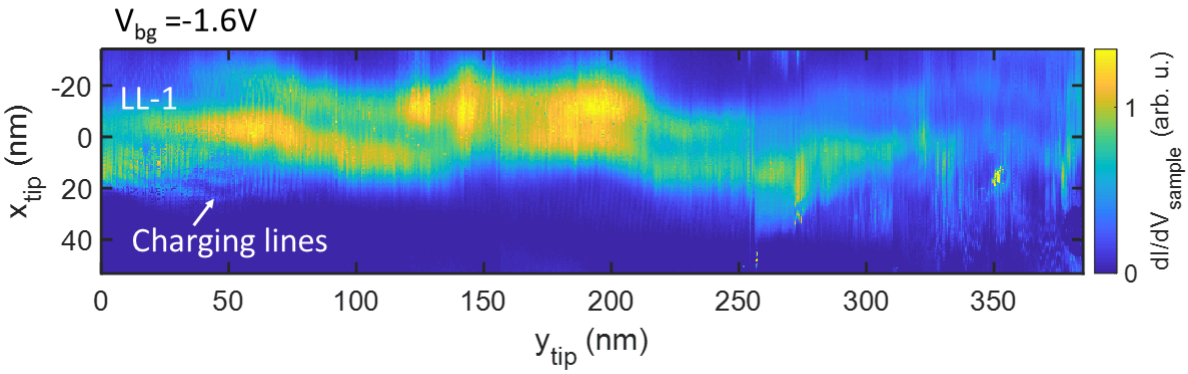

Figure 5.23: $dI/dV_{\mathrm{sample}}(x_{\mathrm{tip}}, y_{\mathrm{tip}})$ for $V_{\mathrm{sample}} = 0\,\mathrm{V}$ and $V_{\mathrm{bg}} = -1.6\,\mathrm{V}$ across the pn interface at $x = 0\,\mathrm{nm}$. $V_{\mathrm{sample}}^{\mathrm{stab}} = -250\,\mathrm{mV}$, $I^{\mathrm{stab}} = 1\,\mathrm{nA}$, $V_{\mathrm{sample}}^{\mathrm{mod}} = 1$ mV, $f^{\mathrm{mod}} = 386.2\,\mathrm{Hz}$.

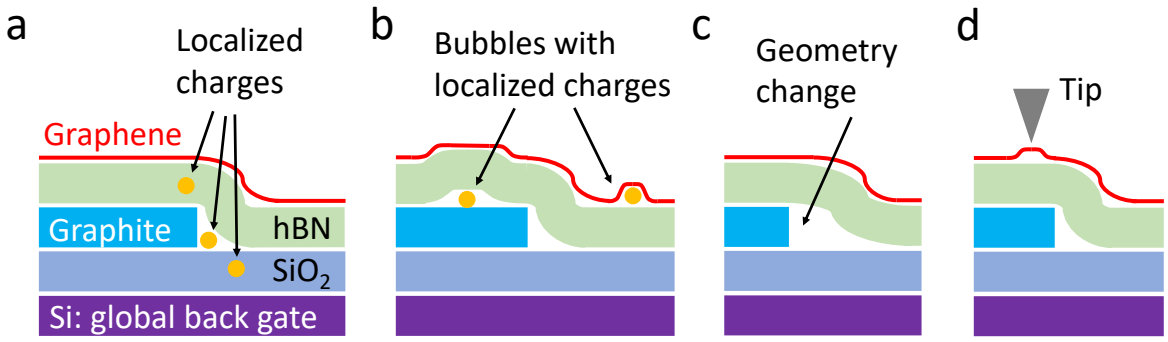

Figure 5.24: Possible mechanisms to explain the meandering of the compressible stripe: a: Localized charges (orange) in the substrate. b: Localized charges (orange) in bubbles. c: Change of geometry increasing the distance between graphene and graphite back gate. d: Change of geometry due to the tip lifting of the graphene flake.

and hBN flake [125] (see figure 5.24a). The AFM topography of the pn interface shown in figure 5.1c exhibits many bubbles close to the pn interface. Also a change in the distance between graphene and graphite along the pn interface depending on how close the hBN flake or the graphene flake is to the graphite back gate or SiO_2 back gate locally could be an explanation for the meandering plateau (see figure 5.24c). Bubbles and folds can give rise to a change in the geometry close to the pn interface. Finally, the van-der-Waals force between tip and sample (see section 3.2) can result in a local lifting of the graphene from the substrate [126, 127] that might spatially vary (see figure 5.24d). This effect is, however, not relevant in this context due to the moderate tunneling conditions with $V_{\text{sample}}^{\text{stab}} = -250\,\text{mV}$ and $I^{\text{stab}} = 1\,\text{nA}$ as checked by $I(z)$ curves.

The width of the plateau also changes depending on the position along the pn interface. $dI/dV_{\text{sample}}(x_{\text{tip}}, V_{\text{sample}})$ taken at different positions exemplary shown in figure 5.25 reveals that a flat plateau is not observed everywhere but instead the LL-1 feature crosses E_{F} without forming a plateau as well. In the middle panel of figure 5.25, a plateau of about 40 nm is visible. The right panel depicts an example of a narrower stripe with less intensity that has a double structure. Additionally, the LL-1 state can split in several parallel branches with different intensity (left panel in figure 5.25).

The plateau in figure 5.23 partially exhibits a double stripe structure as calculated in the TB simulations in figure 5.20a and 5.21b which intensity is varying spatially as well. At some positions for $y_{\text{tip}} \approx 50\,\text{nm}$ and $y_{\text{tip}} \approx 370\,\text{nm}$, in addition, weak CLs appear in the measurement. This indicates that the charge carriers are about to be confined in the band bending below the tip what is similarly observed in figure 5.21a with developing CLs in the same V_{bg} regime. The transitions between different intensities along the pn interface occur smoothly pointing to changes of the electrostatics at the pn interface as the origin. A sudden change observed at $y_{\text{tip}} \approx 255\,\text{nm}$ indicates instead a change of the STM tip, for example by picking up some debris from the sample surface. The QD center or the extremum of the band bending below the tip might be

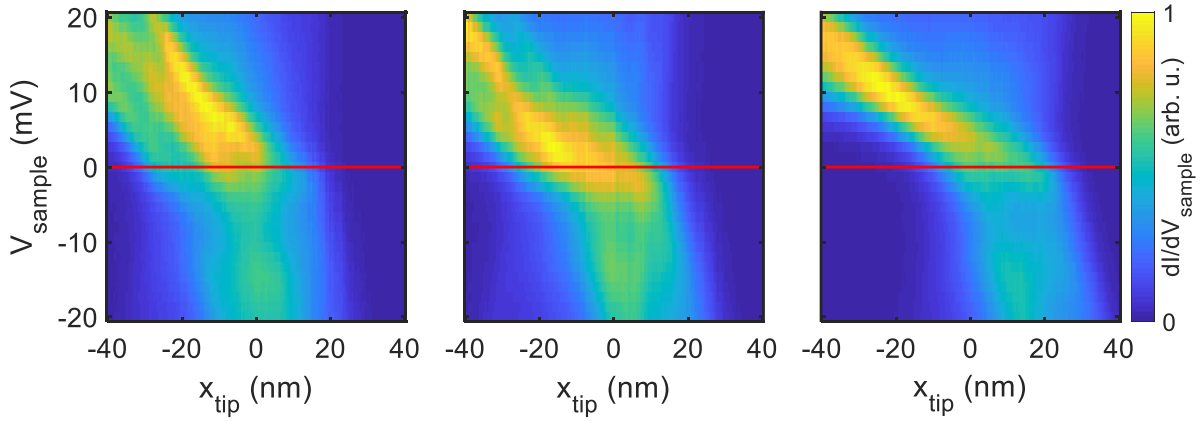

Figure 5.25: $dI/dV_{\mathrm{sample}}(x_{\mathrm{tip}}, V_{\mathrm{sample}})$ for $V_{\mathrm{bg}} = -1.6\,\mathrm{V}$ across the pn interface at $x = 0\,\mathrm{nm}$ for three different positions y separated by about 40 nm distance along the pn interface. The y positions are different than the measurement of figure 5.23. $V^{\mathrm{stab}}_{\mathrm{sample}} = -250\,\mathrm{mV}$, $I^{\mathrm{stab}} = 1\,\mathrm{nA}$, $V^{\mathrm{mod}}_{\mathrm{sample}} = 1$ mV, $f^{\mathrm{mod}} = 386.2\,\mathrm{Hz}$.

displaced with respect to the STM tip at the pn interface as explained in section 5.10 and figure 5.17. Each maximum of the double stripe shape corresponds most likely to a different antinode of either the LL wave function localized at the pn interface or of a m state in the QD. It can not be excluded that the m states of the QD also contribute since CLs partly appear. A possible change of the electrostatics along the pn interface by the tip potential results in two outcomes: Firstly the position of the plateau with respect to the pn interface changes continuously and, secondly, which part of the wave function (m state) is probed by the tunneling center of the tip. These effects must be analyzed in detail by comparison with the TB simulation to obtain a reliable interpretation of the data of figure 5.23 as postponed to future work.

6 Overview: Graphene sample fabrication

6.1 Requirements for graphene samples

A graphene sample has to fulfill certain requirements to be suitable for STM investigations. The graphene surface has to be exposed to the STM tip and it must be electrically contacted to detect the tunnel current. Moreover, it has to be mechanically stable. Furthermore, a clean and flat surface is desirable to ease the measurements by maintaining a stable tip [128]. Finally, a back gate is required to increase the tunability of the experiment [19, 64]. If a second, independent back gate or multiple electrical contacts on the graphene sample are present, the scope of the experiment is further enhanced by either allowing for investigation at a gate defined pn interface [30] (see sections 2.10, 2.12, and 5) or by comparing local and global properties of the same device by simultaneously performed transport measurements [29, 129] (see sections 7.4, 7.5, and 7.3). In addition, there are requirements to ease the approach process of the STM tip to the sample which have been discussed in chapter 4. These conditions determine the choice of the sample layout as well as the fabrication process. It boils down to the graphene layer being supported by a substrate that at the same time serves as a dielectric electrically insulating the graphene layer from the back gate as depicted in figure 6.1. Electrical contacts to the graphene layer must be electrically insulated from each other and the back gate by the substrate as well. The choice of the substrate is

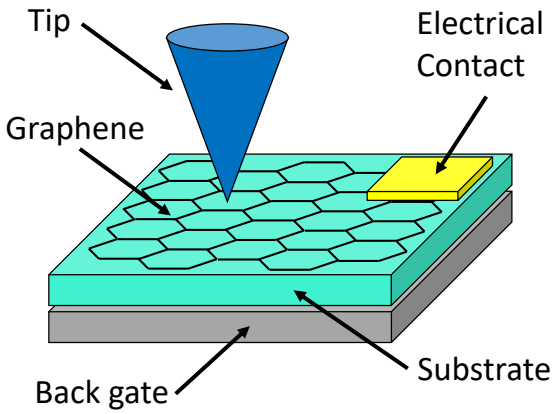

Figure 6.1: Schematic of a graphene sample for STM/STS measurements (not in scale). The graphene layer is represented by a hexagonal lattice and is placed on a substrate (turquoise) on top of a back gate (gray) and electrically connected by a contact pad (yellow). The STM/STS tip is shown in blue.

crucial, since it affects the graphene properties by its proximity [130, 131]. What might be a desired effect is introducing superconductivity [132] or spin-orbit-interaction [133] to graphene by proximity of a corresponding material, mostly turns out to degrade the graphene quality by disorder induced potential fluctuations [74]. Suspended graphene samples circumvent this problem by omitting the substrate below the graphene completely. They show reasonable quality in transport experiments [134]. But they are barely accessible for STM due to the lack of mechanical stability against the vdW forces of the tip [135]. Graphene layers grown on substrates like copper, nickel or silicon carbide lack the possibility of a back gate and are therefor not considered as sample layouts, albeit the graphene quality is high due to complete ultra high vacuum (UHV) fabrication. The high quality is for example proven by the observation of degeneracy lifted LLs states with STM [136].
Other than the substrate used for the graphene samples, the fabrication process itself has considerable influence on the graphene quality due to contaminations left on the graphene surface [125]. These arise mostly in wet chemical processes where polymers are dissolved or substrates etched by acids. In general, any contact to the exposed graphene surface should be avoided. Since widely used transport experiments do not rely on an exposed graphene surface, fabrication processes usually encapsulate the graphene layer from both sides by a substrate [137]. This allows for the use of wet chemical processes afterwards while maintaining a high graphene quality, but is not applicable for STM samples. They have to be based on *dry* fabrication processes in order to achieve a high sample quality.
In the following sections different substrates used in QHE transport experiments and the corresponding fabrication techniques will be presented. Possible applications for the fabrication of STM suitable graphene samples will be pointed out. The discussion is limited to the fabrication without electrical contacting, that will be discussed in section 6.11.

6.2 Silicon oxide

Silicon oxide (SiO_2) is an insulating substrate that has been frequently used for graphene samples [19, 54, 64, 138, 139]. SiO_2 is avaible in wafer scale grown directly on silicon (Si) wafers where the underlying Si is doped and serves as a back gate. Since graphene can be mechanically exfoliated directly on SiO_2 with great optical visibility at a thickness of 300 nm SiO_2 on Si, it offers a quick and clean fabrication as no further fabrication processes are necessary [19] (see figure 6.2). Mechanical exfoliation describes a process in that a van-der-Waals (vdW) bulk crystal (typically $1-10\,\mathrm{mm}$ in size) is cleaved on a tape multiple times and this way thinned down until flakes with thickness of a few layers of the crystal are created. These flakes are transferred to a chip by placing the tape on it and waiting for some time before releasing it again. This process can be improved by heating the chip and the tape during contact [140].
Graphene samples prepared on SiO_2 show charge carrier mobilities in the range of a few thousand up to $50.000\,\mathrm{cm}^2/\mathrm{Vs}$ [138, 139]. In these samples degeneracy lifting in LL0 could be observed at high magnetic field of $B = 30-45\,\mathrm{T}$ [138, 139]. The drawback of SiO_2 is its amorphous crystal structure due to which its roughness [141] and its charge inhomogeneity [74, 75] are both imposed to the graphene. The charge inhomogeneity

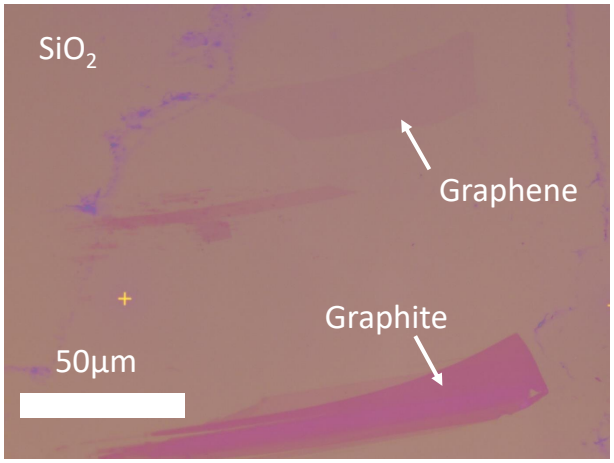

Figure 6.2: Optical image of an exfoliated graphene flake on a SiO_2/Si chip. Next to it is a multilayer graphene or graphite flake.

of the SiO_2 leads to the formation of charge puddles in the graphene [74, 75] that turn into localized quantum dots in the quantum hall regime [54].

6.3 Hexagonal boron nitride (hBN)

Hexagonal boron nitride (hBN) is a widely employed substrate for graphene samples overcoming the problems of SiO_2 [118]. hBN has the same lattice structure as graphite albeit the lattice constant is 1.8% larger [142] and the A and B sublattices are different consisting of boron and nitrogen atoms, respectively. This gives different on-site energies for both sublattices in the tight binding calculation leading to a band gap. This renders hBN an insulator. Due to its lattice structure, individual layers are van-der-Waals bound enabling mechanical exfoliation of hBN flakes on SiO_2 (see figure 6.3). Afterwards graphene can be transfered onto the hBN flake, which improves the graphene quality a lot compared to a SiO_2 substrate. The increased distance to the SiO_2 surface reduces the influence of charge disorder present in SiO_2. The hBN

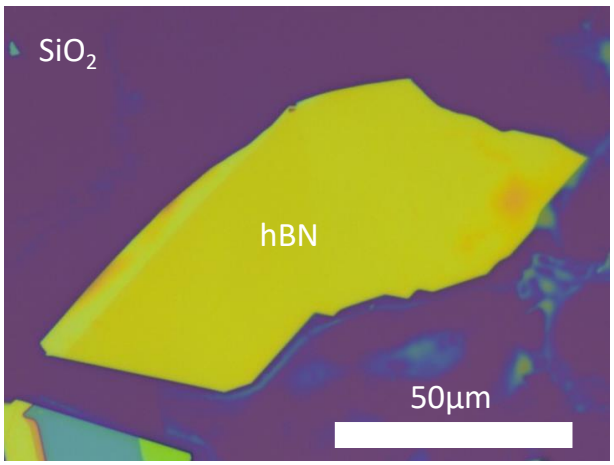

Figure 6.3: Optical image of an exfoliated hBN flake on a SiO_2/Si chip.

flake, moreover, smoothes the rough SiO_2 surface while having an atomic flat surface itself. The challenge in fabricating graphene on hBN samples is the required transfer process of a graphene flake on the hBN flake.

6.4 Transfer processes

In the last decade, many different methods for transferring 2D material flakes and thereby assembling vdW stacks of multiple different 2D material flakes have been developed. They reach far beyond the fabrication of graphene-hBN-stacks [130, 143]. They all rely on a mechanically soft and optically transparent stamp that is made out of a polymer. The differences of the methods manifest in the properties and the fabrication of the stamp and will be presented in more detail below. Most steps in transferring a flake are similar for all methods and are summarized in figure 6.4. In the beginning a 2D material flake is either exfoliated on the stamp (1a) or picked up with the stamp from a chip (2b) on which it is exfoliated beforehand (1b). The stamp is mounted on a micromanipulator with the flake on the stamp flipped upside down (2a) in order to align it to the target flake (3) that is exfoliated on another chip (1c and 2c). The alignment of the flakes is performed with an optical microscope why the stamp has to be transparent (3). Once both flakes are aligned, they are brought into contact by lowering the stamp via the micromanipulator. Often, the temperature is increased for this purpose (4). Afterwards the stamp is released and if successful either the flake from the stamp is transferred to the target flake on the chip (5b) or vice versa (5a) both called a dry transfer. Once stamp and chip are separated, the final stack either

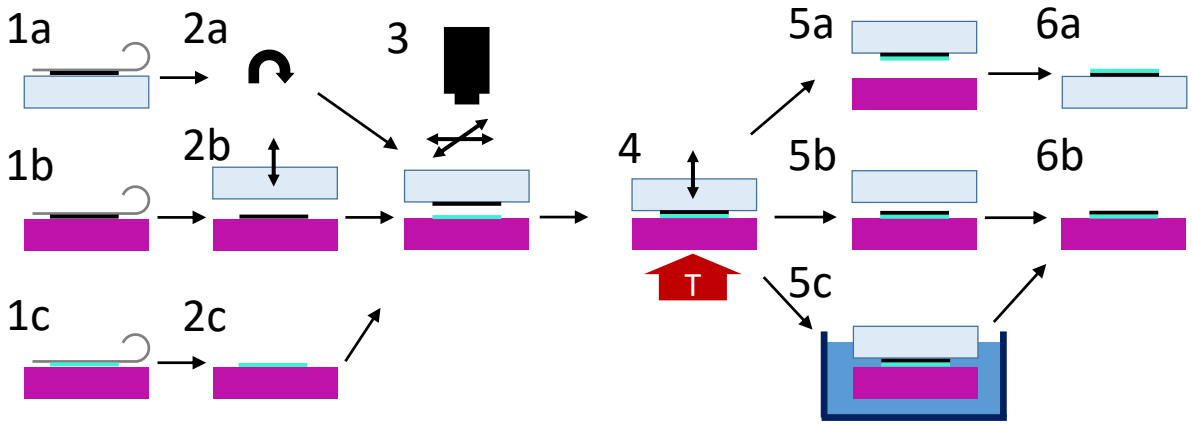

Figure 6.4: Transfer process: 1a: Exfoliation of a flake (black) on the stamp (light blue) for transfer. 1b: Exfoliation of a flake (black) on a chip (violet) for transfer. 1c: Exfoliation of the target flake (turquoise) on a chip (violet). 2a: Flipping of the stamp upside down. 2b: Pick up of the flake to be transferred from a chip with the stamp. 2c: Target flake on a chip. 3: Optical alignment of the flake to be transferred and the target flake. 4. Transfer of flake by pressing the aligned stamp on the target flake. If required the temperature is raised. 5a: After transfer of the target flake on the stamp. 5b: After transfer of the flake onto the target flake on a chip. 5c: Dissolving the stamp in a solvent. 6a: Final stack on the stamp. 6b: Final stack on the chip.

rests on the chip (6b) or the stamp (6a). This depends on the adherence of the flakes to the stamp or chip, respectively, and the size of the flakes. It can additionally be influenced by varying the temperature during the transfer (4). Due to the flat surfaces of the exfoliated 2D material flakes, the van der Waals (vdW) force between them is larger than the adherence to stamp or substrate giving rise to a high yield of successful transfers. This stacking process is repeated until the desired stack of 2D materials is assembled. If the stack is assembled on the stamp it is brought into contact on a target chip and the temperature is raised (4) so that the stamp polymer melts and the stack remains on the target chip. Afterwards the polymer of the stamp is dissolved by a solvent (5c) what is called wet transfer.

6.5 PMMA transfer process

In this process the stamp is made out of a poly(methyl methacrylate) (PMMA) membrane on which the flake can be transferred or exfoliated. To ease the exfoliation, a polyvinyl alcohol (PVA) layer is spin-coated on a Si chip (see figure 6.5 1) and, subsequently, a PMMA layer is spin-coated on top of the PVA layer (see figure 6.5 2) [118]. The thicknesses of both layers is chosen to achieve similar optical contrast like a 300 nm SiO_2 layer on Si [144]. The flake to be transferred is exfoliated on the PMMA layer of the PMMA-PVA-Si chip (see figure 6.5 3). In the next step the PMMA layer is removed from the chip by carefully floating the chip in water so that the PVA layer dissolves while the PMMA layer remains floating on the water surface maintaining the flake surface dry and clean (see figure 6.5 4). Afterwards the floating PMMA layer (see figure 6.5 5) is fished from the water surface with the stamp. This fishing device either consists of a piece of polydimethylsiloxane (PDMS) or a solid ring (out of metal)

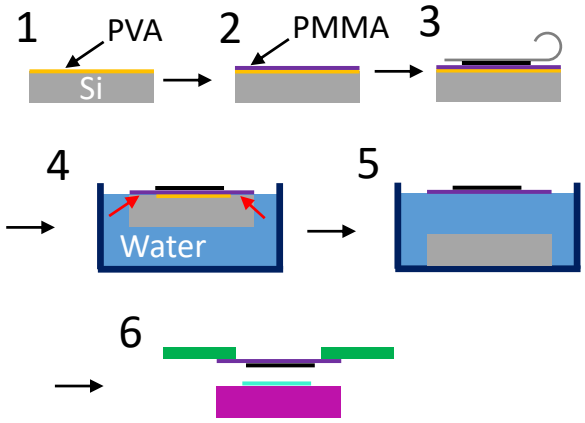

Figure 6.5: PMMA process: 1: Spin coating of a PVA layer (yellow) on a Si chip (gray). 2: Spin coating of a PMMA layer (violet) on top of the PVA layer. 3: Exfoliation of the flake to be transferred (black) on the PMMA layer. 4: Dissolving of the PVA layer (red arrows) by water (blue) in a beaker during which the Si chip is floating. 5: The Si chip sinks down once the PVA layer is completely dissolved. 6: The PMMA membrane (violet) with flake (black) is supported by a fishing device (green) for the transfer onto the target flake (turquoise) on a chip (light violet).

that suspends the PMMA membrane (see figure 6.5 6). The stamp with the flake to be transferred is now prepared for the following transfer process beginning with the alignment of stamp and target flake (see figure 6.5 6 and figure 6.4 3). In early attempts, the PMMA layer is dissolved in acetone [118] to transfer the flake from the stamp onto the target flake once both are aligned in contact (compare figure 6.4 5c). This creates PMMA residues on the flake surface after the transfer. It turned out that a dry transfer with a PMMA membrane is possible as well [145] without the necessity to dissolve the PMMA membrane (compare figure 6.4 5b). This in turn leaves the flake surface very clean as it is not exposed to any solvents, but only comes into contact with the PMMA membrane. For the assembly of a stack consisting of several flakes each flake is transferred one after the other onto the target flake. To this end, a new PMMA membrane has to be fabricated for each flake.

6.6 Copolymer transfer process

To avoid the elaborate fishing step in fabricating the PMMA stamp, another fabrication process has been put foward [146]. The stamp consists of a copolymer that is coated on adhesive tape on a piece of glass. The flake to be transferred is directly exfoliated on the stamp (compare figure 6.4 1a) with the lack of optical contrast during the search for possible flakes to be transferred. To release the flake from the stamp the copolymer is heated up and afterwards dissolved (compare figure 6.4 5c) leading to residues on the flake surface. A dry transfer employing a copolymer stamp is not possible for samples with exposed surface on chip but only if the stack remains on the stamp (compare figure 6.4 6a). By sequentially picking up several flakes with the same stamp a clean graphene sample can be realized by encapsulating it in between two hBN flakes [137].

6.7 PPC transfer process

In [137], polypropylene carbonate (PPC) is used as polymer for the stamp instead of the copolymer used in [146]. The flake to be transferred is either exfoliated on the PPC stamp (compare figure 6.4 1a) or can be picked up by the stamp after exfoliation on a SiO_2 chip (compare figure 6.4 1b and 2b). Using the flake on the stamp, additional flakes can be picked up from several other SiO_2 chips, thereby, creating a stack of flakes on the same stamp. In the last step, the stack is typically released from the stamp by heating the stamp in contact with a substrate and dissolving it (compare figure 6.4 5c). By changing the temperature once the stamp is in contact with the SiO_2 chip, a controlled release without the need to dissolve the stamp could also be achieved [147] allowing for a dry and thereby clean transfer (compare figure 6.4 5b). This makes use of the PPC layers decreasing adhesion to flakes above the glass transition temperature [148]. By preparing the PPC layer with controlled thickness on a separate chip similar to the PMMA process the exfoliation of flakes with good optical contrast is possible as well [148]. After the exfoliation, the PPC layer can be mechanically removed from the chip. In a further development [149–151], the PPC layer is removed by annealing it at 375 °C. This opens up the possibility to flip a stack upside down by placing the PPC membrane on a chip with the stack on top instead of the reversed stack in between PPC membrane and chip if directly released from the PPC membrane.

6.8 QHE results on hBN samples

Graphene prepared on hBN show much higher quality compared to graphene prepared on SiO_2. Mobilities up to $100.000\,cm^2/Vs$ and residual charge carrier densities of $7 \cdot 10^{10}\,cm^{-2}$ are reported [118]. In the QHE the lifting of spin and valley degeneracy is observed at lower magnetic fields of B 5 T in one of the first reports [24] and not only in LL0 but also in higher LLs [24, 27]. In a recent publication [152], this happens at $B \approx 2\,T$ in samples with similar structure. Lower magnetic fields being required to observe the degeneracy lifting imply the observation of smaller energy gaps in line with decreased disorder potential. At higher magnetic fields of $B = 20 - 35\,T$ the fractional Quantum Hall effect (FQHE) is observed in one of the first reported graphene-hBN samples [23]. FQHE states are formed by quasi particles called composite fermions that result from strong correlation of charge carriers. The already mentioned encapsulation of a graphene flake between two hBN flakes [137] protects the graphene not only from substrate induced disorder but also from transfer process related debris. Further improvement in sample quality could be achieved by using a graphite back gate instead of the Si [28] making the FQHE readily observable at lower magnetic fields $B \sim 5 - 10\,T$ and the spin and valley degeneracy lifting below $B < 1.5\,T$ in [28]. The graphite back gate consists out of a graphite flake that is placed in between the hBN flake and the SiO_2 surface and by that screens the charge inhomogeneity of the SiO_2. Additionally, the imposed SiO_2 corrugation on the graphene is reduced due to the cleaved, atomically flat graphite surface and graphite-hBN-interface. Such high quality samples also allow for the observation of superconductivity in magic angle twisted bilayer graphene (MATBG) [153] as well as the electrostatic formation of quantum dots (QDs) in bilayer graphene [154].
For QHE measurements, the edges of the samples remain a source of disorder that strongly affects the edge channels which are probed in a transport experiment. Consequently measurements that probe the bulk of the sample show better results. The Corbino geometry is used to perform transport experiments excluding edge channel transport [150, 151]. The edge disorder is also reduced by replacing the physical edge of the sample by an electrostatically created edge in the interior of the sample to probe the edge channels [32]. Both sample designs also include a graphite top gate resulting in the graphene flake in addition to hBN also being encapsulated by two graphite gates. This additionally reduces the charge disorder and the residual charge carrier density reaches $5 - 6 \cdot 10^{10}\,cm^{-2}$ [150, 151]. These samples exhibit degeneracy lift of the LLs for $B < 1\,T$ and the FQHE at magnetic fields $B \sim 2 - 5\,T$. Another possibility is to perform capacitance measurements of the bulk sample by which even denominator FQHE states have been observed that can not be explained by composite fermions [25]. Also these samples have two graphite gates. Currently, the best graphene samples reported in the literature employ encapsulation both with hBN flakes and graphite top and back gates [25, 26, 32, 150, 151].

6.9 Further improvements in fabrication

Despite the great advantages in preparing graphene on hBN, new problems arise from the transfer process itself. Residues of the exfoliation process or moisture and airborne hydrocarbons aggregate in micron sized bubbles in between flakes. The areas in between bubbles exhibit a self cleaning property which moves residues into the bubbles [125, 145]. The bubbles cause roughness as well as charge and strain disorder in graphene on hBN diminishing the quality. Much effort has been put to avoid the formation of bubbles during the transfer process. It turns out that it is possible to manipulate the bubbles by increasing the temperature up to 180 °C during the transfer and to push them towards the flake edge to eliminate them [155]. The elevated temperature requires to use a different polymer with a higher glass transition temperature. In addition, sub nanometer corrugations in a stack of flakes lead to strain disorder [156]. The strain disorder is reduced by annealing the fully assembled stack at 500 °C and employing contact mode atomic force microscopy (AFM) ironing afterwards [157, 158]. This can improve the mobility of an individual sample by up to one order of magnitude. Thereby, it increases the yield of high quality samples during fabrication whereas the maximum of possibly achievable mobility is not exceeded. The micron sized bubbles however can not be manipulated by this method.

6.10 Sample fabrication for STM

All processes described above are developed for transport measurements and must be adapted to the needs of STM measurements accordingly. Since encapsulation, frequently used for transport experiments, can not be used for STM investigations, contaminations either have to be avoided by a dry transfer method or removed afterwards. Most graphene-hBN samples for STM experiments are fabricated employing the PMMA method both in wet (dissolving the PMMA) and dry way [52, 55, 56, 124, 131, 159–162]. The dry release PPC method is used as well [82]. In the light of intense research of the superconductivity in MATBG, many fabrication processes for STM suitable samples of stacked vdW flakes appeared. In [163–165], the stack is assembled on a stamp similar to the PPC process (see section 6.7) in reverse order. To flip the stack it is transferred to a PDMS stamp that is used to drop the stack on a chip [163, 165]. During this step the top surface (graphene) of the stack that is to be investigated by STM is in contact to the PDMS stamp possibly resulting in contamination. To omit the flip process with the PDMS stamp, the stack can remain on the polymer [164], where the polymer layer including the stack is placed on a chip with graphene as top layer. The chip is used as a back gate. In some samples, the polymer is then removed by annealing [150, 151, 165]. This process is used for experiments except MATBG as well [29, 65, 166, 167]. In particular in [65], the PPC method is employed to fabricate graphene-hBN stacks, and also the PDMS flip process of [163] is used to flip the stacking order. The PPC can be replaced by PVA as well [66, 168]. The stacks are either assembled in reverse order and flipped by transferring them on a PDMS stack or are assembled in correct order and placed on the target chip by dissolving the PVA layer with water. Using both versions of the PVA method in [66], graphene-hBN-graphite stacks are prepared that feature a graphite back gate.

Residues from the (wet) transfer process or electrical contacting are removed by solvents like isopropyl alcohol or acetone. Additionally, samples can be annealed in Ar/H_2 atmosphere [161, 169] or in UHV [29, 65, 124, 131, 159, 160] to remove contaminations. Considering possible options to fabricate high quality samples and neglecting the processes in which the graphene surface is exposed to wet chemicals, only the dry PMMA method and the PPC method remain. The PPC method has the practical advantage compared to the PMMA method, that the stack can be assembled on the PPC stamp by picking up the flakes from a SiO_2 substrate on which they are exfoliated. The SiO_2 substrate can easily be cleaned prior exfoliation by standard procedures and offers a good optical contrast to identify flakes with the correct layer number. After stacking, the PPC layer should be removed by annealing [150, 151, 165], because this way additional contact between the graphene surface and the otherwise needed PDMS stamp is avoided. This procedure is meanwhile often used to fabricate samples for STM experiments of 2D materials [29, 65, 165–167].

6.11 Electrical contacting

Graphene samples for transport measurements are typically electrically contacted by lithographically defined metal leads. This involves polymer resists to cover certain parts of the sample that is removed in a lift-off process. This method to contact samples offers the advantage of great flexibility and low contacts resistances in particular for one dimensional contacts in encapsulated graphene samples [137]. The flexibility allows to adjust the contact lines for each sample individually considering the randomly shaped 2D materials flakes. As in the transfer process, the polymer resist leaves residues after it is dissolved. Since STM suitable samples, however, require a clean surface, lithographically defined contacts are not the best method. Nevertheless, graphene samples for STM measurements are commonly contacted by lithographic defined contacts [29, 65, 131, 159, 160].
Micro soldering offers an alternative contacting method: A μm sized wire of a solder material like indium or Fields metal is molten directly on the sample that for this purpose is heated above the solders melting point [128, 164, 170]. By micro soldering, samples can be electrically contacted in a clean way, since the surface is not covered by any polymer resist. At the same time, micro soldered contacts can be flexibly adjusted to each sample geometry. Moreover, the method is applicable to samples prepared on polymer as substrate that can not be contacted by lithography [164, 171]. The drawback of this method besides challenging practice are unstable and high contact resistances due to an oxide layer formed on the solder [108, 171]. Consequently, it is rarely used [128, 164].
A third method to contact graphene samples is shadow mask evaporation [172–174]. A shadow mask is placed on the sample (see figure 6.6b) while the contacts are deposited by evaporating a metal (see figure 6.6c). The areas of the sample in the shadow of the mask are only exposed to possible contamination from the mask itself or via diffusion from the remaining parts of the sample (see figure 6.6d). Oxide layers in the contacts are prevented by vacuum during evaporation giving stable and low contact resistances. For each geometric configuration of contacts, however, a different shadow mask is needed. Additionally,the geometry of a common shadow mask has to be taken

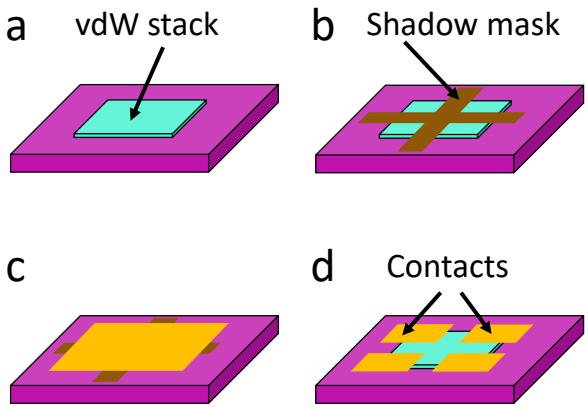

Figure 6.6: Electrical contacting with a shadow mask: a: A vdW stack (turquoise) on a chip (light violet) to be electrically contacted. b: A shadow mask (brown) is aligned to the vdW stack and fixed on the chip. c: A metal (yellow) is evaporated on the chip and through the shadow mask. d: After removal of the shadow mask, electrical contacts (yellow) remain on the vdW stack while the surface of the stack covered by the shadow mask is still exposed for STM measurements.

into account during the assembly of each graphene sample. Many different materials are used as shadow mask ranging form wires [75, 172] or grids with fixed geometry [174] to customized membrane masks made out of Cr coated Si [173] or PMMA [175]. The shadow mask method is occasionally reported for STM investigations [75, 78, 162, 176]. Instead of contacting the graphene sample after assembly, the contacting can also be part of the assembly itself by transferring the vdW stack on predefined contacts on the substrate (see figure 6.7) [55, 56, 66, 163, 165, 166]. These contacts are fabricated by lithography such that contamination left on the contacts is not diminishing the surface cleanliness (see figure 6.7a). Since the sample fabrication is finalized by transferring the vdW stack on the contacts (see figure 6.7b and c) no further processing causing any contamination is performed leaving the sample surface as clean as possible (see figure 6.7d). In order to contact different constituents of the sample special care has to be taken during design and assembly of the vdW stack so that different parts are exposed to the contacts. The flexibility of this method is similar as the shadow mask technique either requiring customized predefined contacts for each sample or awareness during vdW assembly. Precise alignment of vdW stack and contacts during the transfer is required as well (see figure 6.7b and c).

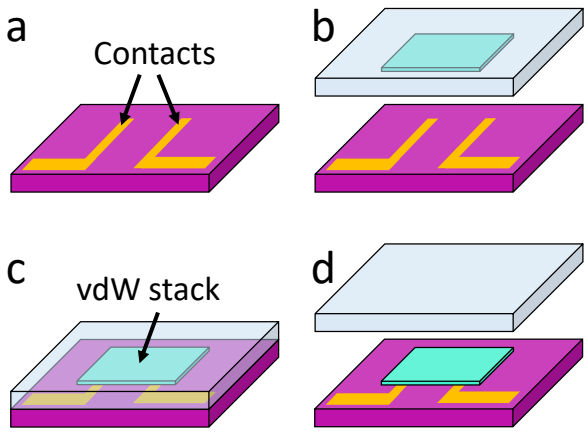

Figure 6.7: Transfer of a vdW stack on prepatterned contacts: a: Electrical contacts (yellow) are patterned on a chip (light violet). b: A vdW stack (turquoise) on a stamp (light blue) is aligned to the contacts on the chip. c: The vdW stack is transferred onto the chip. d: After removal of the stamp, the vdW stack rests on the electrical contacts.

7 Own fabrication and characterization

The graphene sample GR10BN24 has been prepared in the course of my master thesis [171]. The aim was a study of symmetry broken quantum Hall states [65, 66, 177] or the FQHE similar to [178] in graphene combining STM/STS and transport experiments. Transport measurement have already been conduced and the sample indeed exhibits symmetry breaking in the QHE [171]. This sample is employed for further transport and STM measurements presented in this chapter.

7.1 Fabrication process of a stack of flakes

The fabrication based on the PMMA process (see section 6.5) is in detail described in [171, 179], where also earlier transport results are shown. In the following, a brief description of the fabrication process is given. The sample consists of a graphene flake on a hBN flake on a SiO_2/Si chip (see figure 7.1a). Commercial hBN flakes are exfoliated on $4 \times 4\,mm^2$ Si chips with 300 nm of SiO_2 on the surface by using wafer backing tape (see figure 6.3). PVA (4 weight %) and PMMA (950k) are spin coated on $7 \times 7\,mm^2$ Si chips which are used for the exfoliation of graphene flakes from bulk graphite (see figure 6.2). Standard semitransparent pressure-sensitive tape is used for this purpose. After the exfoliation, the PMMA layer at the edge of the chip is scratched and the chip is put in a water filled beaker in such a way that the chip floats on the water

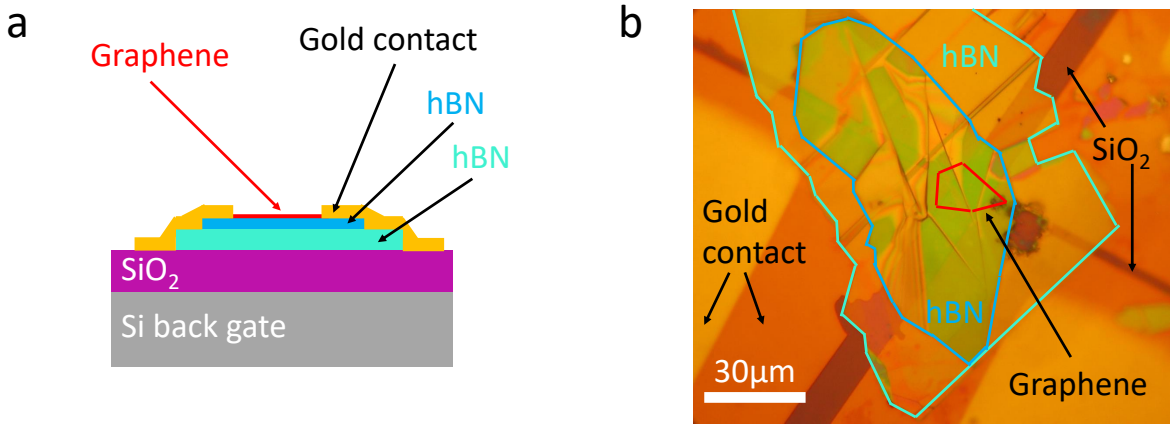

Figure 7.1: a: Schematic sketch of the graphene sample GR10BN24 consisting of a graphene flake (red) on top of a hBN flake (blue and turquoise) on a Si/SiO_2 chip (violet/gray). b: Optical image of the sample with deposited contacts. The flakes are outlined with the same colours as in subfigure a.

surface with the PMMA layer on top. Once the PVA is dissolved by the water, the Si chip sinks down and the PMMA layer remains floating on the water surface. As fishing device and stamp in the following transfer process, a glass slide with a piece of PDMS glued onto it by standard transparent pressure-sensitive tape is used. The PMMA layer with the graphene flake is recovered from the water surface with this fishing device. The dry transfer of the graphene flake from the PMMA layer to the hBN flake on the Si/SiO_2 chip is done with a mask aligner. The fishing device is mounted upside down as the stamp. Both flakes are optically aligned and brought into contact by pressing the chip onto the fishing device while heating the stage to $T = 60\,°C$. Afterwards chip and stamp are separated again such that the graphene flake is transferred from the PMMA layer to the hBN flake, if the process was successful. The experience shows that for a successful transfer the hBN flake should be at least about twice as large as the graphene flake, because otherwise the hBN flake can be transferred to the PMMA layer by the graphene flake. During the fabrication process of graphene sample GR10BN24, this occurred. To solve this issue, the graphene-hBN stack was transferred from the PMMA layer to a larger hBN flake on the Si/SiO_2 chip. After the transfer, the graphene-hBN-stack has to be electrically contacted to allow for transport and STM measurements (see section 7.2).

7.2 Shadow mask for electrical contacting

The electrical contacting of the graphene sample is done via shadow mask evaporation (see section 6.11). The process described in [171, 179] has been further improved as described in [180, 181]. The main concept follows below. A commercial fine mesh grid made out of copper serves a shadow mask [174]. Such grids are available in different geometries and sizes. The fine mesh grid is intended as sample holder for transmission electron microscopy (TEM) and called TEM grid. Here, square TEM grids with bars

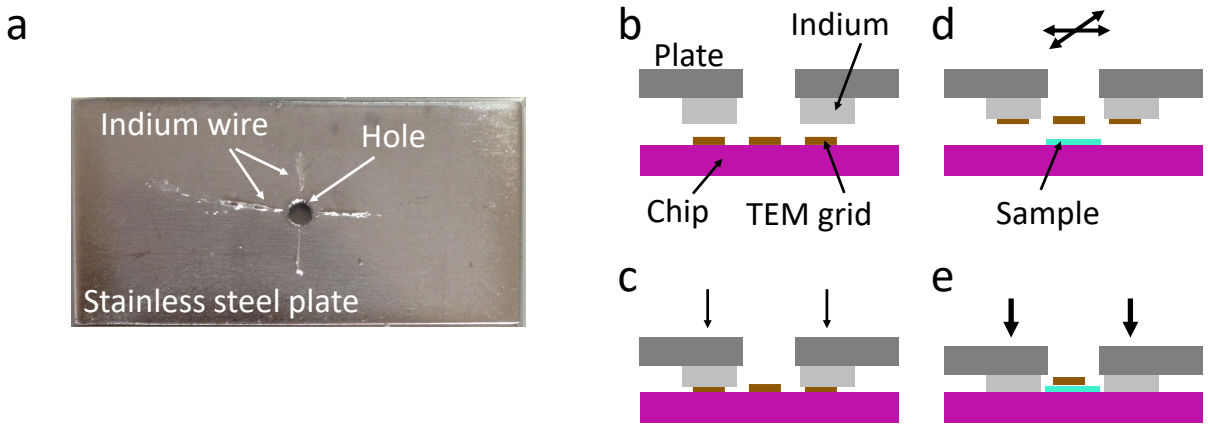

Figure 7.2: a: Image of a stainless steel plate with four indium wires [180]. b to e: Process to fix a shadow mask on a graphene sample. b: Align plate with indium wires to TEM grid. c: Press TEM grid in indium wires. d: Align TEM grid to sample. e: Press TEM grid and indium wires onto sample.

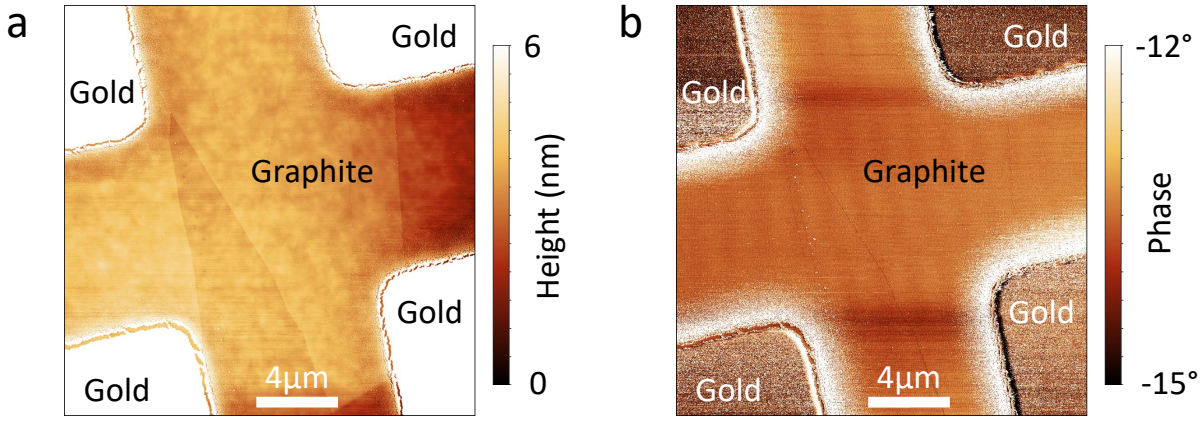

Figure 7.3: a: AFM topography of gold contacts (80 nm thickness) evaporated through a shadow mask on a graphite flake exfoliated on a Si/SiO_2 chip (tapping mode at ambient conditions). The evaporation time is less than 15 s while the sample is cooled below $T = 100$ K. b: Corresponding phase image.

of $5 - 80\,\mu$m width are used in a sequence of two evaporations. Firstly, a grid with narrow bars contacts the graphene flake. Secondly, a wider grid creates contact pads large enough to glue bond wires on them. For the shadow mask evaporation the shadow mask has to be placed above the graphene sample. To this end, a stainless steel plate of similar dimensions as a glass slide with a hole of 1 mm diameter is prepared. Four indium wires are placed in radial direction around the hole via micro soldering [170] (see figure 7.2a). This metal plate is mounted with the indium wires pointing down in the mask aligner and approached to the TEM grid placed on a chip (see figure 7.2b). By the softness of the indium, the TEM grid (and likely the chip as well) can be picked up by pressing the chip with the TEM grid gently against the indium wires as depicted in figure 7.2c and removing it afterwards. The empty chip is easily removed by tweezers. In the next step (see figure 7.2d), the metal plate with TEM grid is aligned to the graphene sample by the mask aligner. Afterwards the chip with the graphene sample is pressed with more force into the indium wires to ensure a stable mechanical contact and a small distance between shadow mask and graphene surface to reduce the penumbra (see figure 7.2d). A precision of a few μm is achieved that is limited by the restricted optical access of the sample through the nontransparent parts of the shadow mask and by uncontrolled movement of the grid while pressing and thereby deforming the indium wires. The metal plate with the TEM grid and graphene sample is loaded into a UHV chamber [179] with a home-built thermal gold evaporator [180]. In order to reduce the diffusion of gold particles below the grid into the shadow area, a fast deposition rate of more than 2 nm/s is selected and (if required) the sample is cooled below $T = 100$ K using a liquid nitrogen bath. With both methods, a diffusion length of gold particles in the shadow area of about $2\,\mu$m on graphite is achieved [181] where an example is presented in figure 7.3. The area around the gold contacts in which gold particles diffuse is in particular visible in the phase image in figure 7.3b. The central part of the graphite flake remains very clean allowing to resolve step edges of about 0.5 nm height of the graphite flake as well as the roughness of the underlying SiO_2

substrate in figure 7.3a. The diffusion of gold particles on graphite is similar to the diffusion on graphene-hBN stacks [182]. The diffusion length of 2 μm makes it possible to use grids with small bars of 7 μm width to prepare well defined contacts with a clean graphene surface in between. This technique is employed for several samples [183, 184] including the pn sample present in chapter 5. For the graphene sample GR10BN24 (see figure 7.1b), glass fibers instead of TEM grids serve as shadow mask [172]. The glass fibers are attached to the sample by a piece of PDMS with a hole in it replacing the stainless steel plate. The evaporation is done at room temperature.

7.3 Charge transport measurements: QHE

Parts of this section have been published in [98]:

An ultrahigh-vacuum cryostat for simultaneous scanning tunneling microscopy and magneto-transport measurements down to 400 mK
M. Liebmann, J. R. Bindel, M. Pezzotta, S. Becker, F. Muckel, T. Johnsen, C. Saunus, C. R. Ast, and M. Morgenstern
Rev. Sci. Instrum. **88**, 123707 (2017)

Transport measurements are carried out to characterize the prepared sample and to make the measurements easily comparable to experiments reported in the literature (see section 6.8 and [23–25, 27, 28, 32, 118, 151]). Both the 003 setup (see section 3.4) and a transport setup ($T_{\mathrm{min}} = 0.3\,K, B_{\mathrm{max}} = 10\,T$) [108] have been employed for these measurements (see section 3.6). The sample GR10BN24, shown in figure 7.1b, features two electrical contacts on the graphene flake leading to the two point configuration that includes contact and line resistances. The resistance $R_{2\mathrm{p}}$ as a function of the back gate voltage V_{bg} tuning the charge carrier density is shown in figure 7.4. It allows to

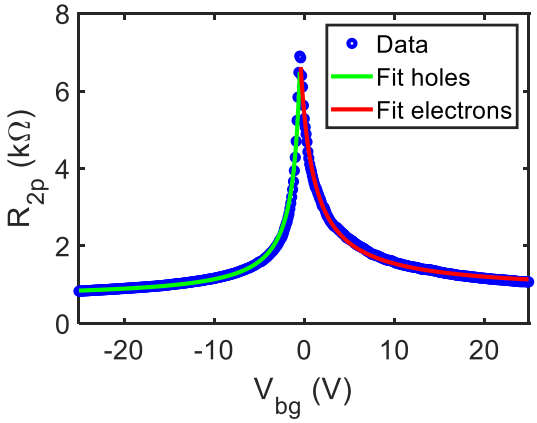

Figure 7.4: Two-point resistance $R_{2\mathrm{p}}$ of graphene sample GR10BN24 depending on V_{bg} (blue). Green and red lines are fits of equation 7.2 giving the mobilities $\mu \approx 25.000\,\mathrm{cm}^2/\mathrm{Vs}$ for holes and $\mu \approx 15.000\,\mathrm{cm}^2/\mathrm{Vs}$ for electrons, respectively. $V_{\mathrm{sd}} = 100\,\mu\mathrm{V}$, $T = 0.5\,\mathrm{K}$, $B = 0\,\mathrm{T}$.

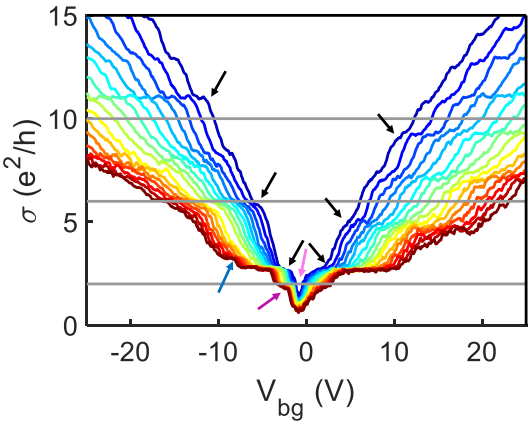

Figure 7.5: Two-point conductance σ_s of graphene sample GR10BN24 for $B = 1.3, 1.5, \ldots, 4.3\,\mathrm{T}$ (blue to red). Gray horizontal lines indicate the expected conductance plateaus at $2\,e^2/h$,$6\,e^2/h$, and $10\,e^2/h$ according to formula 2.13. Black arrows show the position of the corresponding experimental plateaus. Pink, violet and blue arrows show plateaus of symmetry broken states at $\nu = 0$, $\nu = -1$ and $\nu = -3$, respectively. Unfortunately, the recorded I_{sd} has an offset due to incorrect settings of the lock-in amplifier. To compensate for that, the minimum conductance measured at $B = 14\,\mathrm{T}$ is subtracted from the curves as an offset. $V_{sd} = 100\,\mu\mathrm{V}$, $T = 0.5\,\mathrm{K}$.

extract the charge carrier mobility both for electrons and holes. To this end, equations 2.3 and 2.4 are combined and extended by a line and contact resistance R_{line} as well as the offsets $V_{bg,0}$ and $n_{s,0}$:

$$R_{2p} = R_{line} + \frac{L}{W} \cdot \frac{1}{\sigma_s} \tag{7.1}$$

$$= R_{line} + \frac{L}{W} \cdot \frac{1}{e\mu} \frac{ed_C}{\epsilon\epsilon_0 |V_{bg} + V_{bg,0}| + ed_C\, n_{s,0}} \tag{7.2}$$

where L and W describe the length and the width of the graphene sample, respectively. The offset $n_{s,0}$ at charge neutrality, that is at $V_{bg} + V_{bg,0} = 0\,\mathrm{V}$, results from charge inhomogeneity in the sample. Fitting equation 7.2 separately for electrons and holes to the resistance curve of figure 7.4 reveals that at $T = 0.5\,\mathrm{K}$ the holes have a mobility of $\mu \approx 25.000\,\mathrm{cm}^2/\mathrm{Vs}$ and the electrons of $\mu \approx 15.000\,\mathrm{cm}^2/\mathrm{Vs}$. The residual charge carrier density is $n_{s,0} \approx 7 \cdot 10^{10}\mathrm{cm}^{-2}$. The SiO_2 and hBN layers enter with the same $\epsilon = 4$ and a total thickness of $d_C = 480\,\mathrm{nm}$. The aspect ratio of the sample is set to $L/W = 1$.

At magnetic fields as low as $B = 200 - 300\,\mathrm{mT}$, Landau quantization of the charge carriers sets in (see section 2.3) and the electrical conductance forms a plateau close to charge neutrality (not shown). For larger B the measured two point conductance should ideally show quantized values $\sigma_{2p} = |[\nu]|e^2/h$ on the plateaus (see equation 2.13) where the charge carriers are transported by the edge channels. Because of the contact and lines resistances R_{line} included in the two point measurement the resistance R_{2p} is larger and the conductance values on the plateaus should exhibit lower values than $|[\nu]|e^2/h$. The measurements shown in figure 7.5 display in contrast larger conductance σ_s for hole transport and lower values only for electron transport except $\nu = +2$. Unfortunately, the recorded I_{sd} has an offset due to incorrect settings of the lock-in

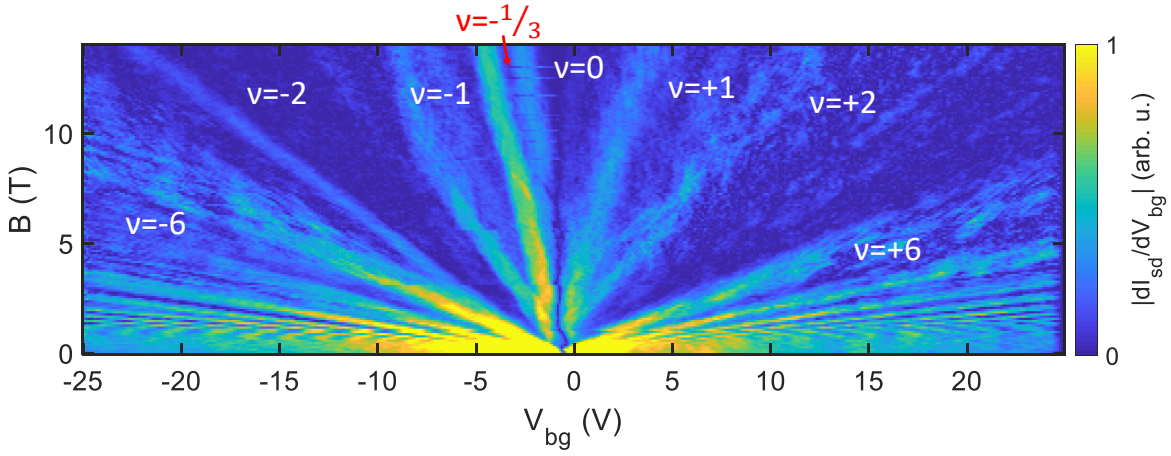

Figure 7.6: Measurement of $|dI_{\mathrm{sd}}/dV_{\mathrm{bg}}|(V_{\mathrm{bg}}, B)$ of graphene sample GR10BN24. The derivative is performed numerically and the data is smoothed afterwards. The red arrow indicates the fractional $\nu = 1/3$ plateau. $V_{\mathrm{sd}} = 100\,\mu\mathrm{V}$, $T = 0.5\,\mathrm{K}$.

amplifier. To compensate for that, the minimum conductance measured at $B = 14\,\mathrm{T}$ is subtracted from the curves in figure 7.5 as an offset. For the $\nu = \pm 2$ plateau the conductance is larger for both electrons and holes. Depending on the samples aspect ratio L/W, however, the conductance values on the plateaus can turn out larger (for wide samples) or smaller (for long samples) than $|[\nu]|e^2/h$ [185]. The opposite deviation from the $|[\nu]|e^2/h$ values on the plateaus for electron and holes could be caused by the different edges of the sample along which electrons and holes are transported due to the chirality of the edge channels. Due to different amounts charged impurities or folds and bubbles close to the different edges the sample might have a different effective aspect ratio than the the sample geometry. This effect should not be encountered in an AC measurement as performed here, however, a small DC offset makes it observable anyways.

A Landau fan up to magnetic fields of $B = 14\,\mathrm{T}$ measured at a temperature of $T = 0.5\,\mathrm{K}$ is shown in figure 7.6. The absolute value of the derivative of the source drain current $|dI_{\mathrm{sd}}/dV_{\mathrm{bg}}|(V_{\mathrm{bg}}, B)$ is plotted. Since $I_{\mathrm{sd}} \sim \sigma_{\mathrm{s}}$, the derivative highlights transitions between conductance plateaus. The central part of the Landau fan is presented in figure 7.7a in dependence of the filling factor ν such that the development of an individual ν with increasing B is tractable. The spin valley degeneracy of LL0 starts to be lifted at magnetic fields of about $B \approx 1\,\mathrm{T}$ (see pink arrow in figures 7.5 and 7.7a) where the conductance develops a minimum at charge neutrality (see section 2.4). The minimum corresponds to the $\nu = 0$ state that does not feature edge channels and makes the sample insulating [186]. It appears if the valley degeneracy of LL0 is lifted and LL0 splits into two. The total fourfold degeneracy of LL0 is lifted at $B \approx 1.6 - 1.7\,\mathrm{T}$ where an additional conductance plateau associated with $\nu = -1$ becomes visible below the $\nu = -2$ plateau (see violet arrow in figures 7.5 an 7.7a) [24, 27]. At about $B \approx 3\,\mathrm{T}$ an additional plateau appearing above the $\nu = -2$ plateau indicates the degeneracy lifting in LL-1 (see blue arrow in figures 7.5 an 7.7a). Another plateau develops at about $B \approx 8\,\mathrm{T}$ that is shown by a red arrow in figure 7.7a and b. The conductance of this plateau has a value of about $\frac{1}{3}$ of the $\nu = -1$ plateau as can be seen in figure 7.7b

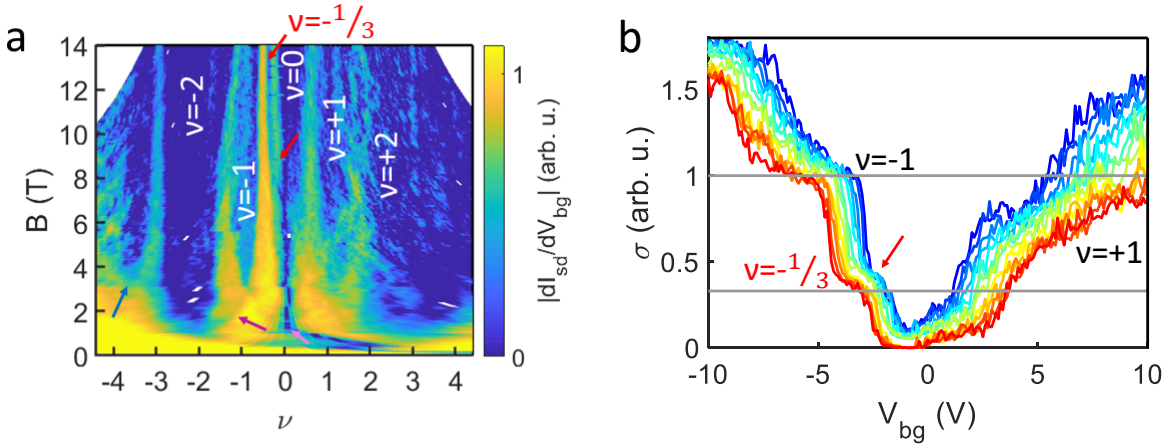

Figure 7.7: a: $|dI_{\mathrm{sd}}/dV_{\mathrm{bg}}|(\nu, B)$ of graphene sample GR10BN24. The derivative is performed numerically and the data is smoothed. Pink, violet and blue arrows show plateaus of symmetry broken states at $\nu = 0$, $\nu = -1$ and $\nu = -3$, respectively. The red arrow indicates the fractional $\nu = -1/3$ plateau. b: Rescaled two-point conductance σ_{s} of graphene sample GR10BN24 for $B = 8, 8.5, \ldots, 14\,\mathrm{T}$ (blue to red). Gray horizontal lines indicate the conductance plateaus at 1 arb. u. and 1/3 arb. u., respectively. The red arrow shows the position of the 1/3 plateau. Unfortunately, the recorded I_{sd} has an offset due to incorrect settings of the lock-in amplifier. To compensate for that, the minimum conductance measured at $B = 14\,\mathrm{T}$ is subtracted from the curves as an offset. $V_{\mathrm{sd}} = 100\,\mu\mathrm{V}$, $T = 0.5\,\mathrm{K}$.

where the conductance is rescaled to be $\sigma_{\mathrm{s}} = 1$ arb. u. on the $\nu = 1$ plateau. This plateau is attributed to the fractional Quantum Hall effect (FQHE) [23, 67, 134, 187, 188]. A direct evidence in terms of the quantized $R_{xy} = \frac{1}{3}e^2/h$ is not possible due to the only two electrical contacts. However the appearance at a higher magnetic field and the conductance value of about $\frac{1}{3}$ of the $\nu = -1$ plateau make this conclusion plausible.

In total, four samples prepared by the same method show similar characteristics in transport experiments (see figure 2.6) [171, 179]. At a temperature of $T = 0.3\,\mathrm{K}$ the observed mobilities range up to $\mu = 50.000\,\mathrm{cm}^2/\mathrm{Vs}$ and the Landau quantization sets in at $B = 150\,\mathrm{mT}$, whereas LL0 is fully split at $B = 3\,\mathrm{T}$. The achieved quality of the QHE for these samples is similar to samples in the literature that consist of a graphene on a hBN flake supported by a SiO_2 substrate [24, 27], even though the charge carrier mobility of $\mu = 25.000\,\mathrm{cm}^2/\mathrm{Vs}$ of the sample GR10BN24 is lower than reported mobilities of up to $\mu = 100.000\,\mathrm{cm}^2/\mathrm{Vs}$ [23]. All these samples show symmetry breaking of the LLs at moderate magnetic fields and fully split LLs at $B = 14\,\mathrm{T}$. The FQHE is however not regularly achieved at moderate magnetic fields, but only at very high magnetic fields [23]. This eventually led to the integration of a graphite back gate into transport samples [28] (see section 6.8).

7.4 STM and STS measurements

The measurements in this section are carried out in the 003 setup (see section 3.4) at a temperature $T = 7.5 - 21\,\mathrm{K}$ and at magnetic fields up to $B = 14\,\mathrm{T}$. The tip is approached to the sample via the EFM method after optical alignment (see sections 4.4 and 4.2). The atomically resolved topography in figure 7.8a reveals the Moiré lattice between the graphene layer and hBN substrate with a lattice constant of $\lambda = 1.8\,\mathrm{nm}$, which correlates with a rotation angle of 7.8° [117].
Figure 7.8b shows a $dI/dV_{\mathrm{sample}}(V_{\mathrm{bg}}, V_{\mathrm{sample}})$ measurement at a fixed position at a magnetic field of $B = 7\,\mathrm{T}$ and a temperature of $T = 16 - 21\,\mathrm{K}$. This measurement equals the one presented in section 5.2 (see figure 5.3a). The LL features show the expected energy sequence (see equation 2.6) and the staircase pattern upon increasing occupation caused by the pinning of E_{F} in the high DOS of the LLs. Charging lines (CLs) appear at the transition between LLs, namely at its right side. This shows that a QD is present below the tip. The slope of the CLs is $m_{\alpha}^{\mathrm{CL}} \approx 0.08$ and much lower than $m_{\alpha}^{\mathrm{CL}} = 0.2 - 1$ in section 5.2. This is due to the large distance to the back gate $d_{\mathrm{C}} = 480\,\mathrm{nm}$ compared to $d_{\mathrm{C}} = 23.5\,\mathrm{nm}$ in section 5.2. It leads to a lower back gate capacitance C_{bg} and accordingly to smaller $m_{\alpha}^{\mathrm{CL}} = -C_{\mathrm{bg}}/C_{\mathrm{tip}}$ (see equation 2.44). Also C_{tip} might be different because it strongly depends on the tip shape. In contrast to section 5.2, the CLs appear at the left end of each LL plateau at E_{F} only rendering the QD electron-like [54] (see figure 2.12). $\Delta_{\mathrm{wfm}} > 0\,\mathrm{V}$ is accordingly positive and is estimated based on the observation that there are no CLs appearing at the transition between LL1 to LL2. Here, the band bending below the tip is small and the QD ceases to exist and thereby the CLs. This implies that $V_{\mathrm{tip,eff}} \approx 0\,\mathrm{V}$ (see equation 5.9) is nearly vanishing such that $\Delta_{\mathrm{wfm}} \approx \mu_{\mathrm{c,gr}}$ for $V_{\mathrm{sample}} = 0\,\mathrm{V}$. Accordingly, $\Delta_{\mathrm{wfm}} \approx 100 - 140\,\mathrm{mV}$ because $\mu_{\mathrm{c,gr}}$ is in between the LL energies of LL1 and LL2 at $B = 7\,\mathrm{T}$.

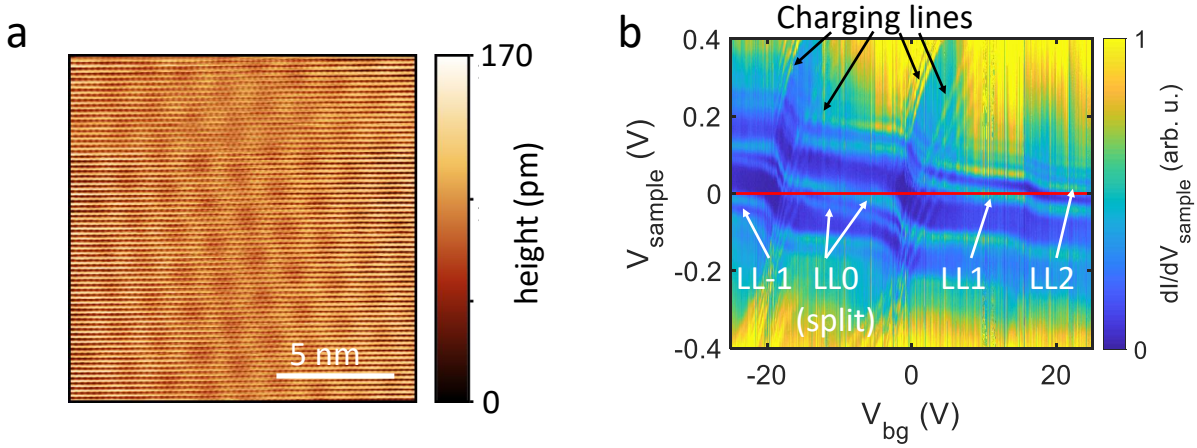

Figure 7.8: a: Atomically resolved topography of graphene on hBN. $V_{\mathrm{sample}} = -500\,\mathrm{mV}$, $I = 150\,\mathrm{pA}$, $V_{\mathrm{bg}} = -39.95\,\mathrm{V}$, $B = 14\,\mathrm{T}$. b: dI/dV_{sample} measurement of graphene sample GR10BN24 on a single spot for varying V_{bg}. The LL states appearing with high intensity are labeled according to their indices. Charging lines are marked with black arrows. E_{F} is shown as a red line. $B = 7\,\mathrm{T}$, $T = 16 - 21\,\mathrm{K}$, $V_{\mathrm{sample}}^{\mathrm{stab}} = -500\,\mathrm{mV}$, $I^{\mathrm{stab}} = 150\,\mathrm{pA}$, $V_{\mathrm{sample}}^{\mathrm{mod}} = 10\ \mathrm{mV}$, $f^{\mathrm{mod}} = 654.5\,\mathrm{Hz}$.

For LL0 and LL1 states, CDs are also observed as the CLs cross E_F. They appear in groups of four again highlighting the fourfold spin and valley degeneracy in graphene. The LL0 plateau at E_F is split into two levels separated by about 40 mV as also seen for the totally unoccupied LL0 feature ($V_{bg} < -18$ V) but not for the completely filled LL0 feature ($V_{bg} > 2.5$ V). This splitting is also observed in smaller extent for LL1 states but not for other LL states in this measurement. For a Zeeman splitting of the different spins in a magnetic field the gap is too large and should be seen independent of filling factor with the same gap. Interestingly, only the lower of the two LL0 states exhibits CDs when crossing E_F.
A possible origin could be different m states of the QD (see section 2.7) which are also seen for LL0 in the measurements of section 5.2 (see figure 5.3c) and at the pn interface in section 5.10. If the tunneling center of the tip is not aligned to the QD center, several m states can be measured in addition to the centered $m = 0$ state. The splitting of the LL0 feature disappears once the LL0 states are occupied and sit below E_F. This could be explained by a decreasing $V_{tip,eff}$ for this V_{bg} range such that the QD and with it the m states no longer exist. Inconsistent with the m state explanation is however the intensity distribution between the individual split LL0 levels. The $m = 0$ level is assumed to have higher intensity than the other m states. This is indeed observed in the measurements of figure 5.3c, where the brightest $m = 0$ state has the highest energy in the hole-like QD. For an electron-like QD the $m = 0$ state with the highest intensity should have lowest energy but the opposite is observed in the measurement.
The sublattice dependence of the LL0 wave function that is restricted to only one sublattice for each valley offers another possible reason for the splitting of LL0. A substrate induced breaking of the sublattice symmetry results in one valley to be favoured in energy in comparison to the other [46, 47, 56]. This results in a split LL0 where the intensity of the split LL0 levels depends on the measurement position with respect to the sublattice. Additionally the energy difference changes within the Moiré unit cell [46, 56]. Overall, the measurements of figure 7.8b show that the sample has a similar quality like the one in section 5.2 fabricated at the University of Manchester or the sample in [52].

7.5 STM and STS measurements at B=14 T

Making use of the 003 setup, the sample is further investigated at a magnetic field of $B = 14\,T$ by repeating the $dI/dV_{sample}(V_{sample}, V_{bg})$ measurement as shown in figure 7.9. As a results of the doubled magnetic field, the LL energies (see equation 2.6) are increased as well as the V_{bg} range of the LL0 plateau at E_F due to the increased degeneracy of each LL (see equation 2.9). The point of nearly vanishing $V_{tip,eff}$ is already reached at the LL0 to LL1 transition ($V_{bg} \approx 5 - 9$ V). Consistently, for $V_{bg} > 10$ V no CLs appear indicating the matching work functions of tip and graphene resulting in a non existent QD. CLs are most prominent at the LL-1 to LL0 transition, where well resolved CDs appear ($V_{bg} < -28$ V). CLs exhibit larger intensity for more negative V_{sample} which increased the QD depth (see figures 5.7a and 5.10). As in section 5.2, CLs are seen through out the LL0 plateau at E_F in figure 7.9, evidencing insulating properties of the graphene bulk.
In both transitions left and right of the LL0 plateau at E_F, the LLs show a non

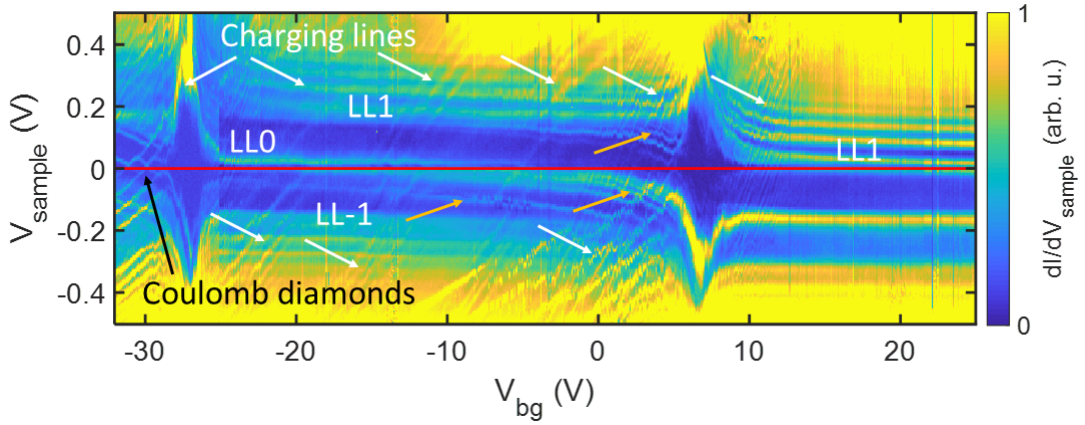

Figure 7.9: $dI/dV_{\text{sample}}(V_{\text{sample}}, V_{\text{bg}})$ measurement of graphene sample GR10BN24. The data is recorded at two different spots for $V_{\text{bg}} < -25\,\text{V}$ and $V_{\text{bg}} \geq -25\,\text{V}$. The LL states appearing with high intensity are labeled according to their indices. Charging lines are marked with white arrows, Coulomb diamonds with a black arrow, and split LLs are marked with orange arrows. E_{F} is shown as a red line. $B = 14\,\text{T}$, $T = 7.5\,\text{K}$, $V_{\text{sample}}^{\text{stab}} = -500\,\text{mV}$, $I^{\text{stab}} = 150\,\text{pA}$, $V_{\text{sample}}^{\text{mod}} = 5$ mV, $f^{\text{mod}} = 654.5\,\text{Hz}$.

monotonic behaviour with V_{bg}, but instead the energy gap between LL0 and LL$\pm$1 is enlarged by a factor of 4 symmetrically around $V_{\text{sample}} = 0\,\text{V}$. This is likely caused by the bulk graphene surrounding the QD that becomes insulting once the bulk LL is almost filled or empty. Then E_{F} is located at strongly localized states (see section 2.3). A significant fraction of the applied V_{sample} drops now in the bulk graphene, which resistance is in the same order as the tunneling gap [189]. A higher $|V_{\text{sample}}|$ is required to observe a feature like a LL at fixed energy to compensate for the voltage drop in the bulk. From the shift of the LL0 features energetic position at $V_{\text{bg}} = 6.55\,\text{V}$ compared to $V_{\text{bg}} > 10\,\text{V}$ of about 115 mV and the tunneling current on the LL0 peak at $V_{\text{bg}} = 6.55\,\text{V}$ of $I = 50\,\text{pA}$ the bulk resistance is estimated to be about $R_{\text{bulk}} \approx 2.3\,\text{G}\Omega$.
The LL0 plateau at E_{F} does not exhibit a clear splitting into two levels as for $B = 7\,\text{T}$ in figure 7.8b. Instead, several split levels show up (see orange arrows in figure 7.9) which number is increasing with occupation as well as their energy lowers with increasing occupation. Similar effects are observed for the LL1 states in the same V_{bg} range. The appearance of several sublevels and the splitting of the LL1 feature rule out a substrate induced sublattice breaking as the cause for these observation as in [46, 47, 56]. Nevertheless, this does not exclude this effect at the $B = 7\,\text{T}$ measurement of figure 7.8b since both measurements at $B = 7\,\text{T}$ and $B = 14\,\text{T}$ are not performed in the same spot on the graphene sample. Instead, the different m states within the QD as described above explain most of the experimental features: Their number increases with increasing QD size and depth for increasing V_{bg}. Indeed, the QD increases both in depth and width with increasing LL occupation because it gets increasingly difficult to add additional electrons in the electron-like QD (see figure 5.7a). Similarly, their energy decreases with increasing QD depth and their energetic separation increases as the QD is getting deeper. Questionable however remains why the m states with highest energy have highest intensity where the lowest $m = 0$ state is assumed to have highest

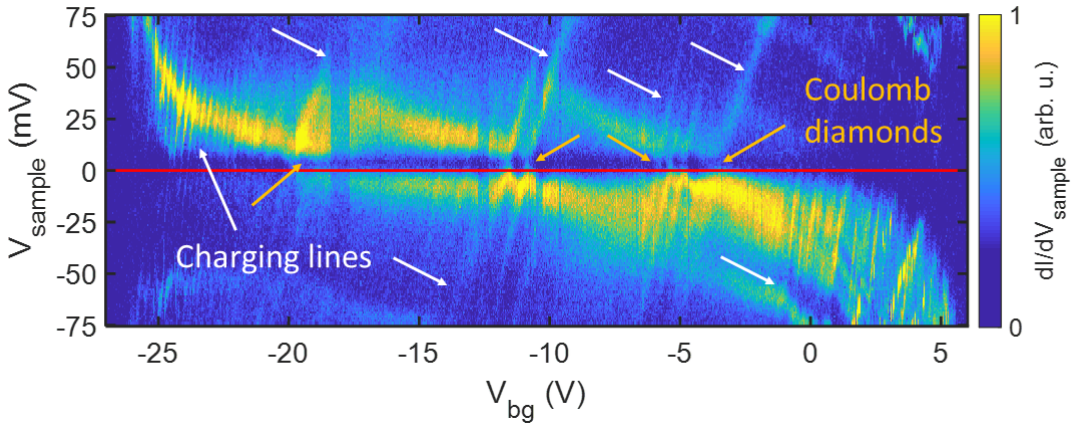

Figure 7.10: $dI/dV_{\text{sample}}(V_{\text{sample}}, V_{\text{bg}}$ measurement of graphene sample GR10BN24 on a single spot. Charging lines are marked with white arrows and Coulomb diamonds are marked with orange arrows. E_{F} is shown as a red line. $B = 14\,\text{T}$, $T = 7.5\,\text{K}$, $V_{\text{sample}}^{\text{stab}} = -500\,\text{mV}$, $I^{\text{stab}} = 150\,\text{pA}$, $V_{\text{sample}}^{\text{mod}} = 1$ mV, $f^{\text{mod}} = 654.5\,\text{Hz}$.

intensity due to its central position in the (electron-like) QD. Consistently with the non existing QD for $V_{\text{bg}} > 10\,\text{V}$, no splitting of the LL states is observed and all LL states except of LL1 at E_{F} consist of a single level with narrower width and higher intensity compared to $V_{\text{bg}} < 10\,\text{V}$.

A more resolved measurement of the LL0 plateau close to E_{F} is shown in figure 7.10. It turns out that prominent CLs group around three values of $V_{\text{bg}} \approx -19, -11, -3\,\text{V}$ which are separated by a regular distance intersecting the LL0 plateau at E_{F} in four V_{bg} sections. Occupied and unoccupied states of LL0 are divided by an energy gap at E_{F} and each section has stepwise increased occupation and correspondingly increased intensity below E_{F} with increasing V_{bg}. The (un-)occupied states itself are not separated into different levels for $V_{\text{bg}} < -5\,\text{V}$. The observations are in line with interaction induced breaking of the fourfold spin valley degeneracy of LL0 in the QD [65, 66, 136, 177] (see section 2.4). The gap at E_{F} shows a triangular shape plotted in figure 7.11 characteristic for localized states [63, 190]. Moreover, the gap between occupied and unoccupied states of the split LL0 feature depends on the LL filling and is enhanced if an additional quarter of LL0 is filled and CLs appear. At these positions exchange enhancement increases the gap because the LL is completely spin valley polarized at quarter filling and the exchange interaction has to be overcome to add the next charge with different spin valley polarization into the LL [63, 178]. Different m states are not a plausible explanation for the observed splitting of LL0 because m states are energetically split independent whether they are occupied or not. In the experiment of figure 7.10, however, the splitting occurs at E_{F} as expected for interactions (see section 2.4). Also each m state is fourfold spin valley degenerated and CLs would appear in groups of four what is not seen in the measurement of figure 7.10. Instead, a single m state is divided in four sublevels by the interaction induced breaking of the spin valley degeneracy.

Transport measurement of the same sample presented in section 7.3 also show symmetry breaking of LL0. Due to more than ten times lower temperature of the transport

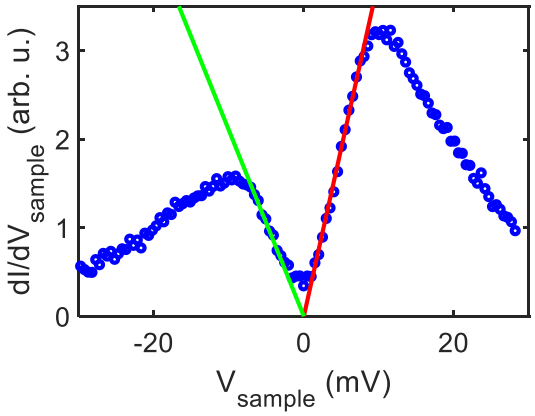

Figure 7.11: $dI/dV_{\mathrm{sample}}(V_{\mathrm{sample}})$ measurement of graphene sample GR10BN24 on a single spot for $V_{\mathrm{bg}} = 15\,\mathrm{V}$ (blue dots). The red and the green line are a guide to the eye for the triangular shape of the Coulomb gap. $B = 14\,\mathrm{T}$, $T = 8\,\mathrm{K}$, $V_{\mathrm{sample}}^{\mathrm{stab}} = -300\,\mathrm{mV}$, $I^{\mathrm{stab}} = 150\,\mathrm{pA}$, $V_{\mathrm{sample}}^{\mathrm{mod}} = 1\ \mathrm{mV}$, $f^{\mathrm{mod}} = 654.5\,\mathrm{Hz}$.

measurement compared to STM measurement ($T = 0.5\,\mathrm{K}$ vs. $T = 7.5\,\mathrm{K}$), the symmetry breaking already sets in below $B = 2\,\mathrm{T}$ and is well observed at $B = 7\,\mathrm{T}$. In contrast, $B = 7\,\mathrm{T}$ is not sufficient to lift the fourfold degeneracy of LL0 in the STM measurements of figure 7.8b. Furthermore, the STM measurements show no evidence of the 1/3 FQHE state observed in transport above $B = 8\,\mathrm{T}$. This is most likely as well caused by the elevated temperature of the STM measurements. Additionally, transport and STM measurements are carried out in different cool downs of the sample between which a time of about three years has elapsed and the sample might have changed its properties during the storage, mostly in UHV.
The quality of the sample enables the observation of symmetry broken states in LL0 at $B = 14\,\mathrm{T}$ and $T = 7.5\,\mathrm{K}$ and makes it thereby competitive to recent publications that further investigate these states [65, 66]. Direct comparison is however difficult as these measurements are performed at different B and T. Most of the samples in [66] feature a graphite back gate that generally results in higher quality samples in transport experiments (see section 6.8) as not being the case for this sample.

8 Novel fabrication techniques

The quality of graphene samples can be improved by using a graphite back gate as described in section 6.8 for transport experiments [28]. Consequently, similar samples for STM measurements are desirable [66]. In these samples, flakes of graphene, hBN, and graphite are stacked together with the order graphite-hBN-graphene from bottom to top as is sketched in figure 8.1. To allow for electrical contacts from the top both to the graphene and graphite flakes, the graphite flake has to be mostly covered by the hBN flake but still exposing a small area of its surface (see figure 8.1b). With the known fabrication process (see section 7.1) the implementation of a graphite back gate turns out to be impossible. In this process a graphite flake exfoliated onto a SiO_2Si chip would be used as a back gate and a hBN flake would be transferred on top of it. Since the hBN flake needs to cover most of the graphite flake it is much larger resulting in the PMMA transfer process to fail by picking up the graphite flake with the hBN flake instead of the other way around. To solve this problem, two novel fabrication processes are developed. They make the fabrication of STM suitable graphene samples with graphite back gate feasible. Their implementation and optimization is carried out by several hard-working master students [181, 191–194]. The concepts of the two processes and the results are presented below, where the details of the processes are found in either [181, 191] or [192–194], respectively.

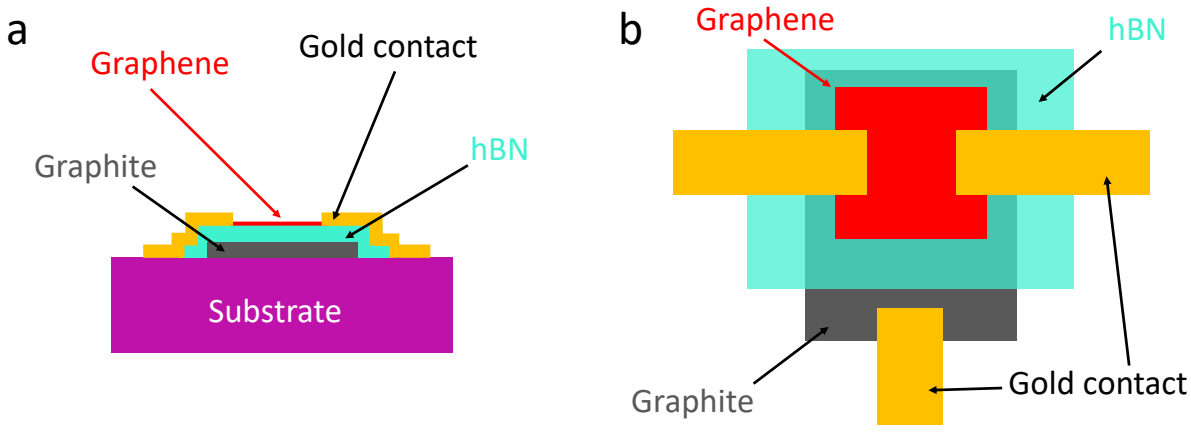

Figure 8.1: Sketch of a graphene sample with graphite back gate. a: Cross section. b: Top view (substrate not shown for clarity).

8.1 Mica substrate

In this process, a mica substrate instead of the conventional Si/SiO_2 chip is used to carry the graphene-hBN-graphite stack (see figure 8.1a). Due to its transparency, the mica substrate can be used as a stamp in the transfer process (see section 6.4 and figure 6.4). Flakes exfoliated on Si/SiO_2 chips can be picked up by this mica stamp. To this end, graphite flakes are exfoliated on the mica substrate (see step 1a in figure 6.4). The mica is thinned down to about 100-150 μm by splitting it with a scalpel [191]. With reduced thickness the mica substrate becomes flexible (see figure 8.2a) making it suitable as a stamp. For the transfer process, the mica substrate is adhered to a piece of PDMS on a glass slide (see figure 8.2b) and mounted in a mask aligner upside down (see steps 2a and 3 in figure 6.4). The graphite flake on the mica is aligned with a hBN flake exfoliated on a Si/SiO_2 chip and brought into contact. During this process, the stage of the mask aligner is heated to 100 °C and the flakes remain in contact for a duration of 5 minutes (see step 4 in figure 6.4). Once the contact is released, the hBN flake is transferred from the Si/SiO_2 chip to the graphite flake on the mica substrate (steps 5a and 6a in figure 6.4) with a success rate larger than 70 % [181]. Afterwards, the same transfer process is repeated with a graphene flake that is transferred onto the hBN flake and the graphene-hBN-graphite stack (see figure 8.1) is completed. The graphene surface is very clean with only few bubbles as can be seen in the topography image recorded by AFM in figure 8.3a [181].
The heating during the transfer process removes water on the mica surface. This increases the vdW force between the flake to be picked up from the SiO_2/Si chip and the mica surface. By heating, the adhesion of flakes to SiO_2 is also lowered such that they can be pushed across the SiO_2 surface by micromanipulated tungsten tips. This way, the mica transfer process allows to pick up larger flakes by smaller flakes in contrast to the PMMA process (see section 7.1). This might be caused by better adhesion of flakes on the flat mica surface compared to the rough, amorphous SiO_2 surface. Employing this advantage of the transfer process, a stack consisting of five

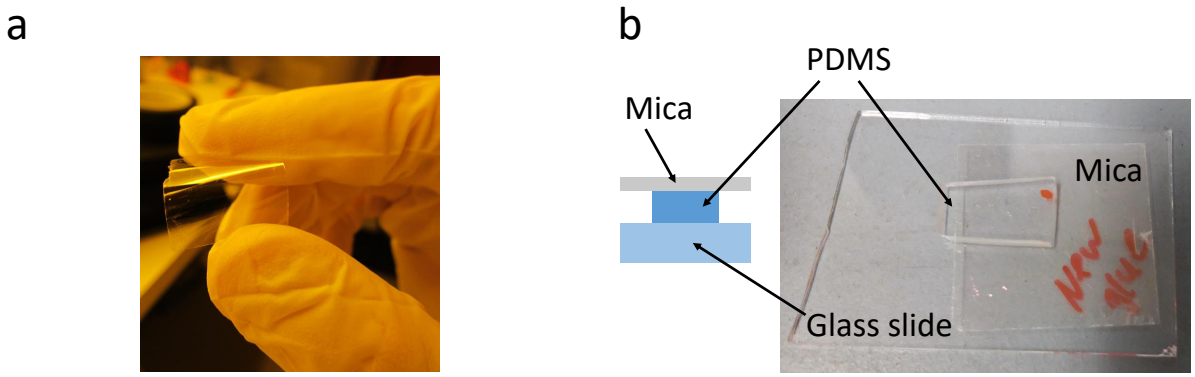

Figure 8.2: a: Thinned down mica substrate as used for the stamp. This mica is flexible. Reprinted from [191]. b: Optical image of the stamp consisting of a glass slide, a PDMS piece attached to it, and a piece of mica. The mica piece is carried by the PDMS piece. A schematic cross section is shown on the left. Reprinted from [181].

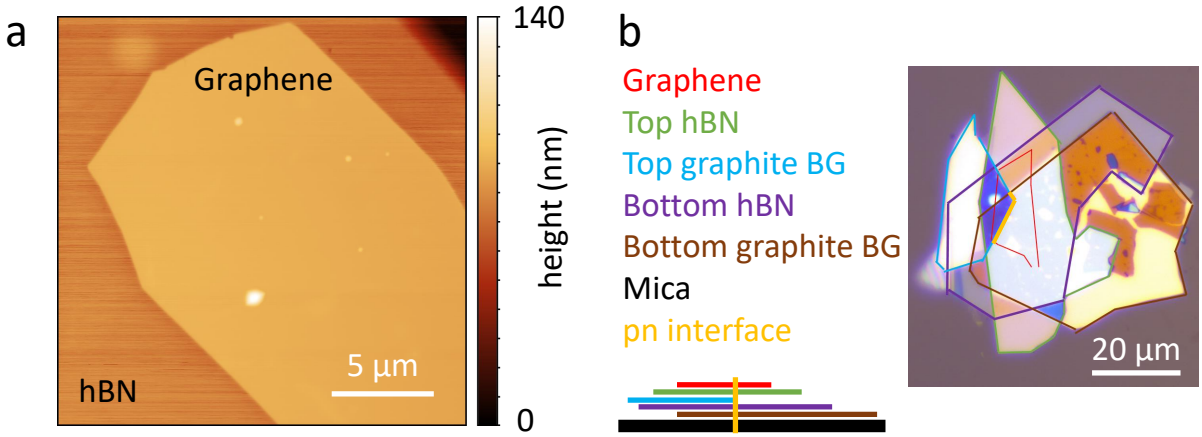

Figure 8.3: a: AFM topography of a graphene-hBN-graphite stack on mica recorded in tapping mode at ambient conditions. Data from [181]. b: Optical image of a graphene pn sample stacked on a mica substrate. A cross section is shown in the bottom left. Individual flakes are outlined in the colours listed. The pn interface is marked in yellow.

flakes forming a pn junction (see chapter 5) is created. An optical image is presented in figure 8.3b. A possible future application might be the transfer of CVD grown materials as well [195] .
The electrical contacts could be prepared either by the shadow mask technique (see section 7.2) or by indium microsoldering (see section 6.11) [170]. In practice, the shadow mask technique failed in contacting the samples due to two different reasons. Either the diffusion of gold particles into the shadow area was too large, since deposited at room temperature. The graphene surface remains covered with gold clusters and is not suited for planed measurements of the QHE. If the sample is cooled below $T = 100\,\mathrm{K}$ during the evaporation to reduce the diffusion, cracks in the graphene flake appeared probably caused by different thermal expansion coefficients of the involved materials [181]. Graphite has a larger thermal expansion coefficient than gold while graphene has a negative thermal expansion coefficient. While the sample warms up from $T = 100\,\mathrm{K}$ to room temperature, the graphite flake stretched, while the graphene flake is contracts. Because both are connected via the gold contacts, the graphene flake ruptures. A possible solution are shadow masks with wider bars, such that the deposition at room temperature with a large diffusion still leaves a clean surface area in the center of the sample. If this could be achieved, a complete polymer free fabrication process for vdW stacks including electrical contacts is developed, such that any residues from polymers are avoided. In particular, this could be beneficial for sample stacking in argon atmosphere [196] or under vacuum conditions [26] where polymers are the main source of residues. The PDMS piece should be replaced by a material with lower vapor pressure and similar mechanical properties as polyimide foam. If the flakes assembled in the stacks can be exfoliated in UHV [197, 198], the complete sample fabrication process could be performed in UHV.
The mica process is partly inspired by the copolymer process (see section 6.6) that was used in [171] to fabricate graphene-hBN-graphite stacks. This employs a copolymer coated glass slide to sequentially pick up exfoilated flakes from Si/SiO_2 chips. However, the electrical contacting by microsoldering was not successful and the shadow mask

technique (see section 7.2) could not be applied due to the softness of the copolymer. By replacing the copolymer coated glass slide with mica the contacting problem, an easier contacting was anticipated.

8.2 Patterned graphite gates

This method aims at a gated graphene sample for STM experiments that can be used for 2-point transport measurements as well. Firstly, a large graphite flake is patterned into three parts by two trenches. The central part of the cut graphite flake is covered with a hBN flake and serves as a back gate (see figure 8.4). The outer parts are used as source and drain contacts for transport measurements through the graphene flake that is placed across all three parts. Thereby, the graphene flake is electrically connected to the outer parts but insulated by the hBN flake from the back gate (central part). The outer parts as well as the central back gate part are each electrically contacted via gold/chromium leads. With this sample design both the contacting problem is solved and a graphite back gate is integrated in the sample. The idea for this fabrication method is inspired by [199], where metallic contacts are deposited on a hBN flake before a WTe_2 monolayer flake is transferred on them. Such a method is similarly applied in [166] (see section 6.11 and figure 6.7). Likewise back gates have been prepared, before MoS_2 samples are transferred on them in [200] and [201].
The fabrication process starts with the exfoliation of a large graphite flake on a SiO_2/Si chip. The trenches to cut the graphite flake are etched by reactive ion etching with an argon oxygen plasma. To this end, the graphite flake is covered by a PMMA layer textured with electron beam lithography[192–194]. The etching then transfers the PMMA mask to the graphite. By inclining the trenches with respect to each other, hBN and graphene flakes of variable size can be chosen to assemble the sample. The contacts

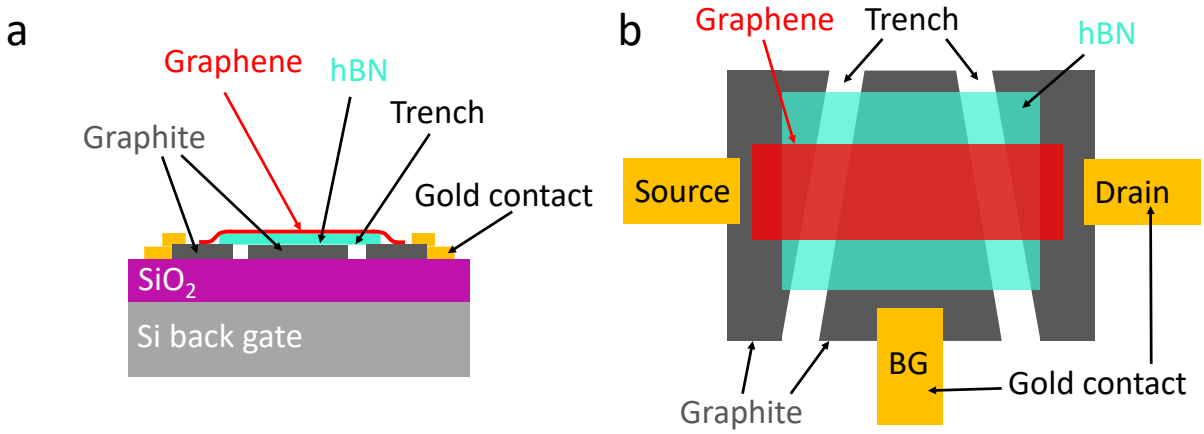

Figure 8.4: Sketch of a graphene sample with patterned graphite gate. Two trenches split the graphite flake into three sections. The left and right parts are source and drain contacts, respectively, and contact the graphene flake. The central part is the back gate and by the hBN flake insulated from the graphene. a: Cross section. b: Top view (Si/SiO_2 not shown for clarity).

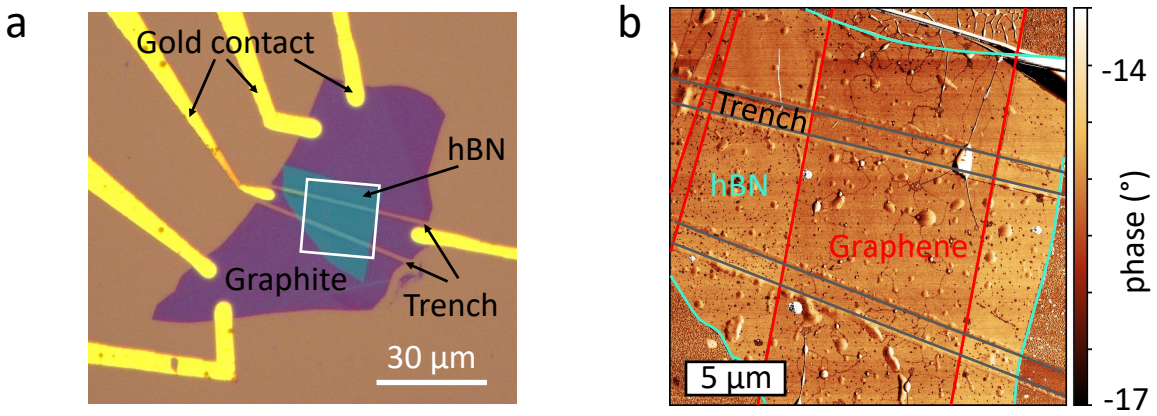

Figure 8.5: a: Optical image of a graphene-hBN-graphite sample with patterned gates. The graphene flake is not visible. The white frame shows the position of the AFM phase image of subfigure b. Data from [194]. b: AFM phase image of the graphene sample shown in subfigure a. The edges of the two flakes are marked in red (graphene) and green (hBN). Data from [194].

to the separated graphite sections are prepared using standard electron beam lithography [192–194]. Both the etching as well as the contacting processes are carried out before the hBN and graphene flakes are transferred, such that residues arising during these processes do not come into contact with the graphene surface. Additionally, cleaning procedures like an ultrasonic bath in solvents or annealing in vacuum are conducted prior to the transfer steps, without the necessity to consider possible damage to the graphene flake. Such etching and contacting processes are regularly applied to fabricate graphene samples designed exclusively for transport measurements. A large experience exists in the institute (group of Prof. Stampfer) resulting in high yield and reliability [192–194].
The following transfer process of hBN and graphene flakes is based on the dry PMMA transfer (see sections 6.5 and 7.1). It employs a transfer system developed at the University of Manchester and not the a mask aligner used in section 7.1. Because both the hBN and the graphene flake are smaller than the large graphite flake, the transfer takes place as desired and the graphite flake is not picked up by the hBN or graphene flake. In figure 8.5, an optical image and an AFM phase image of a completely stacked sample are shown [194]. Several samples have been fabricated [192–194] with yields of up to 70 % for the complete process. After the graphene transfer, the sample is ready for STM and transport measurements in contrast to other the processes (see sections 7.1 and 8.1). There, the electrical contacts are prepared after the graphene transfer introducing a source of dirt for the graphene surface. Similar to the mica process (see section 8.1), this process is suitable for applications in argon atmosphere [196] or under vacuum conditions [26]. The etching and contacting processes as well as the transfer of the hBN flake can be performed prior to the sample stacking in inert environment. Combined with UHV exfoliation [197, 198] of the flakes, the sample can be completed in UHV and can remain there for measurements. Recently it is reported that graphite can be patterned by local anodic oxidation with an AFM tip [202]. This opens the

possibility to replace the etching step resulting in less debris on the patterned graphite gates.

8.3 Transport results

One of the samples prepared by the method of section 8.2 is characterized by low temperature transport measurements in the quantum Hall regime at $T = 0.3\,\mathrm{K}$ [194]. The outer parts of the graphite flake that act as the source and drain contacts for the graphene flake are each connected by two metallic leads (see figure 8.5a) enabling for a four-probe measurement. Due to the geometry of the contacts, the contact resistance between graphene and graphite remains, however, included and only the line resistance of the transport setup is eliminated. As long as only the central graphite back gate voltage V_{bg} is tuned the resistances of the other areas do not change and mimic an additional line resistance. The properties of the graphene sample in the central area can be investigated by changing the back gate voltage. The mobility for both electrons and hole is about $\mu \approx 50.000\,\mathrm{cm}^2/\mathrm{Vs}$ [194] and the Landau quantization of charge carriers sets in at about $B = 60\,\mathrm{mT}$ (not shown).
In the quantum Hall regime, five areas of the graphene flake behave differently as sketched in figure 8.6. The central area (green in figure 8.6) is on the graphite back gate which tunes the filling factor ν_{bg} in this area. The two areas on the trenches (violet in figure 8.6) are instead tuned by the Si back gate of the $\mathrm{Si/SiO_2}$ chip and have filling factor ν_{Si}. The areas (yellow in figure 8.6) where the graphene is in direct contact with the graphite source and drain contacts are not tunable. They are assumed to be irrelevant for the transport measurement because they are shorted by the underlying graphite. On the outer graphite contacts, the graphene is partly on hBN without being

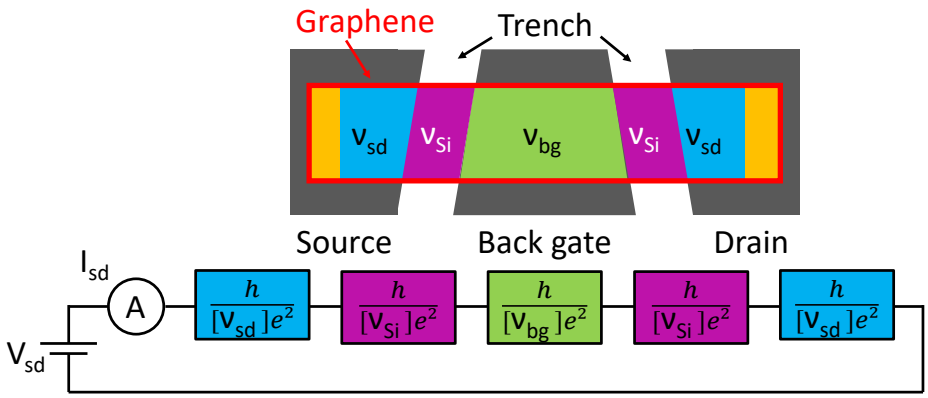

Figure 8.6: Upper part: Schematic representation of the graphene flake (red frame). The sections of the graphene on the graphite back gate (green), on the trenches (violet), and on the graphite source and drain contacts on hBN (blue) have individual filling factors $\nu_{\mathrm{bg}}, \nu_{\mathrm{Si}}$ and $\nu_{\mathrm{sd}} \approx$ const. in the quantum Hall regime, respectively. The yellow areas are in electrical contact with the source and drain contacts. In the lower part the electric replacement circuit is shown with resistors in corresponding colours.

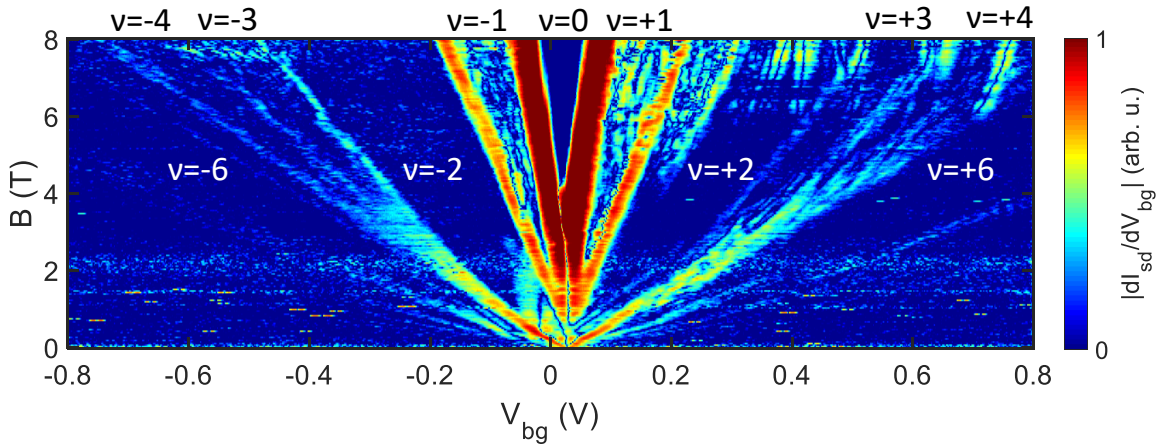

Figure 8.7: Measurement of $|I_{\mathrm{sd}}/V_{\mathrm{bg}}|(V_{\mathrm{bg}}, B)$ of a graphene sample with patterned graphite gates. Plateaus of constant conductance are labeled with the corresponding filling factors ν. The derivative is performed numerically and the data is smoothed. Data from [194]. $V_{\mathrm{sd}} = 100\,\mu\mathrm{V}$, $V_{\mathrm{sd}}^{\mathrm{DC}} = 5\,\mathrm{mV}$, $T = 0.3\,\mathrm{K}$.

tunable by any back gate. In these areas (blue in figure 8.6) the graphene is most likely close to the $\nu_{\mathrm{sd}} \approx 0$ filling factor that becomes insulating [186] with increasing magnetic field above $B = 2 - 3\,\mathrm{T}$. Each interface between different areas is a pn interface (see section 2.10) and the sample can be described by a series of resistances as represented in a circuit diagram in the lower part of figure 8.6. From this geometry, the idea for the measurements of the pn interface in chapter 5 is inspired. In the quantum Hall regime with insulating $\nu_{\mathrm{sd}} \approx 0$ areas, the measurements become challenging and in particular quantized conductance values of a two-probe-measurement (see equation 2.13) can not be observed. However, by taking the derivative of the conductance with respect to the back gate voltage V_{bg} at constant magnetic field B, the transition between different filling factors ν_{bg} in the central graphene area are made visible (see section 7.3 and figures 7.6 and 7.7a). The resulting Landau fan is shown in figure 8.7. An additional DC bias of $V_{\mathrm{sd}}^{\mathrm{DC}} = 5\,\mathrm{mV}$ symmetrically applied between source and drain contacts increases the conductivity of the sample. This is likely due to hopping transport through the insulating parts. At $B = 2\,\mathrm{T}$ the degeneracy of LL0 is completely lifted. At about $B = 4\,\mathrm{T}$ it is also lifted for LL$\pm$1. Multiple other features appearing in the Landau fan for $B \gtrsim 5\,\mathrm{T}$ and $V_{\mathrm{bg}} > 0\,\mathrm{V}$ are probably caused by locally varying filling factors induced by charge impurities either in the trench areas or the insulting areas on the graphite contacts. Some of them can be attributed to an Aharanov-Bohm-interferometer with a diameter of about 400 nm as described in [194].
Comparing the transport results of these samples with patterned graphite gates to the ones prepared with a Si back gate (see section 7.3), an improvement in quality is achieved as the mobility is higher and degeneracy lifting of LLs is observed at lower magnetic fields (see figure 7.6). The disadvantage is the obstructed measurement through the insulating parts on the outer graphite parts. However, the FQHE is not observed. This shows that the quality of samples in the literature is not reached yet [28]. The scope of this comparison is however limited as only one sample with patterned graphite gates has been measured at low temperatures so far. Future measurements

including STM might benchmark this novel fabrication process. From an experimental point of view, these samples offer various possibilities for combined STM and transport investigations since bulk graphene as well as pn interfaces are present that both can be tuned by back gates. Examples could be symmetry broken or fractional ECs as well as locally resolved shot noise measurements along the pn interface [83, 84].

9 Summary and outlook

Firstly, a pn interface in graphene with gate tunable occupation in its left area is investigated with STM/STS in the quantum Hall regime at $B = 7\,\mathrm{T}$ and $T = 7\,\mathrm{K}$. The observed Landau level features change their energy across the chemical potential step at the pn interface. The observation of flat plateaus of about 40 nm width both at E_F and finite energy reveals the electrostatic screening of the potential gradient by the charge carriers as predicted in [13]. The formation of alternating compressible and incompressible stripes along the pn interface is directly observed. In addition, the LL states split into branches that connect adjacent LLs as they approach the pn interface. Charging lines indicate the presence of a tip-induced quantum dot (QD) below the tip that is characterized far away from the pn interface for the same tip. Poisson simulations of the QD without pn interface are carried out to gain the size and depth of the QD in dependence of the applied V_bg and V_sample. By comparison with the charging lines of the experiment, the decisive parameters work function mismatch $\Delta_\mathrm{wfm} = -180\,\mathrm{mV}$ between tip and graphene as well as the tip radius $r_\mathrm{tip} = 25\,\mathrm{nm}$ are determined. Equipped with this knowledge, the pn interface is included in the Poisson simulation. Based on this, the measurement of the pn interface at E_F is only little influenced by the tip for LL-1, LL-2 and LL-3 states at E_F on the left side, while LL0 states are at E_F on the right side. For these parameters, the potential step is only stretched by the tip during the measurement. Tight-binding (TB) calculations incorporating the results of the Poisson simulations at the pn interface give the wave functions of the compressible stripes that are different for individual LLs. If no QD is present below the tip, the wave functions of the compressible stripes are measured largely matching the TB simulations. The measurements resemble that of the unperturbed compressible stripes as is confirmed by the TB simulations. The results are rationalized by a lifting of the LL degeneracy at the pn interface [57, 58, 122] implying that the number of nodes in the wave function is increasing with the LL index. This explains the changing distance of the two branches with energy as partly observed in the measurements. One compressible stripe was also mapped along the pn interface exhibiting the expected meandering of central position and width. Eventually, combing STM/STS measurements with TB simulations provides a great tool to study the structure of compressible and incompressible stripes at a pn interface with high spatial resolution that compose the quantum Hall edge channels (ECs). For other parameters, a QD below the tip is influencing the measurements of the ECs at the pn interface. Due to the potential gradient at the pn interface, the QD is displaced with respect to the tip and the tip accesses QD states with higher m quantum number [62].

Future experiments could be carried out at a pn interface that is gate tunable on both sides. Thereby the wave functions of compressible stripes of other LLs can be studied as well. Going to lower temperature and higher magnetic fields will induce symmetry breaking of the LLs in graphene related to much smaller energy gaps. This reduces

the width of the compressible stripes [29] and puts their size to the magnetic length possibly resulting in more complex quantum mechanical effects. Even more far fetched is the investigation of fractional quantum Hall ECs. The fractional LLs exhibit a reconstruction at the edge that can host neutral as well as multiple charged channels [12]. They are so far not spatially investigated and not fully understood. In the low magnetic field regime, snake states develop at a pn interface before Landau quantization dominates [86]. Their observation requires very clean samples with ballistic transport over several micrometers. However, less surprising results are expected from their measurement compared to the other ECs.
From the technical point of view, it would be desirable to control the QD below the tip and to suppress it if necessary. To this end, a tip with a tunable work function to adjust Δ_{wfm} would offer a solution. Most simply, one could modify the surface by dipping into a certain highly mobile material or by depositing the material by evaporation. Alternatively an annular gate electrode around the tip can counter gate the Δ_{wfm} realizing no band bending below the tip. Furthermore the tip itself can be modified by creating a narrow shape too small to confine charge carriers [66].
Apart from that, several processes are described to fabricate graphene samples of high quality for combined electrical transport and STM measurements. A sample produced with the dry stacking method and contacted with a shadow mask technique exhibits symmetry breaking at $B \approx 3\,\mathrm{T}$ and a fractional state above $B = 8\,\mathrm{T}$ in the quantum Hall effect (QHE) transport. Symmetry breaking was also observed in STS experiments but here only at $B = 14\,\mathrm{T}$. A different approach produces samples by patterning contacts and gates from a graphite flake as the first step. The hBN and graphene flakes are placed on the sample afterwards. In the QHE transport, the quality is slightly better with enhanced charge carrier mobility of $\mu \approx 50.000\,\mathrm{cm}^2/\mathrm{Vs}$ and symmetry breaking at $B = 2\,\mathrm{T}$ already. The transport experiments are hampered by the geometry of the sample as parts with the insulating $\nu = 0$ filling factor are connected in series. STM/STS measurements of these samples are required to reveal their quality. Perspectively, the transfer processes can be performed under inert gas atmosphere or in vacuum allowing the preparation of high quality samples of even air sensitive materials. A third method involves mica as a substrate instead of standard $\mathrm{Si/SiO_2}$ chips. Multiple samples are fabricated by dry stacking the involved flakes on top of each other using mica as a stamp. The shadow mask technique to define electrical contacts was however not successful due to thermal expansion problems after evaporation at $T \sim 100\,\mathrm{K}$. Nevertheless, combing dry stacking on a mica substrate with the shadow mask technique for electrical contacts is a complete polymer free fabrication process that is applicable in inert gas or vacuum conditions.
This thesis also deals with the question, how to approach the tip on the graphene sample. Optical images of the tip at various positions taken through a long distance microscope are overlaid to improve the tip alignment. Moreover, the AFM capability of the 003 setup is used for electrostatic force measurements. By applying different voltages to the individual contacts, the tip position is determined such that the tip could be directed along the interface of different contacts to the sample. During this procedure, the tip is in a large distance from the sample surface (50 nm) avoiding pick-up of dirt from the sample. The implementation of this technique in other setups could make future measurements considerably more reliable.

10 Acknowledgements

First of all I thank Prof. Markus Morgenstern for giving me the opportunity to carry out my thesis in his group and for supervising me during this time. He has supported me in any aspect that he could think of and shared his enormous knowledge with me in numerous fruitful discussions. Noticeable he has given me the freedom to largely follow my own ideas within the topic. He has never lost the trust in me to achieve valuable results and that trust has partly been larger than my own. With his unprecedented never ending enthusiasm he has motivated me to keep going even in difficult times. Altogether he has a big share in the successful outcome of this thesis, in particular in the analysis of the pn interface experiments.
I would like to thank Florian Libisch for being my second examiner.
For complementing the measurements with TB simulations, I thank Christoph Schattauer and Florian Libisch. During many video meetings, we have together learned to understand the experiment in detail thanks to your input.
For fabricating the pn sample and thereby enabling the measurements, I thank Astrid Weston and Matthew Hamer under the supervision of Roman Gorbachev. After the failed twisted bilayer attempt, the pn sample has been the new basis for my work and accordingly I am very grateful for your preparative efforts.
Similarly for their hard work on fabricating samples, I would like to thank my students Michael Weimer, Yanting Liu, Rosen Sofroniev, and Julian Hürtgen. They have pursued my ideas on novel fabrication techniques and, by developing the corresponding routines and procedures, created most of the results on this topic.
Sayanti Samaddar I thank for a great time working together with lots of fun. With her calm and patient attitude, she explained me many physical and technical details specifically about the AFM so that I have learned a lot from her. Also she helped me in any regard without hesitation and backed me in moody phases. I will never forget your famous quotes and the biking experiences.
Next, I would like to thank Peter Nemes for supervising me during my master thesis and the early PhD years. With his positive spirit he has significantly motivated me to start a PhD thesis and helped me often with his huge expertise.
Marcus Liebmann and Marco Pratzer I thank for their constant support in mostly technical aspects in the lab. I have benefited a lot from their knowledge in joint discussions and would have had a much harder time in the lab without their assistance. Additionally I thank them for their organizations related to the morning star group.
I would like to thank the people, I have closely worked with, for the nice atmosphere and their indirect contribution to this thesis. In more detail, these are »team gra**qhe**ne« consisting of Nils Freitag, Felix Jekat, and Peter Nemes, the »KTG 003 team« consisting of Daniel Montag, Sayanti Samaddar, Karim Soliman, and Kai Sotthewes, and the »skyrmions« Christian Saunus Holl and Florian Muckel. Martin Grob and Bertram Schulze Lammers I thank for their design and assembly of the thermal gold evaporator.

Both the mechanical workshop headed by Frank Neubauer and Raoul Sous as well as the electronics workshop consisting of Paul Dinsalge, Lars van Hove, and Uwe Wichmann I would like to thank for manufacturing equipment after my needs and for giving me many helpful advice. Countless sample holders and electronic devices have been the foundation of my experiments.
For the seemingly never ending supply of liquid cryogens and for keeping the liquefiers operational, I thank Jörg Schirra and Sascha Mohr. Without their efforts the experiments could not have been performed.
I thank Beate Nagel, Beatrix Dangela, Margarete Betger, and Ina Kürten for their indispensable bureaucratic work that, thanks to them, for me mostly stayed in the background.
The complete morning star group I thank for the friendly and helpful atmosphere, intensive discussion both scientifically and non-scientifically, happy party times, fantastic trips and smaller or larger assistance in the lab as well as in other occasions. Without a supportive, encouraging, and caring group this thesis would never have been completed.
If not already mentioned above, the group members are in random order: David Cuma, Jeff Strasdas, Bernhard Kaufmann, Tomohiro Sakata, Jens Kellner, Jan Conzen, Marvin Knol, Tim Olschewski, Christian Pauly, Kanji Furuta, Sebsatian Mann, Teresa Weßels, Philipp Küppers, Mike Pezzotta, Christian Philipps, Lukas Deutz, Silke Rose (Hattendorf), Timofey Balashov, Niklas Kercher, Pascal Späing, Simon Mathioudakis, Jonas Duffhauß, Biplab Bhattacharyya, Artoni Ang, Marcus Eßer, Sven Just, Alexander Georgi, Xiaochun Huang, Raphael Bindel, Kilian Flöhr, Priya Bhaskar, Benjamin Pestka, Kevin Janßen, and Til Apel.
I would like to thank the groups of Prof. Bluhm and Prof. Stampfer for having a good community and various discussions be it in the Söllerhaus or in the clean room.
Finally I thank my family for supporting and encouraging me in many ways during my PhD time.

"That's it!"

"Möchte jemand Sekt?"

2.9.2019

Bibliography

1. K. v. Klitzing, G. Dorda, and M. Pepper. “New Method for High-Accuracy Determination of the Fine-Structure Constant Based on Quantized Hall Resistance”. *Phys. Rev. Lett.* **45,** 494 (1980).
2. M. Büttiker. “Absence of backscattering in the quantum Hall effect in multiprobe conductors”. *Phys. Rev. B* **38,** 9375–9389 (1988).
3. B. I. Halperin. “Quantized Hall conductance, current-carrying edge states, and the existence of extended states in a two-dimensional disordered potential”. *Phys. Rev. B* **25,** 2185 (1982).
4. R. J. F. van Haren, W. de Lange, F. A. P. Blom, and J. H. Wolter. “Imaging of edge channels in the integer quantum Hall regime by the lateral photoelectric effect”. *Phys. Rev. B* **52,** 5760 (1995).
5. A. A. Shashkin, A. J. Kent, J. R. Owers-Bradley, A. J. Cross, P. Hawker, and M. Henini. “Hall Photovoltage Imaging of the Edge of a Quantum Hall Device”. *Phys. Rev. Lett.* **79,** 5114 (1997).
6. K. L. McCormick, M. T. Woodside, M. Huang, M. Wu, P. L. McEuen, C. Duruoz„ and J. S. Harris, Jr. “Scanned potential microscopy of edge and bulk currents in the quantum Hall regime”. *Phys. Rev. B* **59,** 4654 (1999).
7. M. E. Suddards, A. Baumgartner, M. Henini, and C. J. Mellor. “Scanning capacitance imaging of compressible and incompressible quantum Hall effect edge strips”. *New J. Phys.* **14,** 083015 (2012).
8. A. Yacoby, H. F. Hess, T. A. Fulton, L. N. Pfeiffer, and K. W. West. “Electrical imaging of the quantum Hall state”. *Solid State Commun.* **111,** 1–13 (1999).
9. Y.-T. Cui, B. Wen, E. Y. Ma, G. Diankov, Z. Han, F. Amet, T. Taniguchi, K. Watanabe, D. Goldhaber-Gordon, C. R. Dean, and Z.-X. Shen. “Unconventional Correlation between Quantum Hall Transport Quantization and Bulk State Filling in Gated Graphene Devices”. *Phys. Rev. Lett.* **117,** 186601 (2016).
10. A. Uri, Y. Kim, K. Bagani, C. K. Lewandowski, S. Grover, N. Auerbach, E. O. Lachman, Y. Myasoedov, T. Taniguchi, K. Watanabe, J. Smet, and E. Zeldov. “Nanoscale imaging of equilibrium quantum Hall edge currents and of the magnetic monopole response in graphene”. *Nat. Phys.* **16,** 164–170 (2020).
11. N. Moreau, B. Brun, S. Somanchi, K. Watanabe, T. Taniguchi, C. Stampfer, and B. Hackens. “Upstream modes and antidots poison graphene quantum Hall effect”. *Nat. Commun.* **12,** 4265 (2021).
12. R. Sabo, I. Gurman, A. Rosenblatt, F. Lafont, D. Banitt, J. Park, M. Heiblum, Y. Gefen, V. Umansky, and D. Mahalu. “Edge reconstruction in fractional quantum Hall states”. *Nat. Phys.* **13,** 491–496 (2017).

13. D. B. Chklovskii, B. I. Shklovskii, and L. I. Glazman. "Electrostatics of edge channels". *Phys. Rev. B* **46,** 4026 (1992).

14. G. Binnig, H. Rohrer, C. Gerber, and E. Weibel. "Surface Studies by Scanning Tunneling Microscopy". *Phys. Rev. Lett.* **49,** 57 (1982).

15. J. W. G. Wildöer, C. J. P. M. Harmans, and H. van Kempen. "Observation of Landau levels at the InAs(110) surface by scanning tunneling spectroscopy". *Phys. Rev. B* **55,** R16013 (1997).

16. L. Canali, J.W.G. Wildöer, O. Kerkhof, L.P. Kouwenhoven. "Low temperature STM on InAs (110) accumulation surface". *arXiv:cond-mat/9708098 [cond-mat.mes-hall]* (1997).

17. G. Li, A. Luican-Mayer, D. Abanin, L. Levitov, and E. Y. Andrei. "Evolution of Landau levels into edge states in graphene". *Nat. Commun.* **4,** 1744 (2013).

18. S.-Y. Li, H. Liu, J.-B. Qiao, H. Jiang, and L. He. "Magnetic-field-controlled negative differential conductance in scanning tunneling spectroscopy of graphene npn junction resonators". *Phys. Rev. B* **97,** 115442 (2018).

19. K. S. Novoselov, A. K. Geim, S. V. Morozov, D. Jiang, Y. Zhang, S. V. Dubonos, I. V. Grigorievaand, and A. A. Firsov. "Electric Field Effect in Atomically Thin Carbon Films". *Science* **306,** 666–669 (2004).

20. A. K. Geim and K. S. Novoselov. "The rise of graphene". *Nat. Mater.* **6,** 183–191 (2007).

21. K. S. Novoselov, Z. Jiang, Y. Zhang, S. V. Morozov, H. L. Stormer, U. Zeitler, J. C. Maan, G. S. Boebinger, P. Kim, and A. K. Geim. "Room-Temperature Quantum Hall Effect in Graphene". *Science* **315,** 1379 (2007).

22. K. S. Novoselov, A. K. Geim, S. V. Morozov, D. Jiang, M. I. Katsnelson, I. V. Grigorieva, S. V. Dubonos, and A. A. Firsov. "Two-dimensional gas of massless Dirac fermions in graphene". *Nature Letters* **438,** 197–200 (2005).

23. C. R. Dean, A. F. Young, P. Cadden-Zimansky, L. Wang, H. Ren, K. Watanabe, T. Taniguchi, P. Kim, J. Hone, and K. L. Shepard. "Multicomponent fractional quantum Hall effect in graphene". *Nat. Phys.* **7,** 693–696 (2011).

24. A. F. Young, C. R. Dean, L. Wang, H. Ren, P. Cadden-Zimansky, K. Watanabe, T. Taniguchi, J. Hone, K. L. Shepard, and P. Kim. "Spin and valley quantum Hall ferromagnetism in graphene". *Nat. Phys.* **8,** 550–556 (2012).

25. A. A. Zibrov, E. M. Spanton, H. Zhou, C. Kometter, T. Taniguchi, K. Watanabe, and A. F. Young. "Even-denominator fractional quantum Hall states at an isospin transition in monolayer graphene". *Nat. Phys.* **14,** 930–935 (2018).

26. Y. Kim, A. C. Balram, T. Taniguchi, K. Watanabe, J. K. Jain, and J. H. Smet. "Even denominator fractional quantum Hall states in higher Landau levels of graphene". *Nat. Phys.* **15,** 154–158 (2019).

27. F. Chiappini, S. Wiedmann, K. Novoselov, A. Mishchenko, A. K. Geim, J. C. Maan, and U. Zeitler. "Lifting of the Landau level degeneracy in graphene devices in a tilted magnetic field". *Phys. Rev. B* **92,** 201412(R) (2015).

28. F. Amet , A. J. Bestwick, J. R. Williams, L. Balicas, K. Watanabe, T. Taniguchi, and D. Goldhaber-Gordon. "Composite fermions and broken symmetries in graphene". *Nat. Commun.* **6,** 5838 (2015).

29. S. Kim, J. Schwenk, D. Walkup, Y. Zeng, F. Ghahari, S. T. Le, M. R. Slot, J. Berwanger, S. R. Blankenship, K. Watanabe, T. Taniguchi, F. J. Giessibl, N. B. Zhitenev, C. R. Dean, and J. A. Stroscio. "Edge channels of broken-symmetry quantum Hall states in graphene visualized by atomic force microscopy". *Nat. Commun.* **12,** 2852 (2021).

30. J. R. Williams, L. DiCarlo, and C. M. Marcus. "Quantum Hall Effect in a Gate-Controlled p-n Junction of Graphene". *Science* **317,** 638–641 (2007).

31. D. A. Abanin, and L. S. Levitov. "Quantized Transport in Graphene p-n Junctions in a Magnetic Field". *Science* **317,** 641–643 (2007).

32. R. Ribeiro-Palau, S. Chen, Y. Zeng, K. Watanabe, T. Taniguchi, J. Hone, and C. R. Dean. "High-Quality Electrostatically Defined Hall Bars in Monolayer Graphene". *Nano Lett.* **19,** 2583–2587 (2019).

33. A. H. Castro Neto, F. Guinea, N. M. R. Peres, K. S. Novoselov, and A. K. Geim. "The electronic properties of graphene". *Rev. Mod. Phys.* **81,** 109–162 (2009).

34. M. O. Goerbig. "Electronic properties of graphene in a strong magnetic field". *Rev. Mod. Phys.* **83,** 1193 (2011).

35. M. I. Katsnelson, K. S. Novoselov, and A. K. Geim. "Chiral tunnelling and the Klein paradox in graphene". *Nat. Phys.* **2,** 620–625 (2006).

36. Y.-J. Yu, Y. Zhao, S. Ryu, L. E. Brus, K. S. Kim, and P. Kim. "Tuning the Graphene Work Function by Electric Field Effect". *Nano Lett.* **9,** 3430–3434 (2009).

37. T. P. Smith, B. B. Goldberg, P. J. Stiles, and M. Heiblum. "Direct measurement of the density of states of a two-dimensional electron gas". *Phys. Rev. B* **32,** 2696(R) (1985).

38. G. L. Yu, R. Jalil, B. Belle, A. S. Mayorov, P. Blake, F. Schedin, S. V. Morozov, L. A. Ponomarenko, F. Chiappini, S. Wiedmann, U. Zeitler, M. I. Katsnelson, A. K. Geim, K. S. Novoselov, and D. C. Elias. "Interaction phenomena in graphene seen through quantum capacitance". *Proc. Natl. Acad. Sci. USA* **110,** 3282–3286 (2013).

39. L. Landau. "Diamagnetismus der Metalle". *Zeitschrift für Physik* **64,** 629–637 (1930).

40. Y. Zheng and T. Ando. "Hall conductivity of a two-dimensional graphite system". *Phys. Rev. B* **65,** 245420 (2002).

41. U. Klaß, W. Dietsche, K. von Klitzing, and K. Ploog. "Imaging of the dissipation in quantum-Hall-effect experiments". *Zeitschrift für Physik B Condensed Matter* **82,** 351–354 (1991).

42. M. O. Goerbig. "Quantum Hall Effects". *Lecture notes arXiv:0909.1998 [cond-mat.mes-hall]* (2009).

43. D. J. Thouless, M. Kohmoto, M. P. Nightingale, and M. den Nijs. "Quantized Hall Conductance in a Two-Dimensional Periodic Potential". *Phys. Rev. Lett.* **49,** 405 (1982).

44. Q. Niu, D. J. Thouless, and Y.-S. Wu. "Quantized Hall conductance as a topological invariant". *Phys. Rev. B* **31,** 3372 (1985).

45. Y.Barlas, K. Yang, and A. H. MacDonald. "Quantum Hall effects in graphene-based two-dimensional electron systems". *Nanotechnology* **23,** 052001 (2012).

46. D. L. Miller, K. D. Kubista, G. M. Rutter, M. Ruan, W. A. de Heer, M. Kindermann, P. N. First and J. A. Stroscio. "Real-space mapping of magnetically quantized graphene states". *Nat. Phys.* **6,** 811–817 (2010).

47. W.-X. Wang, L.-J. Yin, J.-B. Qiao, T. Cai, S.-Y. Li, R.-F. Dou, J.-C. Nie, X. Wu, and L. He. "Atomic resolution imaging of the two-component Dirac-Landau levels in a gapped graphene monolayer". *Phys. Rev. B* **92,** 165420 (2015).

48. R. Shikler, T. Meoded, N. Fried, B. Mishori, and Y. Rosenwaks. "Two-dimensional surface band structure of operating light emitting devices". *J. Appl. Phys.* **86,** 107 (1999).

49. Y. Rosenwaks, R. Shikler, Th. Glatzel, and S. Sadewasser. "Kelvin probe force microscopy of semiconductor surface defects". *Phys. Rev. B* **70,** 085320 (2004).

50. W. Melitz, J. Shen, A. C. Kummel, and S. Lee. "Kelvin probe force microscopy and its application". *Surf Sci Rep* **66,** 1–27 (2011).

51. B. Voigtländer. *Scanning Probe Microscopy* (Springer Berlin, Heidelberg, 2015).

52. J. Chae, S. Jung, A. F. Young, C. R. Dean, L. Wang, Y. Gao, K. Watanabe, T. Taniguchi, J. Hone, K. L. Shepard, P. Kim, N. B. Zhitenev, and J. A. Stroscio. "Renormalization of the Graphene Dispersion Velocity". *Phys. Rev. Lett.* **109,** 116802 (2012).

53. Y. Zhao, J. Wyrick, F. D. Natterer, J. F. Rodriguez-Nieva, C. Lewandowski, K. Watanabe, T. Taniguchi, L. S. Levitov, N. B. Zhitenev, and J. A. Stroscio. "Creating and probing electron whispering-gallery modes in graphene". *Science* **348,** 672–675 (2015).

54. S. Jung, G. M. Rutter, N. N. Klimov, D. B. Newell, I. Calizo, A. R. Hight-Walker, N. B. Zhitenev, and J. A. Stroscio. "Evolution of microscopic localization in graphene in a magnetic field from scattering resonances to quantum dots". *Nat. Phys.* **7,** 245–251 (2011).

55. N. M. Freitag, L. A. Chizhova, P. Nemes-Incze, C. R. Woods, R. V. Gorbachev, Y. Cao, A. K. Geim, K. S. Novoselov J. Burgdörfer, F. Libisch, and M. Morgenstern. "Electrostatically Confined Monolayer Graphene Quantum Dots with Orbital and Valley Splittings". *Nano Lett.* **16,** 5798–5805 (2016).

56. N. M. Freitag, T. Reisch, L. A. Chizhova, P. Nemes-Incze, C. Holl, C. R. Woods, R. V. Gorbachev, Y. Cao, A. K. Geim, K. S. Novoselov, J. Burgdörfer, F. Libisch, and M. Morgenstern. "Large tunable valley splitting in edge-free graphene quantum dots on boron nitride". *Nat. Nanotechnology* **13,** 392–397 (2018).

57. A. Luican-Mayer, M. Kharitonov, G. Li, C.-P. Lu, I. Skachko, A.-M. B. Gonçalves, K. Watanabe, T. Taniguchi, and E. Y. Andrei. "Screening Charged Impurities and Lifting the Orbital Degeneracy in Graphene by Populating Landau Levels". *Phys. Rev. Lett.* **112,** 036804 (2014).

58. Q. Zheng, Y-C. Zhuang, Q.-F. Sun, and L. He. "Coexistence of electron whispering-gallery modes and atomic collapse states in graphene/WSe_2 heterostructure quantum dots". *Nat. Commun.* **13,** 1597 (2022).

59. Nils Freitag. *Graphene Quantum Dots: Gaining Control over the Valley Degree of Freedom.* Dissertation (RWTH Aachen, 2017).

60. G. Giavaras and F. Nori. "Tunable quantum dots in monolayer graphene". *Phys. Rev. B* **85,** 165446 (2012).

61. S. Schnez, K. Ensslin, M. Sigrist, and T. Ihn. "Analytic model of the energy spectrum of a graphene quantum dot in a perpendicular magnetic field". *Phys. Rev. B* **78,** 195427 (2008).

62. M. Morgenstern, D. Haude, V. Gudmundsson, C. Wittneven, R. Dombrowski, and R. Wiesendanger. "Origin of Landau oscillations observed in scanning tunneling spectroscopy on n-InAs(110)". *Phys. Rev. B* **62,** 7257 (2000).

63. O. E. Dial, R. C. Ashoori, L. N. Pfeiffer, and K. W. West. "High-resolution spectroscopy of two-dimensional electron systems". *Nature Letters* **448,** 176–179 (2007).

64. A. Luican, G. Li, and E. Y. Andrei. "Quantized Landau level spectrum and its density dependence in graphene". *Phys. Rev. B* **83,** 041405(R) (2011).

65. A. Coissard, D. Wander, H. Vignaud, A. G. Grushin, C. Repellin, K. Watanabe, T. Taniguchi, F. Gay, C. B. Winkelmann, H. Courtois, H. Sellier, and B. Sacépé. "Imaging tunable quantum Hall broken-symmetry orders in graphene". *Nature* **605,** 51–56 (2022).

66. X. Liu, G. Farahi, C.-L. Chiu, Z. Papic, K. Watanabe, T. Taniguchi, M. P. Zaletel, and A. Yazdani. "Visualizing broken symmetry and topological defects in a quantum Hall ferromagnet". *Science* **375,** 321–326 (2022).

67. D. A. Abanin, B. E. Feldman, A. Yacoby, and B. I. Halperin. "Fractional and integer quantum Hall effects in the zeroth Landau level in graphene". *Phys. Rev. B* **88,** 115407 (2013).

68. Y. Lian, A. Rosch, and M. O. Goerbig. "SU(4) Skyrmions in the $\nu = \pm 1$ Quantum Hall State of Graphene". *Phys. Rev. Lett.* **117,** 056806 (2016).

69. J. Atteia and M. O. Goerbig. "SU(4) spin waves in the $\nu = \pm 1$ quantum Hall ferromagnet in graphene". *Phys. Rev. B* **103,** 195413 (2021).

70. J. Atteia, Y. Lian, and M. O. Goerbig. "Skyrmion zoo in graphene at charge neutrality in a strong magnetic field". *Phys. Rev. B* **103,** 035403 (2021).

71. Y. Lian and M. O. Goerbig. "Spin-valley skyrmions in graphene at filling factor $\nu = \pm 1$". *Phys. Rev. B* **95,** 245428 (2017).

72. M. Kharitonov. "Phase diagram for the $\nu = 0$ quantum Hall state in monolayer graphene". *Phys. Rev. B* **85,** 155439 (2012).

73. S. L. Sondhi, A. Karlhede, and S. A. Kivelson. "Skyrmions and the crossover from the integer to fractional quantum Hall effect at small Zeeman energies". *Phys. Rev. B* **47,** 16419 (1993).
74. J. Martin, N. Akerman, G. Ulbricht, T. Lohmann, J. H. Smet, K. von Klitzing, and A. Yacoby. "Observation of electron-hole puddles in graphene using a scanning single-electron transistor". *Nat. Phys.* **4,** 144–148 (2007).
75. S. Samaddar, I. Yudhistira, S. Adam, H. Courtois, and C. B. Winkelmann. "Charge Puddles in Graphene near the Dirac Point". *Phys. Rev. Lett.* **116,** 126804 (2016).
76. C. Gutiérrez, D. Walkup, F. Ghahari, C. Lewandowski, J. F. Rodriguez-Nieva, K. Watanabe, T. Taniguchi, L. S. Levitov, N. B. Zhitenev, and J. A. Stroscio. "Interaction-driven quantum Hall wedding cake-like structures in graphene quantum dots". *Science* **361,** 789–794 (2018).
77. D. Walkup, F. Ghahari, C. Gutiérrez, K. Watanabe, T. Taniguchi, N. B. Zhitenev, and J. A. Stroscio. "Tuning single-electron charging and interactions between compressible Landau level islands in graphene". *Phys. Rev. B* **101,** 035428 (2020).
78. J. Lee, D. Wong, J. Velasco Jr, J. F. Rodriguez-Nieva, S. Kahn, H.-Z. Tsai, T. Taniguchi, K. Watanabe, A. Zettl, F. Wang, L. S. Levitov, and M. F. Crommie. "Imaging electrostatically confined Dirac fermions in graphene quantum dots". *Nat. Phys.* **12,** 1032–1036 (2016).
79. S.-Y. Li and L. He. "Recent progresses of quantum confinement in graphene quantum dots". *Frontiers of Physics volume* **17,** 33201 (2022).
80. Thomas Ihn. *Semiconductor Nanostructures* (Oxford University Press, 2010).
81. A. K. Paul, M. R. Sahu, C. Kumar, K. Watanabe, T. Taniguchi, and A. Das. "Interplay of filling fraction and coherence in symmetry broken graphene p-n junction". *Communications Physics* **3,** 171 (2020).
82. X. Zhou, A. Kerelsky, M. M. Elahi, D. Wang, K. M. M. Habib, R. N. Sajjad, P. Agnihotri, J. U. Lee, A. W. Ghosh, F. M. Ross, and A. N. Pasupathy. "Atomic-Scale Characterization of Graphene p-n Junctions for Electron-Optical Applications". *ACS Nano* **13,** , 2558–2566 (2019).
83. S. Matsuo, S. Takeshita, T. Tanaka, S. Nakaharai, K. Tsukagoshi, T. Moriyama, T. Ono, and K. Kobayashi. "Edge mixing dynamics in graphene p-n junctions in the quantum Hall regime". *Nat. Commun.* **6,** 8066 (2015).
84. N. Kumada, F. D. Parmentier, H. Hibino, D. C. Glattli, and P. Roulleau. "Shot noise generated by graphene p-n junctions in the quantum Hall effect regime". *Nat. Commun.* **6,** 8068 (2015).
85. F. Amet, J. R. Williams, K. Watanabe, T. Taniguchi, and D. Goldhaber-Gordon. "Selective Equilibration of Spin-Polarized Quantum Hall Edge States in Graphene". *Phys. Rev. Lett.* **112,** 196601 (2014).
86. P. Rickhaus, P. Makk, M.-H. Liu, E. Tóvári, M. Weiss, R. Maurand, K. Richter, and C. Schönenberger. "Snake trajectories in ultraclean graphene p-n junctions". *Nat. Commun.* **6,** 6470 (2015).

87. N. R. Cooper, and J. T. Chalker. "Coulomb interactions and the integer quantum Hall effect: Screening and transport". *Phys. Rev. B* **48,** 4530 (1993).

88. L.-J. Yin, Y. Zhang, J.-B. Qiao, S.-Y. Li, and Lin He. "Experimental observation of surface states and Landau levels bending in bilayer graphene". *Phys. Rev. B* **93,** 125422 (2016).

89. G. Li, A. Luican, and E. Y. Andrei. "Scanning Tunneling Spectroscopy of Graphene on Graphite". *Phys. Rev. Lett.* **102,** 176804 (2009).

90. K. Lai, W. Kundhikanjana, M. A. Kelly, Z.-X. Shen, J. Shabani, and M. Shayegan. "Imaging of Coulomb-Driven Quantum Hall Edge States". *Phys. Rev. Lett.* **107,** 176809 (2011).

91. J. R. Nagel. *Solving the Generalized Poisson Equation Using theFinite-Dierence Method* (2011).

92. J. Bardeen. "Tunnelling from a Many-Particle Point of View". *Phys. Rev. Lett.* **6,** 57 (1961).

93. J. Tersoff and D. R. Hamann. "Theory and Application for the Scanning Tunneling Microscope". *Phys. Rev. Lett.* **50,** 1998 (1983).

94. J. Tersoff and D. R. Hamann. "Theory of the scanning tunneling microscope". *Phys. Rev. B* **31,** 805 (1985).

95. F. J. Giessibl. "The qPlus sensor, a powerful core for the atomic force microscope". *Rev. Sci. Instrum.* **90,** 011101 (2019).

96. Florian Muckel. *Optimierung eines kombinierten Rastertunnel- und Rasterkraftmikroskops.* Diploma thesis (RWTH Aachen, 2013).

97. L. Gross, F. Mohn, N. Moll, P. Liljeroth, and G. Meyer. "The Chemical Structure of a Molecule Resolved by Atomic Force Microscopy". *Science* **325,** 1110–1114 (2009).

98. M. Liebmann, J. R. Bindel, M. Pezzotta, S. Becker, F. Muckel, T. Johnsen, C. Saunus, C. R. Ast, and M. Morgenstern. "An ultrahigh-vacuum cryostat for simultaneous scanning tunneling microscopy and magneto-transport measurements down to 400 mK". *Rev. Sci. Instrum.* **88,** 123707 (2017).

99. Jan Raphael Bindel. *Construction of a 390 mK-14 T scanning tunnelling microscope used for investigations of the random Rashba effect at the nanometre scale.* Dissertation (RWTH Aachen, 2016).

100. Stefan Becker. *Design of a 300 mK-14 T scanning tunneling microscopy system and characterization of quantum Hall systems with respect to Rashba spin splitting, exchange enhancement and Coulomb gap.* Dissertation (RWTH Aachen, 2011).

101. Mike Pezzotta. *A compact all-UHV ^{3}He-system for combined scanning probe and magnetotransport experiments down to 400 mK.* Dissertation (RWTH Aachen, 2018).

102. Jan Raphael Bindel. *Aufbau eines kombinierten Rasterkraft-/Rastertunnelmikroskops für Messungen unter Transportbedingungen.* Diploma thesis (RWTH Aachen, 2009).

103. J. Schwenk, S. Kim, J. Berwanger, F. Ghahari, D. Walkup, M. R. Slot, S. T. Le, W. G. Cullen, S. R. Blankenship, S. Vranjkovic, H. J. Hug, Y. Kuk, F. J. Giessibl, and J. A. Stroscio. "Achieving μeV tunneling resolution in an in-operando scanning tunneling microscopy, atomic force microscopy, and magnetotransport system for quantum materials research". *Rev. Sci. Instrum.* **91,** 071101 (2020).

104. D. Wong, S. Jeon, K. P. Nuckolls, M. Oh, S. C. J. Kingsley, and A. Yazdani. "A modular ultra-high vacuum millikelvin scanning tunneling microscope". *Rev. Sci. Instrum.* **91,** 023703 (2020).

105. T. Mashoff, M. Pratzer, and M. Morgenstern. "A low-temperature high resolution scanning tunneling microscope with a three-dimensional magnetic vector field operating in ultrahigh vacuum". *Rev. Sci. Instrum.* **80,** 053702 (2009).

106. Torge Mashoff. *Design of a low-temperature scanning tunnelling microscope system used to examine graphene nanomembranes.* Dissertation (RWTH Aachen, 2010).

107. C. Saunus, J. R. Bindel, M. Pratzer, and M. Morgenstern. "Versatile scanning tunneling microscopy with 120 ps time resolution". *Appl. Phys. Lett.* **102,** 051601 (2013).

108. Nils Freitag. *Low-Temperature Transport Measurements on Indium Soldered Graphene.* Diploma thesis (RWTH Aachen, 2011).

109. Vitus Merx. *Aufbau eines LN_2-Transportkryostaten.* Bachelorarbeit (RWTH Aachen, 2011).

110. E. Stolyarova, K. T. Rim, S. Ryu, J. Maultzsch, P. Kim, L. E. Brus, T. F. Heinz, M. S. Hybertsen, and G. W. Flynn. "High-resolution scanning tunneling microscopy imaging of mesoscopic graphene sheets on an insulating surface". *Proc. Natl. Acad. Sci. USA* **104,** 9209 –9212 (2007).

111. M Ishigami, J. H. Chen, W. G. Cullen, M. S. Fuhrer, and E. D. Williams. "Atomic Structure of Graphene on SiO_2". *Nano Lett.* **7,** 1643–1648 (2007).

112. G. Li, A. Luican, and E. Y. Andrei. "Self-navigation of a scanning tunneling microscope tip toward a micron-sized graphene sample". *Rev. Sci. Instrum.* **82,** 073701 (2011).

113. R. Decker, Y. Wang, V. W. Brar, W. Regan, H.-Z. Tsai, Q. Wu, W. Gannett, A. Zettl, and M. F. Crommie. "Local Electronic Properties of Graphene on a BN Substrate via Scanning Tunneling Microscopy". *Nano Lett.* **11,** 2291–2295 (2011).

114. Alexander Georgi. Private communication. 2015.

115. Florian Muckel. Private communication. 2021.

116. T. Johnsen, C. Schattauer, S. Samaddar, A. Weston, M. Hamer, K.Watanabe, T. Taniguchi, R. Gorbachev, F. Libisch, and M. Morgenstern. "Mapping quantum Hall edge states in graphene by scanning tunneling microscopy". *arXiv:2210.01831 [cond-mat.mes-hall]* (2022).

117. M. Yankowitz, J. Xue, D. Cormode, J. D. Sanchez-Yamagishi, K. Watanabe, T. Taniguchi, P. Jarillo-Herrero, P. Jacquod, and B. J. LeRoy. "Emergence of superlattice Dirac points in graphene on hexagonal boron nitride". *Nat. Phys.* **8,** 382–386 (2012).

118. C. R. Dean, A. F. Young, I.Meric, C. Lee, L. Wang, S. Sorgenfrei, K. Watanabe, T. Taniguchi, P. Kim, K. L. Shepard, and J. Hone. "Boron nitride substrates for high-quality graphene electronics". *Nature Nanotechnol.* **5,** 722–726 (2010).

119. N. B. Zhitenev, M. Brodsky, R. C. Ashoori, L. N. Pfeiffer, and K. W. West. "Localization-Delocalization Transition in Quantum Dots". *Science* **285,** 715–718 (1999).

120. M.-H. Liu, P. Rickhaus, P. Makk, E. Tóvári, R. Maurand, F. Tkatschenko, M. Weiss, C. Schönenberger, and K. Richter. "Scalable Tight-Binding Model for Graphene". *Phys. Rev. Lett.* **114,** 036601 (2015).

121. V. Lukose, R. Shankar, and G. Baskaran. "Novel Electric Field Effects on Landau Levels in Graphen". *Phys. Rev. Lett.* **98,** 116802 (2007).

122. Y.-S. Fu, M. Kawamura, K. Igarashi, H. Takagi, T. Hanaguri, and T. Sasagawa. "Imaging the two-component nature of Dirac-Landau levels in the topological surface state of Bi_2Se_3". *Nat. Phys.* **10,** 815–819 (2014).

123. J.R. Bindel, J. Ulrich, M. Liebmann, and M. Morgenstern. "Probing the Nodal Structure of Landau Level Wave Functions in Real Space". *Phys. Rev. Lett.* **118,** 016803 (2017).

124. D. Wong, J. Velasco Jr, L. Ju, J. Lee, S. Kahn, H.-Z. Tsai, C. Germany, T. Taniguchi, K. Watanabe, A. Zettl, F. Wang, and M. F. Crommie. "Characterization and manipulation of individual defects in insulating hexagonal boron nitride using scanning tunnelling microscopy". *Nat. Nanotechnology* **10,** 949–953 (2015).

125. S. J. Haigh, A. Gholinia, R. Jalil, S. Romani, L. Britnell, D. C. Elias, K. S. Novoselov, L. A. Ponomarenko, A. K. Geim, and R. Gorbachev. "Cross-sectional imaging of individual layers and buried interfaces of graphene-based heterostructures and superlattices". *Nat. Mater.* **11,** 764–767 (2012).

126. T. Mashoff, M. Pratzer, V. Geringer, T. J. Echtermeyer, M. C. Lemme, M. Liebmann, and M. Morgenstern. "Bistability and Oscillatory Motion of Natural Nanomembranes Appearing within Monolayer Graphene on Silicon Dioxide". *Nano Lett.* **10,** 461–465 (2010).

127. A. Georgi, P. Nemes-Incze, R. Carrillo-Bastos, D. Faria, S. Viola Kusminskiy, D. Zhai, M. Schneider, D. Subramaniam, T. Mashoff, N. M. Freitag, M. Liebmann, M. Pratzer, L. Wirtz, C. R. Woods, R. V. Gorbachev, Y. Cao, K. S. Novoselov, N. Sandler, and M. Morgenstern. "Tuning the Pseudospin Polarization of Graphene by a Pseudomagnetic Field". *Nano Lett.* **17,** 2240–2245 (2017).

128. V. Geringer, D. Subramaniam, A. K. Michel, B. Szafranek, D. Schall, A. Georgi, T. Mashoff, D. Neumaier, M. Liebmann, and M. Morgenstern. "Electrical transport and low-temperature scanning tunneling microscopy of microsoldered graphene". *Appl. Phys. Lett.* **96,** 082114 (2010).

129. R. Masutomi and T. Okamoto. "Adsorbate-induced quantum Hall system probed by scanning tunneling spectroscopy combined with transport measurements". *Appl. Phys. Lett.* **106,** 251602 (2015).

130. A. K. Geim, and I. V. Grigorieva. "Van der Waals heterostructures". *Nature* **499,** 419–425 (2013).

131. C.-P. Lu, G. Li, K. Watanabe, T: Taniguchi, and E. Y. Andrei. "MoS_2: Choice Substrate for Accessing and Tuning the Electronic Properties of Graphene". *Phys. Rev. Lett.* **113,** 156804 (2014).

132. R. Moriya, N. Yabuki, and T. Machida. "Superconducting proximity effect in a $NbSe_2$/graphene van der Waals junction". *Phys. Rev. B* **101,** 054503 (2020).

133. A. Avsar, J.Y. Tan, T. Taychatanapat, J. Balakrishnan, G.K.W. Koon, Y. Yeo, J. Lahiri, A. Carvalho, A.S. Rodin, E.C.T. O'Farrell, G. Eda, A.H. Castro Neto, and B. Özyilmaz. "Spin-orbit proximity effect in graphene". *Nat. Commun.* **5,** 4875 (2014).

134. X. Du, I. Skachko, F. Duerr, A. Luican, and E. Y. Andrei. "Fractional quantum Hall effect and insulating phase of Dirac electrons in graphene". *Nature* **462,** 192–195 (2009).

135. A. Georgi, P. Nemes-Incze, B. Szafranek, D. Neumaier, V. Geringer, M. Liebmann, and M. Morgenstern. "Apparent rippling with honeycomb symmetry and tunable periodicity observed by scanning tunneling microscopy on suspended graphene". *Phys. Rev. B* **94,** 184302 (2016).

136. Y. J. Song, A. F. Otte, Y. Kuk, Y. Hu, D. B. Torrance, P. N. First, W. A. de Heer, H. Min, S. Adam, M. D. Stiles, A. H. MacDonald, and J. A. Stroscio. "High-resolution tunnelling spectroscopy of a graphene quartet". *Nature Letters* **467,** 185–189 (2010).

137. L. Wang, I. Meric, P. Y. Huang, Q. Gao, Y. Gao, H. Tran, T. Taniguchi, K. Watanabe, L. M. Campos, D. A. Muller, J. Guo, P. Kim, J. Hone, K. L. Shepard, and C. R. Dean. "One-Dimensional Electrical Contact to a Two-Dimensional Material". *Science* **342,** 614–617 (2013).

138. Y. Zhang, Z. Jiang, J. P. Small, M. S. Purewal, Y.-W. Tan, M. Fazlollahi, J. D. Chudow, J. A. Jaszczak, H. L. Stormer, and P. Kim. "Landau-Level Splitting in Graphene in High Magnetic Fields". *Phys. Rev. Lett.* **96,** 136806 (2006).

139. Z. Jiang, Y. Zhang, H. L. Stormer, and P. Kim. "Quantum Hall States near the Charge-Neutral Dirac Point in Graphene". *Phys. Rev. Lett.* **99,** 106802 (2007).

140. Y. Huang, E. Sutter, N. N. Shi, J. Zheng, T. Yang, D. Englund, H.-J. Gao, and P. Sutter. "Reliable Exfoliation of Large-Area High-Quality Flakes of Graphene and Other Two-Dimensional Materials". *ACS Nano* **9,** 10612–10620 (2015).

141. V. Geringer, M. Liebmann, T. Echtermeyer, S. Runte, M. Schmidt, R. Rückamp, M. C. Lemme, and M. Morgenstern. "Intrinsic and extrinsic corrugation of monolayer graphene deposited on SiO_2". *Phys. Rev. Lett.* **102,** 076102 (2009).

142. M. Yankowitz, J. Xue, and B. J. LeRoy. "Graphene on hexagonal boron nitride". *J. Phys.: Condens. Matter* **26,** 303201 (2014).

143. Z. Hu, Z.-B. Liu, and J.-G. Tian. "Stacking of Exfoliated Two-Dimensional Materials: A Review". *Chin. J. Chem.* **38,** 981–995 (2020).

144. P. Blake, E. W. Hill, A. H. Castro Neto, K. S. Novoselov, D. Jiang, R. Yang, T. J. Booth, and A. K. Geim. "Making graphene visible". *Appl. Phys. Lett.* **91,** 063124 (2007).

145. A. V. Kretinin, Y. Cao, J. S. Tu, G. L. Yu, R. Jalil, K. S. Novoselov, S. J. Haigh, A. Gholinia, A. Mishchenko, M. Lozada, T. Georgiou, C. R. Woods, F. Withers, P. Blake, G. Eda, A. Wirsig, C. Hucho, K. Watanabe, T. Taniguchi, A. K. Geim, and R. V. Gorbachev. "Electronic Properties of Graphene Encapsulated with Different Two-Dimensional Atomic Crystals". *Nano Lett.* **14,** 3270–3276 (2014).

146. P. J. Zomer, S. P. Dash, N. Tombros, and B. J. van Wees. "A transfer technique for high mobility graphene devices on commercially available hexagonal boron nitride". *Appl. Phys. Lett.* **99,** 232104 (2011).

147. F. Pizzocchero, L. Gammelgaard, B. S. Jessen, J. M. Caridad, L. Wang, J.Hone, P. Bøggild, and T. J. Booth. "The hot pick-up technique for batch assembly of van der Waals heterostructures". *Nat. Commun.* **7,** 11894 (2016).

148. K. Kinoshita, R. Moriya, M. Onodera, Y. Wakafuji, S. Masubuchi, K. Watanabe, T. Taniguchi, and T. Machida. "Dry release transfer of graphene and few-layer h-BN byutilizing thermoplasticity of polypropylene carbonate". *npj 2D Materials and Applications* **3,** 22 (2019).

149. X.-X. Li, Z.-Q. Fan, P.-Z. Liu, M.-L. Chen, X. Liu, C.-K. Jia, D.-M. Sun, X.-W. Jiang, Z. Han, V. Bouchiat, J.-J. Guo, J.-H. Chen, and Z.-D. Zhang. "Gate-controlled reversible rectifying behaviour in tunnel contacted atomically-thin MoS_2 transistor". *Nat. Commun.* **8,** 970 (2017).

150. H. Polshyn, H. Zhou, E. M. Spanton, T. Taniguchi, K. Watanabe, and A. F. Young. "Quantitative Transport Measurements of Fractional Quantum Hall Energy Gaps in Edgeless Graphene Devices". *Phys. Rev. Lett.* **121,** 226801 (2018).

151. Y. Zeng, J. I. A. Li, S. A. Dietrich, O. M. Ghosh, K. Watanabe, T. Taniguchi, J: Hone, and C. R. Dean. "High-Quality Magnetotransport in Graphene Using the Edge-Free Corbino Geometry". *Phys. Rev. Lett.* **122,** 137701 (2019).

152. J, Sonntag, J. Li, A. Plaud, A. Loiseau, J. Barjon, J. H. Edgar, and C. Stampfer. "Excellent electronic transport in heterostructures of graphene and monoisotopic boron-nitride grown at atmospheric pressure". *2D Mater.* **7,** 031009 (2020).

153. Y. Cao, V. Fatemi, S. Fang, K. Watanabe, T. Taniguchi, E. Kaxiras, and P. Jarillo-Herrero. "Unconventional superconductivity in magic-angle graphene superlattices". *Nature* **556,** 43–50 (2018).

154. M. Eich, F. Herman, R. Pisoni, H. Overweg, A. Kurzmann, Y. Lee, P. Rickhaus, K. Watanabe, T. Taniguchi, M. Sigrist, T. Ihn, and K. Ensslin. "Spin and Valley States in Gate-Defined Bilayer Graphene Quantum Dots". *Phys. Rev. X* **8,** 031023 (2018).

155. D. G. Purdie, N. M. Pugno, T. Taniguchi, K. Watanabe, A. C. Ferrari, and A. Lombardo. "Cleaning interfaces in layered materials heterostructures". *Nat. Commun.* **9,** 5387 (2018).

156. N. J. G. Couto, D. Costanzo, S. Engels, D.-K. Ki, K. Watanabe, T. Taniguchi, C. Stampfer, F. Guinea, and A. F. Morpurgo. "Random Strain Fluctuations as Dominant Disorder Source for High-Quality On-Substrate Graphene Devices". *Phys. Rev. X* **4,** 041019 (2014).

157. Y. Kim, P. Herlinger, T. Taniguchi, K. Watanabe, and J. H. Smet. "Reliable Postprocessing Improvement of van der Waals Heterostructures". *ACS Nano* **13,** 14182–14190 (2019).

158. S. Chen, J. Son, S. Huang, K. Watanabe, T. Taniguchi, R. Bashir, A. M. van der Zande, and W. P. King. "Tip-Based Cleaning and Smoothing Improves Performance in Monolayer MoS2 Devices". *ACS Omega* **6,** 4013–4021 (2021).

159. J. Mao, Y. Jiang, D. Moldovan, G. Li, K. Watanabe, T. Taniguchi, M. R. Masir, F. M. Peeters, and E Y. Andrei. "Realization of a tunable artificial atom at a supercritically charged vacancy in graphene". *Nat. Phys.* **12,** 545–549 (2016).

160. Y. Jiang, J. Mao, D. Moldovan, M. R. Masir, G. Li, K. Watanabe, T. Taniguchi, F. M. Peeters, and E. Y. Andrei. "Tuning a circular p-n junction in graphene from quantum confinement to optical guiding". *Nat. Nanotechnology* **12,** 1045–1049 (2017).

161. J. Xue, J. Sanchez-Yamagishi, D. Bulmash, P. Jacquod, A. Deshpande, K. Watanabe, T. Taniguchi, P. Jarillo-Herrero, and B. J. LeRoy. "Scanning tunnelling microscopy and spectroscopy of ultra-flat graphene on hexagonal boron nitride". *Nat. Mater.* **10,** 282–285 (2011).

162. Y. Jiang, X. Lai, K. Watanabe, T. Taniguchi, K. Haule, J. Mao, and E. Y. Andrei. "Charge order and broken rotational symmetry in magic-angle twisted bilayer graphene". *Nature* **573,** 91–95 (2019).

163. Y. Choi, J. Kemmer, Y. Peng, A. Thomson, H. Arora, R. Polski, Y. Zhang, H. Ren, J. Alicea, G. Refael, F. von Oppen, K. Watanabe, T. Taniguchi, and S. Nadj-Perge. "Electronic correlations in twisted bilayer graphene near the magic angle". *Nat. Phys.* **15,** 1174–1180 (2019).

164. A. Kerelsky, L. J. McGilly, D. M. Kennes, L. Xian, M. Yankowitz, S. Chen, K. Watanabe, T. Taniguchi, J. Hone, C. Dean, A. Rubio, and A. N. Pasupathy. "Maximized electron interactions at the magic angle in twisted bilayer graphene". *Nature* **572,** 95–100 (2019).

165. Y. Xie, B. Lian, B. Jäck, X. Liu, C.-L. Chiu, K. Watanabe, T. Taniguchi, B. A. Bernevig, and A. Yazdani. "Spectroscopic signatures of many-body correlations in magic-angle twisted bilayer graphene". *Nature* **572,** 101–105 (2019).

166. F. Lüpke, D. Waters, S. C. de la Barrera, M. Widom, D. G. Mandrus, J. Yan, R. M. Feenstra, and B. M. Hunt. "Proximity-induced superconducting gap in the quantum spin Hall edge state of monolayer WTe_2". *Nat. Phys.* **16,** 526–530 (2020).

167. H. Li, S. Li, M. H. Naik, J. Xie, X. Li, J. Wang, E. Regan, D. Wang, W. Zhao, S. Zhao, S. Kahn, K. Yumigeta, M. Blei, T. Taniguchi, K. Watanabe, S. Tongay, A. Zettl, S. G. Louie, F. Wang, and M. F. Crommie. "Imaging moiré flat bands in three-dimensional reconstructed WSe_2 /WS_2 superlattices". *Nat. Mater.* **20,** 945–950 (2021).

168. X. Liu, C.-L. Chiu, J. Y. Lee, G. Farahi, K. Watanabe, T. Taniguchi, A. Vishwanath, and A. Yazdani. "Spectroscopy of a tunable moir'e system with a correlated and topological flat band". *Nat. Commun.* **12,** 2732 (2021).

169. A. G. F. Garcia, M. Neumann, F. Amet, J. R. Williams, K. Watanabe, T. Taniguchi, and D. Goldhaber-Gordon. "Effective Cleaning of Hexagonal Boron Nitride for Graphene Devices". *Nano Lett.* **12,** 4449–4454 (2012).

170. C. Ö. Girit, and A. Zettl. "Soldering to a single atomic layer". *Appl. Phys. Lett.* **91,** 193512 (2007).

171. Tjorven Johnsen. *Herstellung von Graphenproben auf Bornitrid und Charakterisierung mittels Magnetotransport.* Master thesis (RWTH Aachen, 2014).

172. N. Staley, H. Wang, C. Puls, J. Forster, T. N. Jackson, K. McCarthy, B. Clouser, and Y. Liu. "Lithography-free fabrication of graphene devices". *Appl. Phys. Lett.* **90,** 143518 (2007).

173. W. Bao, G. Liu, Z. Zhao, H. Zhang, D. Yan, A. Deshpande, B. LeRoy, and C. N. Lau. "Lithography-free fabrication of high quality substrate-supported and freestanding graphene devices". *Nano Res.* **3,** 98–102 (2010).

174. D. H. Tien, J.-Y. Park, K. B. Kim, N. Lee,and Y. Seo. "Characterization of Graphene-based FET Fabricated using a Shadow Mask". *Sci Rep* **6,** 25050 (2016).

175. F.-Y. Shih, S.-Y. Chen, C.-H. Liu, P.-H. Ho, T.-S. Wu, C.-W. Chen, Y.-F. Chen, and W.-H. Wang. "Residue-free fabrication of high-performance graphene devices by patterned PMMA stencil mask". *AIP Advances* **4,** 067129 (2014).

176. Y. Zhang, V. W. Brar, F. Wang, C. Girit, Y. Yayon, M. Panlasigui, A. Zettl, and M. F. Crommie. "Giant phonon-induced conductance in scanning tunnelling spectroscopy of gate-tunable graphene". *Nat. Phys.* **4,** 627–630 (2008).

177. S.-Y. Li, Y. Zhang, L.-J. Yin, and L. He. "Scanning tunneling microscope study of quantum Hall isospin ferromagnetic states in the zero Landau level in a graphene monolaye". *Phys. Rev. B* **100,** 085437 (2019).

178. O. E. Dial, R. C. Ashoori, L. N. Pfeiffer, and K. W. West. "Anomalous structure in the single particle spectrum of the fractional quantum Hall effect". *Nature Letters* **464,** 566–570 (2010).

179. Felix M. Jekat. *Graphen-Proben für Rastertunnelspektroskopie im Quanten-Hall Bereich Präparation und Transportcharakterisierung.* Master thesis (RWTH Aachen, 2015).

180. Bertram Schulze Lammers. *Aufbau und Test eines Au-Verdampfers.* Bachelor thesis (RWTH Aachen, 2016).

181. Michael Weimer. *Optimization of Graphene/hBN/Graphite Stacks on Mica.* Master thesis (RWTH Aachen, 2018).

182. L. Liu, Z. Chen, L. Wang, E. Polyakova (Stolyarova), T. Taniguchi, K. Watanabe, J. Hone, G. W. Flynn, and L. E. Brus. "Slow Gold Adatom Diffusion on Graphene: Effect of Silicon Dioxide and Hexagonal Boron Nitride Substrates". *J. Phys. Chem. B* **117,** 4305–4312 (2013).

183. A. Schäpers, J. Sonntag, L. Valerius, B. Pestka, J. Strasdas, K. Watanabe, T. Taniguchi, L. Wirtz, M. Morgenstern, B. Beschoten, R. J. Dolleman, and C. Stampfer. "Raman imaging of twist angle variations in twisted bilayer graphene at intermediate angles". *2D Mater.* **9,** 045009 (2022).

184. Daniel Montag. Private communication. 2020.

185. D. A. Abanin and L. S. Levitov. "Conformal invariance and shape-dependent conductance of graphene samples". *Phys. Rev. B* **78,** 035416 (2008).

186. A. F. Young, J. D. Sanchez-Yamagishi, B. Hunt, S. H. Choi, K. Watanabe, T. Taniguchi, R. C. Ashoori, and P. Jarillo-Herrero. "Tunable symmetry breaking and helical edge transport in a graphene quantum spin Hall state". *Nature* **505,** 528–532 (2014).

187. K. I. Bolotin, F. Ghahari, M. D. Shulman, H. L. Stormer, and P. Kim. "Observation of the fractional quantum Hall effect in graphene". *Nature Letters* **462,** 196–199 (2009).

188. H. L. Stormer. "Nobel Lecture: The fractional quantum Hall effect". *Rev. Mod. Phys.* **71,** 875–889 (1999).

189. S. Becker, C. Karrasch, T. Mashoff, M. Pratzer, M. Liebmann, V. Meden, and M. Morgenstern. "Probing Electron-Electron Interaction in Quantum Hall Systems with Scanning Tunneling Spectroscopy". *Phys. Rev. Lett.* **106,** 156805 (2011).

190. A. L. Efros, and B. I. Shklovskii. "Coulomb gap and low temperature conductivity of disordered systems". *J. Phys. C: Solid State Phys.,* L49 (1975).

191. Michael Weimer. *Herstellung und Charakterisierung von Graphen auf Bornitrid auf Glimmer.* Bachelor thesis (RWTH Aachen, 2016).

192. Yanting Liu. *Novel Design of Graphene/hBN/Graphite Based Transistor.* Master thesis (RWTH Aachen, 2019).

193. Rosen Sofroniev. *Gated graphene/hBN/graphite stacks for combined measurements by transport and scanning tunneling microscopy.* Master thesis (RWTH Aachen, 2020).

194. Julian Hürtgen. *Implementing a reliable Process for gated Graphene-Stacks compatible with Scanning Tunneling Microscopy.* Master thesis (RWTH Aachen, 2021).

195. L. Banszerus, M. Schmitz, S. Engels, J. Dauber, M. Oellers, F. Haupt, K. Watanabe,T. Taniguchi, B. Beschoten, and C. Stampfer. "Ultrahigh-mobility graphene devices from chemical vapor deposition on reusable copper". *Sci. Adv.* **1,** e150022 (2015).

196. Y. Cao, A. Mishchenko, G. L. Yu, E. Khestanova, A. P. Rooney, E. Prestat, A. V. Kretinin, P. Blake, M. B. Shalom, C. Woods, J. Chapman, G. Balakrishnan, I. V. Grigorieva, K. S. Novoselov, B. A. Piot, M. Potemski, K. Watanabe, T. Taniguchi, S. J. Haigh, A. K. Geim, and R. V. Gorbachev. "Quality Heterostructures from Two-Dimensional Crystals Unstable in Air by Their Assembly in Inert Atmosphere". *Nano Lett.* **15,** 4914–4921 (2015).

197. Z. Sun, X. Han, Z. Cai, S. Yue, D. Geng, D. Rong, L. Zhao, Y.-Q. Zhang, P. Cheng, L. Chen, X. Zhou, Y. Huang, K. Wu, and B. Feng. "Exfoliation of 2D van der Waals crystals in ultrahigh vacuum for interface engineering". *Science Bulletin* **67,** 1345–1351 (2022).

198. A. Grubišić-Čabo, M. Michiardi, C. E. Sanders, M. Bianchi, D. Curcio, D. Phuyal, M. H. Berntsen, Q. Guo, and M. Dendzik. "In-situ exfoliation method of large-area 2D materials". *arXiv:2209.15030 [cond-mat.mtrl-sci]* (2022).

199. Z. Fei, T. Palomaki, S. Wu, W. Zhao, X. Cai, B. Sun, P. Nguyen, J. Finney, X. Xu, and D. H. Cobden. "Edge conduction in monolayer WTe2". *Nat. Phys.* **13,** 677–682 (2017).

200. K. Choi, Y. T. Lee, S.-W. Min, H. S. Lee, T. Nam, H. Kim, and S. Im. "Direct imprinting of MoS_2 flakes on a patterned gate for nanosheet transistors". *J. Mater. Chem. C* **1,** 7803 (2013).

201. L. Yu, D. El-Damak, U. Radhakrishna, X. Ling, A. Zubair, Y. Lin, Y. Zhang, M.-H. Chuang, Y.-H. Lee, D. Antoniadis, J. Kong, A. Chandrakasan, and T. Palacios. "Design, Modeling, and Fabrication of Chemical Vapor Deposition Grown MoS_2 Circuits with E-Mode FETs for Large-Area Electronics". *Nano Lett.* **16,** 6349 (2016).

202. L. A. Cohen, N. L. Samuelson, T. Wang, K. Klocke, C. C. Reeves, T. Taniguchi, K. Watanabe, S. Vijay, M. P. Zaletel, and A. F. Young. "Tunable fractional quantum Hall point contacts in graphene via local anodic oxidation of graphite gates". *arXiv:2204.10296 [cond-mat.mes-hall]* (2022).